Imaging neural activity in vitro and in vivo using genetically-encoded calcium indicators

Walker, Alison Sarah

Awarding institution:
King's College London

Imaging neural activity *in vitro* and *in vivo* using genetically-encoded calcium indicators

Alison Walker

A thesis for the Degree of Doctor of Philosophy

March 2014

MRC Centre for Developmental Neurobiology

King's College London

Table of Contents

Figures....5
Abstract....7
Acknowledgements....8
Abbreviations....9
1 Introduction 11
1.1 Calcium Indicators 11
1.1.1 Synthetic dyes and genetically-encoded calcium indicators 11
1.1.1.1 FRET-based genetically-encoded calcium indicators 12
1.1.1.2 Single fluorophore genetically-encoded calcium indicators 13
1.2 Recording synaptic transmission with GECIs 16
1.2.1 Presynaptic calcium influx 16
1.2.1.1 Measuring calcium influx at the presynapse 16
1.2.2 Postsynaptic calcium influx 17
1.2.2.1 Glutamate Receptors 18
1.2.2.2 Voltage-gated calcium channels 19
1.2.2.3 Internal Stores 21
1.2.2.4 Measuring calcium concentrations at the postsynapse 21
1.2.3 Quantal variability 23
1.2.3.1 Postsynaptic sources of quantal variability 23
1.2.3.2 Presynaptic sources of quantal variability 25
1.2.4 Synaptic democracy 27
1.2.4.1 Distance-dependent scaling of AMPA receptors 27
1.2.4.2 Biophysical properties of dendrites and spines 28
1.3 Using GECIs to study neuronal output *in vivo* in the larval zebrafish 30
1.4 The zebrafish retinotectal system 31
1.4.1 Development of the retinotectal system in zebrafish 34
1.4.1.1 Functions of the zebrafish visual system 35
1.4.1.2 Mechanisms of direction-selectivity 36
1.4.1.3 Mechanisms of orientation-selectivity 38
1.5 Thesis outline 39
2 Materials and Methods 41
2.1 Materials 41
2.1.1 Plasmids 41
2.1.2 Drugs and chemicals 41
2.1.3 Experimental Solutions 42
2.2 Methods 42
2.2.1 Sub-cloning of CMV:GECIs 42
2.2.2 Preparation of dissociated hippocampal cultures 43

2.2.3 Transfection of hippocampal neurons 43
2.2.4 Imaging of dissociated hippocampal neurons 44
2.2.5 FM 4-64 labelling of SyGCaMP3 expressing neurons 45
2.2.6 Characterisation of GECIs with extracellular field stimulation 45
2.2.7 Data analysis of characterisation of GECIs with extracellular field stimulation . 45
2.2.8 Correction for rundown of RGECO, SyGCaMP3 and SyRGECO 46
2.2.9 MNI-glutamate uncaging and imaging 47
2.2.10 Analysis of MNI-glutamate uncaging data 48
2.2.11 Imaging spontaneous neurotransmitter release 48
2.2.12 Analysis of spontaneous data 49
2.2.13 Immunocytochemistry 50
2.2.14 Zebrafish 51
2.2.15 Mosaic labelling of single neurons in the larval zebrafish 52
2.2.16 Drifting bar stimulation of RGCs and tectal neurons 52
2.2.17 Imaging of larval zebrafish 54
2.2.18 Voxel-wise analysis of orientation- and direction-selectivity 54
3 Chapter 3: Characterisation of genetically-encoded calcium indicators 56
3.1 Introduction 56
3.2 Results 58
3.2.1 Characterisation of RGECO 58
3.2.2 Characterisation of SyGCaMP3 and SyRGECO 68
3.2.3 Characterisation of PSDGCaMP3 73
3.3 Discussion 79
3.3.1 Characterisation of RGECO 79
3.3.2 Characterisation of SyGCaMP3 and SyRGECO 81
3.3.3 Characterisation of PSDGCaMP3 82
3.3.4 Future Work 85
4 Chapter 4: Mapping quantal synaptic properties across dendritic trees using GCaMP3 ... 88
4.1 Introduction 88
4.2 Results 90
4.2.1 Characterisation of calcium transients evoked by spontaneous neurotransmitter release 90
4.2.2 Variability in QCT amplitude and frequency 97
4.2.3 The spatial distribution of activity across dendritic trees 104
4.2.3.1 How do functional correlations with dendritic distance arise? 111
4.3 Discussion 116
4.3.1 Postsynaptic calcium transients in dendritic spines of cultured hippocampal neurons 116
4.3.2 Single spine variability in quantal calcium transient amplitude 116
4.3.3 Relative distance-dependent correlations along dendritic branches 118

4.3.4 Putative mechanisms to assemble distance-dependent scaling 121
4.3.5 Rundown in QCT amplitude may represent a biological process 123
4.3.6 ΔF/F is a suitable metric for recording QCTs..... 123
4.3.7 Future work..... 124
5 Chapter 5: The structural and functional development of direction- and orientation-selectivity in the larval zebrafish *in vivo* 125
5.1 Introduction 125
5.2 Results..... 128
5.2.1 The functional development of single SyGCaMP3-expressing RGCs in response to moving bar stimuli 128
5.2.1.1 Developmental refinement of single orientation-selective RGCs..... 131
5.2.1.2 Developmental invariance of a single direction-selective RGC 137
5.2.2 The functional development of single RGECO expressing tectal neurons in response to moving bar stimuli 137
5.2.2.1 Development of single orientation-selective tectal neurons 138
5.2.2.2 Morphological examination of vertically tuned OS tectal cells 141
5.3 Discussion..... 143
5.3.1 The functional and structural development of an example direction-selective RGC 143
5.3.2 The functional and structural development of example orientation-selective RGCs 144
5.3.3 Putative mechanisms for differential developmental programming of direction- and orientation-selective RGCs..... 146
5.3.4 The functional and structural development of vertically-tuned orientation-selective tectal cells 147
5.3.5 Future Work..... 148
6 Summary..... 150

Figures

Chapter 1: Introduction

Figure 1.1 Schematic of GECI calcium binding and neuronal expression patterns……..15
Figure 1.2 The synapse……..22
Figure 1.3 Zebrafish visual system……..33
Figure 1.4 Timeline of zebrafish visual system development……..35

Chapter 2: Materials and Methods

Figure 2.1 Potential normalisation routines for RGECO rundown……..47
Figure 2.2 Building dendritic trees……..51
Figure 2.3 The experimental set-up for visual stimulation of larval zebrafish……53

Chapter 3: Characterisation of genetically-encoded calcium indicators

3.2 Results

Figure 3.2.1 GCaMP3 and RGECO respond to extracellular stimulation in co-transfected dissociated hippocampal neurons……..59
Figure 3.2.2 RGECO responses exhibit a progressive rundown……..60
Figure 3.2.3 RGECO rundown is caused by exposure to excitation light……62
Figure 3.2.4 Characterisation of GCaMP3 and RGECO using confocal microscopy prevents RGECO rundown……..63
Figure 3.2.5 RGECO exhibits both a high dynamic range and high sensitivity……..65
Figure 3.2.6 Characterisation of GCaMP3 and RGECO in singly transfected hippocampal neurons using widefield microscopy……66
Figure 3.2.7 Rise and decay phase kinetics for RGECO and GCaMP3……67
Figure 3.2.8 SyGCaMP3 and SyRGECO expression is localised to presynaptic boutons……..69
Figure 3.2.9. Characterisation of SyGCaMP3 and SyRGECO in co-transfected neurons in response to extracellular stimulation……..70
Figure 3.2.10 Comparison of synaptophysin-fusion and cytosolic GECIs……..72
Figure 3.2.11 Characterisation of PSDGCaMP3 in dissociated hippocampal neurons in response to synaptic activation……74
Figure 3.2.12 Cytosolic GCaMP3 acts similarly to PSDGCaMP3 in response to synaptic activation……..76

3.3 Discussion

Figure 3.3.1 Different length uncaging pulses recruit different sources of calcium influx…84

Chapter 4: Mapping quantal synaptic properties across dendritic trees using GCaMP3

4.1 Introduction

4.2 Results

Figure 4.2.1 GCaMP3 and RGECO detect QCTs which are NMDA receptor dependent……..91
Figure 4.2.2 QCT amplitude and frequency decrease over a 10 minute period in control conditions……93
Figure 4.2.3 Contribution of AMPA receptors and R-type voltage-gated calcium channels to QCTs……95
Figure 4.2.4 Contribution of calcium-activated potassium channels and internal stores to QCTs……96
Figure 4.2.5 Cell-wide QCT amplitude and frequency are highly heterogeneous……98
Figure 4.2.6 QCTs have both a large interspine and intraspine variability……99
Figure 4.2.7 High variability of intraspine QCT amplitude is not due to time-dependent rundown in QCT amplitude or limitations in temporal resolution……101
Figure 4.2.8 Repetitive uncaging of glutamate at single spines induces calcium transients with high variability in amplitude……102

Figure 4.2.9 AMPA receptors, internal stores, R-type VGCCs and SK calcium-activated potassium channels do not contribute to high intraspine amplitude variability……103
Figure 4.2.10 High instantaneous frequency predicts lower QCT amplitudes……104
Figure 4.2.11 The distribution of activity across dendritic trees……..105
Figure 4.2.12 QCT amplitude scales with relative distance but not number of nodes, nor distance from soma……107
Figure 4.2.13 Distance dependence of the integral, instantaneous frequency and CV of QCTs……..108
Figure 4.2.14 The ΔG/R response metric reports QCTs similar to the ΔF/F metric……110
Figure 4.2.15 TagRFP intensity scales with relative distance across dendritic trees……..112
Figure 4.2.16 PSD-95 and GluN1 inversely scale with relative distance……..114
Figure 4.2.17 Relative distance-dependent correlations with amplitude is not seen with glutamate uncaging across the dendritic tree……115
4.3 Discussion
4.3.1 Putative mechanism for spines at high relative distance having larger calcium transients……..121

Chapter 5: The structural and functional development of direction- and orientation-selectivity in the larval zebrafish *in vivo*
5.1 Introduction
5.1 The development of direction- and orientation-selective RGC axon termination zones within the tectal neuropil……126
5.2 Results
Figure 5.2.1 Analysing the functional and structural properties of single RGC axon arbours in the larval zebrafish……130
Figure 5.2.2 Example RGC 1: Qualitative analysis of structural and functional development..132
Figure 5.2.3 Example RGC 1: Quantitative analysis of orientation-selectivity at different developmental stages……..133
Figure 5.2.4 Example RGC 2: Structural analysis and description of orientation-selectivity at different development at stages……..135
Figure 5.2.5 Example RGC 3: Structural analysis and description of orientation-selectivity at different development at stages……..136
Figure 5.2.6 Example RGC 4: Structural analysis and description of direction-selectivity at different development at stages……..138
Figure 5.2.7 Example tectal cell 1: Qualitative and quantitative analysis of structural and functional development. ……..140
Figure 5.2.8 Example tectal cell 2: Quantitative analysis of functional development……141
Figure 5.2.9 Morphological similarities of vertically tuned orientation-selective neurons…….142
5.3 Discussion

Abstract

The projects in this thesis use genetically-encoded calcium indicators (GECIs) to investigate neural activity both *in vitro,* in dissociated hippocampal neurons, and *in vivo,* in the visual system of the larval zebrafish. We first characterised the properties of established and newly-generated GECIs in dissociated hippocampal neurons. Our first question dealt with understanding how quantal excitatory activity is distributed across the dendritic tree of dissociated hippocampal neurons. In neurons expressing GCaMP3 we recorded small NMDA receptor-dependent calcium transients, in the presence of tetrodotoxin. These were localised to dendritic spines and highly heterogeneous in terms of amplitude and frequency, both at single synapses and across the dendritic tree. Precise mapping of quantal synaptic events onto dendritic arbours of individual neurons determined that the amplitude of calcium transients correlated with the location of the spine within a branch, with larger calcium transients found closer to branch ends. One aim of this thesis was to investigate how this spatial distribution of activity arises. A second question was to understand how single motion-sensitive neurons in the retinotectal system of the larval zebrafish develop their functional properties? The function of single retinal ganglion cells labelled with SyGCaMP3, or single tectal cells labelled with RGECO was probed by playing a drifting bar visual presentation to the same awake larvae at different timepoints during their development (3-7 days post fertilisation). As larval zebrafish can see prior to the full maturation of their visual circuitry, our approach gives insight into how ongoing circuit maturation impacts on the function output of single neurons. We discovered that some classes of motion-sensitive neurons appear functionally invariant during development, suggesting insensitivity to ongoing circuit refinement, while others classes mature through a period of functional refinement.

Acknowledgements

I would like to start by thanking my supervisors Martin Meyer and Juan Burrone. Your support, encouragement and enthusiasm have been invaluable. Thank you for letting me be a part of your labs. It feels like it's flown by so quickly but it's been a fantastic experience from beginning to end.

Next I'd like to thank the lab. Paul Hunter ('the nicest guy I know without being annoying') has had the dubious honour of becoming my go-to guy. I would like to thank him for being so patient with my questions and always taking the time and effort to go through things with me. Thank you Nikolas Nikolaou, you've been so dependable over the last 3 years, and a veritable fountain of knowledge. And finally, Fatima Abbas, thank you for helping me about the lab and amusing me with your wickedly dry humour.

I need to say a big thank you to Andrew Lowe for creating the software that is used in this thesis, and for both having the patience to explain it to me and doing that so well that I actually understand it. Thanks Mideia Kotsogianni for all the hippocampal cultures you have done over the past 3 years, and the Grubb Lab for letting me snaffle up your spares.

Ian Thompson, Britta Eickholt and Ester Bell have been fantastic postgraduate supervisors over the last 4 years, always ready with advice and encouragement.

I'd like to take this opportunity to say what an amazing time I have had being part of the MRC Centre for Developmental Neurobiology. From the first minute of my interview I felt such a good vibe about this place. Everyone has been so friendly; from the people I play Thursday football with, the crowd in coffee club, fellow demonstrators and science event people to everyone at each of our fantastic retreats. It has been an amazingly fun few years so thank you.

I'd like to thank some friends and housemates for making my time in London so enjoyable. Thank you for being such good friends Toni, Cat, Adele, Sophie B, Laura, Ange, Vicky, Lisa, Chloe, Tash, Callum, Alex, Jason, Jay, Sophie P, Morag, Guy, Ben, Dave and last but not least Sarah.

Mark, I can't imagine now what doing my PhD would have been like without you, you've been such an important part of it from our very first day. Thank you so much for the love and support you give me.

I'd like to finish by thanking my family. It's been amazing knowing you'll always be there to support me; Mum, Pops, Helen, Phil, Andrew and Becca. And of course for I have to mention my little ray of sunshine, Mellymoo, who I can't believe wasn't even born when I started this PhD, and now I'm so happy that there's little Leo too.

Abbreviations

AIS	Axon initial segment
AMPA	α-Amino-3-hydroxy-5-methyl-4-isoxazolepropionic acid
AP	Action Potential
APV	2-amino-5-phosphovaleric acid
ath5	Athonal homolog 5
bpAP	Back-propagating action potential
CA	Cornu Ammonis
CNQX	6-cyano-7-nitroquinoxaline-2,3-dione
DG	Dentate granule
dH_20	Distilled water
dpf	Days post-fertilisation
DS	Direction-selective
DSI	Direction-selectivity index
EM	Electron microscopy
EPSC	Excitatory postsynaptic current
EPSP	Excitatory postsynaptic potential
FM 4-64	[N-(3-triethylammoniumpropyl)-4-(6-(4-diethylamino)phenyl)hexatrienyl)pyridinium dibromide]
FRET	Förster resonance energy transfer
GABA	γ-Aminobutyric acid
GECI	Genetically-encoded calcium indicator
HBSS	Hank's balanced salt solution
INL	Inner nuclear layer
IPL	Inner Plexiform Layer
LGN	Lateral geniculate nucleus
mEPSC	Miniature excitatory postsynaptic current
MIP	Maximum intensity projection
NBQX	2,3-dihydroxy-6-nitro-7-sulfamoyl-benzo[f]quinoxaline-2,3-dione
NMDA	*N*-Methyl-D-aspartate
ONL	Outer nuclear layer
OPL	Outer plexiform layer
OS	Orientation-selective
OSI	Orientation-selectivity index
pS	Picosiemens
PSD	Postsynaptic density
PSDGCaMP3	PSD-95-GCaMP3
PVN	Periventricular neurons

QCT	Quantal calcium transient
RGC	Retinal ganglion cell
RGECO	RGECO-1
RP	Reserve pool
RRP	Readily-releasable pool
SAC	Stratum album central
S.E.M	Standard error of the mean
SFGS	Stratum fibrosum et griseum superficiale
SGC	Stratum griseum central
SLM	Stratum lacunosum-moleculare
SNARE	Soluble NSF (N-ethylmaleimide-sensitive factor) attachment receptor
SO	Stratum opticum
SPV	Stratum periventriculare
SR	Stratum radiatum
SyGCaMP3	Synaptophysin-GCaMP3
SyRGECO	Synaptophysin-RGECO
TTX	Tetrodotoxin
VGCCs	Voltage-gated calcium channels

1 Introduction

The projects that have been pursued in this thesis are reliant on recording from neurons non-invasively and over extended periods of time *in vivo*, and recording neural activity at the site of synaptic transmission. Additionally, it was important in these experiments that recordings were made with adequate spatial resolution to describe activity in relation to neuronal structure and morphology. None of these tasks are easily achieved using electrophysiology, which is in general invasive and difficult to conduct over long timescales. The relatively large size of electrodes renders it difficult to record electrophysiologically at small subcellular compartments. In addition, limitations arising from recording from single sites greatly reduce the spatial resolution of this method. Instead, calcium imaging can fulfil all these requirements. Monitoring intracellular calcium concentration acts as an indirect measure of action potential firing because when a neuron fires an action potential a wave of depolarisation will travel both down the axon and antidromically into the dendrites. Voltage-gated calcium channels (VGCCs) expressed within the axon, soma and dendrites will be activated by suprathreshold depolarisation, permitting the flux of calcium into the cell. The magnitude of this calcium influx is highly proportional to the amount of neuronal activity (Helmchen et al., 1996; Smetters et al., 1999). In addition, calcium influx plays key roles in both the pre- and postsynapse during neurotransmission (see below). Calcium indicators are fluorescent molecules which measure intracellular calcium concentration through their binding to calcium, which causes a change in indicator fluorescence intensity. Intuitively, there are several qualities a good calcium indicator needs to have, i.e. a fluorescence signal which can proportionally read out both low and high amounts of neural activity with good temporal resolution. Other qualities include permitting visualisation of individual neurons and neuronal morphology and the ability to chronically image activity over long timescales. There are different types of calcium indicators which vary in their ability to fulfil these criteria, which I will outline here below.

1.1 Calcium Indicators

1.1.1 Synthetic dyes and genetically-encoded calcium indicators

Synthetic calcium dyes typically consist of ethylene glycol tetraacetic acid (EGTA) or 1,2-bis(o-aminophenoxy) ethane-N,N,N',N'-tetraacetic acid (BAPTA) calcium chelating organic compounds, incorporated with fluorescent groups. The gold standard synthetic dye is Oregon Green 488 BAPTA-1 (OGB) which exhibits high sensitivity to the firing of a single action

potential and has fast rise and decay kinetics (Hendel et al., 2008). As such, OGB has been used to study neural activity in many different model systems and for many applications (Svoboda et al., 1999; Ohki et al., 2006; Hunter et al., 2013; Sumbre and Poo, 2013). However, synthetic dyes have some limitations. To label single neurons calcium dyes are often loaded into cells via patch pipettes. This technique is invasive and prevents imaging over extended time periods. An alternative method of delivery is electroporation, which is less invasive, however, only a finite amount of dye crosses the membrane which can be quickly broken down or leaks out diminishing useful timescales for imaging. Populations of cells can be less-invasively bolus loaded using synthetic calcium dyes tagged with lipophilic motifs but this method generates high background noise and reduces spatial resolution.

With the development of genetic methods to label defined subsets of neurons, genetically encoded calcium indicators (GECIs), which are based on fluorescent proteins fused to calcium binding proteins, have begun to replace the use of synthetic calcium dyes. While historically not exhibiting the same sensitivity to single spikes and fast kinetics as OGB (although see Chen et al., 2013), the main advantage of GECIs is that they can be genetically targeted to specific cell subsets. Therefore, their expression is non-invasive and compatible with long-term chronic imaging. GECIs can read-out calcium binding either by Förster resonance energy transfer (FRET) or single fluorophore fluorescence emission.

1.1.1.1 FRET-based genetically-encoded calcium indicators

The first FRET-based indicators engineered were the cameleon family, for which iterative improvements led to the generation of YC 3.60, which consists of an enhanced cyan fluorescence protein (ECFP) and a yellow fluorescent protein variant, Venus (Nagai et al., 2004). These fluorophores are linked by a region which contains calcium-binding calmodulin (CaM) and CaM-binding myosin light chain synthetic peptide (M13) domains. Calcium binding to CaM induces a conformational change in the YC 3.60 molecule bringing the ECFP and Venus in close apposition to enable FRET. Thus, calcium binding is measured as a ratio between the decrease in ECFP intensity, and the simultaneous increase in Venus intensity (Figure 1.1 A). FRET-measurements of intracellular calcium concentrations generate signals which are resistant to movement artefacts, conferring an advantage over single fluorophore indicators. CaM is a molecule endogenous to neurons and interacts with many cellular targets. To avoid this, a variant with a mutated CaM domain was generated (D3cpVenus (Palmer et al., 2006)) and a variant where Troponin C was added in the place of CaM was generated (TN-XXL (Mank et al., 2008)). Troponin C is a calcium binding protein which is endogenously expressed only in

muscle and so has no endogenous binding partners in neurons. The sensitivity and dynamic range of these GECIs varies. YC 3.60 exhibits a linear response to at least 10 APs *in vitro*, and single spike sensitivity in the mouse neocortex *in vivo* (Lutcke et al., 2010). D3cpVenus and TN-XXL characterised *in vitro* exhibit linear responses between 5 and 40 action potentials. D3cpVenus in the mouse neocortex has been found to be highly sensitive single spikes *in vivo* (Wallace et al., 2008) and TN-XXL has been used to record orientation-selectivity of neurons in the mouse visual cortex (Mank et al., 2008).

1.1.1.2 Single fluorophore genetically-encoded calcium indicators

The most widely used single fluorophore GECIs at present are from the GCaMP family. These GECIs consist of a single circularly permuted enhanced GFP fluorophore which is flanked by a CaM domain on one side and a M13 domain on the other. The binding of four calcium ions to the CaM domain induces the interaction of CaM with M13, and a conformational change in overall molecular structure resulting in a rearrangement of the circularly permuted GFP and an increase in green fluorescence (Figure 1.1 A). On comparison to FRET-based sensors, GCaMPs, being based on single fluorophores are much smaller than FRET-based indicators and therefore are easier to genetically manipulate or virally infect.

From the original GCaMP molecule iterative rounds of protein engineering have produced successive generations of improved GCaMP variants (Akerboom et al., 2012; Ohkura et al., 2012; Chen et al., 2013). At the time of this study, the most optimised version of GCaMP was GCaMP3 (Tian et al., 2009). Compared to its predecessor GCaMP2, GCaMP3 exhibits larger ΔF/F signals, higher signal to noise ratios, increased dynamic range which is linear to 20 APs (@83 Hz), and a 3-fold higher baseline fluorescence. Therefore, GCaMP3 constitutes an excellent tool to study neural activity *in vivo* and indeed GCaMP3 has been used in many model systems including the zebrafish, drosophila and the mouse (Seelig et al., 2010; Gabriel et al., 2012; Huber et al., 2012a; Wachowiak et al., 2013). Limitations of GCaMP3 include unreliable sensitivity to single action potentials and slow kinetics in comparison to synthetic calcium dyes (Tian et al., 2009). On direct comparison of the FRET-based indicators D3cpVenus and TN-XLL with GCaMP3 in dissociated hippocampal neurons it was found that GCaMP3 exhibited much larger ΔF/F signals and higher signal to noise ratios. GCaMP3 also exhibited greater photostability and faster decay times than the FRET-based GECIs (Tian et al., 2009). The excellent performance of GCaMP3 over FRET-based calcium reporters has perhaps led to a greater focus in the development of single-fluorophore GECIs (Akerboom et al., 2012; Ohkura et al., 2012; Chen et al., 2013), over FRET-based generations.

Until recently single fluorophore GECIs have been limited to the green region of the colour spectrum. A recent study used protein engineering to expand the colour palette of single fluorophore GECIs to create both red- shifted (R-GECO-1) and blue-shifted (B-GECO) GCaMP variants(Zhao et al., 2011b). Of particular interest are red spectrally-shifted variants, which exhibit less phototoxicity than blue variants and greater tissue penetration as is associated with longer wavelengths. R-GECO-1, referred to here simply as RGECO, is 80 nm red-shifted with respect to conventional green GCaMPs and does not spectrally overlap with GFP-based GECIs, allowing for simultaneous two-colour functional imaging. RGECO was engineered by replacing the circularly permuted GFP molecule in GCaMP3 with a circularly permuted red-shifted fluorescent protein, mApple (Figure 1.1 A). RGECO detects spontaneous calcium oscillations, and calcium influx in response to potassium chloride-induced depolarisation in dissociated hippocampal neurons, but the precise relationship of RGECO signal to action potential firing was not characterised.

At the time of this study, RGECO was the only red-shifted GECI engineered, however, since this work a second red-shifted GECI 'RCaMP' has been engineered with a circularly permuted variant of the red fluorescent protein mRuby in the place of GFP (Akerboom et al., 2013a). The performance of this GECI was characterised in hippocampal neurons *in vitro* to numbers of action potentials where it was shown to respond to a minimum of 5 field stimuli. In addition, it was shown to be able to detect sensory responses in neurons of Caenorhabditis elegans and zebrafish larvae *in vivo* to odour and electrical stimulation respectively, and field stimulated responses in drosophila larval motor neurons *ex vivo* (Akerboom et al., 2013a).

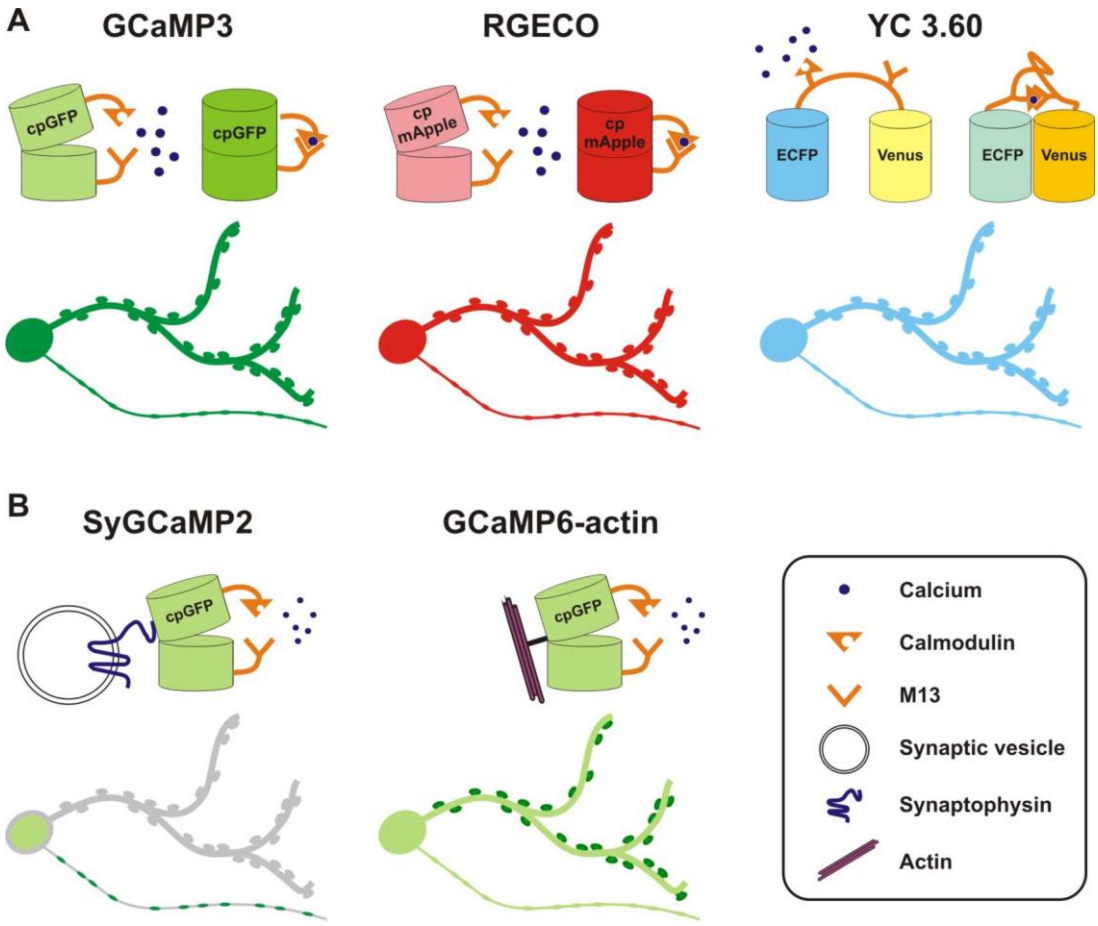

Figure 1.1 Schematic of GECI calcium binding and neuronal expression patterns. **(A)** Cytosolic GECIs. GCaMP3, RGECO and YC 3.60 all utilise Calmodulin as a calcium sensor. For each GECI calcium-calmodulin binding causes M13 interaction and conformational changes in molecular structure. Calcium binding in GCaMP3 and RGECO causes a modification in their cpGFP or mApple structure. Activation of YC 3.60 brings ECFP and Venus fluorophores in close apposition for donor photons from the ECFP to be accepted by Venus leading to a decrease in ECFP emission and an increase in Venus emission. These three GECIs are expressed uniformly within the neuron. **(B)** Fusion-GECIs. These GECIs are fused to specific proteins to restrict their expression to subcellular locations. SyGCaMP2 is localised to presynaptic terminals, while GCaMP6-actin is enriched in dendritic spines. SyGCaMP2 is made from a fusion of GCaMP2 (similar to GCaMP3 above) and synaptophysin which localises SyGCaMP2 to synaptic vesicles. GCaMP6-actin is made from a fusion of GCaMP6 (similar to GCaMP3 above) to which is enriched in dendritic spines. M13, myosin light chain kinase; cp, circularly permuted.

1.2 Recording synaptic transmission with GECIs

As mentioned above, the action potential output of a neuron can be estimated by measuring changes in intracellular calcium concentration. This type of recording is usually performed at the cell body, as this is a relatively large cellular region and as such has good spatial resolution and a large concentration of GECI molecules. However, recordings of neural and synaptic activity using GECIs can also be performed at individual synapses.

1.2.1 Presynaptic calcium influx

In evoked neurotransmitter release, the arrival of an action potential in the presynapse triggers calcium influx through $Ca_v2.1$, $Ca_v2.2$ and $Ca_v2.3$ VGCCs, also known as P-Q-, N- or R-type channels respectively, which are concentrated at presynaptic terminals (Figure 1.2 C; reviewed in Catterall, 2011). Calcium binds to effector proteins such as the calcium sensor synaptotagmin1 (Syt1) to trigger a cascade that leads to SNARE-mediated vesicle fusion and neurotransmitter release (Pang et al., 2006; Südhof, 2008).In this way, increases in intrabouton calcium concentration can reflect the action potential output of a cell. In addition, bouton calcium concentration is proportional to the third or fourth power of neurotransmitter release (the calcium power law); meaning that a 2-fold increase in presynaptic calcium concentration can promote an 8- to 16-fold increase in neurotransmitter release (Dodge and Rahamimoff, 1967; Katz and Miledi, 1970).

1.2.1.1 Measuring calcium influx at the presynapse

To study calcium influx specifically at the presynapse several studies have recently taken advantage of being able to localise genetically-encoded calcium indicators to presynaptic terminals (Dreosti et al., 2009; Nikolaou et al., 2012). This approach was first used by Dreosti et al., (2009) who generated synaptophysin-GCaMP2 (SyGCaMP2) by fusing of GCaMP2 to the synaptic vesicle protein, synaptophysin (Figure 1.1 B). Localising SyGCaMP2 to the site of calcium entry improved the dynamic range and temporal resolution of this GECI compared to cytosolic GCaMP2. This approach is particularly advantageous when recording activity from presynaptic boutons of many cells as it reduces background signals from labelled axons or cell bodies (Dreosti et al., 2009; Nikolaou et al., 2012). Recently, the highly reflective relationship between neurotransmitter release and intrabouton calcium concentration has been determined for specific stimulations by comparison of fluorescence signals of synaptopHluorin,

which measures vesicle fusion, and SyGCaMP2 indicating levels of bouton calcium influx (Zhao et al., 2011a; Odermatt et al., 2012; Nikolaev et al., 2013). Thus, calcium concentrations in presynaptic terminals can act as an indirect measurement for both neuronal activation, and the amount of neurotransmitter release.

It is important to note that the relationship between intrabouton calcium concentration and spontaneous neurotransmitter release is far less studied. Spontaneous neurotransmitter release occurs without an action potential being triggered in the presynaptic cell. Spontaneous neurotransmitter release was first discovered by Fatt and Katz (1952) and was thought to represent the background activity of nerve terminals. The physiological relevance of spontaneous release is still debated, but it has been shown that this neurotransmission can regulate the strength of individual synapses as well as effect local protein synthesis (Thiagarajan et al., 2005; Sutton et al., 2006). The mechanisms and machinery underlying spontaneous and evoked neurotransmitter release can differ. Despite the lack of a trigger it seems the vast majority of spontaneous neurotransmitter release is dependent on calcium, shown by the almost complete block of spontaneous neurotransmitter release in the presence of the high affinity calcium chelator BAPTA-AM (Xu et al., 2009). Although spontaneous neurotransmitter release appears less reliant on calcium influx from extracellular sources and can occur in the absence of extracellular calcium, calcium may be released from internal stores or enter via stochastic opening of VGCCs (Emptage et al., 2001; Südhof, 2008). However, functional imaging of changes in intrabouton calcium concentration during spontaneous neurotransmitter release has not yet been published. Yet, functional imaging can be utilised to monitor spontaneous neurotransmitter release by recording the calcium responses to this release in the postsynapse.

1.2.2 Postsynaptic calcium influx

Postsynaptic calcium influx plays a highly important role in the postsynapse, especially following glutamatergic excitatory synaptic transmission. The postsynaptic sites of excitatory neurotransmission can be easily identified as the majority (79%) of excitatory synapses are found at structures, called dendritic spines (Beaulieu and Colonnier, 1985). Dendritic spines are morphological specialisations found along dendrites, typically ~0.5-2 µm in length and 0.5 µm in diameter and separated from the dendritic shaft by a spine neck around 0.5 µm in length and 0.1 µm in diameter (reviewed in Hering and Sheng, 2001; Higley and Sabatini, 2012). Spines contain an electron dense region called the postsynaptic density (PSD) which is typically immediately opposed to a single active zone of a glutamatergic presynaptic terminal (Spacek

and Hartmann, 1983). PSDs are usually disc-shaped in smaller synapses, while larger synapses have perforated PSDs. The PSD is characterised by an abundance of scaffolding proteins such as PSD-95, which contain multiple domains for protein-protein interactions to bind to and organise ligand-gated receptors, cytoskeletal elements, trans-synaptic adhesion molecules and cytoplasmic signalling molecules (Figure 1.2 B; reviewed in Sheng and Kim, 2011). In terms of calcium influx, the spine head contains the constituents, including several receptors, channels and store associated membranes, which permit calcium entry into the spine head, which I will be outline below.

1.2.2.1 Glutamate Receptors

Postsynaptic calcium transients are observed following synaptic activation in the hippocampus and the neocortex (among others regions) which are restricted to small regions of the dendrite and isolated to dendritic spines (Murphy et al., 1995; Murthy et al., 1997; Yuste et al., 1999; Conti and Lisman, 2003). Ionotropic glutamate-gated NMDA receptors are considered the major source of these transients as application of NMDA receptor antagonists blocks these events (Murthy et al., 1997; Emptage et al., 1999; Yuste et al., 1999). NMDA receptors are ideal to mediate this calcium influx as they are concentrated at the postsynaptic density, have a high affinity for glutamate (~500 times higher than AMPA receptors; Zito and Scheuss, 2009 p.1157) and a high single channel conductance of which calcium ions constitute approximately 15% of the current (Schneggenburger et al., 1993; Nicholson et al., 2006). In synaptic transmission, glutamate binding to AMPA receptors (also ionotropic glutamate receptors) leads to the influx of sodium (Na^+) and potassium (K^+) cations into the postsynapse (Figure 1.2 C). While AMPA receptors lacking the GluA2 subunit are calcium permeable, in adulthood, the vast majority of AMPA receptors are GluA2 containing and are therefore calcium impermeable. AMPA receptor activation mediates the depolarisation constituting fast neurotransmission. Unlike AMPA receptors, the NMDA receptor can only be activated when both glutamate and glycine binding sites are filled. In addition, current influx is blocked by a Mg^{2+} ion which sits within the channel pore at rest. The Mg^{2+} block is voltage-dependent and is removed at depolarised potentials due to electrostatic repulsion (Jahr and Stevens, 1990). Depolarisation to remove the Mg^{2+} block can be mediated locally at the synapse by AMPA receptor-mediated depolarisation. Upon activation, NMDA receptors are highly permeable cations (Na^+, K^+ and Ca^2). The number of NMDA receptors at a single spine that are activated by a single synaptic event can be low (~1-5 receptors), but the slow deactivation of these receptors (>100 ms) and high single channel conductance (~30-50 pS; Zito and Scheuss, 2009 p.1157) means that the

total amount of calcium that each NMDA receptor can pass is relatively large (Nimchinsky et al., 2004). While at rest the NMDA receptor channel is typically blocked by a Mg^{2+} ion, the nature of this block is stochastic, and therefore it is possible for the NMDA receptor can pass calcium independently of local AMPA receptor-mediated depolarisation, when bound to glutamate (Jahr and Stevens, 1990). The functions of the NMDA receptor are perhaps best described by its use as a 'coincidence detector' of pre- and postsynaptic activity. This 'coincidence detection' behaviour of the NMDA receptor means it can acts as a receptor sensor of high levels of activity and is known to initiate synaptic plasticity mechanisms through calcium-dependent signalling cascades (reviewed in Molnár, 2011; Bliss and Collingridge, 2013).

As outlined above, activation of NMDA receptors can be regulated by postsynaptic depolarisation mediated by AMPA receptors. The application of AMPA receptor antagonists have been shown to prevent calcium influx in spines under normal Mg^{2+} conditions. In low Mg^{2+} conditions blocking AMPA receptors with CNQX had less effect on NMDA receptor-mediated calcium transients, indicating that AMPA receptor-mediated depolarisation is indirectly required to remove the NMDA receptor Mg^{2+} block (Emptage et al., 1999). However, a different study using the same technique only in acute, as opposed to organotypic hippocampal slices, found that CNQX only decreased NMDA receptor mediated calcium currents by only 30%, perhaps reflecting the stochasticity of the Mg^{2+} block at rest and therefore the activation of NMDA receptors in the absence of depolarisation (Kovalchuk et al., 2000). NMDA receptor calcium currents can be isolated experimentally by patch-clamping neurons and holding them at positive potentials or by removing Mg^{2+} from the extracellular medium. These techniques remove the NMDA channel Mg^{2+} block meaning that NMDA receptor activation only requires agonist binding. Under these conditions it was found that the application of the AMPA receptor selective antagonist NBQX had no effect on calcium transients (Mainen et al., 1999). The lack of effect observed with AMPA receptor antagonists in this study indicates that little contribution to spine calcium transients are made directly by calcium permeable AMPA receptors. This supports the notion that most AMPA receptors are calcium impermeable, at least in the excitatory hippocampal neurons tested in these studies (Wenthold et al., 1996).

1.2.2.2 Voltage-gated calcium channels

Another source of spine calcium is via VGCCs which are integral proteins that are selectively permeable to calcium at depolarised membrane potentials. VGCCs typically consist of four or

five subunits, of which the α1 subunit confers the major properties of the channel containing extracellular binding sites for drugs and toxins, as well as intracellular binding sites for second messengers. The other accessory subunits (α2, β and γ) have mainly modulatory properties regulating the localisation, kinetics and voltage dependence of the channel (reviewed in Catterall and Few, 2008). Dependent on the channel properties conferred by the α1 subunit VGCCs are classified as L-type ($Ca_v1.2$), P/Q-type ($Ca_v2.1$), N-type ($Ca_v2.2$), R-type ($Ca_v2.3$) and T-type (Ca_v3). These channels show specific cell type and subcellular expression patterns. For hippocampal neurons P/Q-type channels mediate most of the calcium influx in presynaptic boutons, while L-, R- and T-type channels mediate calcium influx in the dendritic shaft, and mainly R- and T-type channels mediate calcium influx in dendritic spine heads (Sabatini and Svoboda, 2000). At the postsynapse VGCCs can be activated by strong depolarisation following spatial and temporal summation of synaptic inputs or by back-propagating action potentials from the soma (Magee and Johnston, 1995; Sabatini and Svoboda, 2000; Yasuda et al., 2003). However, activation of VGCC in spines by unitary synaptic stimulation is more contentious with cell-type specific differences evident. For example one study using layer 5 cortical pyramidal neurons showed that calcium signals evoked by glutamate uncaging were reduced by 75% in the presence of the R- and T-type channels blocker (Schiller et al., 1998). In the specialised thorny excrescence postsynapse of CA3 hippocampal neurons and in Purkinje neurons calcium influx is mediated by AMPA receptor mediated activation of VGCCs following stimulation of presynaptic fibres (Eilers et al., 1995; Reid et al., 2001). Recently, for CA1 neurons in acute hippocampal slices, calcium transients evoked by glutamate uncaging were reduced by ~30% when VGCCs were blocked (Bloodgood and Sabatini, 2007). It was found that calcium influx by R-type VGCCs actually feedback to modulate NMDA receptor-mediated calcium influx through coupling to small conductance (SK) calcium-activated potassium channels. Activation of these channels causes a repolarisation of dendritic spine membrane potential to enforce the NMDA receptor Mg^{2+} block, thus decreasing the amplitude of NMDA receptor-mediated transients (Bloodgood and Sabatini, 2007). However, this is in contrast with an earlier study in rat CA1 hippocampal neurons in organotypic slices where addition of R- and T-type antagonist, Nickel, had no effect on spine calcium transients induced by the stimulation of presynaptic fibres (Emptage et al., 1999). This discrepancy may reflect species dependent differences in VGCC expression and function or differences between organotypic and acute hippocampal slice preparations. In addition, the concentration of glutamate released by the uncaging stimulus used by Bloodgood and Sabatini (2007) will have a large effect on the route of calcium entry, which is based in part on the magnitude of spine depolarisation.

1.2.2.3 Internal Stores

A final potential source of spine calcium influx in dendritic spines is from internal stores. Internal stores are smooth endoplasmic reticulum-derived organelles which in spines are sometimes referred to as the 'spine apparatus'. Internal stores membranes invade into larger spines but are not often found in smaller spines. Typically internal stores buffer and sequester calcium but they can also release calcium into the cytoplasm upon activation of IP_3 receptors or ryanodine receptors located on the stores membrane. In dendritic spines of CA1 hippocampal neurons, internal stores express ryanodine receptors, but not IP_3 receptors. Ryanodine receptors are activated by calcium initiating calcium-induced calcium release (CICR). Thus calcium influx in spines via NMDA receptors and VGCCs as discussed above, may activate an amplifying release of calcium from internal stores (Berridge, 1998). Indeed, it has been shown that stimulation of presynaptic fibres leads to an NMDA receptor-dependent release of calcium from internal stores, which is blocked by application of the ryanodine receptor antagonist, ryanodine, or by blocking internal store refilling using cyclopiazonic acid (CPA; Emptage et al., 1999). In this study the blockade of ryanodine receptors completely abolishes spine calcium transients, indicating that the NMDA receptor contribution itself to spine calcium is minimal. However, other studies using similar techniques found that blocking the refilling of stores with CPA had little (30% reduction) or no effect of spine calcium transients (Mainen et al., 1999; Kovalchuk et al., 2000). This discrepancy may arise from differences in sizes of recorded spines, where small spines will lack a spine apparatus. In addition, the data may reflect differences in experimental preparations, for example acute (Mainen et al., 1999; Kovalchuk et al., 2000) versus organotypic (Emptage et al., 1999) hippocampal slices.

1.2.2.4 Measuring calcium concentrations at the postsynapse

Many studies that have measured calcium influx in dendritic spines these have tended to use synthetic calcium dyes, often introduced to cells via patch pipettes. Following a similar rationale presynaptic GECI targeting (i.e. SyGCaMP), specific targeting GECIs to postsynaptic compartments has been achieved by fusing GCaMP2 or GCaMP6 to β-actin, a cytoskeletal protein which is enriched in dendritic spines (Figure 1.1 B; Mao et al., 2008; Ohkura et al., 2012). However, unlike the SyGCaMPs, localisation to dendritic spines conferred no advantage in GECI response properties over cytosolic GCaMP2 in response to action potential and glutamate uncaging stimuli (Mao et al., 2008). GCaMP6-actin, on the other hand, showed robust responses to minimal and evoked stimulation of presynaptic fibres *in vitro* but was not compared to the cytosolic GCaMP6 (Ohkura et al., 2012). However, cytosolic calcium indicators

and dyes can be used to specifically record postsynaptic calcium influx in the absence of subcellular targeting due to the identification of postsynaptic sites through the morphological properties of dendritic spines. Indeed, spine calcium measurements have recently been recorded using cytosolic GECIs which read-out the orientation-selectivity of single spines belonging to a orientation-selective neuron in the mouse V1 cortex *in vivo* (Chen et al., 2013).

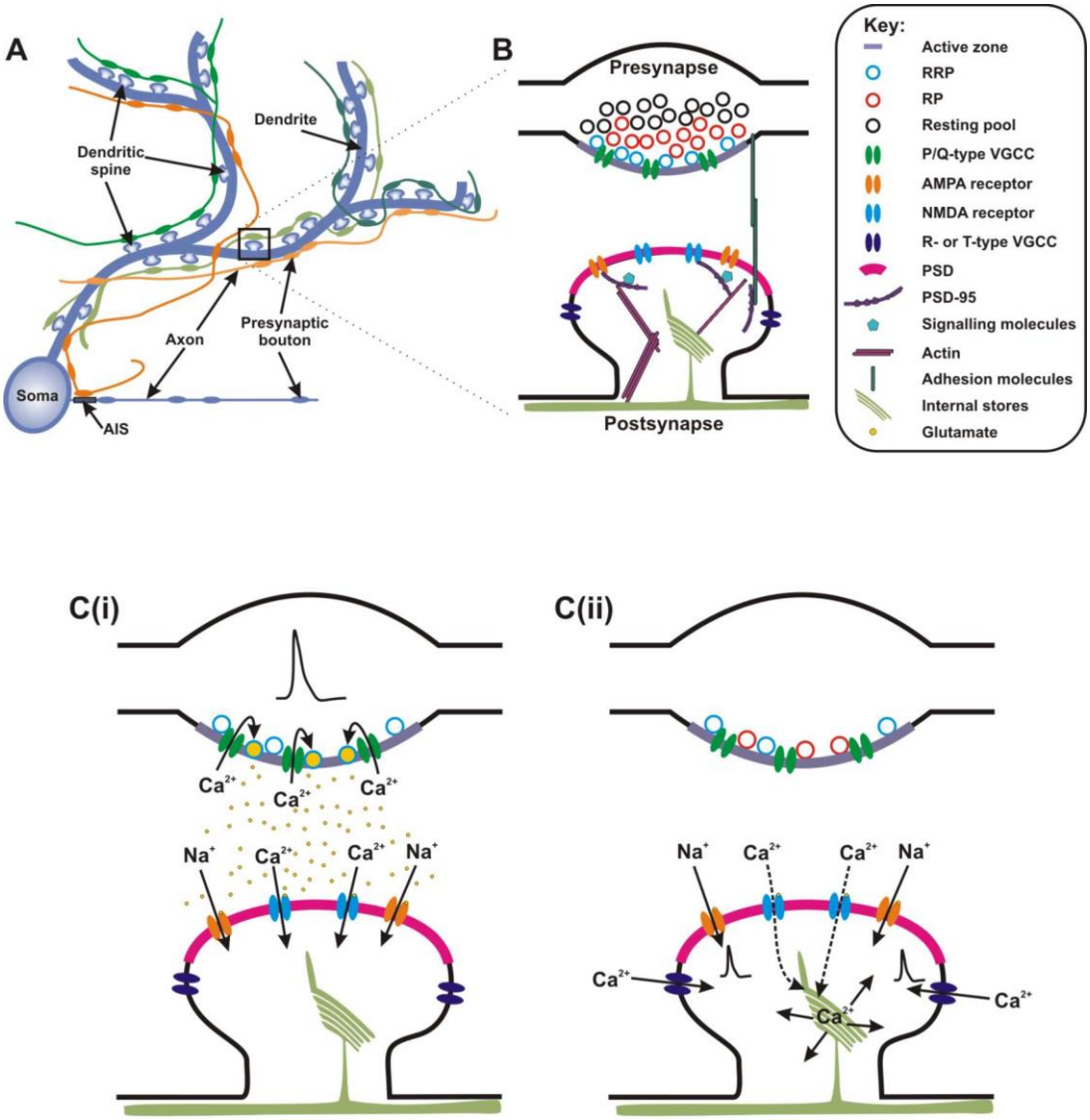

Figure 1.2 The synapse. (A) A hippocampal neuron (blue) with presynaptic boutons from other neurons which are excitatory (green) and inhibitory (orange). Note that excitatory boutons make synapses onto dendritic spines, whereas inhibitory boutons make synapses onto dendritic shafts, the soma or the AIS. **(B)** Key structural components of the pre and postsynapse. **C(i)** Glutamatergic synaptic transmission. A depolarisation in the presynaptic terminal causes VGCCs to open and subsequent calcium influx. Calcium influx triggers vesicle fusion and glutamate release which diffuses across the synaptic cleft. AMPA and NMDA receptors are activated allowing Na^+ and Ca^{2+} ions, respectively, to flow into the postsynapse. **C(ii)** Postsynaptic calcium sources. NMDA receptors can directly mediate calcium influx. Local depolarisation can activate VGCCs and Ca^{2+} influx (typically via NMDA receptors) can stimulate Ca^{2+} release from internal stores. AIS, axon initial segment, RP, resting pool, RRP, readily-rleaseable pool; PSD, postsynaptic density; VGCCs, voltage-gated calcium channels.

1.2.3 Quantal variability

In Chapter 4 we record and investigate variability in the amplitude of calcium transients occurring at individual dendritic spines. Variability in mEPSC amplitude recorded electrophysiologically has been a well-documented feature of quantal synaptic transmission, characterised by a positively skewed mEPSC amplitude distribution with coefficients of variation (CV) greater than 0.5 (Bekkers et al., 1990; Forti et al., 1997; Liu et al., 1999; McAllister and Stevens, 2000). Historically recorded at the cell body, it was not known if this large variability reflected heterogeneity in the strength of different synapses, or variability due to fluctuations in mEPSC amplitude at single synapses. Recordings from small numbers of synapses indicated that mEPSC variability was high within single spines (Bekkers et al., 1990; Smith et al., 2003). In addition, high CV values (CV=0.72) calculated from dendritic recordings of mEPSCs which show that this variability is occurring local to the dendrite and is therefore not a by-product of different attenuation rates (Smith et al., 2003). However, not all studies agree. A loose-patch study found mEPSC distributions to be normally (Gaussian) distributed with low variability at single synapses (CV=0.3; Forti et al., 1997). While quantal variability recorded electrophysiologically tends to represent variability in AMPA receptor-mediated current influx, isolated NMDA receptor currents have been shown to be highly variable when measured in response to spontaneous neurotransmitter release (CV=0.66; McAllister and Stevens, 2000). In addition, the calcium permeability of NMDA receptors has allowed NMDA receptor-mediated variability to be measured at identified synapses using calcium imaging (Murphy et al., 1995; Yuste et al., 1999; Conti and Lisman, 2003). It has been found that individual spines showed a high level of variability in the amplitude of calcium transients recorded by calcium sensitive synthetic dyes in response to both extracellular stimulation of presynaptic fibres and focal uncaging of glutamate (CV~0.6; Conti and Lisman, 2003; Bloodgood and Sabatini, 2007). Furthermore, the CV for different spines has a large range (CV range 0.08-0.62; Conti and Lisman, 2003). It of a great interest to isolate and understand the mechanisms which underlie quantal variability and several sources for single synapse mEPSC variability have been suggested which are either presynaptic or postsynaptic in origin.

1.2.3.1 Postsynaptic sources of quantal variability

Postsynaptic origins of mEPSC variability at single synapses are mainly focused around (1) receptor desensitisation, (2) receptor saturation and (3) channel noise. If receptors are desensitised after a single release event, this would preclude their ability to respond maximally to a second release event. This is a time-dependent process, where response amplitude

depends on instantaneous frequency (i.e. time to previous event). However, correlations between mEPSC amplitude and inter-event interval were not observed when recording mEPSCs globally from the soma nor when recording form single synapses (Forti et al., 1997). In addition, blocking AMPA receptor desensitisation using cyclothiazide has no effect of AMPA receptor variability (Smith et al., 2003). This suggests that AMPA receptors are not desensitized in response to quantal release events.

Another possible source that could influence mEPSC variability is receptor saturation. As synaptic vesicles are filled with ~2000 glutamate molecules and the synaptic cleft has such a small volume, the concentration of glutamate reached in the cleft will be very high. To test for AMPA receptor saturation, one study made recordings of mEPSCs at the cell body triggered both by spontaneous release and by the release of glutamate from a synaptically sited micropipette. They found that the amplitude of mEPSCs generated by micropipette glutamate release were larger than those generated by spontaneous neurotransmission, indicating that AMPA receptors are not saturated during quantal release (Liu et al., 1999). On the other hand NMDA receptors have a higher affinity for glutamate, compared with AMPA receptors, which may increase the probability that receptor saturation occurs. However, ionophoretic glutamate release at individual spine can induce larger mEPSCs than those engendered by quantal release suggesting that NMDA receptors are also not saturated by a quantum (Mainen et al., 1999; McAllister and Stevens, 2000). In addition, it has been proposed that the high glutamate affinity of NMDA receptors may make them less susceptible to variability originating from the spatial and temporal characteristics of synaptic cleft glutamate concentration than AMPA receptors (Murnick et al., 2002).

A final source of postsynaptic variability comes from channel noise. AMPA receptor channel noise refers to the multiple conductance levels of AMPA receptors which can be measured using single-channel recordings (Prieto and Wollmuth, 2010). However, these experiments are difficult to perform in neurons. Instead, the role of channel noise in quantal variability was explored in a theoretical model which found that fluctuations in the closed and open conducting states of the channel accounted for only ~8% of the total variability (Franks et al., 2003). However, new insights into the conductance states of the AMPA receptor show they are highly dependent on membrane potential and glutamate occupancy, characteristics which were not built into the above model (Prieto and Wollmuth, 2010).

1.2.3.2 Presynaptic sources of quantal variability

As outlined above, there is little direct evidence to suggest a particular postsynaptic source of quantal variability. Additional experiments however, have indirectly suggested a presynaptic origin for variability. Two studies bypassed variability from presynaptic vesicle release by activating AMPA and NMDA receptors using fixed concentrations of glutamate via ionophoresis. They found that AMPA and NMDA receptor responses evoked by this controlled glutamate stimulation were highly similar, with variability decreasing significantly for AMPA receptors from a CV of 0.5 to 0.1, and from 0.65 to 0.1 for NMDA receptors (Liu et al., 1999; McAllister and Stevens, 2000). This result is indicative of a presynaptic source for quantal variability, for which possible mechanisms include; (1) variability in vesicle volume, (2) location of vesicle fusion and (3) multi-vesicular release.

Ultrastructural analysis of presynaptic terminals has shown that vesicle diameter can be variable (CV=~0.3; Takamori et al., 2006) which equates to an even larger variability in vesicle volume. Presuming a uniform intravesicular glutamate concentration, the number of glutamate molecules exocytosed per release event will therefore be variable. An investigation in drosophila using different neuronal cell-types with different vesicle volumes found a linear relationship between vesicle volume and quantal size indicating that intravesicular glutamate concentration is in fact uniform (Karunanithi et al., 2002). It is not possible to directly determine vesicle diameter for individual release events, but instead the effect of vesicle volume on quantal variability has been modelled. Franks et al., (2003) found they could recapitulate the majority (58%) of the variance of experimentally recorded mEPSCs in a model where vesicle diameters were altered within physiological constraints. In fact the range of vesicle diameters modelled had a CV of 0.14, less than observed by EM, and thus vesicle diameter and concomitant variability in the amount of glutamate released in each release event could account for the vast majority of quantal variability. However, a different study has suggested that intravesicular glutamate concentration is not uniform and is instead a major source of quantal variability. In large Calyx-like neurons of the rat brainstem, presynaptic terminals were patched and increases in capacitance, indicative of vesicle fusion events, were measured. The size of the capacitance response is directly related to the amount of vesicular membrane that fuses with the plasma membrane. Here, it was found that the size of capacitance jumps were unrelated to the size of the postsynaptic mEPSC measured at the same synapse, leading the authors to suggest that vesicle diameter is not the source of variability (Wu et al., 2007). Nevertheless, many agree that quantal content does appear to be an important factor.

It has been shown that AMPA receptor density is not uniform over the PSD. Immunogold electron microscopy (EM) and EM tomography have given interesting insight on AMPA receptor distribution within the PSD. While there seem to be large cell-type specific differences, AMPA receptors have been found both to cluster in hotspots directly apposed to presynaptic release sites and at sites in the immediate periphery of PSDs, often surrounding an NMDA receptors inner core (reviewed in MacGillavry et al., 2011). This non-uniform distribution of AMPA receptor density means that the size of the postsynaptic response could be greatly altered depending on whether vesicle release occurs apposed to an area of high or low AMPA receptor density. This is an important consideration given that per release event only ~25% of the total PSD size is exposed to glutamate concentrations large enough to cause receptor activation. This is mainly due to the high glutamate concentration gradient in the synaptic cleft. Although difficult to test experimentally, variability in the position of vesicle release sites (release location dependence; RLD) has been modelled (Franks et al., 2003). In this model, AMPA receptors were first uniformly distributed across a disk-like PSD. It was found that postsynaptic currents decreased on the tangential removal of release sites from the centre of the active zone, producing a CV of 0.28 when release is simulated from 51 different active zone positions. When the postsynaptic array of AMPA receptors in modelled with an annular arrangement the CV actually decreased, showing that a ring-like arrangement of AMPA receptors does not promote an RLD origin for quantal variability (Franks et al., 2003).

A third mode in which quantal size can be variable is via multiquantal release. It was historically thought that only single vesicles were released at single synapses during synaptic transmission, however studies have since shown that multiquantal release can occur in CNS synapses (Wall and Usowicz, 1998). It has been observed that within the variable population of mEPSCs, larger events tend to have slower rise times (Magee and Cook, 2000). However, when vesicle diameter is altered by taking advantage of the fact that glutamate concentration per vesicle increases with development, or by simulations, rise times do not change, and in fact get faster for larger quanta (Franks et al., 2003; Yamashita et al., 2003). Correlations between mEPSC amplitude and rise-times can instead be reproduced in models where quantal variability is caused by multiquantal release (Raghavachari and Lisman, 2004). In classic experiments by del Castillo and Katz (1954) postsynaptic amplitudes were recorded to evoked stimulation which fell into multiple distributions where amplitude is dependent on the number of vesicles released (DEL CASTILLO and KATZ, 1954). However, spontaneous multiquantal release does not show this binomial distribution of amplitudes and instead the distribution of amplitudes shows a single skewed population with a large variability. This is because spontaneous multivesicular fusion is not triggered, therefore multiple vesicles are released

with a temporal jitter in which the rise time and amplitude are dependent on the summation of the two vesicle release events (Raghavachari and Lisman, 2004).

In summary, a presynaptic source has been suggested to be the main proponent underlying variability in mEPSC amplitudes, however, the origin of presynaptic variability remains controversial with vesicle volume and multiquantal release perhaps the most likely candidates.

1.2.4 Synaptic democracy

In Chapter 4 we investigate how the location of spines across the dendritic tree may alter synaptic transmission and synaptic weight, measured through the recording of calcium transients. Dendritic tree location may alter synaptic properties as the morphology of dendrites can have a large effect on the propagation of signals from dendrites to the soma. Wilfred Rall first modelled the electrotonic properties of dendrites (reviewed in Segev, 2006). Importantly, he outlined that dendrites should be treated as passive cables which leak current during electrical propagation, meaning that there will be a relative attenuation in amplitude and a slowing in the kinetics of a signal recorded at the cell soma in comparison to the synapse. Therefore, the longer the distance of propagation, the larger the attenuation. This biophysical property of dendrites means that distal presynaptic inputs will have less influence on action potential firing than more proximal inputs. However, in hippocampal CA1 neurons, the amplitude of EPSPs recorded at the cell body did not predict the dendritic location of synapses. Since this discovery, several mechanisms have been studied which may allow for signals from distal dendrites to be normalised with respect to proximal signals leading to a 'synaptic democracy' at the cell body. While this issue remains unresolved, there are several mechanisms which have been proposed to account for synaptic democracy which I will outline below.

1.2.4.1 Distance-dependent scaling of AMPA receptors

The normalisation of synaptic input at the cell body from distal dendritic locations can be achieved by increasing EPSC amplitude at postsynaptic sites located further from the cell soma. When EPSCs were recorded locally in dendrites of the stratum radiatum (SR) in CA1 hippocampal neurons it was found that synapses in the proximal SR had relatively weaker EPSCs compared to synapses in the distal SR (Magee and Cook, 2000; Andrasfalvy and Magee, 2001; Smith et al., 2003). However, this effect was found not to be caused by a distance-

dependent difference in the amount of glutamate released, the size of the RRP or the probability of vesicle release at these two sites (Smith et al., 2003). Instead, it was found that the number of AMPA receptors is approximately two-fold larger at distal versus proximal SR synapses (Andrasfalvy and Magee, 2001; Smith et al., 2003; Nicholson et al., 2006). Interestingly, while this result is seen in CA1 hippocampal neurons it is not observed in layer 5 neocortical neurons (Williams and Stuart, 2002). The same distance-dependent effect was also not observed when focusing on NMDA receptors and appeared to be exclusive to AMPA receptors (Andrasfalvy and Magee, 2001; Nicholson et al., 2006). In agreement with this, distance-dependent scaling is not observed in a GluA1 knock-out suggesting a role for this AMPA receptor subunit (Andrásfalvy et al., 2003). At least within the SR, it appears that scaling of AMPA receptor numbers and therefore local EPSC amplitudes can explain the normalisation of distal inputs when measured at the soma. However, it is not possible to record electrophysiologically from more distal dendritic regions, such as the stratum lacunosum-moleculare (SLM), nor from oblique branches due to the thinness of these dendrites. An immunogold electron microscopy study determined that AMPA receptor number and density on these thin branches was in fact lower than that observed in the proximal SR (Nicholson et al., 2006). Thus, it is likely that these dendrites undergo a different type of distance-dependant arrangement, distinct from the scaling observed along the primary dendrite in the SR. How changes in synaptic strength are triggered in the SR (i.e. how a distal synapse knows it needs to have more AMPA receptors) is unknown. A recent model however, has suggested a role for bpAPs (Sterratt et al., 2012). Synaptic position within a dendritic tree could be specified by the amplitude of the bpAP which will attenuate with distance from the soma. This model relies on the coincidence detection of NMDA receptors, where synaptic activation plus depolarisation from the bpAP will induce calcium influx. The amount of calcium influx will be regulated by the magnitude of the bpAP-mediated depolarisation (i.e. lower calcium influx distally as bpAPs have attenuated). AMPA receptor number can then be homeostatically regulated, with lower calcium concentrations causing AMPA receptor insertion distally, and higher calcium concentration causing AMPA receptor removal proximally (Sterratt et al., 2012).

1.2.4.2 Biophysical properties of dendrites and spines

A second important mechanism relates to the biophysical properties of dendrites. As dendrites taper towards the tip ends of their branches their input impedance (resistance) will increase. This means that any current entering a thin dendrite will produce a concomitantly large voltage change (Gulledge et al., 2012). When the size of EPSP is modelled for synaptic inputs

along a tapering dendrite, taking into account the increase in input impedance, EPSP amplitudes are larger at more distal locations (Gulledge et al., 2012). This local amplification may lead to local summation of signals within the dendrites to generate enough local depolarisation to activate voltage-dependent channels and initiate a dendritic spike (reviewed by London and Häusser, 2005). These spikes can then propagate under certain conditions to the cell soma to influence action potential firing.

The above model considered excitatory inputs directly onto spines which were uniform in biophysical properties. However, it is known that spines show a large variability in shape and size (reviewed in Hering and Sheng, 2001; Higley and Sabatini, 2012). In fact spine volume along the dendrites of a single cell can vary by an order of magnitude (Katz et al., 2009). It is also know that there is significant correlation between the size or volume of the spine head and the strength of that synapse, measured as AMPA receptor currents, so that larger spines show larger evoked AMPA currents (Matsuzaki et al., 2001). However, the structure–function relationship at the dendritic spine is further complicated by another important morphological feature: the spine neck, which acts as a resistor. Although it varies in diameter quite widely from one spine to the next, it can be thin enough to influence the local voltage responses at the spine head and alter signals as they pass to the dendritic shaft since the signal is filtered as it crosses the neck (reviewed in Yuste, 2013). In fact, spine neck resistance is directly correlated to the magnitude of the spine head voltage response and inversely correlated to the response measured at the soma (Araya et al., 2006; Harnett et al., 2012). Therefore a distance-dependent change in spine neck diameter could also, in principle, help shape dendritic democracy. Small spines tend to have smaller necks than large spines (Noguchi et al., 2005), meaning that small spines will have the largest input resistance but the smallest input current as they will have fewer number of glutamate channels (Nusser et al., 1998; Mackenzie et al., 1999; Matsuzaki et al., 2001). The influence of the spine neck in shaping biochemical signals, such as calcium, has also been studied. Here, the spine neck acts to restrict molecular diffusion and calcium ions become highly compartmentalised within spines. The degree of calcium compartmentalisation is dependent on spine neck diameter, with thin necks shown to compartmentalise calcium to a greater extent than larger diameter spine necks. Calcium imaging performed on spines of CA1 hippocampal neurons activated by glutamate uncaging found that small spines with small necks show much larger synaptic calcium transients than large spines with larger necks (Noguchi et al., 2005). This inverse relationship between calcium concentration and spine size has also been reported in a number of other studies (Kasai et al., 2003; Nimchinsky et al., 2004).

Therefore, dendritic scaling controlled by a scaling in synaptic strength (i.e. and increase in glutamate receptor numbers) might result in an increase in spine size for more distal synapses. Indeed, one study has reported that spine size increases with distance in CA1 hippocampal neurons using EM (Megías et al., 2001). However, if a mechanism exists where the diameter of the spine neck and the resulting resistance and biochemical compartmentalisation are important, a decrease in spine size at distal synapses should be observed. A recent study reconstructing individual dendritic branches using serial-section electron microscopy showed that within oblique branches of CA1 neurons, spine size decreases closer to branch end tips (Katz et al., 2009). The discrepancy between these two studies might be due to the fact that Megías et al., (2001) did not take measurements along entire branches but made averages over many neurons and over many dendritic locations and describe their spine size measurements as semi-quantitative.

1.3 Using GECIs to study neuronal output *in vivo* in the larval zebrafish

In Chapter 4 we have used calcium imaging to chart the synaptic input onto a single neuron in culture. In Chapter 5 calcium imaging was used to record the action potential output of single neurons by recording both at the cell soma and in individual presynaptic boutons of neurons in the larval zebrafish visual system. The aim of this chapter was to use this neuronal output to understand the progression of circuit building or visual networks during development. GECIs were essential tools to this study as they are non-invasive and can be used to track neuronal activity of single identified neurons in a chronic manner.

The larval zebrafish visual system has become a widely-used model for studying the formation and function of the circuitry underlying visually-guided behaviour. In general, the zebrafish is an excellent model system; they are easy to house, a single breeding pair can produce many (~200) embryos and embryos are highly accessible as they develop ex-utero. The zebrafish genome is fully sequenced, and genetic manipulation of the zebrafish is established. The use of the Gal4 system has led to the flexible targeting of genes to particular groups of cells, and the creation of a database with many driver lines. In addition, it is relatively quick and easy to generate new transgenic lines as zebrafish reach maturity by 3-4 months of age. The small size and transparency of the larvae are highly advantageous for functional imaging techniques. Therefore, the ascendency of the zebrafish is partly a consequence of engineering of and improvements in genetic functional tools such as genetically-encoded calcium indicators and channel rhodopsin. In particular the visual system has provided a useful model to study neural circuits using calcium indicators. The position of the tectum, as the most dorsal brain area,

makes this region particularly accessible for functional imaging. Components of the visual system are relatively well characterised, as is the development of the visual system. Many visually-guided behaviours have also been characterised in the zebrafish, and thus can provide measurable outputs of visual processing. Finally, the visual system is online early in development, meaning that visual stimulation can be used to assess functional development during a well-defined period of RGC and tectal cell structural maturation and synaptogenesis.

1.4 The zebrafish retinotectal system

The visual system of the zebrafish consists of the retina and the retinorecipient areas of the brain represented by ten arbourisation fields named AF1-10 (Burrill and Easter, 1994). The retina is made up of multiple nuclear and plexiform layers, the organisation of which is highly conserved across all vertebrates (Figure 1.3 A). Photopic visual information is passed from cone photoreceptors to cone bipolar cells to retinal ganglion cells, with horizontal and amacrine cell interneurons modifying signals at the first and second synapse, respectively. RGCs have cell bodies located in the ganglion cell layer. These constitute a morphologically diverse cell type (dependent on the species there are ~30 RGC subtypes, ~15 in the zebrafish (Mangrum et al., 2002)) which are often classed based on morphology and the position of their dendritic laminations in the IPL. RGCs have mono-, bi- or tristratified RGC dendritic trees or diffuse dendrites to sample combinations of information transcribed by bipolar cell axons arranged in specific laminae (Kolb et al., 1981; Amthor et al., 1984; Mumm et al., 2006). Simple examples are OFF-RGCs, which project dendrites into the distal IPL to contact with OFF-bipolar cells, and ON-RGCs which project dendrites to the proximal IPL to make contacts with ON-bipolar cells (Nelson et al., 1978). RGCs with bistratified dendrites laminating in both the ON and the OFF lamina of the IPL are designated ON-OFF RGCs (Amthor et al., 1984). RGCs are glutamatergic cells which are the sole neuronal output of the eye. In the zebrafish, RGC axons exit the eye, cross the midline and terminate within a single or multiple contralateral arbourisation fields in the brain (Figure 1.3 B).

The optic tectum (AF10) is the main retinorecipient region of the zebrafish brain and is described as analogous to the superior colliculus in mammals. The tectum is broadly subdivided into a more superficial neuropil region where RGC axons and tectal cell dendrites terminate, and a deep nuclear region, called the *stratum periventriculare* (SPV), which contains the majority of tectal cell bodies. The neuropil region is subdivided into layers based on anatomically defined strata (Nevin et al., 2010). Working from the most superficial to deeper layers these are named; *stratum opticum* (SO), *stratum fibrosum et griseum superficiale*

(SFGS), *stratum griseum central* (SGC) and *stratum album central* (SAC). Although, recent work suggests these 4 layers are further subdivided, and that there are a total of 10 strata within the tectal neuropil (Robles et al., 2013). RGC axon arbours are laminar in structure and so only target a single stratum (Xiao and Baier, 2007). The SFGS is the largest stratum containing ~80% of RGC axons, and is further subdivided into 3 strata (b, d and f). The SO contains ~15% of RGC axons, and thus the two most superficial neuropil layers make up almost all RGC input into the tectum. RGC terminations along the anterior to posterior axis of the tectum are topographically arranged with respect to the nasal to temporal position of RGC cell bodies in the retina. As such the zebrafish tectum has been extensively studied to investigate retinotopic map formation. The most numerous tectal neurons are the periventricular neurons (PVN), which have their cell bodies in the SPV. These cells have a characteristic unipolar morphology, with processes which extend into the neuropil. The axons of PVNs are often morphologically indistinguishable from the dendrites, although immunostaining can separate the two compartments (Robles et al., 2011).

PVNs with axons within the tectum are interneurons (Meek, 1981). Efferent PVNs have been discovered which are identified by axonal processes which project to non-tectal brain regions (Kinoshita et al., 2006; Robles et al., 2011). In addition to being classed as a projection neuron or an interneuron, PVN subtypes are identified based on the morphology of their dendritic trees; their extent, their number of stratifications, whether stratifications are planar or diffuse and the position of stratifications within the layers of the tectal neuropil (Meek and Schellart, 1978; Meek, 1981; Robles et al., 2011). It is thought that morphologically defined tectal cell subtypes may share physiological characteristics, although this work is in its infancy. One recent study has described two tectal cell types based on differential morphology and functional properties to moving bar visual stimulation (Gabriel et al., 2012). There are also non-PVN classes of tectal cells which often demonstrate a bipolar or diffuse dendritic structure, and have cell bodies located within the various strata of the neuropil (Meek and Schellart, 1978). One of these tectal cell subtypes are the superficial inhibitory neurons (SINs) which have cell bodies between the SO and SGFS neuropil laminae and dendrites which extend within the superficial SFGS (Del Bene et al., 2010).

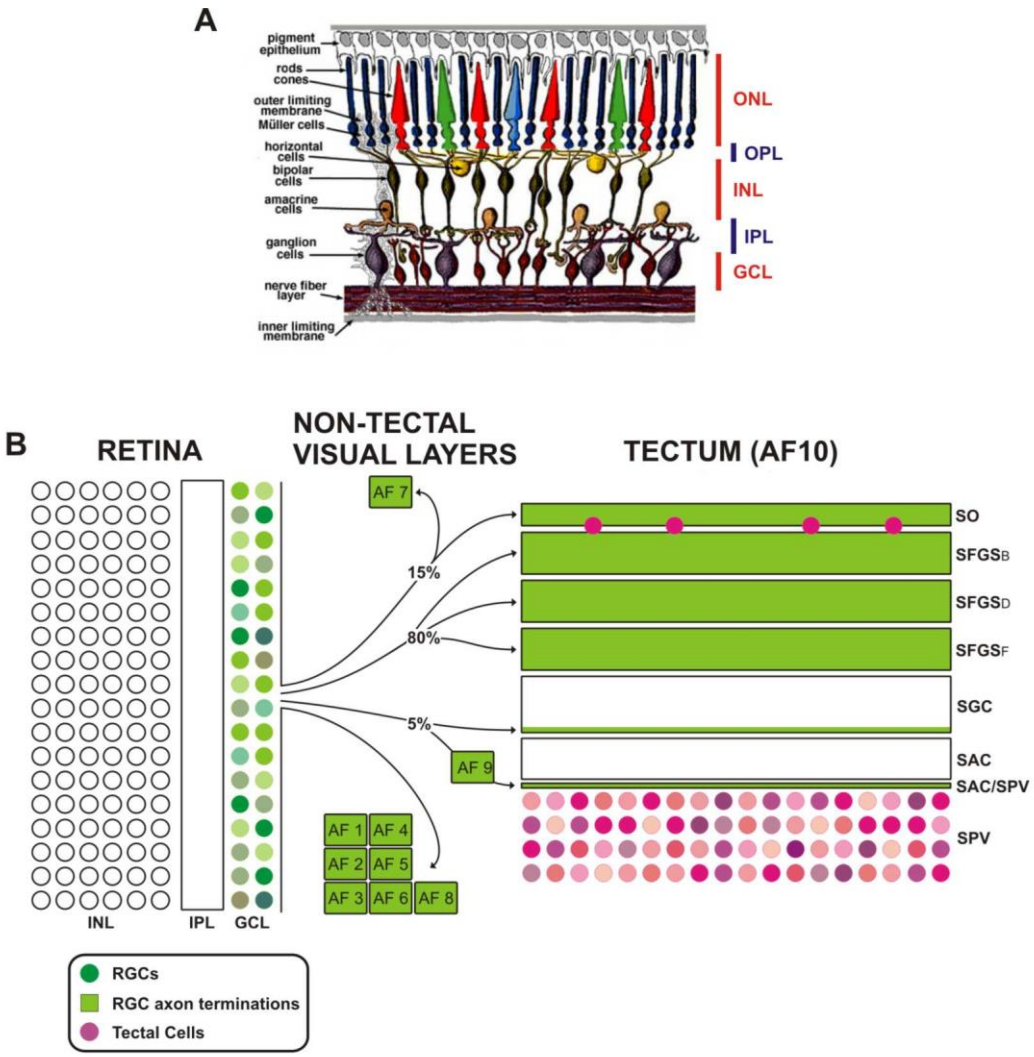

Figure 1.3 Zebrafish visual system. (A) A schematic of the vertebrate retina. The retina is highly a structured organ comprising of alternate nuclear and plexiform layers. Visual information flows from the ONL to the GCL. Photoreceptors are found in the ONL. They make synaptic contacts with bipolar and horizontal cells processes in the OPL which also contact each other. Bipolar cells, horizontal cells and amacrine cells have their cell bodies in different areas of the INL. Bipolar cells make synaptic contacts with amacrine cells and retinal ganglion cell processes in the IPL. RGCs have cell bodies in the GCL and send axons to retinorecipient areas of the brain. **(B)** Retinorecipent areas in the larval zebrafish. RGC cell bodies (green circles) are located in the GCL. Different shades of green coloured circles represent different RGC subtypes. RGC axons leave the retina and terminate within arbourisation fields 1-10. The optic tectum (AF10) receives the majority of RGC innervation. Within the optic tectum RGC termination is mostly restricted to the superficial laminae. Tectal cells are located in the SPV as indicated by pink circles. Different shades of pink coloured circles represent different tectal cell subtypes. ONL, outer nuclear layer; OPL outer plexiform layer; INL, inner nuclear layer; IPL, inner plexiform layer; GCL, ganglion cell layer; RGC, retinal ganglion cell; AF, arbourisation field; SO, stratum opticum; SFGS, stratum fibrosum et griseum superficiale; SGC, stratum griseum central; SAC, stratum album central; SPV, stratum periventriculare. **(A)** is modified from from kolb *et al*., (2007). **(B)** is modified from Nevin *et al*., (2004) by S. Hammond and A. Walker

1.4.1 Development of the retinotectal system in zebrafish

The zebrafish retina develops rapidly, in a columnar fashion; RGCs are specified first, then the cells of the INL, then the photoreceptor layer, in a wave that sweeps across the retina originating from the ventronasal area (Figure 1.4; Hu and Easter, 1999). RGCs differentiate at about 30 hours post fertilisation (hpf) and immediately send out axons which begin to invade the tectum at around 45 hpf (Stuermer, 1988; Schmitt and Dowling, 1999). Between 50 and 55 hpf horizontal and amacrine interneurons are first detected, and photoreceptors specialise their outer segments. Between 60 and 70 hpf synaptic triads form with cone photoreceptors and bipolar cells develop axons with presynaptic ribbon synapses (Schmitt and Dowling, 1999). From 24-30 hpf the tectum can be recognised as a distinct brain structure. Tectal cells first appear at ~3 days post fertilisation (dpf) exhibiting highly immature dendritic trees (Niell et al., 2004). Also at 3 dpf RGCs innervate the tectal neuropil (Stuermer, 1988). At 3 dpf the first visual responses are recorded and the first visually guided behaviours are observed, such as a startle response upon sudden decreases in light intensity, and the optokinetic response (OKR) in which movement relative to a surround is tracked by the eyes (Easter and Nicola, 1996). However, the full repertoire of zebrafish visually-guided behaviours has not been attained, which may be due to the fact that retinotectal development is not complete. While synaptic transmission from cone photoreceptors occurs at 3 days post fertilisation (dpf), it is not fully functional until 5 dpf, and the number of cone ribbon synapses continues to increase until 7 dpf (Biehlmaier et al., 2003). Rods develop very late in the relative development of the zebrafish visual system, becoming functional at 15 dpf, and mature at ~30 dpf (Bilotta et al., 2001). RGCs, despite being the first cell type in the retina to differentiate, undergo a relatively protracted period of dendritic specification in the laminar IPL. *In vivo* time-lapse imaging of RGC dendrites over a period of 3 to 8 dpf showed that most RGCs show laminar stratifications at early timepoints, but the architecture is highly dynamic, with the addition or elimination of stratifications appearing at late timepoints (Mumm et al., 2006). A minority of RGCs have diffuse dendrites early in development which later resolve into multistratified arbours (Mumm et al., 2006). RGC axons enter the tectal hemisphere at the anterior pole at 3 dpf and traverse the anterior to posterior pole of the tectum in their putative neuropil strata and terminate directly in topographically correct tectal positions. However, at early stages RGC axonal arbours and tectal cell dendrites are highly dynamic, extending and retracting branches with a high rate of turnover (O'Rourke et al., 1994; Niell et al., 2004). The total branch length of RGC axon arbours and the number of presynaptic terminals increases rapidly from 3-6 dpf before plateauing (Meyer and Smith, 2006). The dendrites of tectal cells increase rapidly in both total branch length and number of postsynaptic sites between 3 and 8 dpf before reaching a plateau (Niell et al., 2004). This ongoing arbour formation and synaptogenesis between 3 and 8 dpf

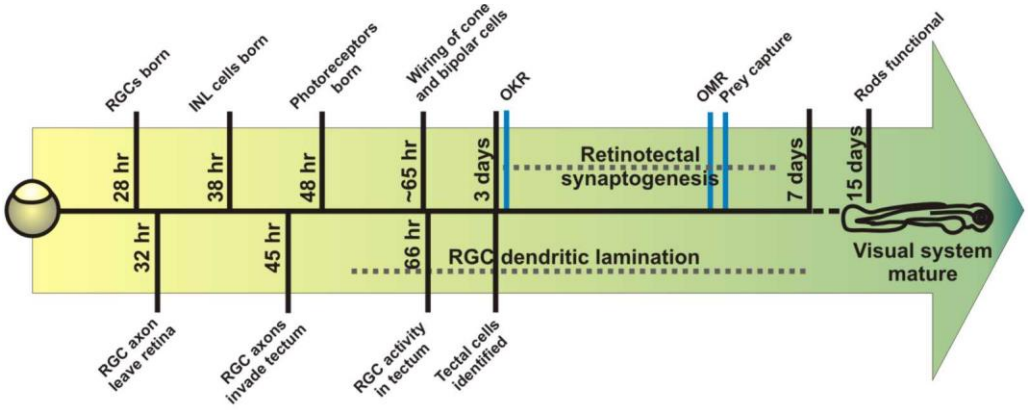

Figure 1.4 Timeline of zebrafish visual system development. Key developments in the visual system are highlightedas black lines and annotated. Maturation occurs from left to right (not to scale). The protracted processes of RGC dendritic lamination and retinotectal synaptogenesis are indicated by dotted grey lines. Key behavioural timepoints are shown as blue lines and annotated. OKR, optokinetic response; OMR, optomotor response.

both in the retina and the tectum suggests that the retinotectal system is undergoing refinement in this period. This maturation is evinced by the improved OKR performance of larvae, which is comparable to adult zebrafish by 4-5 dpf (Easter and Nicola, 1997). In addition, larvae are able to robustly perform more complex visually guided behaviours from 6 dpf such as the optomoter response (Bilotta, 2000), where a fish will swim in the perceived direction of motion, and prey capture (Gahtan et al., 2005).

1.4.1.1 Functions of the zebrafish visual system

The general role of the optic tectum is known. It converts visual signals into motor commands and is vital for phototaxis, visual obstacle avoidance, visual escape response, prey capture and predator avoidance (Bilotta, 2000; Bilotta et al., 2001; Gahtan et al., 2005; Burgess et al., 2010). However, little is known about tectal circuitry and how visual information is actually processed in the tectum. It is known that RGCs terminate in specific neuropil lamina dependent on their functional properties (Nikolaou et al., 2012), and tectal cell dendrites show stratifications which target either a single lamina or a combination of laminae (Meek and Schellart, 1978; Scott and Baier, 2009; Robles et al., 2011), suggesting that functional coupling of tectal cells and RGCs may occur in specific laminae. A recent study has indeed shown that a morphologically and functionally defined tectal cell type has dendrites which sample from RGC axons with similar functional properties (Gabriel et al., 2012). However, it has also been shown that intratectal circuitry can modulate visual characteristics. A study by Del Bene et al., (2010) found that while the deep non-RGC terminating strata of the neuropil,l which contain the

dendrites and axons of PVNs, showed selectivity for detecting small size objects, the superficial retinorecipient strata of the neuropil did not show size-selectivity. This study determined PVNs received non-size tuned excitatory inputs from RGCs but also inhibitory input from SINs, which were selective for large size objects, thus conferring small size-selectivity onto PVNs (Del Bene et al., 2010). Indeed, the ablation of SINs abolished PVN size selectivity highlighting the function of this intratectal connectivity. The zebrafish tectum is increasingly used to dissect circuitry underlying visual processing, the most studied is direction-selectivity, which is outlined below.

1.4.1.2 Mechanisms of direction-selectivity

Direction-selectivity describes neurons which respond maximally to motion in one direction, known as the 'preferred' direction, and minimally to the opposite or 'null' direction. In the mouse, RGCs can be direction-selective (DS) for the four cardinal directions (movement up, down, right and left). Direction-selectivity has been less well studied in the mouse brain (superior colliculus, lateral geniculate nucleus and visual cortex) although direction selective cells have been recorded in the visual cortex (Priebe and Ferster, 2005). In the zebrafish three classes of DS RGCs have been identified which prefer motion in the anterior (265˚), dorsocaudal (164˚) and ventrocaudal (30˚) directions (Nikolaou et al., 2012). However, in the zebrafish brain, four populations of DS PVN tectal cells preferring motion in the four cardinal directions; anterior (261˚), posterior(89˚), upwards (8˚) and downwards (169˚) were found (Hunter et al., 2013).

Studies in the mouse retina have shown that direction-selectivity emerges from the connectivity between starburst amacrine cells (SACs) and RGCs in the retina (Wei et al., 2011). DS RGCs receive strong inhibitory input from SACs when motion is in the null direction (Weng et al., 2005; Wei et al., 2011; Yonehara et al., 2011). When SACs are genetically ablated direction-selectivity of RGCs is lost, accompanied by an increase in firing to the null direction, which suggests a lack of null side inhibitory input (Yoshida et al., 2001; Amthor et al., 2002). In addition, DS RGCs receive strong excitatory input when motion is in the preferred direction (Weng et al., 2005; Wei et al., 2011). To understand the underlying circuitry Yonehara et al., (2011) used channelrhodopsin to activate SACs surrounding an RGC with a known preference for downward movement. They found that while excitatory acetylcholine derived currents from SACs were comparable at all directions, SACs on the preferred side provided smaller inhibitory currents than those on the null side. Similarly, a study by Wei et al., (2011) found using paired cell electrophysiology that while SACs and DS RGCs were connected on all sides,

there was stronger inhibitory unitary conductance when the SAC was located on the null side. This increased inhibition was not caused by changes in wiring on the preferred side as no asymmetry in synapse density was found between the null or preferred sides (Wei et al., 2011). There is also a case that the temporal pattern of excitation and inhibition can underlie direction-selectivity. During null direction movement the inhibitory input coincides with the excitatory, effectively 'shutting down' the contribution of the excitatory input. This timing may be produced by the spatial offset of inhibitory and excitatory activation. These mechanisms, studied in the mouse, are likely to also be found in the zebrafish due to the highly conserved nature of the vertebrate retina.

In the mammalian visual cortex, there appears to be a different mechanism where excitatory (from the LGN) and inhibitory (from intracortical collaterals) inputs onto simple cells are both maximal for the preferred direction of motion. Tuning is created by the relative lag of the inhibitory input compared to the excitatory in the preferred directions (Priebe and Ferster, 2005). In the zebrafish several studies have tried to elucidate the neural circuitry underlying direction-selectivity in tectal cells. A recent study by Gabriel et al., (2012) used transgenic lines with sparse labelling in the tectum, to identify three classes of DS tectal cells. It was found that the DS tectal cells were driven by excitatory inputs which were tuned to the preferred direction. Inhibitory inputs were also discovered, presumably from local tectal interneurons, which were tuned for motion in the null direction, thus amplifying the direction-selectivity conferred onto these cells from tuned excitatory inputs. The simplest model is that these tectal cells receive feed forward excitation from DS RGCs. Indeed two to the tectal cell types in this study showed dendrites which terminate in the superficial SFGS lamina of the tectal neuropil, where it is known that DS RGC axons terminate (Nikolaou et al., 2012). Although another DS tectal cell class preferring downward motion do not synapse directly with RGCs. While these cells clearly receive tuned DS excitatory inputs, it is as yet unknown from where these inputs pertain. It should be noted that another tectal cell class, observed by Gabriel et al., (2012), which prefer posterior motion, was not found when the direction tuning of all RGCs was sampled in a population study by Nikolaou et al., (2012) and therefore are unlikely to receive monosynaptic feedforward input from RGCs. Other studies suggest that direction-selectivity of tectal neurons can be solely determined by intratectal connectivity. Ramdya and Engert (2008) re-routed RGC axons to innervate the ipsilateral tectum by removing the contralateral tectum, thus creating a single tectal hemisphere that was innervated by RGCs from both eyes. They found tectal cells that were DS to the same preferred motion when moving stimuli were played to either eye. It has been suggested that DS RGCs from both eyes may target the same tectal lamina, and therefore may both synapse onto, and be sampled from the same tectal neuron (Gabriel et al., 2012). However, this cannot explain a result where

the tectal cell exhibited a caudal-rostral DS response when a single dot was flashed onto the caudal right eye, and the rostral left eye. Thus no single eye could generate a DS response from a single flash, suggesting the DS response of the tectal neuron was computed in the tectum itself. This study determined that DS tectal cells receive non-tuned excitatory inputs, and DS inhibitory inputs from tectal interneurons. The temporal timing of these inputs is such that for motion in the preferred direction excitation precedes inhibition with the converse arising for movement in the null direction. The summation of these excitatory and inhibitory inputs thus underlies tectal cell direction-selectivity.

These different mechanisms for tectal cell direction-selectivity can be brought together when we consider that not all the circuit components for this system have been identified. There may be multiple tectal cell subtypes which make up the DS tectal cell classes and different mechanisms and local circuitry may account for direction-selectivity in these different subtypes.

1.4.1.3 Mechanisms of orientation-selectivity

Orientation- or axis-selectivity describes neurons that fire maximally to an object orientated along one axis and minimally to an object orientated along the orthogonal axis. In a seminal study by Levick (1967), RGCs were discovered in the rabbit retina that responded preferentially to the orientation of moving black bars or to strips of light orientated vertically or horizontally. The receptive fields of these cells showed a central 'ON' or 'OFF' core, flanked by antagonist strips in register (Levick, 1967; Bloomfield, 1994). The orientation of these receptive fields dictates the preferred orientation. A bar aligned in the preferred orientation of an ON-orientation selective (OS) RGC, will activate the first antagonistic strip, then on-centre, causing RGC firing, then the second antagonistic strip. However a bar orthogonal to the receptive field will activate both the centre and both flanks of the antagonistic surround simultaneously inhibiting the activation of the cell (Bloomfield, 1994). In the rabbit retina, orientation-selectivity is proposed to be a product of amacrine cell GABAergic and glycinergic inhibition of bipolar cells (Venkataramani and Taylor, 2010). In the cat visual cortex, Hubel and Wiesel (1962) first described simple cells which responded with selectivity to the orientation of moving or stationary bars along the vertical and horizontal axes. Like the RGCs in the rabbit retina described above, the receptive fields of simple cells have excitatory and inhibitory regions which are in register for a particular orientation, these narrow simple cell receptive fields are combined by complex cells sampling from many simple cells (Hubel and Wiesel, 1962). Complex and simple cells responding to the same orientation are organised into

functional columns within V1 (Hubel and Wiesel, 1974). It was thought that the lateral geniculate nucleus (LGN), a relay station between the retina and the visual cortex, responded specifically to spots, thus orientation-selectivity in V1 was suggested to be formed by highly organised converging 'spot' information onto simple cells (Hubel and Wiesel, 1962). However, orientation-selectivity along the horizontal (anterioposterior) axis has recently been identified in the mouse LGN, in addition to DS LGN neurons which were predominately selective for anterior and posterior motion (Marshel et al., 2012). This study suggested a theoretical model whereby orientation-selectivity and direction-selectivity in the LGN were a consequence of random wiring of anterior and posterior DS RGCs inputs with LGN neurons. A separate study in the mouse has also observed orientation-selectivity in the mouse LGN but suggest these neurons receive feed-forward OS input from identified OS RGCs (Zhao et al., 2013). In the zebrafish, a recent studies have shown that there are four populations of OS RGCs which show preferred motion along the vertical and horizontal axis, as well as 2 populations flanking the vertical axis (Nikolaou et al., 2012; Lowe et al., 2013). In addition, four classes of OS PVN tectal cells were identified which preferred motion along the same axes as observed for RGCs. While OS RGC and tectal cell classes have been characterised in the zebrafish visual system, to my knowledge no studies have tried to elucidate the circuitry underlying orientation-selectivity in this system. Given that the same populations of OS RGCs and tectal cells have been identified the simplest model would be one of simple feedforward excitation of OS RGCs onto OS tectal cells.

1.5 Thesis outline

In this thesis two main projects are tackled. In Chapter 4 the excitatory drive onto a single hippocampal neuron is assessed *in vitro* by performing calcium imaging in dendritic spines across entire dendritic trees. NMDA receptor-mediated calcium influx was recorded in identifiable synapses and the location of these synapses was then assessed in relation to the morphology of the dendritic tree. This allowed us to investigate how synapses might normalise for cell-wide distance-dependent attenuation of excitatory information and alter local excitability dependent of dendritic location. In Chapter 5 the structural and functional development of orientation- and direction-selectivity is assessed in the retinotectal system of the larval zebrafish *in vivo*. Calcium imaging of single identifiable retinal ganglion cells (RGCs) and tectal cells was recorded in response to moving bar stimuli over a period of days, during the maturation of the visual system.

These projects, while different in terms of individual aims and model systems, share a requirement for optical measurement of neural activity. In Chapter 4, the spatial location of postsynaptic activity is crucial. In Chapter 5, non-invasive functional recordings were required over several days. In addition, fluorescent labelling is essential for identification of single cells over time and the recording of axon arbour and dendritic structure. Fluorescent calcium indicators are versatile tools which have been used to record neuronal activity in many cell types, in many model systems, and to answer many disparate questions and thus were chosen as the tool of choice in these studies. In order to have a good understanding of how the signals of our chosen calcium indicators relate to neural activity a thorough characterisation in response to action potentials was initially conducted using highly amenable dissociated hippocampal cultures (Chapter 3).

2 Materials and Methods

2.1 Materials

2.1.1 Plasmids

Insert	Vector	Fluorescence	Source
CMV:GCaMP3	pEGFP-N2	Green	Gift from Martin Meyer
CMV:SyGCaMP3	pEGFP-N2	Green	Gift from Martin Meyer
CMV:PSDGCaMP3	pEGFP-N2	Green	Gift from Martin Meyer
CMV:RGECO	Customised	Red	Addgene plasmid #32444
CMV:SyRGECO	pEGFP-N2	Red	Gift from Martin Meyer

Table 2.1 DNA plasmids for hippocampal neuron transfection

Insert	Vector	Fluorescence	Source
5UAS:SyGCaMP3	pEGFP-N2	Green	Gift from Martin Meyer
5UAS:SyRGECO	pEGFP-N2	Red	Gift from Martin Meyer
HuC:Gal4:5UAS:RGECO	pBluescript-SK(+)	Red	Gift from Martin Meyer
ath5:Gal4	pBluescript-SK(+)	None	Gift from Steve Wilson, UCL

Table 2.2 DNA Plasmids for microinjection into embryonic larval zebrafish

2.1.2 Drugs and chemicals

Table 2.3 Drugs and chemicals

Chemical	Action	Final concentration	Diluent	Supplier
TTX	Na^{2+} channel antagonist	1 µM	dH_20	Alomone Labs
APV	NMDA receptor antagonist	25 or 50 µM*	dH_20	Sigma-Aldrich
CNQX	AMPA receptor antagonist	20 µM	dH_20	Sigma-Aldrich
FM 4-64	Labels vesicular endo/exocytosis	10 µM	dH_20	Invitrogen
MNI-Glutamate	Caged glutamate	0.5 mM	dH_20	Tocris (1490)
NBQX	AMPA receptor antagonist	10 µM	dH_20	Tocris
Ryanodine	Ryanodine receptor antagonist	30 µM	Ethanol	Abcam
SNX-482	R-type VGCC antagonist	500 nM	dH_20	Sigma
Apamin	SK calcium-activated potassium channel antagonist	100 nM	dH_20	Abcam

*As specified in the Methods.

2.1.3 Experimental Solutions

Hepes buffer saline (HBS) (in mM): 136 NaCl, 2.5 KCl, 10 Hepes, 10 D-glucose, 2 $CaCl_2$, 1.3 $MgCl_2$ (pH 7.3 and 290 mOsmol).

HBS-extracellular stimulation: HBS supplemented with 25 µM APV and 20 µM CNQX.

HBS-spontaneous: (in mM): 137.3 NaCl, 2.5 KCl, 10 Hepes, 10 D-glucose, 2 $CaCl_2$ (pH 7.3 and 290 mOsmol). Supplemented with 1 µM TTX.

HBS-glutamate uncaging: (in mM): 137.3 NaCl, 2.5 KCl, 10 Hepes, 10 D-glucose, 2 $CaCl_2$ (pH 7.3 and 290 mOsmol). Supplemented with 1 µM TTX and 0.5 mM MNI-glutamate.

High K^+HBS: (in mM): 78.5 NaCl, 60 KCl, 10 Hepes, 10 D-glucose, 2 $CaCl_2$, 1.3 $MgCl_2$ (pH 7.3 and 290 mOsmol).

Danieau (in mM): 1000 NaCl, 250 HEPES, 30 $Ca(NO_3)_2$, 20 $MgSO_4$.

Paraformaldehyde (PFA): 4% PFA in 3% sucrose, 60 mM PIPES, 25 mM HEPES, 5 mM EGTA, 1 mM $MgCl_2$.

2.2 Methods

All work in this study was approved by the local Animal Care and Use Committee (King's College London), and was carried out in accordance with the Animals (Experimental Procedures) Act, 1986, under licence from the United Kingdom Home Office.

2.2.1 Sub-cloning of CMV:GECIs

All reagents were from Invitrogen unless otherwise stated. Plasmids for GCaMP3, SyGCaMP3, PSDGCaMP3 and SyRGECO were gifted in a modified pEGFP-N2 vector, where their expression was downstream of a sequence coding for 5 x UAS repeats (5UAS). Sub-cloning was conducted to replace the 5UAS sequence with the CMV sequence from the un-modified pEGFP-N2 plasmid. The 5UAS and CMV sequences were removed from their respective vectors using AseI and EcoRI restriction enzymes (NEB: New England BioLab). 1 µg of plasmid DNA was diluted in nuclease free water (Sigma), into which 10x enzyme buffer (NEB) and restriction enzymes were added at a 1:10 ratio. Following incubation at 37˚C for 1-2 hours, digestion products were mixed with 10x Bluejuice gel loading buffer to make a final concentration of 1x and were run on a gel (1% agarose, diluted in TAE (40mM Tris-Acetate, 1mM EDTA) supplemented with 0.5µg/ml ethidium bromide (Sigma)). A UV illuminator was used to identify bands which were

cut from the gel and the DNA extracted using the Qiagen extraction kit. The CMV insert and the EGFP-N2 vector minus the 5UAS sequence were ligated using ligation buffer and T4 DNA ligase. The ligation mix was left overnight 18°C. Ligated DNA was transformed into the DH5α bacterial strain by a 30 second heat shock at 37°C. Bacteria were plated onto kanamycin containing agar plates (0.02 g/ml LB broth (Sigma), 0.015 g/ml Agar (Sigma), 0.064 mg/ml NaOH and 50 µg/ml Kanamycin) and left overnight at 37°C. Qiagen midi prep kit and mini prep kits were used to extract and purify plasmid DNA, which were amplified from positive bacterial colonies overnight at 37°C in LB broth supplemented with the antibiotic Kanamycin (50 µg/ml).

2.2.2 Preparation of dissociated hippocampal cultures

Hippocampi were dissected from embryonic day 18 Sprague Dawley rats (Charles River Laboratory) in cold sterile HBSS (zero Ca^{2+}, zero Mg^{2+}). Hippocampal neurons were dissociated using trypsin (0.5 mg/ml) in HBSS for 15 min at 37°C; Worthington). The majority of the trypsin-containing solution was removed, the tissue washed in HBSS and then triturated using fire polished Pasteur pipettes, in Neurobasal media containing 2% fetal calf serum and 1% glutamax. Following cell counting using a haemocytometer, the dissociated cells were plated onto previously prepared 18 mm diameter coverslips (Menzel Gläser, Germany) at a density of 90,000 cells per coverslip in Neurobasal media containing 1% fetal calf serum, 1% B-27 supplement, 1% glutamax and 0.5% penicillin streptomycin (Sigma). The preparation of coverslips was conducted by first washing in 60% ethanol and 40% hydrochloric acid for 10 minutes. Coverslips were rinsed with distilled water and washed in 100% ethanol for a further 10 minutes. Coverslips were subsequently rinsed with distilled water and then sterilised in a dry oven for 1 hour at 180˚C. Coverslips were incubated with poly-D-lysine (50 µg/ml) for 1 hr at 37°C, washed thoroughly first with sterile water and then PBS (Sigma) and coated with laminin (20 µg/ml) for 1 hr at 37°C. Neurons were maintained at 37°C in a humidified incubator with 6% CO_2. At 2-3 days post plating half of the culture medium was removed and replaced with Neurobasal media containing 2% B-27 supplement, 1% glutamax and 1% penicillin streptomycin.

2.2.3 Transfection of hippocampal neurons

Dissociated hippocampal neurons were transfected at 7 days in *vitro*. Prior to transfection half of the conditioned media was removed from the cultures and replaced with Neurobasal media

containing 2% B-27 supplement, 1% glutamax and but no penicillin streptomycin (Sigma) as antibiotics can interfere with the transfection process. Plasmids were transfected using Lipofectamine 2000. 0.5 µl Lipofectamine 2000 per well was diluted in Optimum media at a ratio of 1µl Lipofectamine 2000 to 25 µl Optimem, and incubated at room temperature for 5 minutes. 0.5 µg per well of plasmid DNA was diluted in Optimem media at a ratio of 0.5 µg DNA to 25 µl Optimem. The Lipofectamine 2000 and DNA containing solutions were mixed and incubated at room temperature for 20 minutes. 50 µl of the transfection mix was added drop-wise into each well and incubated at 37˚C for 15 minutes. The culture media was then aspirated and replaced with culture media consisting 50% filtered conditioned media, and 50% fresh Neurobasal media containing 2% B-27 supplement, 1% glutamax and 1% penicillin streptomycin.

2.2.4 Imaging of dissociated hippocampal neurons

Imaging of hippocampal neurons was performed using widefield or confocal microscopy. Widefield imaging was performed using an Olympus IX71 inverted microscope with a CCD camera (Coolsnap HQ) controlled by Slidebook software (Intelligent Imaging Innovations), equipped with a 40X/1.0 NA oil-immersion objective (Olympus). The excitation light source was a xenon-arc lamp (Lambda LS; Sutter Instruments), in which light exposure was regulated by a rapid shutter (smartShutter; Sutter Instruments) controlled by a Sutter Instruments lambda 10-3 controller. Two filter settings were chosen dependent on the excitation and emission spectra of the fluorophore. For widefield imaging of green-shifted fluorescence such as for GCaMP3, 470 ± 20nm band pass excitation and 515 ± 20 nm band pass emission (Chroma Technology Corporation) filter sets were used. For widefield imaging of red-shifted fluorescence such as for RGECO, FM 4-64 and TagRFP 565 ± 22 nm band pass excitation and 590-nm long pass dichroic plus 650 ± 36 nm band pass emission (Chroma Technology Corporation) filter sets were used. Confocal imaging was performed with an Olympus FV1000 confocal microscope equipped with a 40X/0.8 NA water-immersion objective (Olympus). For confocal microscopy imaging of green-shifted fluorescence such as for GCaMP3, SyGCaMP3, Alexa 488 secondary antibody excitation was provided by a 488nm laser line, with emission collected via a 505-525 nm band pass emission filter. Red-shifted fluorescence, such as for RGECO, SyRGECO and Alexa 568 secondary antibodies, was excited with a 543nm laser line, with emission collected via a 560-660 nm band pass emission filter.

2.2.5 FM 4-64 labelling of SyGCaMP3 expressing neurons

Neurons were depolarised for 90 seconds in high K^+ (60 mM) HBS supplemented with 1 µM TTX, 25 µM APV, 20 µM CNQX and 10 µM FM 4-64 to load the recycling pool of synaptic vesicles. Neurons were washed in HBS containing 1 µM TTX for 10 minutes to remove non-endocytosed FM 4-64. Z-stack images were acquired using widefield microscopy with 0.5 µm step interval. Images were collapsed and analysed as maxiumum intensity projections (MIPs) using ImageJ and custom written Matlab routines. Puncta intensity of both SyGCaMP3 and FM 4-64 were calculated within 7 x 7 pixel ROIs picked dependent on SyGCaMP3 fluorescence. To determine the degree of co-localisation that arises through chance, analysis was also performed on datasets in which the SyGCaMP3 image was rotated 180˚ relative to the FM 4-64 image.

2.2.6 Characterisation of GECIs with extracellular field stimulation

For extracellular field stimulation, coverslips, on which neurons were cultured, were mounted in a custom-made chamber fitted with a pair of parallel platinum electrodes, 5 mm apart. During imaging and stimulation, neurons were incubated in HEPES-buffered saline containing 25 µM APV and 20 µM CNQX at room temperature. Neurons were stimulated by delivering 1-2 ms, 80 V voltage pulses at 20 Hz. Each pulse approximates a single action potential (AP) (Zhao et al., 2011a). Single, 2, 5, 10, 20, 40, and 60 pulse stimulations were delivered, with multiple 10 AP stimulations interleaved during the time course of each experiment. 1 to 20 AP stimuli were pseudo-randomised, however, 40 and 60 AP stimuli were always delivered at the end of the stimulus sets to prevent possible activity-induced plasticity. Fluorescence signals from neurons co-transfected with both GCaMP3 and RGECO, or SyGCaMP3 and SyRGECO were recorded sequentially to avoid spectral cross–talk. The GECI imaged first was alternated for each cell tested. Functional time-series were acquired using confocal microscopy at a rate of approximately 6 Hz and 0.2 x 0.2 µm resolution. Functional time-series were acquired using widefield microscopy at a rate of approximately 6 Hz and with 0.25 x 0.25 µm resolution.

2.2.7 Data analysis of characterisation of GECIs with extracellular field stimulation

Characterisation data was analysed using a voxel-wise Matlab (Mathworks) based analysis software ‘AFID’ written by Andrew Lowe (KCL, London), in conjunction with custom written

Matlab routines. Normalised signal intensity changes (ΔF/F) were calculated on time-series with maximum and integral responses over the epoch-interval determined at each voxel. Summary images were generated displaying the peak ΔF/F or integral ΔF/F during the stimulation period for each voxel. For RGECO and GCaMP3, the mean of a square (10 x 10 voxels) region of interest (ROI) applied to summary images gave the peak response. As RGECO, but not GCaMP3, was expressed in the nucleus, ROIs were selected within the cytoplasmic region of the cell body. For SyGCaMP3 and SyRGECO expressing neurons, ROIs were defined by an empirically derived threshold based on the summary images for the first 10 AP stimulation. Once defined these ROIs were applied to all other stimulations. RGECO and GCaMP3 detection thresholds for single-APs were calculated as peak ΔF/F responses greater than 3 standard deviations of baseline noise. Rise and decay kinetics for all GECIs were calculated for 10 AP stimulations using semi-automated spike analysis software (Synaptosoft Inc.). In experiments where rundown occurred, kinetics were calculated from solely the first 10 AP stimulation to prevent bias from rundown. To determine the degree of co-localisation of SyGCaMP3 and SyRGECO, puncta intensities of both probes were calculated within 7 x 7 voxel ROIs. To determine the degree of co-localisation that arises through chance, analysis was also performed on datasets in which the SyGCaMP3 image was rotated 180˚ relative to the SyRGECO image.

2.2.8 Correction for rundown of RGECO, SyGCaMP3 and SyRGECO

Several normalisation routines were trialled to generate stimulus-response plots corrected for rundown (Figure 2.1). By normalising for the response at each time point by the mean value of flanking 10 AP responses we recover a fair stimulus-response plot, but by assigning all 10 AP responses a value of 1 we introduce inconsistencies in the error for each stimulation. A linear regression generated in Microsoft Excel was trialled to fit the decay observed in 10 AP responses, but while in general the fit was strong (R^2=0.96 for RGECO rundown), the responses at the final timepoints were more poorly fit, causing a rebound effect for 60 APs seen in the linear normalised stimulus-response plots. We found that the best fit for rundown in 10 AP responses was by an exponential decay generated in Microsoft Excel (R^2=0.99 for RGECO rundown) and subsequently stimulus-response plots were generated using a correction factor derived from the slope of the exponential decay for each cell.

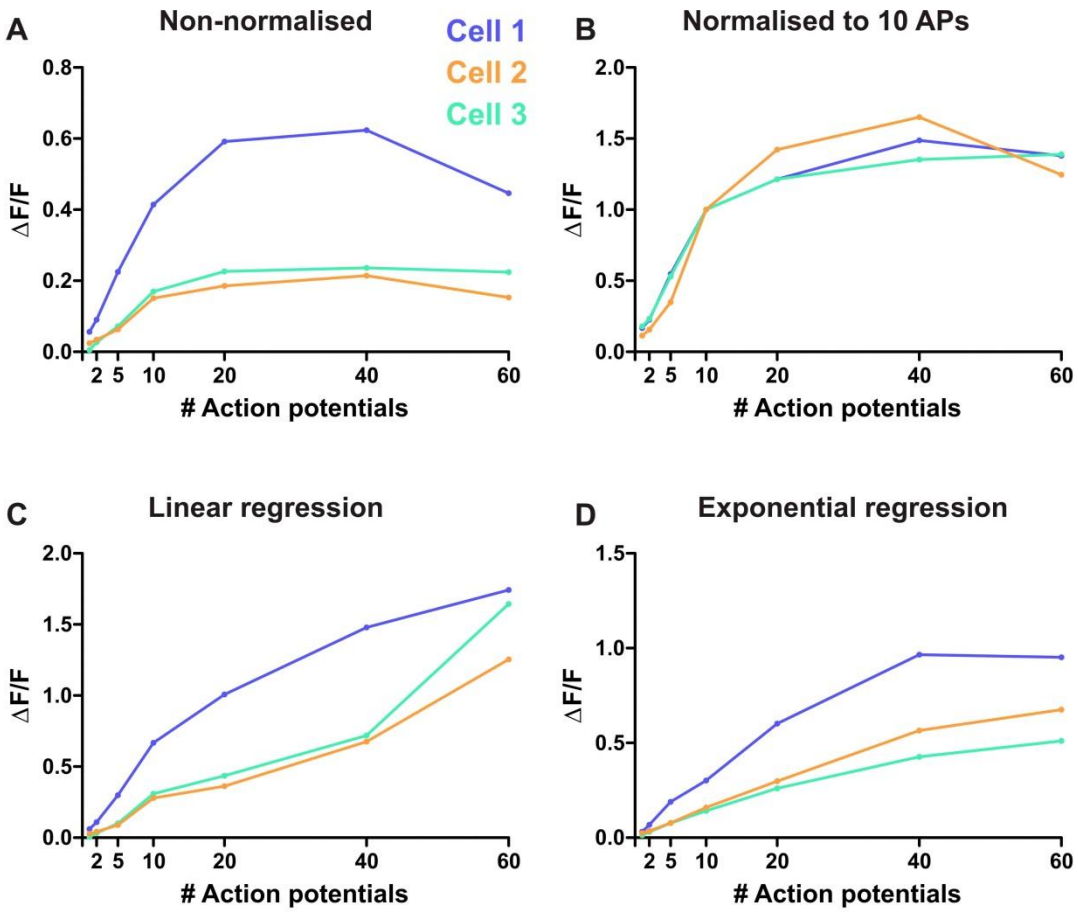

Figure 2.1 Potential normalisation routines for RGECO rundown. (A) RGECO stimulus-response plots for three co-transfected hippocampal neurons for different numbers of action potentials. Note that rundown leads to a early plateau of RGECO responses to high number action potential stimulations delivered later in the stimulus protocol. **(B-D)** The normalisation of RGECO rundown using different techniques. **(B)** Responses to 1, 2, 5, 20,40 and 60 APs are scaled in relation to the mean peak ΔF/F of flanking 10 AP responses which are interspersed within the experiment. Note that this routine artificially sets all 10 AP responses to 1. **(C-D)** Normalisation to a line fitted to peak ΔF/F of all 10 AP responses interspersed within the experiment. Responses to all numbers of APs were normalised with respect to the slope of the fitted rundown using a linear regression **(C)** or a exponential regression **(D)**. Note that the inability for the linear regression to describe the rundown at the end of the experiment leads to an artificial amplification of 40 and 60 AP responses.

2.2.9 MNI-glutamate uncaging and imaging

Coverslips with neurons expressing either PSDGCaMP3 or cytosolic GCaMP3 were mounted into a custom built chamber and bathed in HBS-glutamate uncaging solution (see Materials section 2.1) which was supplemented with 0.5 mM MNI-glutamate. Glutamate was released from the MNI motif by destabilisation of the bond joining them with photostimulation using a 405 nm UV laser (FV5LDPSU; Olympus) at 4.69 mW intensity. Photostimulation was applied at

a single pixel between 0.25-2 µm from the principal spine. Timeseries were acquired on an Olympus FV1000 confocal microscope (as above). For characterisation experiments pulses of UV light were given for 0.05, 0.1, 0.25, 0.5, 0.75, 1, 2.5, 5 and 10 ms. Functional timeseries for PSDGCaMP3 had acquisition rates between 2 and 5 Hz, with a resolution of either 0.115x0.115 or 0.31x0.31 µm, and for cytosolic GCaMP3 between 3 and 5 Hz and with 0.062 x 0.062 µm resolution. For repetitive uncaging experiments a small range of stimuli were tested to find an uncaging length which permitted a response local to a single spine (0.025-0.25 ms). Pulses of fixed uncaging length were delivered to single spines every 15 seconds for between 17-31 trials per spine. Functional time-series were acquired at rates between 9 and 18 Hz, with a resolution of either 0.31x0.31 or 0.388x0.388 µm resolution. For glutamate uncaging across the dendritic tree small windows were chosen at different locations. Several uncaging stimuli were trialled to find a stimulus length which promoted a small calcium transient localised to a single spine and a 0.25 ms pulse was chosen. Uncaging length as well as imaging parameters such as laser intensity were kept constant at all areas studied. Functional time-series were acquired at approximately 5.5 Hz, with a resolution of 0.31x0.31 µm resolution.

2.2.10 Analysis of MNI-glutamate uncaging data

GECI responses to glutamate uncaging were analysed using custom written Matlab routines. 6x6 voxel ROIs were drawn around the spine uncaged upon (the principal spine) and the adjacent dendritic shaft, identified by expression pattern and morphology. For each timeseries background was chosen as an area away from the cell, and was subtracted from the image. Peak ΔF/F was calculated as a mean of the ΔF/F of all voxels within each ROI during the uncaging epoch.

2.2.11 Imaging spontaneous neurotransmitter release

Coverslips were mounted into a custom built chamber and bathed in HBS-spontaneous solution. Time series were acquired using a widefield microscopy (Olympus IX71 inverted microscope with a CCD camera). Functional timeseries were acquired at a rate of approximately 6 Hz and with 0.32x0.32 µm resolution. For each cell, two timeseries were typically recorded sequentially, each lasting approximately 1.5 minutes.

Pharmacology experiments using 10 µM NBQX, 500 nM SNX, 100 nM apamin and 30 µM ryanodine (see section 2.1.2) were performed recording activity from entire dendritic trees

using widefield microscopy as outlined above. Pharmacology experiments using 50 µM APV and 1.3 mM Mg^{2+} were performed using confocal microscopy. For all pharmacology experiments baseline calcium transients were recorded from cells in a 500 µl bath of HBS-spontaneous solution. 250 µl of this solution was removed and replaced with 250 µl fresh HBS-spontaneous solution supplemented with double the final concentration of drug. For control experiments, 250 µl of this solution was removed and replaced with 250 µl fresh HBS-spontaneous solution. Following a 10 minute wait period calcium transients were recorded from the same cell.

Linescan imaging was performed on GCaMP3 expressing neurons bathed in HBS-spontaneous solution. Freehand tracings using Olympus FV1000 software perpendicular to the dendritic branch positioned the line over the centre of many spines. Linescans were acquired at a rate of approximately 125 Hz.

2.2.12 Analysis of spontaneous data

GECI responses to spontaneous neurotransmitter release were analysed using custom written Matlab routines. 6x6 voxel ROIs were drawn around all dendritic spines identified by expression pattern and morphology. For each timeseries background was chosen as an area away from the cell, and was subtracted from the image. Baseline fluorescence for each ROI was calculated as the median fluorescence intensity from all timepoints to reduce contamination from calcium transient spikes. ΔF/F traces for each ROI were calculated and analysed using semi-automated spike analysis software (Synaptosoft Inc.). The ΔG/R metric for each ROI was calculated by generating ΔG, which is identical to ΔF. ΔG is then normalised by the mean intensity of TagRFP intensity calculated from the same ROI. Dendritic structure is traced using the NeuronJ plugin for ImageJ, creating a text file containing the co-ordinates of branch positions (Figure 2.2 A). Using in-house Matlab routines each branch is stitched together and the start co-ordinate assigned as a 'node' or branch point and the end co-ordinate assigned as an 'end point' (Figure 2.2 B). ROI co-ordinates are imported (Figure 2.2 C)and assigned a parent branch dependent on the shortest distance between ROI co-ordinates and branch co-ordinates (Figure 2.2 D). Three distance metrics were used. Absolute distance, which is the distance of each ROI to the cell soma, was calculated by an algorithm which searches for the shortest path along the branches to the cell body. Number of nodes was determined by the number of node points encountered during calculation of absolute distance. Relative distance was calculated as the absolute distance divided by the distance from the soma to the furthest branch tip. This was calculated using an algorithm that searches

for the longest path from each ROI to a branch tip in addition to the absolute distance. For the histograms of quantal calcium transient (QCT) amplitude for each bin of relative distance a two component fit was chosen based on a straight line plus an exponential decay. Cumulative frequencies are calculated from the area under the fitted curve of these histograms, i.e. the sum of the straight line plus the exponential decay.

2.2.13 Immunocytochemistry

Coverslips were fixed in 4% PFA for 20 minutes. Cells were washed 5 times in PBS and permeablised using PBS supplemented with 0.25% Triton-X100 (Sigma, UK) for 5 minutes. Cells were blocked by incubation in PBS supplemented with 10% goat serum (Sigma, UK) for 1 hour at room temperature. This solution was removed and replaced with PBS containing 2% Goat serum and primary antibodies either rabbit αPSD-95 (1:500, Millipore) or mouse αGluN1 (1:100, Thermo-Scientific), plus a chicken αGFP (1:1000, Abcam) and incubated either overnight at 4°C or for 5 hours at room temperature. Cells were then washed 5 times in PBS. Cells were incubated in fluorophore-conjugated secondary antibodies for 1 hour at room temperature, then washed 5 times in PBS. Coverslips were mounted onto glass microscope slides using mowiol solution. Mowiol was made by dissolving 5 g mowiol (Calbiochem) in 20 ml PBS, stirred overnight at room temperature. 10 ml glycerol was added and the solution stirred for a further 16 hours. Centrifugation was used to remove undissolved mowiol and DABCO (Sigma) was added before use.

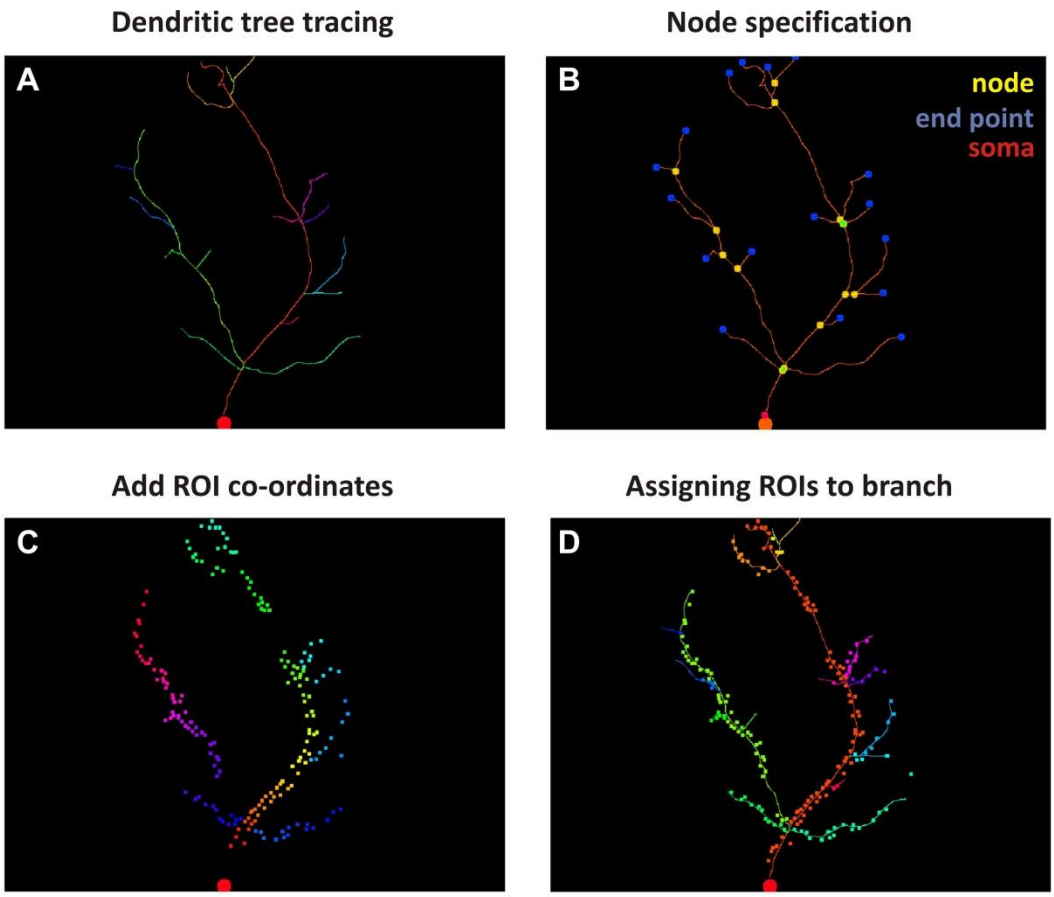

Figure 2.2 Building dendritic trees. (A) The dendritic tree is reconstructed using co-ordinates from tracings made using NeuronJ software (ImageJ). Each branch os assigned an identity displayed here by colour-coding. **(B)** The start and end co-ordinates from each branch are assigned as either a node or an end point, respectively. **(C)** ROIs picked in Matlab. **(D)** Each ROI is assigned to the closest branch and therefore is given a positional identity within the dendritic tree. ROIs are colour-matched to nearest branch.

2.2.14 Zebrafish

All experiments using larval zebrafish were conducted in a *nacre* mutant background. *Nacre* fish (from Robert Kelsh, University of Bath) are homozygous for the recessive *nacre* (*nac*^{w2}) mutation, resulting in a loss of melanophores throughout life (Lister et al., 1999). However, the pigmented epithelium of the retina develops normally, as these cells are derived from a separate cell-lineage. Larval zebrafish were raised at 28.5˚C on a 14 hr ON/10 hr OFF light cycle in danieau solution.

2.2.15 Mosaic labelling of single neurons in the larval zebrafish

Nacre embryos were harvested and microinjected at the 1-4 cell stage of development with plasmid DNA diluted in Danieau solution. A small drop of plasmid DNA (~1.5 nl), diluted in Danieau solution was pressure injected into a single cell of each embryo. Single cells were labelled transiently using the *Gal4-5UAS* system, adapted from the *Drosophila melanogaster* (see plasmids table section 2.1.1). This technique requires the injection of an effector plasmid, coding for a cell-type specific promoter directly upstream of the yeast transcriptional activator protein Gal4, and an effector plasmid where the Gal4 DNA binding motif, the Upstream Activation Sequence (UAS) is in frame with the GECI of interest. Only cells where the activator promoter is normally active will express Gal4, and expression of GECI will only occur if the effector plasmid is also present, and subsequently 'switched on' through Gal4-UAS binding. The probability of these two events occurring is rare and thus mosaic expression of GECIs is achieved. Expression of SyGCaMP3 in retinal ganglion cells (RGCs) was driven by an activator plasmid containing the *ath5* promoter, expression of which is important in the determination of retinal ganglion cells during neurogenesis in the retina (Kay et al., 2001). Expression of RGECO in single tectal cells used a variant of the above Gal4-5UAS system, where only a single plasmid was injected containing the pan-neuronal promoter HuC driving expression of Gal4 directly upstream of the UAS sequence, lying in frame with RGECO.

2.2.16 Drifting bar stimulation of RGCs and tectal neurons

Microinjected larvae were mounted dorsally on glass slides in 1% low melting point agarose (Sigma, UK). Danieau solution was added on top of the set agarose to hydrate the larvae. Larvae were screened for expression of SyGCaMP3 in RGC single axon arbours in the tectal neuropil, or RGECO expression in single tectal neurons. Positive larvae were removed from the agarose and left in danieau to recover for > 45 minutes. These larvae were then restrained in 2% low melting point agarose, mounted dorsally onto a customised glass platform. The agarose was sufficient to restrain the larvae so that anaesthesia was not required. Agarose was removed from one eye, and the larva positioned with this eye facing a screen onto which visual stimuli were projected, while timeseries were simultaneously captured from the contralateral tectum (Figure 2.3). The projected image filled a visual field of approximately 97° by 63°. Visual stimuli consisted of dark bars (8cd/m_2) (25% of mean) on a mean grey background (32cd/m_2). Each bar was 10º in width moving at 20°/second and separated from the preceding bar by 30° - enabling more than one bar on the screen at any one time. The long axis of the bar was orthogonal to the direction of motion. A drifting bar stimulus has been used previously to

define direction and orientation selectivity in the non-mammalian visual system (Bilotta and Abramov, 1989; Engert et al., 2002). Bars were presented at 12 different directions evenly spaced across 360˚ and displayed in a pseudo-random order. A blank screen null condition of 2 seconds was also randomly interleaved. Each inter-epoch interval was 8 seconds to enable the SyGCaMP3 and RGECO signals to return to baseline. Visual experiments were generated and controlled using custom written Labview and Matlab code (MathWorks) implemented on a ViSaGe stimulus presenter (Cambridge Research Systems, UK) and delivered via a DLP pico projector (Optoma).

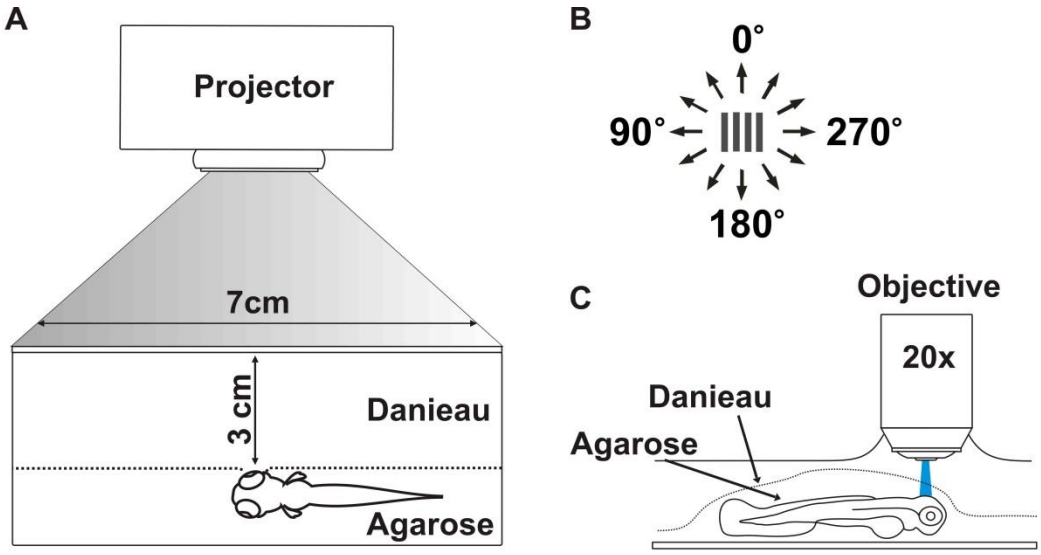

Figure 2.3 The experimental set-up for visual stimulation of larval zebrafish. The functional responses of SyGCaMP3-expressing single RGCs or RGECO-expressing tectal cells were assessed in responses to visual stimulation. **(A)** Larvae were mounted in agarose and placed in a custom-made chamber filled with Danieau solution. The larvae were positioned so that the eye contralateral to the tectal hemisphere of interest faced a screen. **(B)**The visual stimualation comprises of dark bars drifting in 12 directions. The distance of the projector to the screen and the screen to the larvae was calibrated for bar measurements to be made with respect to degrees of the zebrafish visual field. **(C)** The objective was placed above the tectum to image the RGC axon arbour or the tectal cell body of interest during simultaneous visual stimulation.
Diagram modified from S. Hammond (M. Meyer Lab)

2.2.17 Imaging of larval zebrafish

Confocal imaging of visually-evoked responses was performed using an LSM 710 confocal microscope equipped with a spectral detection scan head and a 20X/1.0 NA water-immersion objective (Carl Zeiss). Excitation of RGECO was provided by a 543 nm laser line and of SyGCaMP3 with a 488 nm multi-line laser. For SyGCaMP3 expressing RGCs functional time-series were acquired at a rate of 4 Hz and 0.415 x 0.415 µm voxel resolution (256x256 voxels). For RGECO expressing tectal cells functional time-series were acquired at a rate of 6.5 Hz and 0.208 x 0.208 µm voxel resolution (256x256 voxels). The average diameter of a presynaptic bouton in zebrafish RGCs is ~0.8µm (Meyer and Smith, 2006).Thus, the X-Y resolution of voxels is below that of a typical presynaptic bouton. Optical sections were obtained at <1.6 µm intervals and maximum intensity projections of RGECO and SyGCaMP3 expressing neurons were generated using NIH ImageJ. The Simple Neurite Tracer in FIJI (a processing package based on ImageJ released under the General Public License) was used to perform semi-automated tracing of z-stacks for 3D reconstruction of arbours and calculation of total branch lengths.

2.2.18 Voxel-wise analysis of orientation- and direction-selectivity

The confocal time-series were post-processed prior to analysis as follows: time-series images from each experiment were corrected for motion with a rigid-body algorithm (spm8–www.fil.ion.ucl.ac.uk/spm); spatially smoothed with a 2D Gaussian kernel = 2 voxels (0.83 µm) to improve signal-to-noise and; low-frequency drifts in baseline corrected using a cubic-spline algorithm extrapolating between knots averaged from 5 seconds of the inter-epoch-interval data. Normalised signal intensity changes (ΔF/F) were calculated on the time-series at each voxel and the integral response over the epoch-interval calculated to provide a single response metric of each presented orientation. All voxels that reached an empirically derived integral threshold were regarded as visually responsive and subjected to further characterisation: direction- and orientation-selectivity. Orientation and direction-selective responses were determined using direction- and orientation-selective indices (DSI and OSI; Niell and Stryker, 2008) based on fitted von-Mises profiles. OSI and DSI preferred angles were determined from the peak of von-Mises curves. To generate polar plots, for every integral ΔF/F image, each summarising the response to a different direction of drifting bars, a mean integral ΔF/F value was calculated from all voxels within an ROI, encompassing either all responsive pixels for RGCs or the cell body for tectal cells. To generate grouped polar plots, the mean integral ΔF/F values calculated above for each direction were normalised to the maximum response within

each timeseries. Following this, the mean and standard deviation were calculated across timeseries from the same cell for each direction of drifting bars presented.

3 Chapter 3: Characterisation of genetically-encoded calcium indicators

3.1 Introduction

Calcium imaging has become an increasingly valuable tool in neuroscience. The usefulness of calcium imaging is dependent on improved calcium indicators, the latest revolution occurring in genetically-encoded calcium indicators (GECIs). GECIs combine the advantages of genetics such as non-invasive expression, and cell-type and subcellular targeting, with good functional properties for reading out changes in calcium concentration which accompany neural and synaptic activity. The most widely used GECIs are from the GCaMP family of green spectrum indicators based on GFP. Genetic engineering of existing GCaMP molecules has led to an array of GCaMP variants being generated in recent years. For newly generated GECIs to be used with confidence to detect neural activity it is essential to understand their properties, in particular with reference to their performance at reporting different numbers of action potentials.

To permit simultaneous two-colour functional imaging, efforts have been made to generate GECIs which are spectrally distinct from the classic GFP-based single fluorophore indicators. Recently, a red-shifted GECI 'RGECO' was engineered with little spectral overlap with GCaMPs (Zhao et al., 2011a). However, the characterisation of RGECO in the original study was not exhaustive. A quantitative analysis was provided only for a signal change following exposure to a high calcium concentration when RGECO is expressed in bacterial periplasm. In neurons, the analysis was highly qualitative in nature, simply noting that a calcium transient is detected when neurons are activated with potassium chloride (Zhao et al., 2011a). Thus, prior to use in measuring complex neuronal activity both *in vivo* and *in vitro* it is essential to understand the dynamic range, sensitivity kinetics and reliability of RGECO in reporting neural activity in neurons. In this chapter, we have undertaken a thorough characterisation of RGECO in dissociated hippocampal neurons in response to extracellular field stimulation. To provide a meaningful 'benchmark' GCaMP3 was characterised alongside RGECO.

The targeting of GECIs to presynaptic boutons by fusion to synaptophysin (SyGCaMP2) has been shown to improve the reporting properties of cytosolic GCaMP2 whilst allowing the indirect measure of neurotransmitter release based on bouton calcium influx (Dreosti et al., 2009). We hypothesised that by applying this strategy to other, more recently generated GECIs, we could generate subcellularly targeted indicators with improved properties. To test this, fusions of synaptophysin to improved GCaMP variants GCaMP3 and RGECO were generated. In this chapter, SyGCaMP3 and SyRGECO were characterised in terms of dynamic

range, sensitivity, kinetics and reliability to report extracellular field stimuli in dissociated hippocampal neurons. Again, to contextualise the performance of these newly generated tools, these presynaptically targeted GECIs were compared to their cytosolic parent GECIs.

Similar to presynaptic targeting, GECIs can be targeted to postsynaptic compartments through fusion with postsynaptic proteins, such as β-actin (Mao et al., 2008; Ohkura et al., 2012). Unlike synaptophysin fusions, improvements in reporting properties compared to cytosolic parent molecules is less clear. Here, a new postsynaptically-targeted GECI was generated by fusing GCaMP3 to PSD-95, an essential PSD component. The potential reporting properties of this novel GECI were unknown, therefore in this chapter a characterisation of PSDGCaMP3 was undertaken, in parallel with cytosolic GCaMP3. Performance was tested to synaptic activation both in response to glutamate uncaging and spontaneous neurotransmitter release in dissociated hippocampal neurons.

3.2 Results

3.2.1 Characterisation of RGECO

The performance of GECIs will vary according to the assay used to assess functional properties and the experimental set-up of the laboratory. Thus, we decided to not simply characterise RGECO alone, but in comparison to GCaMP3, a well-characterised and widely used GECI (Tian et al., 2009; Huber et al., 2012b; Nikolaou et al., 2012; Weitz et al., 2013). In order to directly compare the performance of RGECO with GCaMP3 both GECIs were co-expressed in dissociated hippocampal neurons (Figure 3.2.1 A). Expression of GCaMP3 and RGECO permitted visualisation of neuronal morphology. Consistent with previous observations (Yamada and Mikoshiba, 2012), GCaMP3 was excluded from the nucleus, whereas RGECO was not (Figure 3.2.1 A). Robust increases in GCaMP3 and RGECO fluorescence intensity were observed in response to extracellular field stimulation (10x 1 ms pulse at 80 V, 20 Hz; Figure 3.2.1 B). The performance of GCaMP3 and RGECO was assessed using the normalised fluorescence change (ΔF/F), a metric that corrects for variation in expression levels of each GECI. We noted that peak ΔF/F values for both RGECO and GCaMP3 generally occurred in cell bodies (Figure 3.2.1 B) and so confined our analysis to the cytoplasmic region of this subcellular compartment, where both GCaMP3 and RGECO were expressed.

The performance of GCaMP3 and RGECO were recorded in response to varying numbers of action potentials (APs; 1, 2, 5, 10, 20, 40 and 60) delivered at a frequency of 20 Hz. To test whether GECI performance was stable over time, responses to a 10 AP test stimulus were measured at regular intervals during each experiment (Figure 3.2.2 A). RGECO responses to these test stimuli show a large successive decrease in response amplitude over time. While some GCaMP3 responses do show a small decrease in response amplitude, this was not stereotyped for all cells and overall no decreasing trend in response amplitude was observed (Figure 3.2.2 A-B). The impact of this progressive decrease in RGECO amplitude, hereafter referred to as rundown, was clearly seen in the mean traces for 40 and 60 APs which are routinely delivered at the end of the stimulus paradigm, and have lower peak ΔF/F values than responses recorded to fewer numbers of APs delivered earlier in the stimulus set (Figure 3.2.2 C). This contrasts with GCaMP3 where the peaks of the mean response traces increased steadily with stimulus strength until they plateau at approximately 40 APs regardless of the sequence of the stimuli (Figure 3.2.2 C).

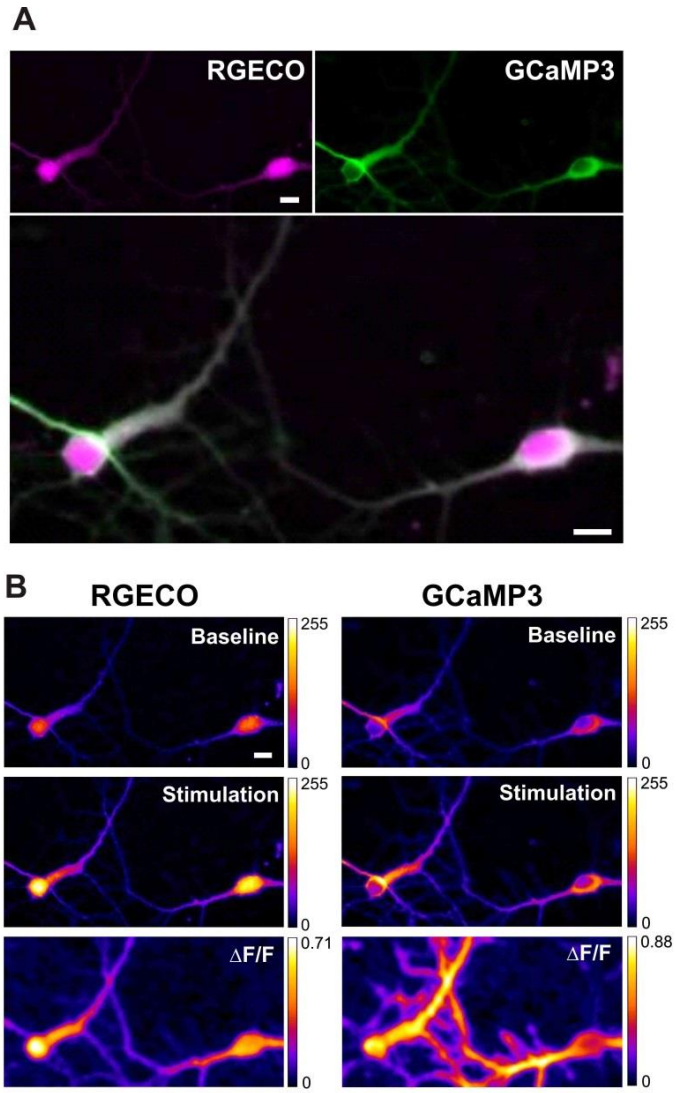

Figure 3.2.1 GCaMP3 and RGECO respond to extracellular stimulation in co-transfected dissociated hippocampal neurons. (A) GCaMP3 and RGECO expressed in the same hippocampal neuron in culture. Note the different nuclear expression patterns for RGECO compared with GCaMP3. **(B)** Summary images demonstrating changes in GCaMP3 and RGECO fluorescence intensity to 10 APs (10 x 1 ms 80 V pulse delivered at 20 Hz). Top and middle panels show raw fluorescence images during baseline and stimulation epochs, colour-coded by pixel intensity (scale to the right). For each GECI, baseline summary images are scaled to the maximum pixel intensity of the stimulation summary image. Bottom panels show peak ΔF/F response summary images. Pixels are colour-coded according to the maximum recorded ΔF/F value for each probe (scale to the right). All scale bars = 10 µm.

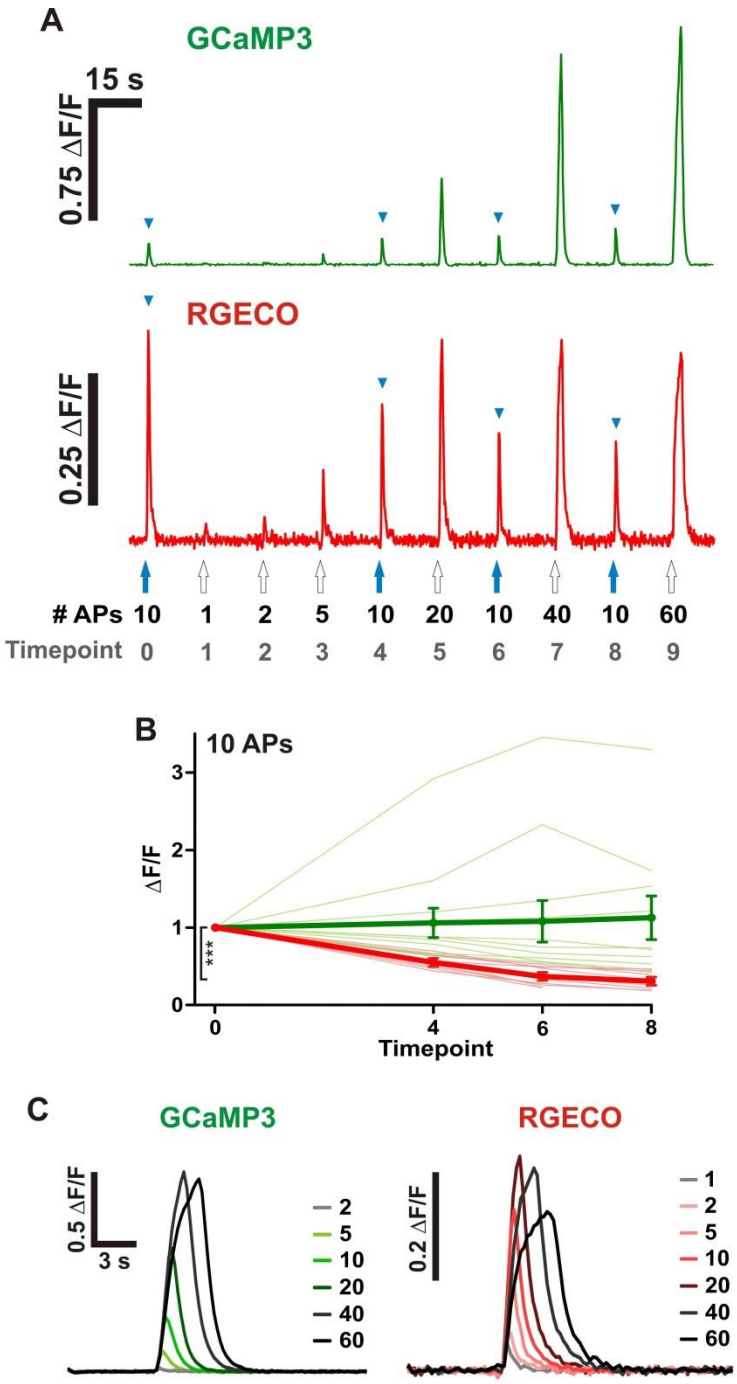

Figure 3.2.2 RGECO responses exhibit a progressive rundown. (A) Concatenated traces of RGECO and GCaMP3 responses from the same hippocampal neuron to a typical experimental stimulation paradigm. A two minute recovery period was observed between timepoints. The number of APs and the timepoint within the paradigm is indicated, and blue arrows and arrowheads highlight stimulation by, and responses to interspersed repeats of 10 APs, respectively. **(B)** Peak ΔF/F responses of GCaMP3 and RGECO to 10 AP test stimulations interspersed throughout the timecourse of the experiment (n=12 cells). Mean responses and responses of individual cells are shown in bold and faint lines, respectively. For each cell responses are normalised to the response at timepoint zero. Note the significant rundown of RGECO responses (red traces) compared to GCaMP3 responses (green traces) between the 0-8 timepoints. Kruskall-Wallis one-way ANOVA followed by Dunn's post-test. P value: ***<0.001.**(C)** Mean traces of GCaMP3 and RGECO in response to a range of APs delivered in ascending order as seen in **(A)**. Traces are colour-coded according to AP number (key to the right for each GECI; n=8 cells).

We became interested in investigating the underlying cause of RGECO rundown. Given that mApple, the fluorescence protein on which RGECO is based, exhibits a ~270-fold increase in bleaching under arc lamp illumination compared to the scanned laser illumination used in confocal imaging (Shaner et al., 2008) we hypothesised that the prolonged excitation associated with widefield microscopy, which was used for these experiments, might cause RGECO rundown. Alternatively, electrical stimulation may induce adaption of calcium channels. To test which of these scenarios may be true we developed paradigms to dissociate the effects of fluorescence light exposure and electrical stimulation (Figure 3.2.3 A). For 'Control', responses to 10 AP stimuli delivered repeatedly at 2 minute intervals were recorded. As noted above, over time RGECO showed a very large (~80%) stereotyped decrease in response while GCaMP3 showed a smaller, and variable reduction in response (Figure 3.2.3 B). When a similar experiment was conducted, where the number of exposures to fluorescence matched the Control paradigm, but 10 AP stimuli were delivered for each GECI every 12 minutes (Minimal Stimulation) compared to every 2 minutes for Control, the GCaMP3 and RGECO responses recapitulated the control data exactly (Figure 3.2.3 B; black points). However, when 10 AP stimuli were delivered as per the Control paradigm (every 2 minutes), but exposure to excitation light for each GECI occurred every 10 minutes, compared to every 2 minutes (Minimal Excitation) we saw a marked reduction in RGECO rundown (Figure 3.2.3 B). This demonstrates that the exposure of RGECO to fluorescence excitation is linked to the expression of rundown. In fact, the magnitude of RGECO responses from the Control and Minimal Excitation paradigms were exactly matched on the basis of the number of exposures of RGECO to fluorescence (Figure 3.2.3 C).

The marked rundown in RGECO responses caused by the excitation method used in widefield microscopy led to subsequent characterisation being carried out using confocal microscopy, in which fluorescence excitation scanned across the field of view substantially reduces the exposure of each voxel to fluorescence. To permit adequate temporal resolution the field of view was reduced to encompass only the cell body (Figure 3.2.4 A-B). Similar to using widefield fluorescence we found robust increases in fluorescence intensity in response to extracellular field stimulation using confocal microscopy, which were again measured as normalised ΔF/F values (Figure 3.2.4 B). As predicted from the experiments outlined above we observed no rundown in RGECO responses to repeats of 10 APs interspersed throughout the experiment (Figure 3.2.4 C-D).

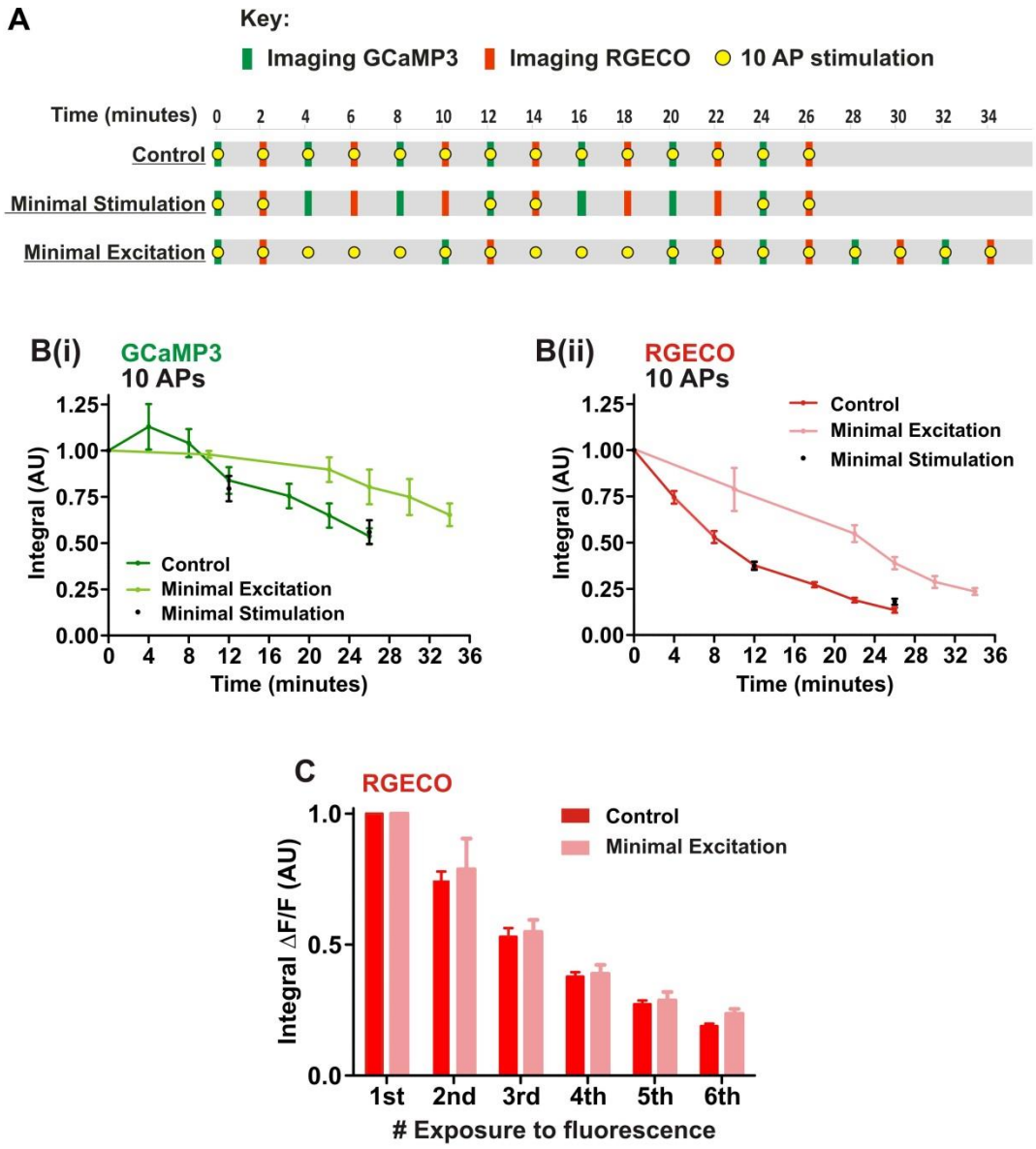

Figure 3.2.3 RGECO rundown is caused by exposure to excitation light. (A) A schematic detailing three experimental paradigms used to determine the aetiology of rundown in GCaMP3 and RGECO co-transfected neurons. The 'Control' paradigm repeatedly tests GCaMP3 and RGECO responses to 10 AP stimuli. The 'Minimal Stimulation' paradigm has fewer 10 AP stimulations compared to control. The 'Minimal Excitation' paradigm has fewer periods of fluorescence excitation compared to the control. **(B)** Mean integral ΔF/F responses to 10 AP stimulations over time for GCaMP3 **(i)** and RGECO **(ii)**, as per paradigm in **(A)**, where responses are normalised to the integral ΔF/F of the first recording (Control n=5 cells; Minimal Excitation n=4 cells; Minimal Stimulation n=5 cells). Note that by reducing the number of fluorescence excitations less rundown is observed (Minimal Excitation). **(C)** Side-by side comparison of the RGECO integral ΔF/F values for the Control and Minimal Excitation data (from **B(ii)**) for the number of RGECO fluorescence exposures, irrespective of time.

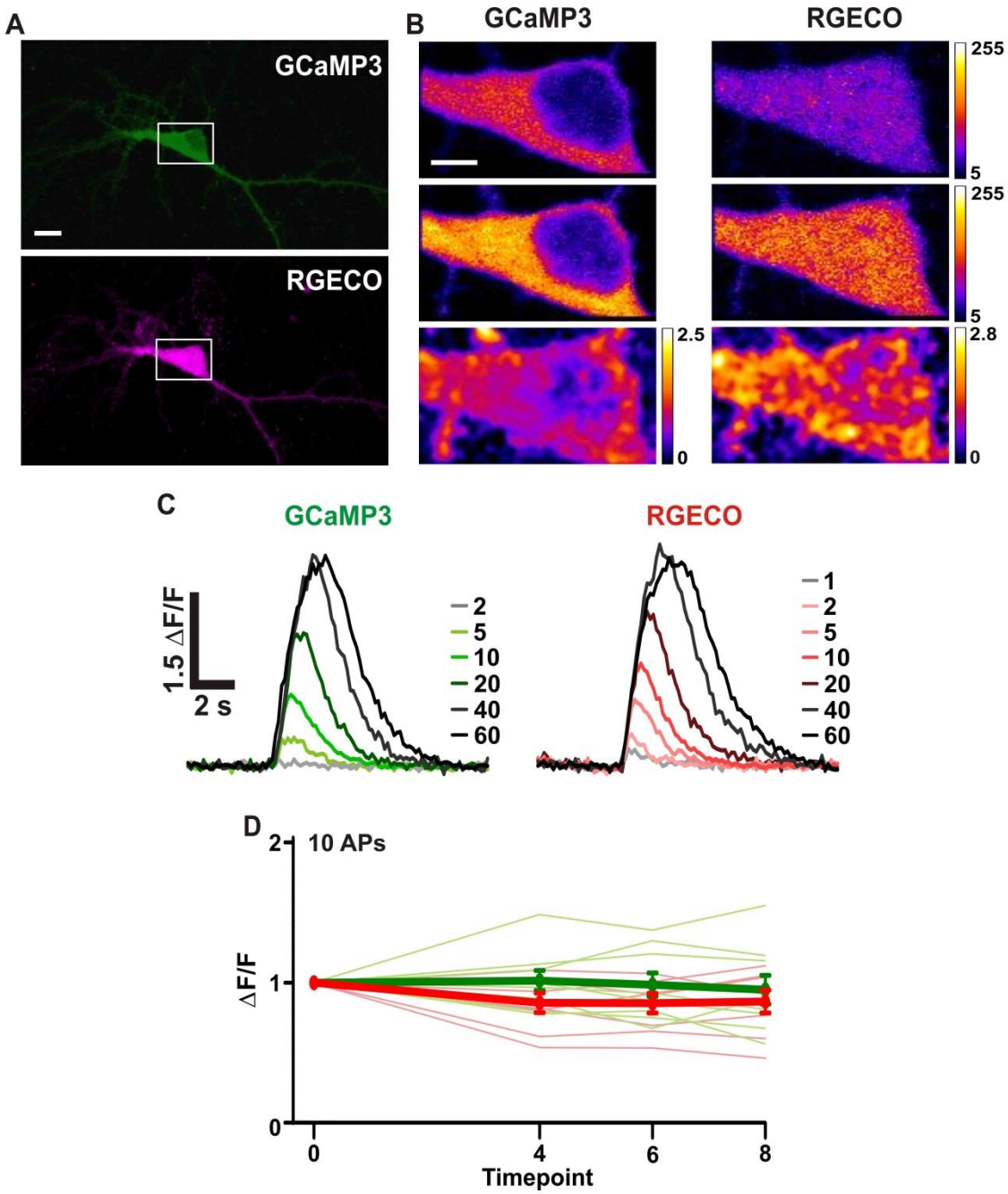

Figure 3.2.4 Characterisation of GCaMP3 and RGECO using confocal microscopy prevents RGECO rundown (A) GCaMP3 and RGECO co-expressed in the same hippocampal neuron. Scale bar = 10 µm. White boxes indicate the area used for functional imaging; these small fields of view had frame rates comparable to widefield fluorescence imaging. **(B)** Summary images demonstrating changes in GCaMP3 and RGECO fluorescence intensity to 10 APs extracellular field stimulation. Top and middle panels show raw fluorescence images during baseline and stimulation epochs, colour-coded by pixel intensity (scale to the right). Bottom panels show peak ΔF/F response summary images. Pixels are colour-coded according to the maximum recorded ΔF/F value for each GECI (scale to the right). Scale bar = 5 µm. **(C)** Mean traces of GCaMP3 and RGECO in response to a range of APs. AP number is colour-coded as shown to the right for each GECI. (n=7 cells). **(D)** Peak ΔF/F responses of GCaMP3 and RGECO to 10 AP test stimulations interspersed throughout the timecourse of the experiment (n=7 cells). Mean responses and responses of individual cells are shown in bold and faint lines, respectively. For each cell responses are normalised to the response at timepoint zero. Note the absence of rundown of RGECO responses (red traces) which are similar to GCaMP3 responses (green traces).

Responses to varying numbers of APs showed GCaMP3 and RGECO display a very similar dynamic range, for both the peak ΔF/F and the integral ΔF/F metrics (Figure 3.2.5 A(i) and B(i)). In addition, RGECO proved to be a more robust reporter of low-number action potentials. In fact, single action potentials were detected by RGECO in 88% of trials compared to 38% by GCaMP3 (threshold set at 3 standard deviations of baseline noise). Interestingly, the dynamic range and sensitivity of GCaMP3 and RGECO recorded using confocal microscopy are mirrored by recordings made using widefield fluorescence when a correction factor derived from the stereotyped exponential rundown of RGECO was applied to RGECO responses (see Materials and Methods) (Figure 3.2.5 A(ii) and B(ii)). In fact, following this correction the sensitivity of RGECO appeared significantly greater than that of GCaMP3 up to 10 APs, however, it is possible that this was an effect of the correction factor which was applied only to RGECO.

Side-by-side characterisation of GCaMP3 and RGECO in co-transfected neurons is highly advantageous for making direct comparisons between the performances of these GECIs. However, there is concern that the presence of one GECI may interfere with the properties of the other, or with the normal activity of the neuron. To address this, the characterisation paradigm used above was performed on neurons transfected with either GCaMP3 or RGECO alone (Figure 3.2.6 A). These experiments were performed using widefield microscopy prior to understanding the role of fluorescence exposure in rundown. While the stereotypical nature of rundown allows for its adequate correction, ideally, this experiment would be repeated using confocal microscopy. We observed rundown in RGECO but not GCaMP3 responses to interleaved 10 AP test stimuli when these GECIs were singly transfected, similar to results in co-transfected neurons (Figure 3.2.6 B). Following correction for rundown of RGECO, we found that the magnitudes, sensitivity, and dynamic range of GCaMP3 and RGECO responses in singly-transfected were overall similar to those measured in co-transfected neurons (Figure 3.2.6 C). These data suggest that co-transfection does not alter the response properties of either RGECO or GCaMP3.

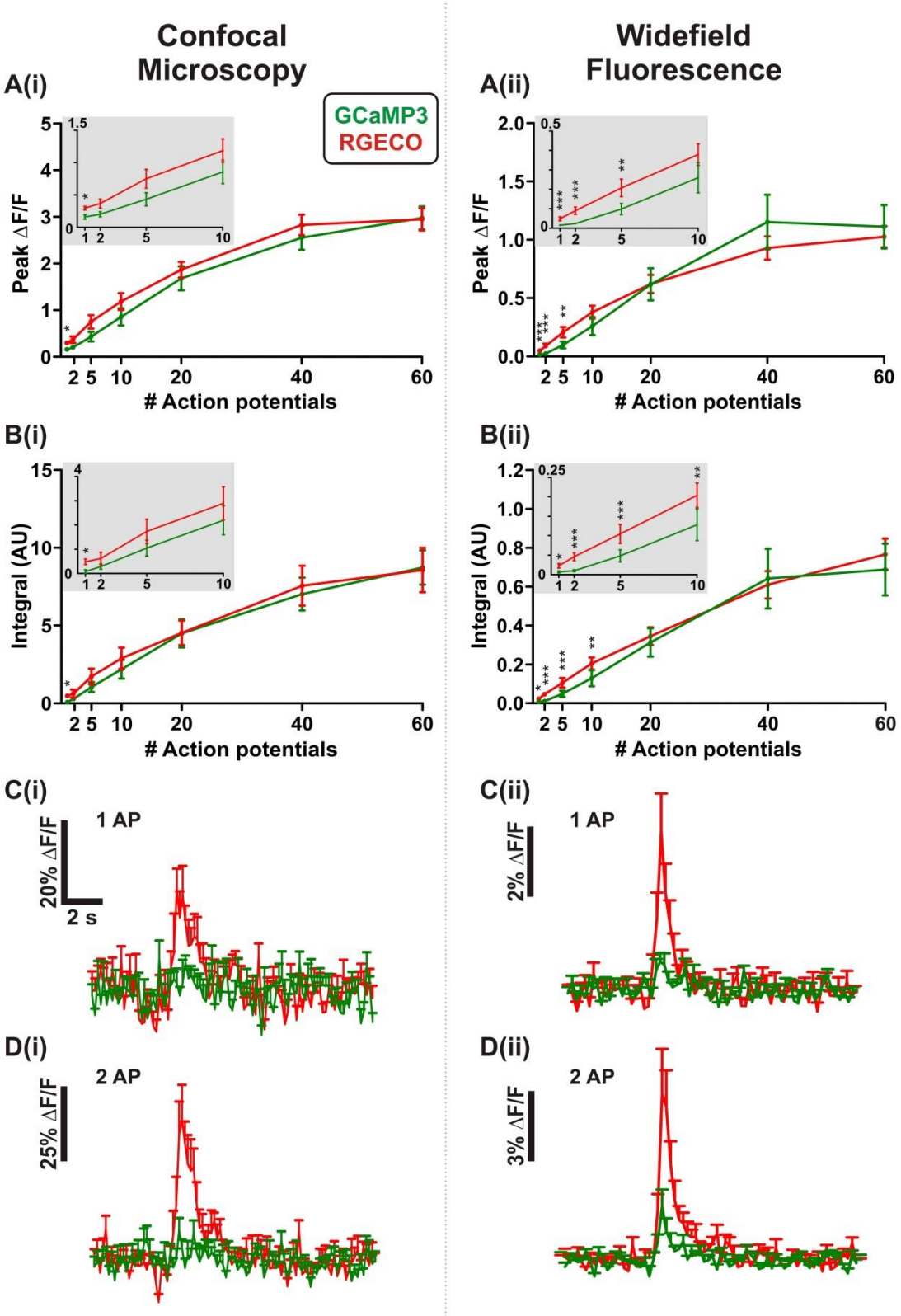

Figure 3.2.5 RGECO exhibits both a high dynamic range and high sensitivity. (A-B) Characterisation of GCaMP3 and RGECO to different numbers of APs using confocal **(i)** and widefield **(ii)** microscopy. **(A)** Peak ΔF/F over number of APs. **(B)** Integral ΔF/F over number of APs. RGECO responses using widefield microscopy were corrected for rundown (see 'Materials and Methods'). Insets show a magnified (1-10 AP) region of the plots to highlight the sensitivity of RGECO compared to GCaMP3 to low numbers of action potentials; Wilcoxen signed rank tests. (confocal n=7 cells; widefield n= 12 cells). **(C-D)** Mean traces with standard error of the mean bars for RGECO and GCaMP3 responses to 1 AP **(C)** and 2 AP **(D)** stimulation obtained using confocal **(i)** and widefield **(ii)** microscopy (confocal n=6 cells; widefield n=8 cells). P values *<0.05, **<0.01, ***<0.001.

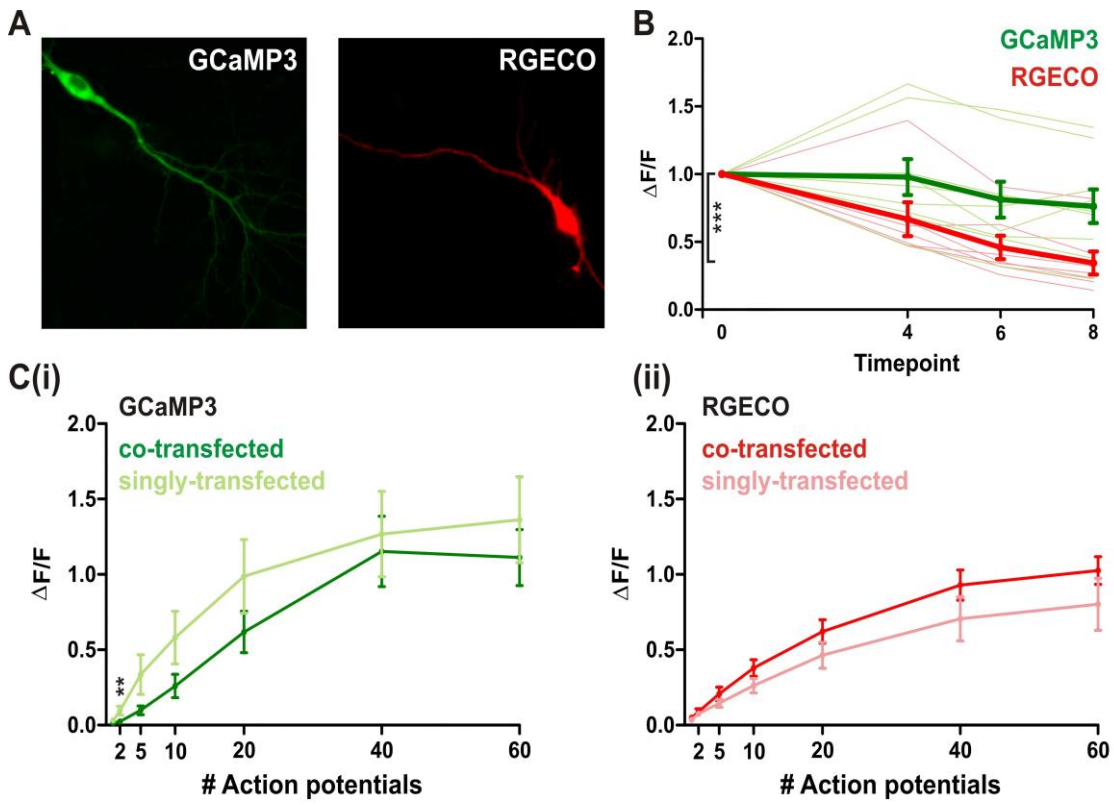

Figure 3.2.6 Characterisation of GCaMP3 and RGECO in singly transfected hippocampal neurons using widefield microscopy. (A) Dissociated hippocampal neurons expressing either GCaMP3 or RGECO. **(B)** Peak ΔF/F responses of GCaMP3 and RGECO to 10 AP test stimulations interspersed throughout the timecourse of the experiment (GCaMP3 n=7 cells; RGECO=6 cells). Mean responses and responses of individual cells are shown in bold and faint lines, respectively. For each cell responses are normalised to the response at timepoint zero. Kruskal-Wallis one-way ANOVA followed by Dunn's post test. **(C)** Peak ΔF/F over AP number for GCaMP3 **(i)** and RGECO **(ii)** measured in single- and co-transfected neurons using widefield microscopy (single-transfected: GCaMP3 n=7cells, RGECO n=6 cells; co-transfected: n=12 cells). Responses of RGECO were corrected for rundown (see Materials and Methods). Mann Whitney test. P values *<0.05, **<0.01, ***<0.001.

It is possible that co-transfection of both GCaMP3 and RGECO may affect calcium binding, altering the kinetics of responses of co-transfected neurons in comparison to singly transfected neurons (Figure 3.2.7 A). However, we found no significant difference (one-way ANOVA) in the 90% rise and decay kinetics for GCaMP3 and RGECO responses to 10 APs between singly- and co-transfected neurons recorded using widefield microscopy (Figure 3.2.7 B). When comparing the kinetics of RGECO and GCaMP3 we found that both the rise and decay kinetics to 10 APs stimulation were similar for RGECO and GCaMP3 whether these GECIs were singly- or co-transfected, and independent of whether recordings were made using widefield or confocal microscopy (Figure 3.2.7 B). However, there was a trend toward RGECO exhibiting a faster rise time and also exhibiting a slower decay time. In addition, we noted some differences in our experimental set-ups; the confocal generated slower rise and decay times for both RGECO and

GCaMP3 than using widefield microscopy (two-way ANOVA, P=<0.05). While there is no clear explanation as to why this may occur, it demonstrates the importance of characterising tools in-house.

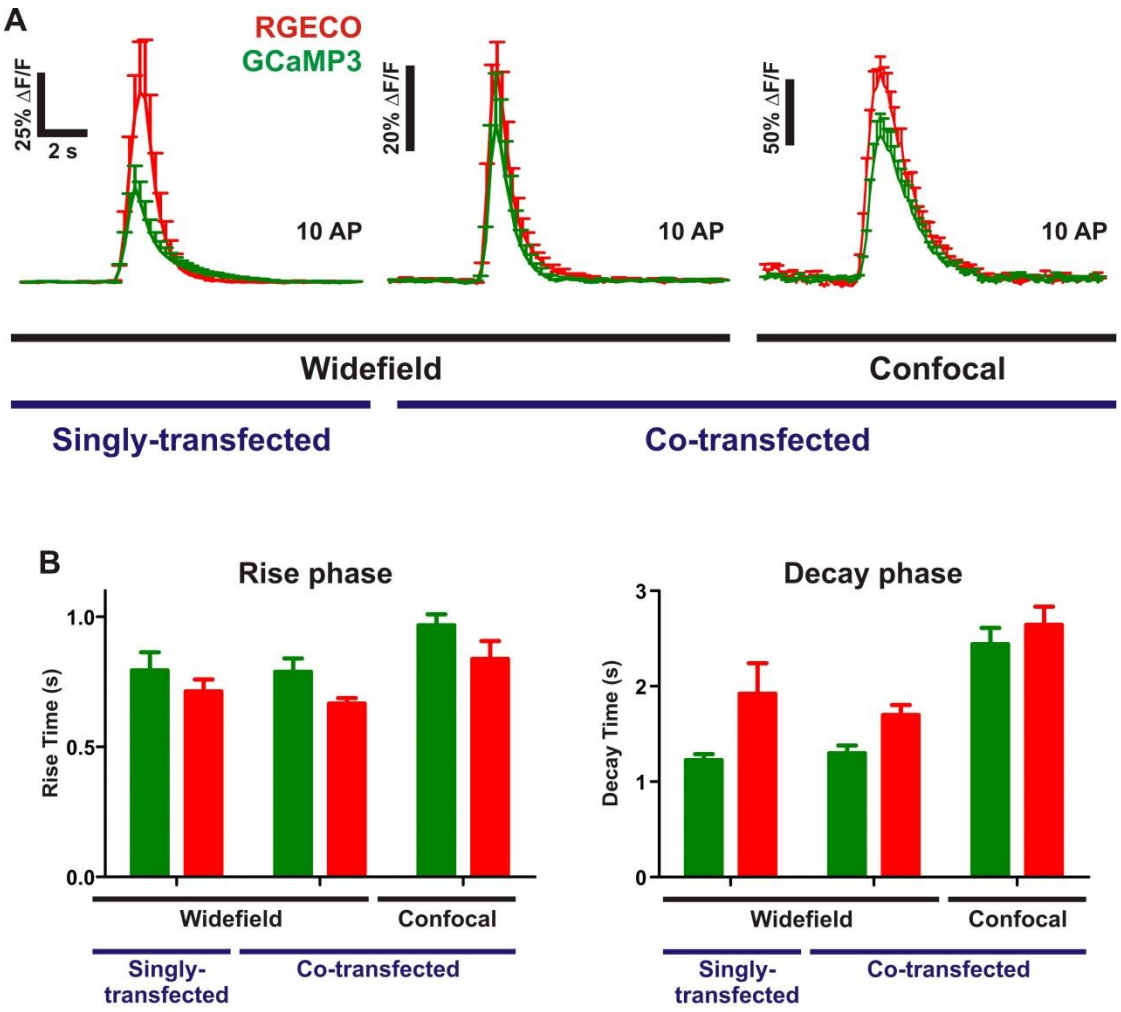

Figure 3.2.7 Rise and decay phase kinetics for RGECO and GCaMP3. (A) Mean traces with standard error of the mean bars for RGECO and GCaMP3 responses to 10 APs stimulation. Single- or co-transfection and the microscopy used for recordings are indicated below the traces. **(B)** 90% rise and decay times calculated for singly- or co-transfected neuron responses to 10 APs stimulation. Single- or co-transfection and the microscopy used for recordings are indicated below the graphs. Kinetics were calculated only in response to the initial 10 AP stimulation for widefield microscopy due to rundown. For responses recorded using confocal microscopy all 10 AP repeats were included (widefield: singly transfected RGECO n=8 cells, GCaMP3 n=9 cells; co-transfected n=12 cells; confocal: co-transfected n=31).

3.2.2 Characterisation of SyGCaMP3 and SyRGECO

One of the strengths of using GECIs is the ability to target their expression to specific subcellular compartments. Targeting GECIs to synaptic boutons allows recording of calcium transients which specifically trigger the release of neurotransmitter. Here, we have used a previously described strategy (Dreosti et al., 2009) to restrict GECI expression to presynaptic terminals through fusion of GCaMP3 and RGECO to synaptophysin, a synaptic vesicle protein, creating SyGCaMP3 and SyRGECO respectively.

Dissociated hippocampal neurons co-transfected with SyGCaMP3 and SyRGECO showed a punctate expression pattern (Figure 3.2.8 A). The intensity of SyGCaMP3 and SyRGECO fluorescence at different puncta was highly correlated in 3 axons which were imaged with different image settings (Spearman's co-efficient; axons 1-3 P value <0.0001) indicating that the expression of SyGCaMP3 and SyRGECO was as expected co-localised (Figure 3.2.8 B). To exclude that SyGCaMP3 and SyRGECO co-localisation occurred by chance, the SyGCaMP3 image was rotated 180˚ to disassociate the SyGCaMP3 and SyRGECO images and no correlation was observed (pale blue, green and red points colour matched to those of unaltered SyGCaMP3 images). Spearman's co-efficient; P values axon 1=0.8, axon 2=0.3 and axon 3=0.5 (Figure 3.2.8 B).

To confirm that the punctate expression of synaptophysin-fusion GECIs corresponded to sites of synaptic vesicle cycling we adopted a functional approach using FM dyes which were used to label synaptic vesicles in an activity-dependent manner (Betz and Bewick, 1992). The steryl dye FM 4-64 accumulated at activated presynaptic boutons during a brief depolarising 60 mM potassium chloride treatment of SyGCaMP3 expressing neurons (Figure 3.2.8 C). SyGCaMP3 fluorescence and FM 4-64 fluorescence were highly correlated at identified SyGCaMP3 puncta in 3 axons which were imaged with different image settings (Spearman's co-efficient; axons 1-3 P value <0.0001; Figure 3.2.8 D). These data suggest that SyGCaMP3 was reliably targeted to presynaptic sites. This co-localisation did not occur by chance as when the FM 4-64 image was rotated 180˚ no correlation was observed (pale blue, green and red points colour matched to those of unaltered SyGCaMP3 images). Spearman's co-efficient; P values axon 1=0.2, axon 2=0.5 and axon 3=0.9 (Figure 3.2.8 D).

The performance of SyGCaMP3 and SyRGECO was characterised side-by side in co-transfected hippocampal neurons using confocal microscopy which, as described above, is less likely to induce rundown of RGECO. Both SyGCaMP3 and SyRGECO showed robust increases in fluorescence intensity in response to extracellular field stimulation (Figure 3.2.9 A). When stimulated, the peak response (ΔF/F) was mainly localised to presynaptic boutons with much

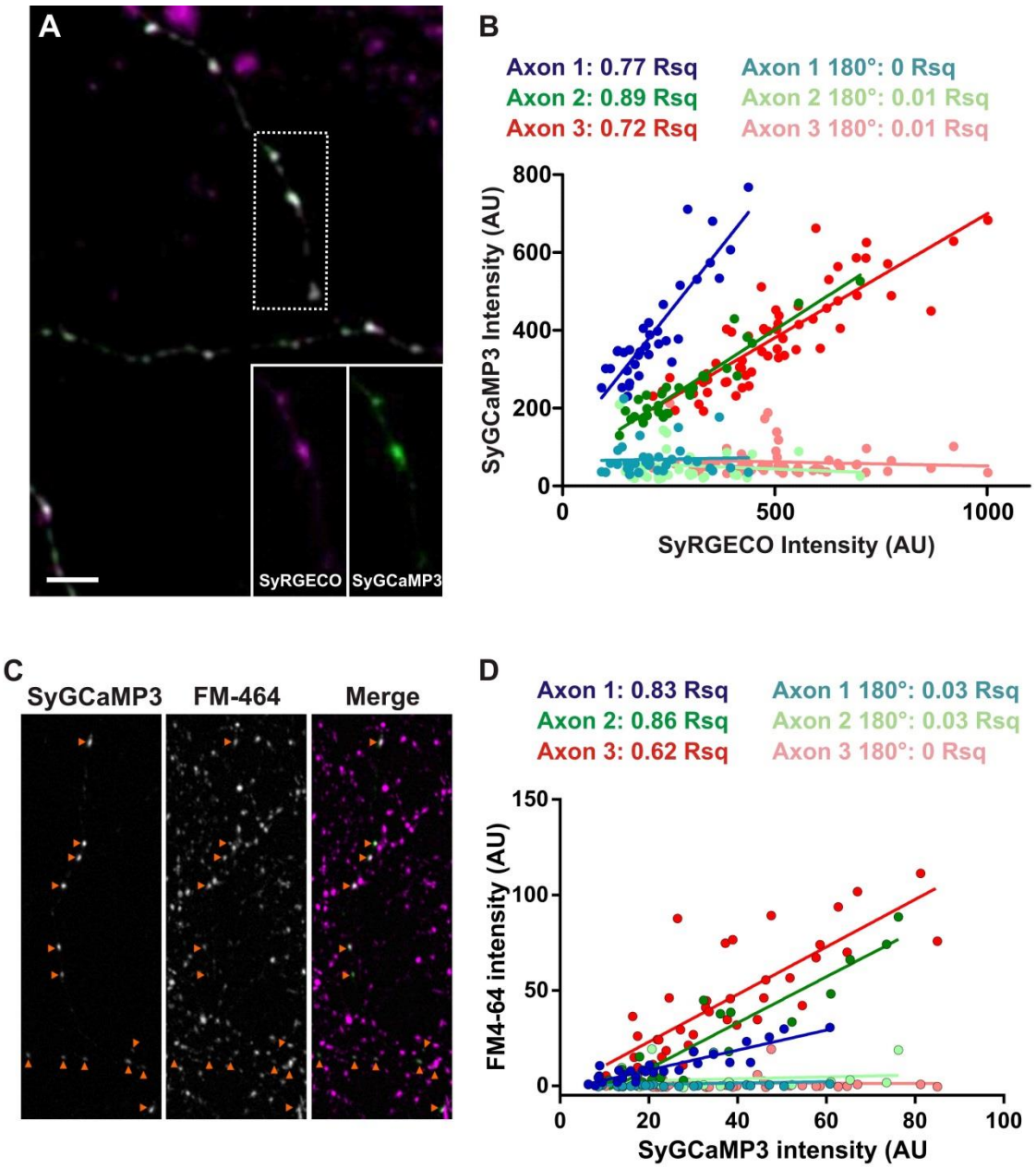

Figure 3.2.8 SyGCaMP3 and SyRGECO expression is localised to presynaptic boutons (A) Neurons co-expressing SyGCaMP3 (green) and SyRGECO (magenta). Scale bar=5 µm. Dotted box indicates the area in insets. **(B)** SyGCaMP3 and SyRGECO expression is highly co-localised showing a significant correlation of pixel intensities at identified puncta for 3 axons (bold blue, green and red points; P<0.0001 for each axon, Spearman's co-efficient; total n=125 puncta). No correlation is observed when the SyGCaMP3 image is rotated 180˚ (pale colour matched points; pale blue P=0.8, green P=0.3 and red P=0.5, Spearman's co-efficient). R-squared (Rsq) values are annotated above the plot. **(C)** SyGCaMP3 expression co-localises with FM 4-64 staining, which labels synaptic vesicles in an activity-dependent manner. Left panel, SyGCaMP3; central panel, FM 4-64 staining; right panel, merged image (green, SyGCaMP3; magenta, FM 4-64). **(D)** SyGCaMP3 expression is highly co-localised with FM 4-64 staining showing a significant correlation of pixel intensities at identified SyGCaMP3 puncta for 3 axons (bold blue, green and red points; P<0.0001 for each axon, Spearman's co-efficient; total n=75 puncta). No correlation is observed when the FM image is rotated 180˚ (pale colour matched points; pale blue P=0.2, green P=0.5 and red points P=0.9, Spearman's co-efficient). R-squared (Rsq) values are annotated above the plot.

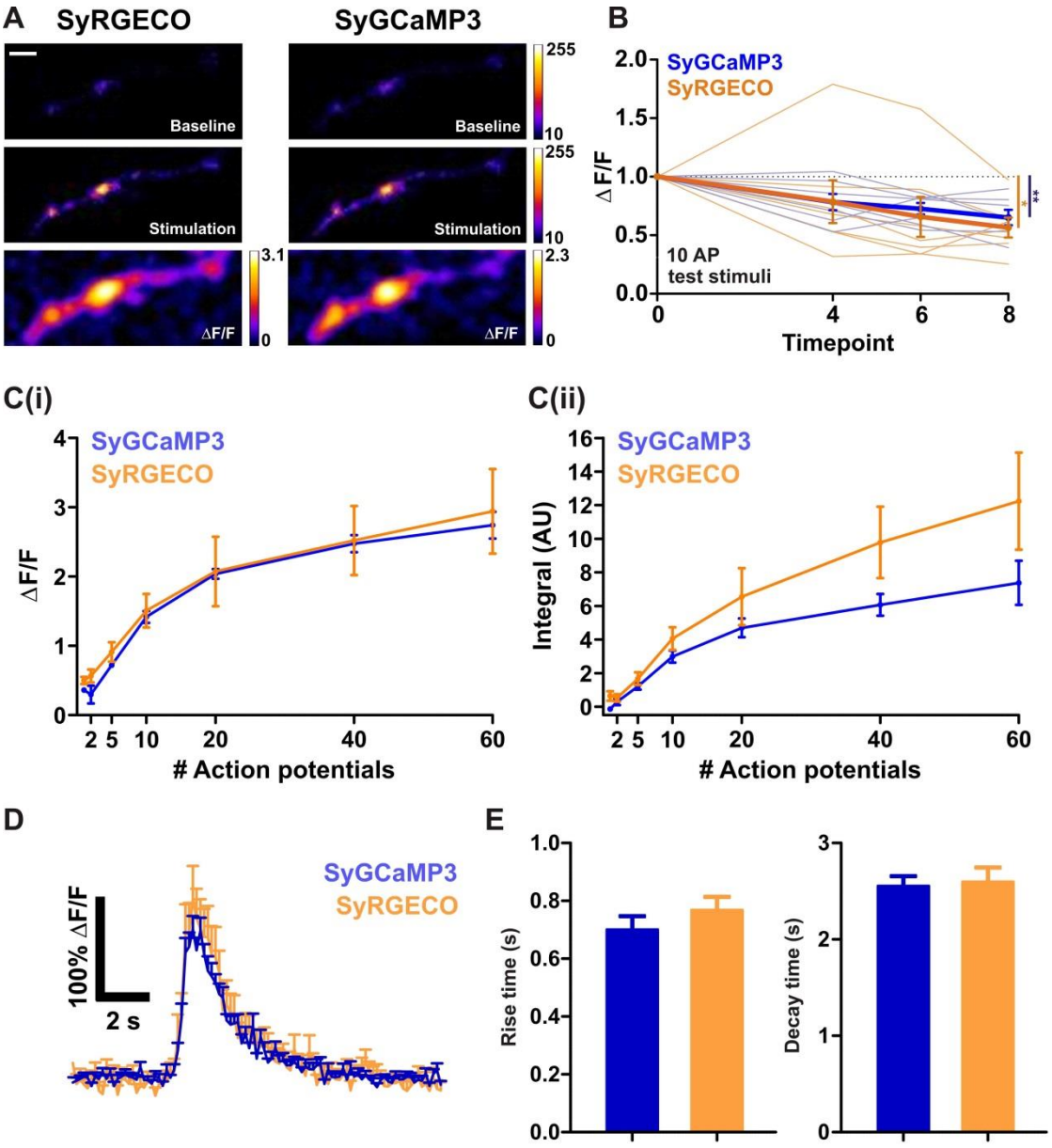

Figure 3.2.9. Characterisation of SyGCaMP3 and SyRGECO in co-transfected neurons in response to extracellular stimulation. (A) Summary images demonstrating changes in SyGCaMP3 and SyRGECO fluorescence intensity to 10 APs stimulation. Top and middle panels show raw fluorescence images during baseline and stimulation epochs, colour-coded by pixel intensity (scale to the right). Bottom panels show peak ΔF/F response summary images. Pixels are colour-coded according to the maximum recorded ΔF/F value for each GECI (scale to the right). Scale bar = 2 µm. **(B)** Peak ΔF/F responses of SyGCaMP3 and SyRGECO to 10 AP test stimulations interspersed throughout the timecourse of the experiment. Mean responses and responses of individual cells are shown in bold and faint lines, respectively. For each cell responses are normalised to the response at timepoint zero. Note both SyGCaMP3 (blue traces) and SyRGECO (orange traces) responses exhibit a modest rundown (n=7 cells). Kruskall-Wallis one-way ANOVA followed by Dunn's post-test. **(C)** Characterisation of SyGCaMP3 and SyRGECO to different numbers of APs as peak ΔF/F over number of APs **(i)**, or integral ΔF/F over number of APs **(ii)** (n=7 cells). Both SyGCaMP3 and SyRGECO responses were corrected for rundown (see 'Materials and Methods'). **(D)** Mean traces with standard error of the mean bars for SyGCaMP3 and SyRGECO responses to initial 10 AP stimulations (n=7 cells). **(E)** 90% rise and decay times calculated for responses to 10 APs stimulation. Kinetics were calculated only in response to the initial 10 AP stimulation to prevent affects from rundown (n=7 cells). P values *<0.05, **<0.01.

lower signals produced in the adjoining axon (Figure 3.2.9 A). Using the same stimulation paradigms that characterised cytosolic RGECO we found that responses of both SyGCaMP3 and SyRGECO were not stable over time, with both exhibiting an approximately 40% rundown in response to 10 AP test stimulations interspersed throughout the experiment (Figure 3.2.9 B). Application of a correction factor derived from the slope of the rundown led to the generation of stimulus-response curves. We found that SyGCaMP3 and SyRGECO exhibited very similar responses at all stimulus strengths for both peak ΔF/F ((Figure 3.2.9 C(i)) and integral ΔF/F (Figure 3.2.9 C(ii)) metrics. Furthermore, the rise and decay kinetics for SyGCaMP3 and SyRGECO in response to 10 APs stimulation were also highly similar (Figure 3.2.9 D-E).

In comparison to the cytosolic forms, we found that peak ΔF/F SyGCaMP3 responses exhibited greater sensitivity to low numbers of APs compared to GCaMP3 (Figure 3.2.10 A(i)). This property however was not echoed when SyGCaMP3 and GCaMP3 were compared using the integral ΔF/F response metric (Figure 3.2.10 B(i)) which indicated a potential difference in response kinetics. Indeed, although we observed no difference in the 90% decay time, we did see a significant decrease in the 90% rise time for SyGCaMP3 in comparison with cytosolic GCaMP3 (Figure 3.2.10 C). SyRGECO appeared more sensitive to single spikes than cytosolic RGECO, although in general the stimulus-response curve of SyRGECO more closely resembled that of cytosolic RGECO when using either the peak ΔF/F or integral ΔF/F metrics (Figure 3.2.10 A(ii) and B(ii)). In addition, cytosolic RGECO and its synaptically targeted form shared very similar rise and decay kinetics (Figure 3.2.10 D). These results demonstrate that RGECO, when targeted to presynaptic terminals, retains its high sensitivity and large dynamic range but while localised the functional properties of this GECI change little.

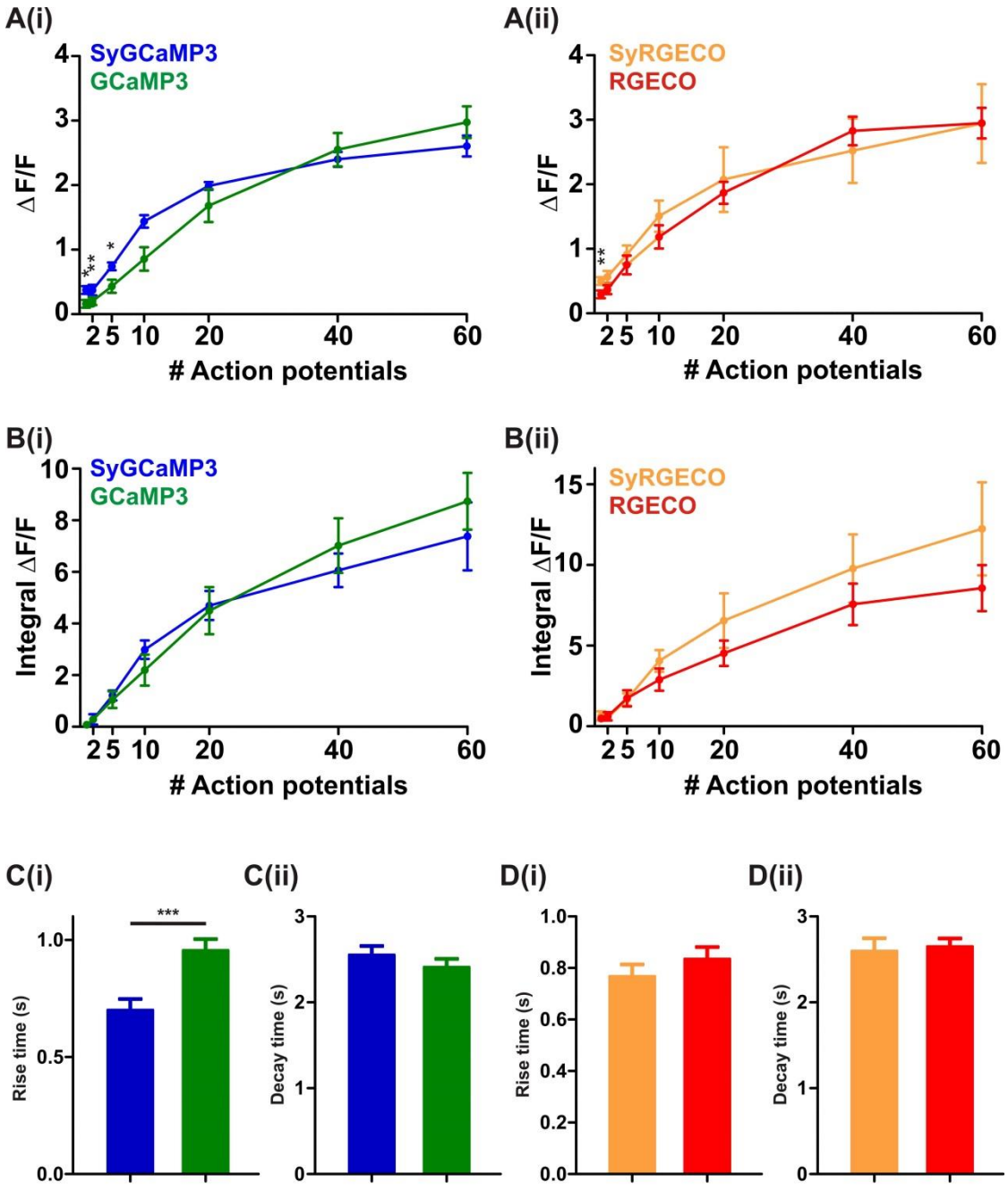

Figure 3.2.10 Comparison of synaptophysin-fusion and cytosolic GECIs. (A-B) Comparison of the peak ΔF/F over AP number **(A)** and integral ΔF/F over AP number **(B)** for SyGCaMP3 and cytosolic GCaMP3 **(i)**; and for SyRGECO and cytosolic RGECO **(ii)** using confocal microscopy (for all GECIs n=7 cells). SyGCaMP3 and SyRGECO responses were both corrected for rundown (see 'Materials and Methods'). **(C)** Comparison of 90% rise **(i)** and decay times **(ii)** calculated in response to 10 APs stimulation for SyGCaMP3 and cytosolic GCaMP3. **(D)** Comparison of 90% rise **(i)** and decay times **(ii)** calculated in response to 10 APs stimulation for SyRGECO and RGECO. For SyGCaMP3 and SyRGECO kinetics were calculated only in response to the initial 10 AP stimulation due to rundown. Kinetics were calculated for each presynaptic bouton (n=18 boutons from 7 cells). For GCaMP3 and RGECO responses to all 10 AP repeats were included (n=22 repeats from 7 cells). Mann Whitney tests. P values *<0.05, **<0.01, ***<0.001.

3.2.3 Characterisation of PSDGCaMP3

The fusion of GCaMP3 to synaptophysin focuses recordings of activity to presynaptic terminals, a subcellular location of special interest in understanding the functional output of a neuron. In addition, this fusion technique improved the sensitivity of this GECI to low number APs. Another subcellular site of particular interest is dendritic spines, where neurons receive the majority of their excitatory input. Could localisation of GCaMP3 to dendritic spines improve the ability of GCaMP3 to detect postsynaptic calcium transients triggered by synaptic transmission?

PSDGCaMP3 was made by fusing GCaMP3 to PSD-95, a scaffold protein that localises to the post-synaptic density (Sampedro et al., 1981). Dissociated hippocampal neurons expressing PSDGCaMP3 showed accumulation of the GECI in dendritic spines, although fluorescence was also detected throughout the neuron (Figure 3.2.11 A). In general, overall levels of baseline fluorescence were low, although a minority of neurons showed an overexpression phenotype resulting in some brightly labelled but enlarged dendritic spines (Figure 3.2.11 E). We recorded calcium transients at dendritic spines under conditions which promoted the activation of NMDA receptors; i.e. neurons were imaged in the absence of Mg^{2+} to release the NMDA receptor pore blockade. Recordings were also made in the presence of 1 µM TTX to prevent the firing of action potentials.

To stimulate individual dendritic spines glutamate was uncaged in close proximity to a spine (the principal spine) eliciting an increase in PSDGCaMP3 fluorescence which was localised to the principal spine (Figure 3.2.11 B). The length of the UV light flash used for uncaging was proportional to the amount of glutamate uncaged (Figure 3.2.11 C) thus, PSDGCaMP3 was characterised based on the peak ΔF/F response to varying lengths of uncaging pulse. Short uncaging pulses (0.1-0.75 ms) preferentially activated the principal spine compared to the adjacent dendrite, but longer uncaging pulses (>2.5 ms) activated both the principal spine and the adjacent dendritic shaft equally (Figure 3.2.11 D).

In the absence of glutamate uncaging, calcium transients were recorded which were highly localised to individual dendritic spines (Figure 3.2.11 E-G). These calcium transients occur randomly in space and time (Figure 3.2.11 F-G) supporting the notion that they resulted from spontaneous vesicle fusion events. As this approach allowed recordings of postsynaptic responses to both glutamate uncaging and spontaneous neurotransmitter release we used this system to determine whether the amount of glutamate released by short uncaging pulses in our PSDGCaMP3 characterisation related to physiological levels of vesicular glutamate release.

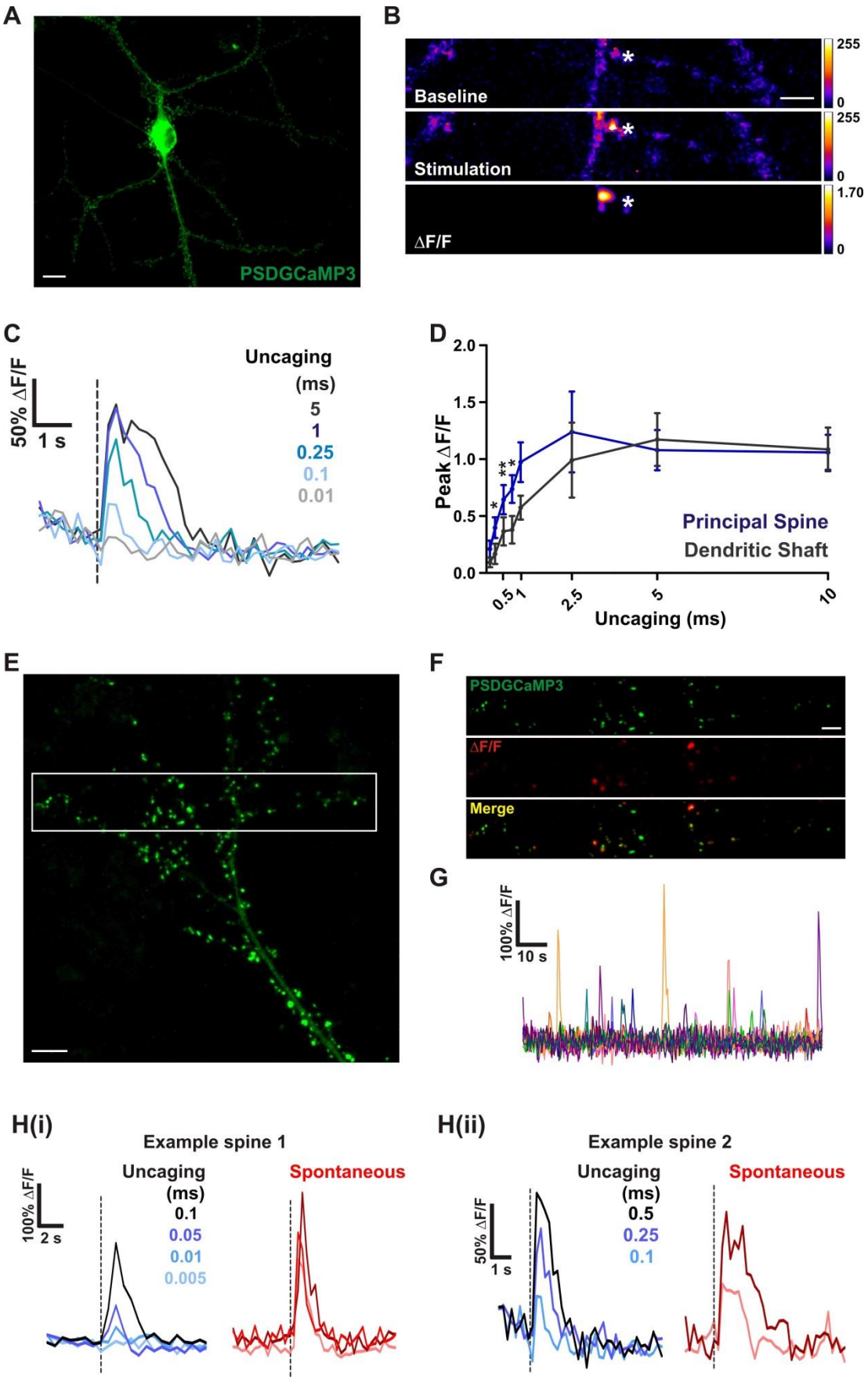
A
PSDGCaMP3
B
Baseline
Stimulation
ΔF/F
255
0
255
0
1.70
0
C
50% ΔF/F
1 s
Uncaging (ms)
5
1
0.25
0.1
0.01
D
Peak ΔF/F
2.0
1.5
1.0
0.5
0.0
Principal Spine
Dendritic Shaft
0.5
1
2.5
5
10
Uncaging (ms)
E
F
PSDGCaMP3
ΔF/F
Merge
G
100% ΔF/F
10 s
H(i)
Example spine 1
100% ΔF/F
2 s
Uncaging (ms)
0.1
0.05
0.01
0.005
Spontaneous
H(ii)
Example spine 2
50% ΔF/F
1 s
Uncaging (ms)
0.5
0.25
0.1
Spontaneous

Figure 3.2.11 Characterisation of PSDGCaMP3 in dissociated hippocampal neurons in response to synaptic activation. (A) A typical hippocampal neuron transfected with PSDGCaMP3. Scale bar = 10 µm. **(B)** Summary images demonstrating changes in PSDGCaMP3 fluorescence intensity to a 0.25 ms glutamate uncaging pulse. The location of the uncaging pulse is indicated by the white asterisk. Top and middle panels show raw fluorescence images during baseline and stimulation epochs, colour-coded by pixel intensity (scale to the right). The bottom panel shows the peak ΔF/F response summary image. Pixels are colour-coded according to the maximum recorded ΔF/F value for each GECI (scale to the right). Scale bar = 3 µm. **(C)** Example ΔF/F traces of principal spine PSDGCaMP3 responses to a range of glutamate uncaging lengths, as colour-coded (see right of traces). **(D)** Peak ΔF/F PSDGCaMP3 responses in either the principal spine (blue) or the adjacent dendritic shaft (grey) over the length of glutamate uncaging. Wilcoxen signed rank tests (n= 11 cells). **(E)** Hippocampal neuron expressing PSDGCaMP3. White box indicates area used for imaging in **(F)**. Scale bar = 10 µm. **(F)** PSDGCaMP3 responses to spontaneous neurotransmitter release. Top panel shows expression of PSDGCaMP3 localised to dendritic spines. The middle panel shows a summary ΔF/F image indicating the location and spatial extent of spontaneous increases in fluorescence intensity. The bottom panel shows an overlay. Note that the ΔF/F 'hotspots' are restricted to the dendritic spines. Scale bar = 5 µm. **(G)** ΔF/F traces from the timeseries summarised in **(F)**. ΔF/F traces of each responsive spine are shown in a different colour. **(H)** ΔF/F traces from two cells **(i)** and **(ii)** where recordings were made in response to both uncaging stimuli of varying lengths (blue traces; color-coded, key to the right of traces) and to multiple spontaneous neurotransmitter release events (red traces; different colour traces indicate discrete spontaneous events).

PSDGCaMP3 responses were recorded to uncaging pulses of varying lengths, and at the same spine fluorescence changes in response to spontaneous neurotransmitter release were also recorded. We found that for these spines uncaging pulses of 0.1-0.5 ms generated responses with amplitudes and kinetics which were highly similar to those recorded in response to spontaneous glutamate release (Figure 3.2.11 H). The absolute length of an uncaging pulse needed to mimic spontaneous responses is harder to determine however, as the magnitude of spontaneous responses was variable at single spines, and we found that sensitivity for uncaging was synapse-dependent (Figure 3.2.11 H). We determined that our uncaging technique was highly sensitive as we could elicit postsynaptic responses to very short uncaging pulses which were smaller than those seen with spontaneous glutamate release (Figure 3.2.11 H).

In order to target the localisation of GCaMP3 to dendritic spines its fusion to PSD-95 is required. However, overexpression of PSD-95 is known to alter normal spine formation as well as the functional properties of mature spines (El-Husseini et al., 2000). In addition, localised expression rendered the majority of PSDGCaMP3 expressing neurons difficult to identify as their resting fluorescence levels were low. As an alternative to using PSDGCaMP3, we characterised cytosolic GCaMP3 as a reporter of postsynaptic calcium transients in dendritic spines. Glutamate uncaging was used to discover whether the postsynaptic targeting of PSDGCaMP3 improved the performance of GCaMP3 in the same way that targeting GCaMP3 to presynaptic terminals did.

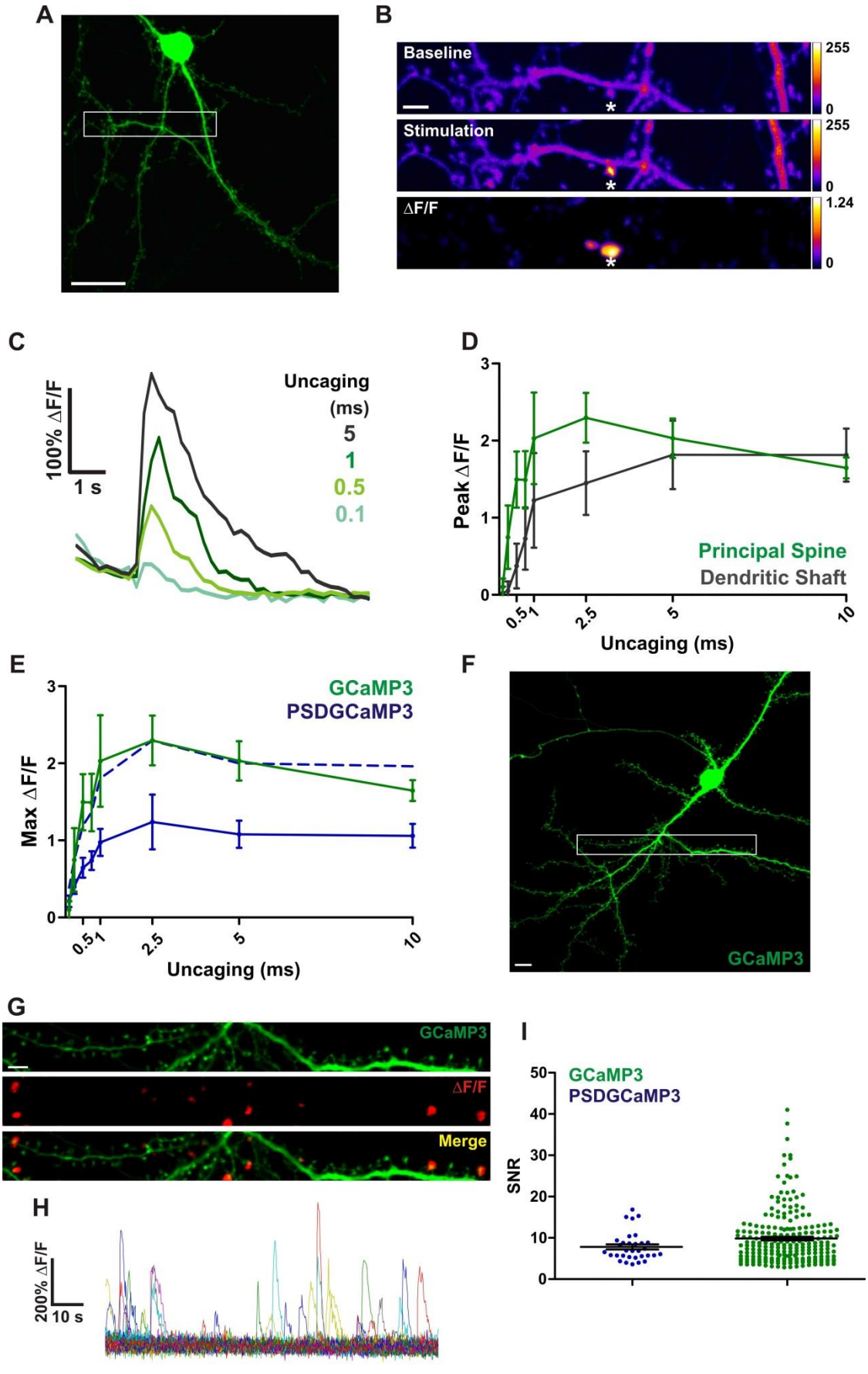
A
B
Baseline
Stimulation
ΔF/F
255
0
255
0
1.24
0
C
100% ΔF/F
1 s
Uncaging (ms)
5
1
0.5
0.1
D
Peak ΔF/F
Principal Spine
Dendritic Shaft
Uncaging (ms)
E
GCaMP3
PSDGCaMP3
Max ΔF/F
Uncaging (ms)
F
GCaMP3
G
GCaMP3
ΔF/F
Merge
H
200% ΔF/F
10 s
I
GCaMP3
PSDGCaMP3
SNR

Figure 3.2.12 Cytosolic GCaMP3 acts similarly to PSDGCaMP3 in response to synaptic activation. (A) A typical hippocampal neuron transfected with cytosolic GCaMP3. The white box indicates the area stimulated in **(B)**. Scale bar = 10 µm. **(B)** Summary images demonstrating changes in GCaMP3 fluorescence intensity to a 0.5 ms glutamate uncaging pulse. The location of the uncaging pulse is indicated by the white asterisk. Top and middle panels show raw fluorescence images during baseline and stimulation epochs, colour-coded by pixel intensity (scale to the right). The bottom panel shows the peak ΔF/F response summary image. Pixels are colour-coded according to the maximum recorded ΔF/F value for each GECI (scale to the right). Scale bar = 3 µm. **(C)** Example ΔF/F traces of principal spine GCaMP3 responses to a range of glutamate uncaging lengths, as colour-coded (see right of traces). **(D)** Peak ΔF/F of GCaMP3 responses in either the principal spine (green) or the adjacent dendritic shaft (grey) over length of glutamate uncaging (n= 5 cells), **(E)** A comparison of peak ΔF/F over uncaging length for GCaMP3 (green) and PSDGCaMP3 (blue) at the principal spine. The dotted blue line represents PSDGaMP3 values scaled to the maximum mean GCaMP3 response (GCaMP3 n=5 cells, PSDGCaMP3 n=11 cells). **(F)** A hippocampal neuron expressing cytosolic GCaMP3. White box indicates the area used for imaging in **(G)**. Scale bar = 10 µm. **(G)** GCaMP3 responses to spontaneous neurotransmitter release. Top panel shows expression of GCaMP3 which fills the dendrite. The middle panel shows a summary ΔF/F image indicating the location and spatial extent of spontaneous increases in fluorescence intensity. The bottom panel shows an overlay. Note that the ΔF/F 'hotspots' are restricted to the dendritic spines. Scale bar = 5 µm. **(H)** Typical ΔF/Ftraces from the timeseries summarised in **(G)**. Traces of each responsive spine are shown in a different colour. **(I)** Signal to noise ratio of spontaneous responses for PSDGCaMP3 and GCaMP3 (PSDGCaMP3 n=32 spines, GCaMP3 n=218 spines). Each dot represents the mean signal to noise ratio of all events occurring at a single spine.

Cytosolic GCaMP3-expression in neurons allowed visualisation of cell bodies and all neuronal processes, and had excellent baseline fluorescence which made transfected cells easily visible (Figure 3.2.12 A). Despite the high expression of GCaMP3 in all areas of dendritic segments imaged, when glutamate was uncaged at a single spine, in zero Mg^{2+} and 1 µM TTX bath conditions as above, increases in GCaMP3 fluorescence were observed which were localised only to spines nearest to the uncaging pulse, and not the entire dendrite (Figure 3.2.12 B). Similar to PSDGCaMP3, the magnitude of the GCaMP3 fluorescence response was dependent on the amount of glutamate uncaged (Figure 3.2.12 C). Generation of stimulus-response plots of peak ΔF/F over length of uncaging pulse for both the principal spine and the adjacent dendritic shaft showed, similar to PSDGCaMP3, that the principal spine was preferentially activated by short uncaging pulses. When longer pulses were applied there was no discrimination in the magnitude of response between principal spine and the adjacent dendritic shaft (Figure 3.2.12 D). This result was unable to be verified statistically however, due to the low sample size (n=5 cells). On comparison with PSDGCaMP3, when PSDGCaMP3 responses were scaled in line with the maximum GCaMP3 response (dotted navy plot) PSDGCaMP3 and GCaMP3 exhibited a similar dynamic range to uncaging stimuli (Figure 3.2.12 E). However, when no scaling was applied PSDGCaMP3 signals were much smaller than GCaMP3 responses (Figure 3.2.12 E). In neurons expressing cytosolic GCaMP3 we also recorded spontaneous neurotransmitter release events as changes in fluorescence restricted

to dendritic spines (Figure 3.2.12 F-G). As above, these events occurred randomly in space and time (Figure 3.2.12 G-H). As a comparison of the relative ability of PSDGCaMP3 and cytosolic GCaMP3 to detect spontaneous calcium transients we calculated the signal to noise ratio for each GECI and found no statistical difference in the readout of these events (Figure 3.2.12 I).

In summary, both PSDGCaMP3 and GCaMP3 share the ability to detect calcium transients in dendritic spines induced by either glutamate uncaging or spontaneous glutamate release. However, overexpression of PSD-95, low resting fluorescence of PSDGCaMP3 and the poor PSDGCaMP3 signals compared to GCaMP3 are all disadvantages of PSDGCaMP3 compared to cytosolic GCaMP3.

3.3 Discussion

3.3.1 Characterisation of RGECO

The generation of a red-shifted GECI 'RGECO' has opened the door for two colour-functional imaging (Zhao et al., 2011a). However, in the original paper describing its generation, the properties of RGECO in neurons were not fully characterised particularly in response to action potentials (APs) making it difficult to assess the potential use of RGECO in neuroscience (Zhao et al., 2011a). One aim of this chapter was to characterise the newly engineered RGECO in response to different numbers of APs in dissociated hippocampal neurons, highlighting both its advantages and limitations.

In RGECO and GCaMP3 co-expressing neurons RGECO was expressed in the nucleus, but GCaMP3 was not. Whereas GCaMP3 nuclear expression can indicate cytomorbidity (Tian et al., 2009) the differential expression of RGECO and GCaMP3 suggests RGECO nuclear expression, in agreement with other studies, does not (Yamada and Mikoshiba, 2012; Akerboom et al., 2013b). We found that the performance of RGECO was not significantly different to that of GCaMP3 in co-expressed neurons in terms of dynamic range, ΔF/F signal and kinetics when imaged using confocal microscopy. In fact, RGECO shows a greater sensitivity than GCaMP3 for detecting single action potentials. This data suggests that RGECO, like GCaMP3, is a useful tool for detecting a range of activity patterns in neurons (Tian et al., 2009; Huber et al., 2012a). Co-expression of RGECO with GCaMP3 did not alter the performance of either probe relative to cultures transfected with a single probe, suggesting that RGECO can also be used in combination with the traditional GFP-based GECIs (Tian et al., 2009; Akerboom et al., 2012; Chen et al., 2013), as well as other optical activity sensors such as synaptopHluorins (Miesenböck et al., 1998) and glutamate sensors (Marvin et al., 2013).

Our findings are in agreement with a recent study where RCaMP, a newly generated red-shifted GECI, is characterised alongside RGECO (Akerboom et al., 2013b). They found that RGECO demonstrated a high dynamic range, large ΔF/F signals, high sensitivity and moderate to fast kinetics, characteristics which were in fact superior to RCaMP. However, these findings contrast with those of a previous study in which RGECO was found to perform poorly in comparison to GCaMP3 (Yamada and Mikoshiba, 2012). During the course of our investigation we have discovered that differences in methods of RGECO excitation could provide a likely explanation for this discrepancy.

During characterisation experiments using widefield excitation, we consistently recorded an exponential rundown in mean RGECO response to 10 AP stimulations interspersed within the

experiment. Mean GCaMP3 responses to interspersed 10 AP stimulations did not exhibit rundown. As rundown differentially occurred for RGECO and GCaMP3 responses in co-expressed neurons this suggested that rundown was not a consequence of neuron ill-health. An experiment was conducted to investigate the role of stimulation and widefield fluorescence excitation in the aetiology of rundown. A control paradigm consisting of sequential 10 AP stimulations induced a large exponential rundown in RGECO responses. Reducing the number of stimulations comparable to the control paradigm had no effect on the extent of RGECO rundown. However, reducing the number of exposures to widefield excitation compared to the control paradigm did reduce the degree of rundown. This suggests that RGECO performance is negatively affected by exposure to prolonged or high levels of fluorescence excitation. This conclusion was supported by the absence of RGECO rundown observed when imaging with confocal microscopy, where laser scanning across pixels prevents the sustained excitation of RGECO. Surprisingly, mean GCaMP3 responses displayed rundown to the control paradigm, however the progression of GCaMP3 rundown was highly variable between cells and to a much lesser extent compared to RGECO. This is in contrast to GCaMP3 responses to 10 AP stimuli interspersed within the characterisation experiments, where only a few isolated cells showed a small rundown. The reason for this discrepancy is unknown.

Differences between the good performance of RGECO recorded here and by Akerboom et al., (2013) compared to Yamada and Mikoshiba (2012) may therefore be a consequence of differences in image acquisition and subsequent RGECO rundown. The confocal frame scan rate used in our study was fairly modest (6 Hz) and was targeted to the cell soma. Thus, RGECO excitation-emission cycling rates are likely to be much lower than those used by Yamada and Mikoshiba (2012) where RGECO was characterised using rapid (200 Hz) 2-photon line-scanning over a region of apical dendrite. In addition, RGECO rundown is also likely to be exacerbated by imaging in low volume regions such as dendritic and axonal processes where there is less naïve probe available to replenish the light-depleted pool compared to imaging at the cell body.

The basis for light-induced rundown of RGECO responses is not clear from our experiments. While mApple is highly sensitive to photobleaching under widefield illumination (Shaner et al., 2008) this cannot fully explain RGECO rundown as our response metric (ΔF/F) specifically normalises for baseline fluorescence. Previously, we suggested that excitation light may alter the ability of RGECO to bind to calcium, or to report calcium-binding by emitting fluorescence (Walker et al., 2013). A recent study by Akerboom et al., (2013) elaborated on this finding showing that excitation of RGECO with green light caused an increase (~50%) in fluorescence when RGECO is calcium free, i.e. baseline fluorescence will be artificially high. Upon calculation of the response metric ΔF/F, normalisation of responses (ΔF) by an artificially high baseline

value (F) will generate artificially lower ΔF/F measurements. Akerboom *et al*. found that photoactivation caused transient effects, whereas the RGECO rundown reported here appears to be permanent, or at least have a very long recovery time. This may be due to each timeseries in this study having relatively long exposures to fluorescence (~17 seconds per time-series) which may induce longer-lasting effects.

In summary, RGECO exhibits an excellent ΔF/F signal, dynamic range, sensitivity and kinetics comparable to those of GCaMP3, suggesting RGECO can read out a physiologically relevant range of neuronal activation. The performance of RGECO is also superior to other red-shifted GECIs, such as RCaMP (Akerboom et al., 2013b), in terms of ΔF/F signal, dynamic range, sensitivity and kinetics. However, the rundown in RGECO responses observed using widefield illumination suggests that RGECO, under certain conditions, can become an unreliable reporter of neural activity.

3.3.2 Characterisation of SyGCaMP3 and SyRGECO

Localisation of a GCaMP2 to presynaptic terminals by the GECI SyGCaMP2 was found to improve the dynamic range and temporal resolution of cytosolic GCaMP2 (Dreosti et al., 2009). A second aim for this chapter was to characterise new GECIs which were generated from the fusion of GCaMP3 and RGECO to synaptophysin (SyGCaMP3 and SyRGECO, respectively). The performance of SyGCaMP3 and SyRGECO were compared with one another, as well as with their parent GECIs (GCaMP3 and RGECO).

To test for successful targeting of SyGCaMP3 to presynaptic terminals, neurons were co-labelled with FM 4-64 which stains functional presynaptic terminals. Co-localisation can be described by applying an intensity threshold for SyGCaMP3 and FM 4-64 fluorescence and describing puncta that are suprathreshold for both as co-localised. However, using this approach the threshold which is set is generally arbitrary. Here, we found we could show FM 4-64 and SyGCaMP3 co-localisation by an alternative method as SyGCaMP3 and FM 4-64 fluorescence intensities co-correlate at individual boutons. The saturating 60 mM potassium chloride stimulation used here causes FM 4-64 to be incorporated into all vesicles comprising both the readily-releasable and reserve pool, thus FM 4-64 intensity represents the number of vesicles in each presynaptic terminal. The co-correlation between SyGCaMP3 and FM 4-64 intensities indicates not only is SyGCaMP3 localised to presynaptic terminals, but that the number of SyGCaMP3 molecules localised to a terminal is related to the number of vesicle 'hosts' present. Similarly, the intensity of SyGCaMP3 and SyRGECO co-correlates, which is

again likely determined by the number of vesicle 'hosts' at each terminal and suggests that both are equally distributed across the vesicle pool. These results indicate that both SyGCaMP3 and SyRGECO are trafficked correctly and accumulate at presynaptic boutons.

SyGCaMP3 and SyRGECO both exhibited rundown when imaged with confocal microscopy, a property not described for the parent cytosolic GECIs. The tethering of these probes to synaptic vesicles limits probe motility and therefore decreases GECI turnover. For neurons expressing cytosolic RGECO imaged with widefield illumination, rundown-corrected stimulus-response plots were generated by application of a correction factor derived from the function and slope of RGECO rundown. These corrected RGECO stimulus-response plots accurately reproduced those generated using confocal microscopy indicating our method of correction is sound. We applied the same correction strategy to synaptophysin-tagged GECIs to generate stimulus-response plots. SyRGECO and SyGCaMP3 are very similar in terms of dynamic range, peak ΔF/F signals and sensitivity. However, we do find that SyRGECO shows larger integral ΔF/F values in response to higher numbers of AP stimulation compared to SyGCaMP3. On comparison of SyGCaMP3 to cytosolic GCaMP3 we find that SyGCaMP3 generated higher peak ΔF/F signals than cytosolic GCaMP3 to low number action potentials. However, we see no such increase in sensitivity using the integral as a measure; this may likely be due to a significant decrease observed in SyGCaMP3 in rise time kinetics. The dynamic range of SyGCaMP3 appears reduced compared to cytosolic GCaMP3 indicating SyGCaMP3 saturation to higher number AP stimulations. On comparison of SyRGECO compared to RGECO there is very little difference in dynamic range or peak ΔF/F signals. However, SyRGECO does show significantly higher peak and integral responses to single action potentials compared to cytosolic RGECO.

In summary, SyGCaMP3 and SyRGECO show good ΔF/F signals, dynamic range, sensitivity and kinetics which make them good GECIs for reporting a range of neural activity at presynaptic terminals. However, the reliability of these probes is less certain as rundown was exhibited when using confocal microscopy. The fusion of GCaMP3 and RGECO to synaptophysin does not confer striking differences in performance compared to the parent GECIs, although SyGCaMP3 does exhibit some improvement in sensitivity and kinetics over GCaMP3, it exhibits a poorer dynamic range (although see Nikolaou et al., 2012).

3.3.3 Characterisation of PSDGCaMP3

A third aim of this chapter was to generate and characterise a GECI targeted to postsynaptic sites to record postsynaptic calcium transients. To target expression to the postsynapse

GCaMP3 was fused to PSD-95 to generate PSDGCaMP3. PSD-95 is the most abundant scaffolding protein at the postsynaptic density (PSD) and plays a critical role by anchoring glutamate receptors, amongst others, to correct synaptic locations (Chen et al., 2011). We were interested to establish whether localisation to the site of postsynaptic calcium entry would improve the reporting properties of GCaMP3 and so characterised PSDGCaMP3 alongside cytosolic GCaMP3 in dissociated hippocampal neurons in response to synaptic stimulation.

PSDGCaMP3 transfected neurons showed a range of expression phenotypes, with the majority exhibiting poorly localised, dim expression as in Figure 3.2.11 A and a minority of neurons showing highly localised over-expression (Figure 3.2.11 E). These expression patterns may reflect the nascent activity states of these neurons as PSDGCaMP3 expression was driven under the activity-dependent cytomegalovirus (CMV) promoter. The weak expression of PSDGCaMP3 made identification of transfected neurons very difficult. Conversely, while the neurons over-expressing PSDGCaMP3 were easy to identify, over-expression of PSD-95 is well known to cause changes to synaptic structures, such as the morphological engrossment of spines and a corresponding increase in AMPA receptors clustering at the postsynaptic density (El-Husseini et al., 2000).

Glutamate uncaging was used to assess the performance of both PSDGCaMP3 and GCaMP3. This approach provides tunable control over synaptic activation where the length of laser excitation determines the amount of glutamate uncaged. Short glutamate uncaging pulses (<1 ms), previously characterised as quantal (Kay et al., 2011), induced PSDGCaMP3 and GCaMP3 responses preferentially localised to principal dendritic spines. With longer lengths of uncaging pulses (≥1 ms) the dendritic shaft was activated to an equal extent as dendritic spines, most likely reflecting activation of non-synaptic receptors. Preliminary data from a PSDGCaMP3 expressing neuron shows that the localisation of calcium transients may reflect the route of calcium entry (Figure 3.3.1). Short uncaging pulses (0.05 ms) induce NMDA receptor-dependent calcium influx which is localised to the principal spine head, and blocked by the NMDA receptor antagonist, APV. Long uncaging pulses (5 ms) activate NMDA receptor-independent calcium influx which is no longer restricted to the principal spine and is observed in the dendritic shaft. This calcium influx is likely mediated by AMPA receptor dependent depolarisation, leading to the opening of VGCCs which are expressed throughout the dendrites as well as spines. This calcium influx to 5 ms uncaging was subsequently blocked by the AMPA receptor antagonist CNQX.

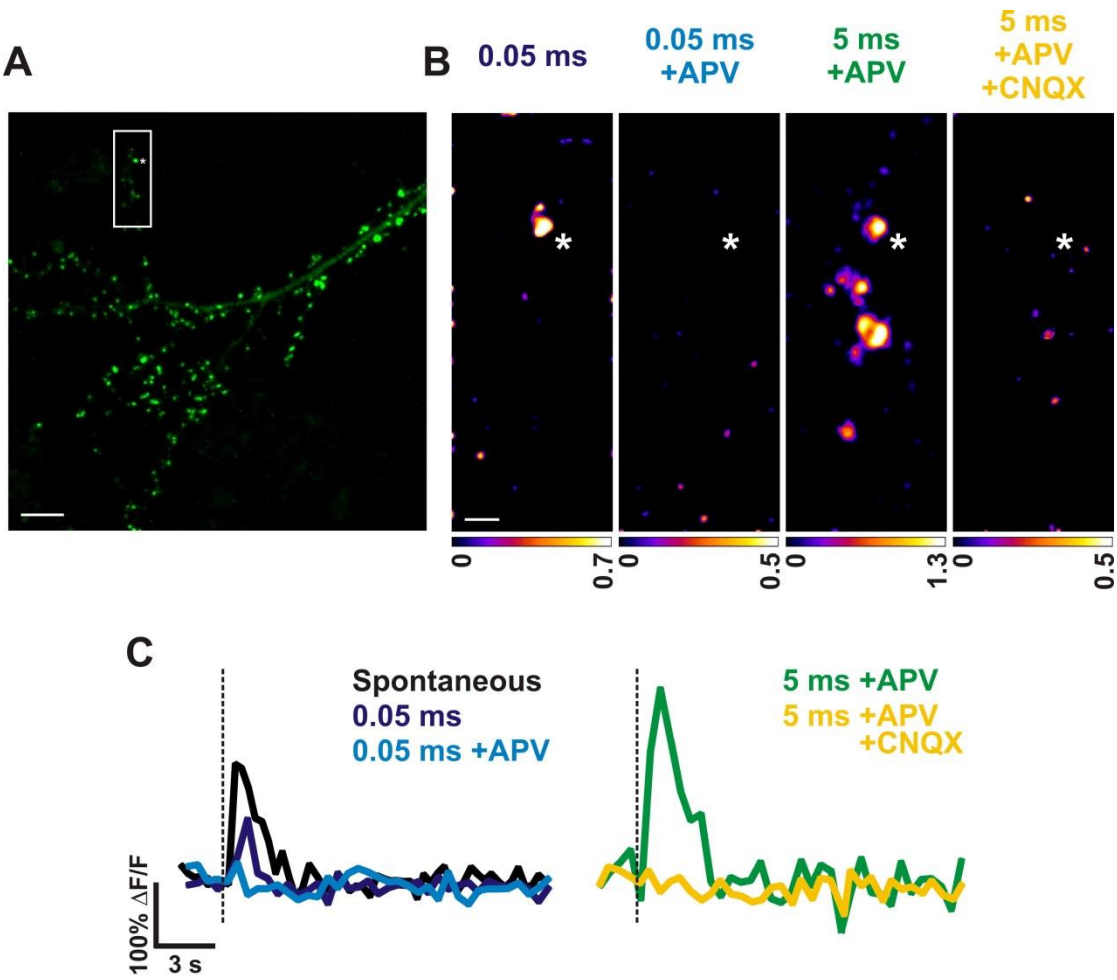

Figure 3.3.1 Different length uncaging pulses recruit different sources of calcium influx. (A) PSDGCaMP3 expressing neuron. White box indicates region shown in **(B)**.Scale bar = 10 µm.**(B)** Peak ΔF/F response summary images for different uncaging lengths and in the presence 50 µM APV and 20 µM CNQX as labeled above. Voxels are colour-coded according to the maximum recorded ΔF/F value for each GECI (scale to the bottom). Scale bar = 4 µm. **(C)** ΔF/F traces of PSDGCaMP3 responses for the principal spine during glutamate uncaging and in the presence of 50 µM APV and 20 µM CNQX as labeled. A spontaneous response at the principal spine is included to indicate the scale of responses.

GCaMP3 and PSDGCaMP3 perform similarly in terms of sensitivity and dynamic range to uncaging stimuli, however, PSDGCaMP3 exhibits lower ΔF/F signal changes compared to GCaMP3. Both GCaMP3 and PSDGCaMP3 are able to detect spontaneous postsynaptic calcium events as a consequence of quantal neurotransmitter release, and report these spontaneous calcium transients with very similar signal to noise ratios. Quantal calcium transients are highly localised to dendritic spines for both GECIs, likely due to the tight coupling of pre- and postsynaptic compartments, spine structure and the strict localisation of responsive elements (such as NMDA receptors) to the spine head.

In hippocampal neurons the vast majority of excitatory neurotransmission occurs onto dendritic spines. As dendritic spines can be defined morphologically, the use of PSDGCaMP3, which showed no improvements in performance over GCaMP3, confers no advantage over GCaMP3. In fact, given the expression-based concerns of PSDGCaMP3 and the better signals of cytosolic GCaMP3, GCaMP3 is the more appropriate GECI for examination of excitatory postsynaptic activity in hippocampal neurons. However, in neurons or organisms which lack dendritic spines, such as the zebrafish, the ability of PSDGCaMP3 to highlight postsynaptic sites is an important advantage. Indeed, PSDGCaMP3 was trialled in tectal neurons of the larval zebrafish (experiments conducted by F. Abbas, KCL) but the low resting fluorescence of this probe rendered its use especially challenging in an *in vivo* setting. Yet the strategy is still viable, depending on the properties of the parent GECI. GCaMP3 remains the GCaMP variant with the highest baseline fluorescence, but in the future GECIs with improved resting fluorescence may make this fusion-GECI a viable tool. An alternative approach would be to fuse GECIs to other postsynaptic proteins. A fusion of GCaMP2 with β-actin, a cytoskeletal protein which is enriched in dendritic spines, has been generated but showed no advantage over cytosolic GCaMP2 in response to action potential and glutamate uncaging stimuli (Mao et al., 2008).

3.3.4 Future Work

The characterisation performed here shows that RGECO and SyRGECO emit large signals and have good sensitivity and dynamic range; properties which recommend these red-shifted GECIs for experimental use. The use of red-shifted genetically-encoded reporters allows for direct functional imaging together with the expression of EGFP tagged proteins of interest. Perhaps more interestingly, it also allows the simultaneous use of functional reporters with different wavelengths. Below I describe a number of different experiments that could benefit from the use of RGECO and SyRGECO.

One particular application for SyRGECO may be in the direct correlation of neurotransmitter release and intra-bouton calcium influx. Neurotransmitter release can be studied using genetically-encoded green spectrum indicators; for example synaptopHluorin which is a synaptobrevin-fusion pH detector, and reports vesicle fusion, or iGluSNFR which is a glutamate sensor consisting of a bacterial glutamate binding protein fused to a circularly permuted GFP (Miesenböck et al., 1998; Marvin et al., 2013). While studies have shown the similarities between vesicle fusion and intra-bouton calcium influx (Zhao et al., 2011a; Odermatt et al., 2012; Nikolaev et al., 2013), the overlapping spectral range of the tools used, synaptopHluorin and SyGCaMP2 respectively, prevent their use at the same synapses. Co-expression of

SyRGECO with synaptopHluorin or iGluSNFR within the same presynaptic terminals will allow a direct comparison of neurotransmitter release and presynaptic calcium influx. Direct comparison is particularly interesting given that individual presynaptic boutons are highly heterogeneous, with release probabilities varying by many orders of magnitude along a single axon. This, in turn, should also result in very different temporal dynamics at each bouton, governed by different forms of short-term plasticity that are tightly linked to release probability (reviewed in Ribrault et al., 2011). It would therefore be interesting to probe the relationship between neurotransmitter release and intrabouton calcium influx in the same terminal, especially during high frequency stimulation, to understand how calcium influx is linked to release probability. This kind of approach may help elucidate synapse-specific mechanisms of short-term plasticity.

The spectral shift of RGECO means it can be used in conjunction with green-spectrum GECIs such as GCaMP3. This may be useful when the simultaneous activity of presynaptic and postsynaptic cells is of interest. One way of achieving this would be to express (by means of viruses or electroporation techniques) a set of presynaptic neurons (i.e. CA3 neurons in the hippocampus) with RGECO or SyRGECO and set of postsynaptic neurons (i.e. CA1 neurons) with GCaMP3. Coupling of pre- and postsynaptic activation can then be probed by two-colour function imaging of individual synapses under different presynaptic stimulation routines. A specific use of RGECO and GCaMP3 could be in the incorporation of these GECIs into a rabies virus-based trans-synaptic tracer (reviewed in Osakada et al., 2011). A scenario may be envisioned where an infected postsynaptic cell would express RGECO and, following virus transmission, all connected presynaptic cells would express GCaMP3. This approach would allow recording of the distribution and weighting of presynaptic drive onto a single postsynaptic cell while permitting comparison with the output of that postsynaptic cell.

An exciting use for red-shifted calcium indicators is in concert with channelrhodopsin-2 (ChR2). ChR2 is a blue-light activated non-specific cation channel which, when activated can rapidly depolarise neurons to induce action potential firing (reviewed in Fenno et al., 2011). The amount of blue light needed to trigger an action potential varies for the cell type, developmental stage and for the expression level of ChR2. Thus, it would be extremely useful to have a direct feedback of the activation of ChR2 neurons during blue light stimulation. This could be achieved by co-expression and simultaneous imaging of RGECO. However, while preliminary experiments have shown that RGECO is stable during two-colour imaging, it has only been tested under conditions of low-level illumination. As RGECO has been shown to be sensitive to high levels of illumination, in experiments which require high intensity excitation,

such during optogenetic stimulation using ChR2, RGECO may not be a reliable candidate (Akerboom et al., 2013b).

In summary, the experimental applications for two-colour functional imaging are far-reaching, and the large signals, high sensitivity and dynamic range of RGECO make it an ideal candidate in many studies. However, in all applications the photoactivation of RGECO is an important concern and its use should be evaluated accordingly.

4 Chapter 4: Mapping quantal synaptic properties across dendritic trees using GCaMP3

4.1 Introduction

Synaptic transmission has been studied for over 50 years by recording the postsynaptic reaction to neurotransmitter release (FATT and KATZ, 1952; DEL CASTILLO and KATZ, 1954; Katz and Miledi, 1970). Historically, this has been performed using electrophysiological techniques. However, while electrophysiology allows the experimenter to view synaptic currents with excellent temporal resolution, the spatial resolution provided is poor. Recently, the advent of novel molecular and imaging tools allows synaptic transmission to be viewed in a new light (Zhao et al., 2011b; Chen et al., 2013). In this chapter, we exploited the genetically-encoded calcium indicator GCaMP3 to record calcium transients at single dendritic spines. This approach was sensitive enough to allow the quantal excitatory drive onto single neurons to be recorded with good spatio-temporal resolution. Recordings of quantal calcium transients (QCTs) in dissociated hippocampal neurons outlined several key observations.

The first observation made was that the amplitude of QCTs was highly variable over time at single, identified spines. Quantal variability, in general, is well documented, and has been studied most extensively by recording AMPA receptor mediated mEPSC amplitudes recorded at the cell body or larger dendrites (Bekkers et al., 1990; Liu et al., 1999; McAllister and Stevens, 2000). Although there is much debate into pre- and postsynaptic mechanisms (see introduction, section 1.2.3), there is as yet no clear candidate for the cause of this variability. The proposed mechanisms are often contradictory, which may reflect the spatial limitations of electrophysiology, i.e. the inability to confidently define activity as from a single synapse. In addition, contradictions may arise from the relatively low sample size recorded using methods which aim to activate single synapses, such as minimal stimulation and local sucrose perfusion (Bekkers et al., 1990; Liu et al., 1999; McAllister and Stevens, 2000). Some studies have utilised calcium imaging to report quantal variability in NMDA receptor mediated spine calcium influx (Murphy et al., 1995; Yuste et al., 1999; Conti and Lisman, 2003), however, these reports lacked the spatial resolution to record more than a handful of spines in any given experiment. In this chapter, we address these limitations by performing functional imaging on entire dendritic trees. This approach allows a large sample of spines to be recorded simultaneously and thereby introduces a robust framework in which to investigate the mechanisms that underlie heterogeneity of quantal synaptic responses.

The second important observation made when imaging quantal synaptic calcium transients, was that the distribution of synaptic activity and synaptic weight was not uniform across dendritic trees. The banner term 'synaptic democracy' describes the process whereby the strengths of individual synapses are altered dependent on their proximity to the cell body (see Introduction, section 1.2.4). Distance-dependent scaling acts to counter attenuation during signal propagation to normalise the amplitude of responses at the cell body from all locations across the dendritic tree (Magee and Cook, 2000). It is known that to do this more distal synapses can have a relatively larger complement of AMPA receptors than proximal synapses (Andrasfalvy and Magee, 2001; Nicholson et al., 2006). However, in these studies functional data could not be collected at all points across dendritic trees. Due to the size of the patch pipette, synaptic input was recorded at 'distal' and 'proximal' locations in relatively large dendrites (Andrasfalvy and Magee, 2001; Smith et al., 2003). In addition, using this technique, the individual synapses contributing to the electrical signal could not be identified. These disadvantages can be bypassed using calcium imaging, where there are no spatial restrictions on the collection of functional data, and activity is recorded from and simply assigned to individual synapses. Other mechanisms underlying synaptic democracy can also be tested using calcium imaging. For example, it has been suggested that the biophysical properties of the dendritic tree such as dendrite diameter, spine volume and spine neck diameter can influence synaptic potentials through impedance mechanisms (Noguchi et al., 2005; Araya et al., 2006; Katz et al., 2009; Gulledge et al., 2012). The measurement of activity using calcium imaging allowed us to investigate several structural components of individual spines and relate these components to underlying functional differences on a spine by spine basis

.

4.2 Results

4.2.1 Characterisation of calcium transients evoked by spontaneous neurotransmitter release

Timeseries of dendritic trees from individual neurons expressing cytoplasmic GCaMP3 were recorded under conditions that favoured spontaneous neurotransmitter release and NMDA receptor-driven postsynaptic calcium influx (1μM TTX, 0 mM Mg^{2+}, 2 mM Ca^{2+}). Using this approach we were able to resolve quantal calcium transients (QCTs) that were distributed along the dendritic tree (Figure 4.2.1 A(i)). These calcium events were mostly highly localised to dendritic spines with calcium signals rarely found in the adjacent dendritic shaft (Figure 4.2.1 B). In the previous chapter we determined that RGECO, a red-shifted calcium indicator, is more sensitive than GCaMP3 in response to low level extracellular stimulation. Under similar conditions we imaged neurons expressing RGECO and found that this reporter was also able to report QCTs (Figure 4.2.1 A(ii)). However, RGECO was less reliable at detecting quantal events than GCaMP3, as indicated by the significant decrease in the frequency of QCTs observed (Figure 4.2.1 C). For this reason, for the rest of this chapter we will be studying QCTs using GCaMP3.

We next wanted to explore the source of this calcium influx into spines. One of the main candidates are NMDA receptors, known to be highly permeable to calcium and highly localized to PSD of dendritic spines. Experiments were carried out by recording QCTs in single neurons during an initial imaging session (I_1) performed prior to the addition of either the NMDA receptor antagonist APV (50 μM) or the NMDA channel blocker Mg^{2+} (1.3 mM). Following a ten minute period a second imaging session was recorded (I_2) on the same cell (Figure 4.2.1 D). Indeed, we found that all calcium events were highly sensitive to the addition of APV and Mg^{2+} to the extracellular medium, indicating that QCTs are dependent on the activation of NMDA receptors (Figure 4.2.1 E-F).

These results suggest that QCTs may be driven directly by calcium influx through NMDA receptors. However, there are other possible contributors to postsynaptic calcium transients which can act either in concert with, or downstream of NMDA receptor activation. To assess the potentially subtle roles of downstream calcium sources and NMDA receptor modulators in the generation of QCTs, we performed a pharmacological dissection of possible candidates known to affect calcium concentration at the spine. To properly establish the effect that each drug had on QCTs, we performed a side-by-side control in sister cultures where QCTs were measured in control conditions (no drugs added) throughout the same time period as the

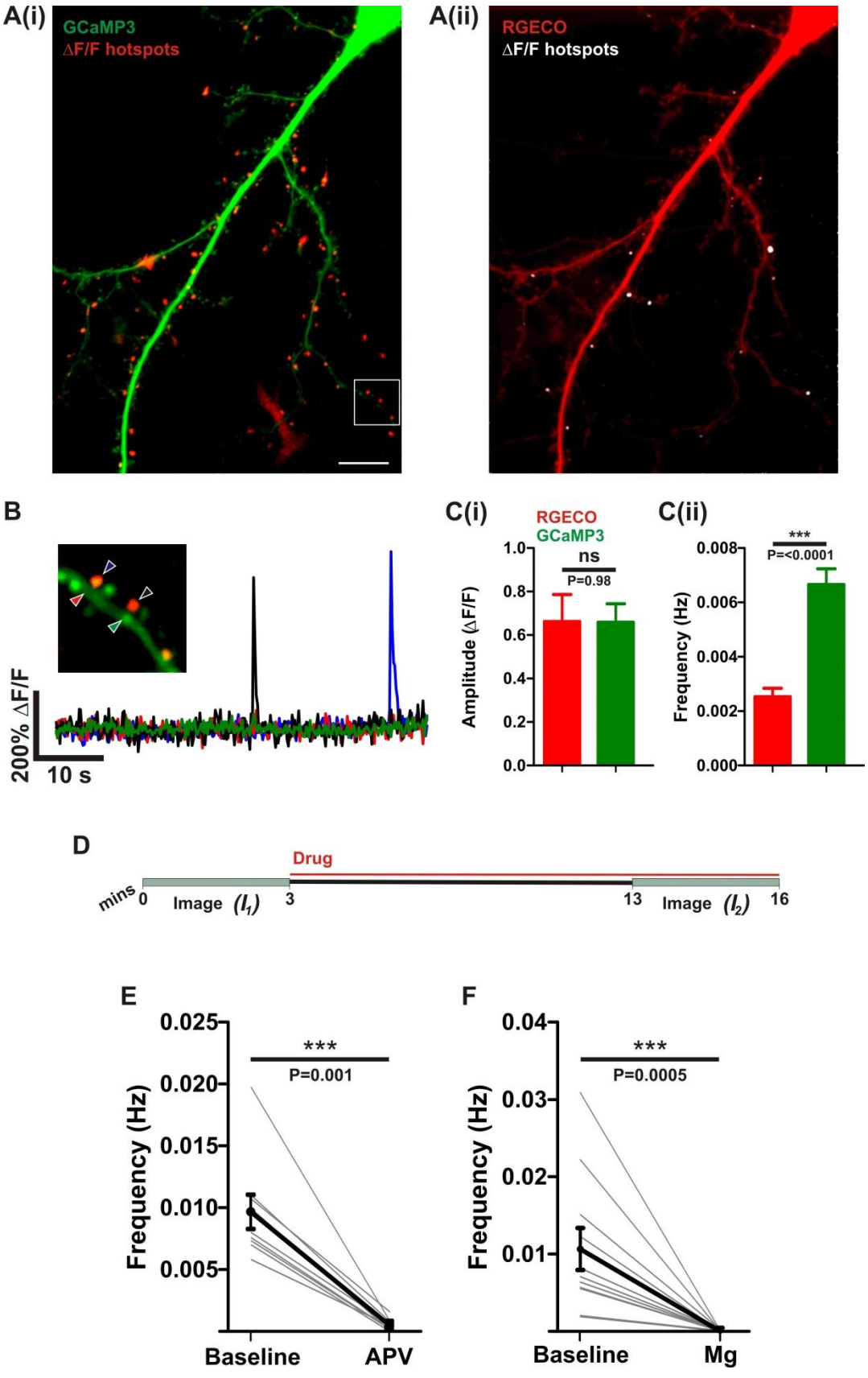
A(i)
GCaMP3
ΔF/F hotspots
A(ii)
RGECO
ΔF/F hotspots
B
200% ΔF/F
10 s
C(i)
RGECO
GCaMP3
ns
P=0.98
Amplitude (ΔF/F)
1.0
0.8
0.6
0.4
0.2
0.0
C(ii)
***
P=<0.0001
Frequency (Hz)
0.008
0.006
0.004
0.002
0.000
D
Drug
mins
0
Image (I1)
3
13
Image (I2)
16
E
***
P=0.001
Frequency (Hz)
0.025
0.020
0.015
0.010
0.005
Baseline
APV
F
***
P=0.0005
Frequency (Hz)
0.04
0.03
0.02
0.01
Baseline
Mg

Figure 4.2.1 GCaMP3 and RGECO detect QCTs which are NMDA receptor dependent. **(A(i))** A dissociated hippocampal neuron expressing GCaMP3 (green) overlaid with a ΔF/F summary image of calcium transient hotspots in red. White box indicates area in **(B)**. **(A(ii))** RGECO expression in the same neuron overlaid with a ΔF/F summary image of calcium transient hotspots in white. Scale bar = 10 µm. **(B)** Zoom in of a dendritic section from **(A(i))**. ΔF/F traces from square ROIs which encompassed spine and dendritic regions in locations indicated by arrowheads. Each trace is colour-matched to an arrowhead. **(C)** Bar charts of mean amplitude **(i)** and frequency **(ii)** per spine recorded with RGECO or GCaMP3 co-expressed in the same neurons (n = 2 cells; amplitude: RGECO n=109 spines; GCaMP3 n=240 spines; Unpaired t-test, frequency: RGECO and GCaMP3 n=507 spines). **(D)** Schematic of the experimental paradigm. Calcium imaging of baseline activity (I_1) preceded the addition of drug-containing solution into the extracellular medium. Calcium imaging in drug conditions (I_2) follows a 10 minute equilibration and drug action period. **(E)** Faint grey lines show the mean frequency of QCTs for each cell for baseline and in the presence of 50 µM APV. Bold lines show the mean and S.E.M for all cells (n=10 cells). **(F)** Faint grey lines show the mean frequency of QCTs for each cell for baseline and in the presence of 1.3 mM Mg^{2+}. The bold lines show the mean and S.E.M for all cells (n=11 cells). All statistics are Wilcoxon signed rank tests, unless stated otherwise. Significance and P values shown on each graph.

drug-treated neurons (Figure 4.2.2 A). To our surprise we found that in control conditions alone there is an approximately 15% drop in the amplitude and a 40-50% drop in the frequency of QCTs following the 10 minute wait period recorded using widefield microscopy or confocal microscopy (Figure 4.2.2 C -D). The overall change in a cells activity is given by calculating the relative amplitude and frequency before (I_1) and after (I_2) drug addition at single spines ((I_2-I_1)/ (I_1+I_2)), which generates a sample size on which meaningful statistics can be performed (Figure 4.2.2 E). A negative sign indicates that the amplitude or frequency has decreased between I_1 and I_2, a positive sign that it has increased (Figure 4.2.2 B). Spines where no QCTs occurred in either one of the imaging sessions will have either a value of 1 or -1, depending on which imaging session zero events were recorded (Figure 4.2.2 B). These relative activity plots show, as suggested by the cell wide data (Figure 4.2.2 C-D), that most spines in control conditions exhibit a decrease in both amplitude and frequency between the two imaging sessions (Figure 4.2.2 E). This decrease is not significantly different whether neurons were recorded with widefield or confocal microscopy (Figure 4.2.2 E). These findings suggest that some rundown does occur during the imaging session and must be taken into account when calculating the effect of drugs on QCT amplitude and frequency. This drop in activity under control conditions mean that the action of drugs in altering activity between I_1 and I_2 was compared to the change in activity between I_1 and I_2 recorded in control cells, taken from sister coverslips.

AMPA receptors, like NMDA receptors are triggered by glutamate and as such are activated in parallel with NMDA receptors in response to spontaneous glutamate release. Although they are not typically calcium permeable, they do mediate cation influx upon activation. Thus,

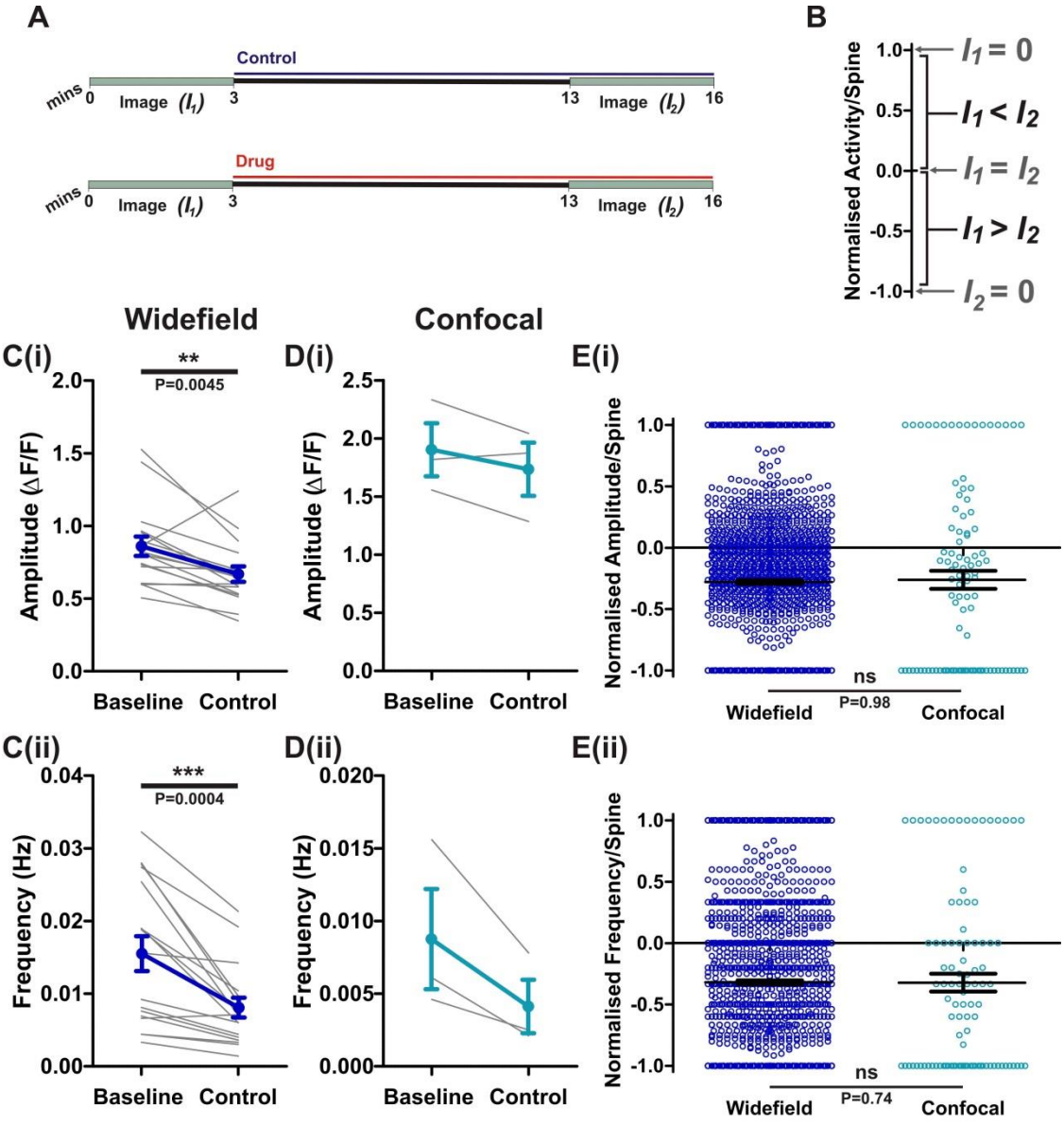

Figure 4.2.2 QCT amplitude and frequency decrease over a 10 minute period in control conditions. (A) Schematic detailing the experimental paradigm. Calcium imaging of baseline activity (I_1) preceded the addition of drug-containing or control solutions into the extracellular medium, followed by a second imaging period (I_2) ten minutes later. **(B)** Schematic summarising the normalisation plots used in **(E)** generated by the calculation $(I_2-I_1)/(I_1+I_2)$. **(C)** Faint grey lines indicate the mean amplitude **(i)** and frequency **(ii)** for each cell in baseline and control conditions using widefield microscopy. Bold dark blue lines show the mean and S.E.M for all cells (n=17 cells). **(D)** Faint grey lines indicate the mean amplitude **(i)** and frequency **(ii)** for each cell in baseline and control conditions using confocal microscopy. Bold light blue lines show the mean and S.E.M for all cells (n=3 cells). Note the low n numbers prevent the use of meaningful statistics. **(E)** Summary of the difference in amplitude **(i)** and frequency **(ii)** at individual spines between baseline and control conditions using widefield (dark blue) or confocal (light blue) microscopy. Widefield n=1913 spines; confocal=100 spines. All statistics are Mann-Whitney tests, with significance and P values indicated on each graph.

AMPA receptors together with NMDA receptors will contribute to the depolarisation of dendritic spines that could activate voltage-gated calcium channels. However, on addition of a selective AMPA receptor antagonist NBQX (10 µM) to the extracellular bath, a decrease in both QCT amplitude and frequency was observed that was similar in magnitude to control cells (Figure 4.2.3 A-C). The relative change in amplitude and frequency between I_1 and I_2 calculated for each spine shows that there is no significant difference between control and NBQX treated cells (Figure 4.2.3 C).

In dendritic spines, R-type voltage gated calcium channels (VGCCs) are a major contributor of VGCC-mediated calcium influx (Sabatini and Svoboda, 2000). R-type VGCCs can be activated by evoked synaptic transmission (Reid et al., 2001) and by bpAPs (Bloodgood and Sabatini, 2007) and could therefore contribute to the QCT responses observed here. In addition, calcium entry into spines via R-type VGCCs specifically triggers small conductance (SK)-calcium activated potassium channels which repolarise the membrane enhancing the NMDA Mg^{2+} block (Bloodgood and Sabatini, 2007). On addition of SNX-482 (500 nM), a selective R-type VGCC antagonist, a drop in mean QCT amplitude and frequency was observed which was similar in extent to that recorded in control cells (Figure 4.2.3 D-F). The relative change in amplitude and frequency between I_1 and I_2 calculated for each spine shows that there is no significant difference between control and SNX-482 treated cells (Figure 4.2.3 F). Apamin is a specific antagonist for SK-calcium activated potassium channels. Upon the addition of apamin (100 nM) to the extracellular bath a drop is recorded in both the mean amplitude and frequency of QCTs similar to control cells (Figure 4.2.4 A-C). Examination of the relative frequency shows no different from control, while the relative amplitude shows a lower drop than controls, this shows that SK-channels do not in fact depress NMDA receptor activity (Figure 4.2.4 C).

The contribution of internal stores to spine calcium concentration during synaptic transmission is controversial (reviewed in Higley and Sabatini, 2012), yet it is possible that calcium influx through NMDA receptors may activate the release of calcium from internal calcium stores to amplify QCTs. In general, calcium-induced calcium release is triggered by activation of either ryanodine or IP_3 receptors, but only ryanodine receptors are found in spines (Berridge, 1998). Here, ryanodine receptors were blocked by the addition of ryanodine (30 µM) to the extracellular bath. The mean amplitude and frequency of QCTs decreased for both control and ryanodine treated cells between I_1 and I_2 (Figure 4.2.4 D-F). Upon addition of ryanodine the relative change in amplitude and frequency shows a bigger drop compared to controls (Figure 4.2.4 F). This indicates that internal stores do not amplify the amplitude or frequency of QCTs.

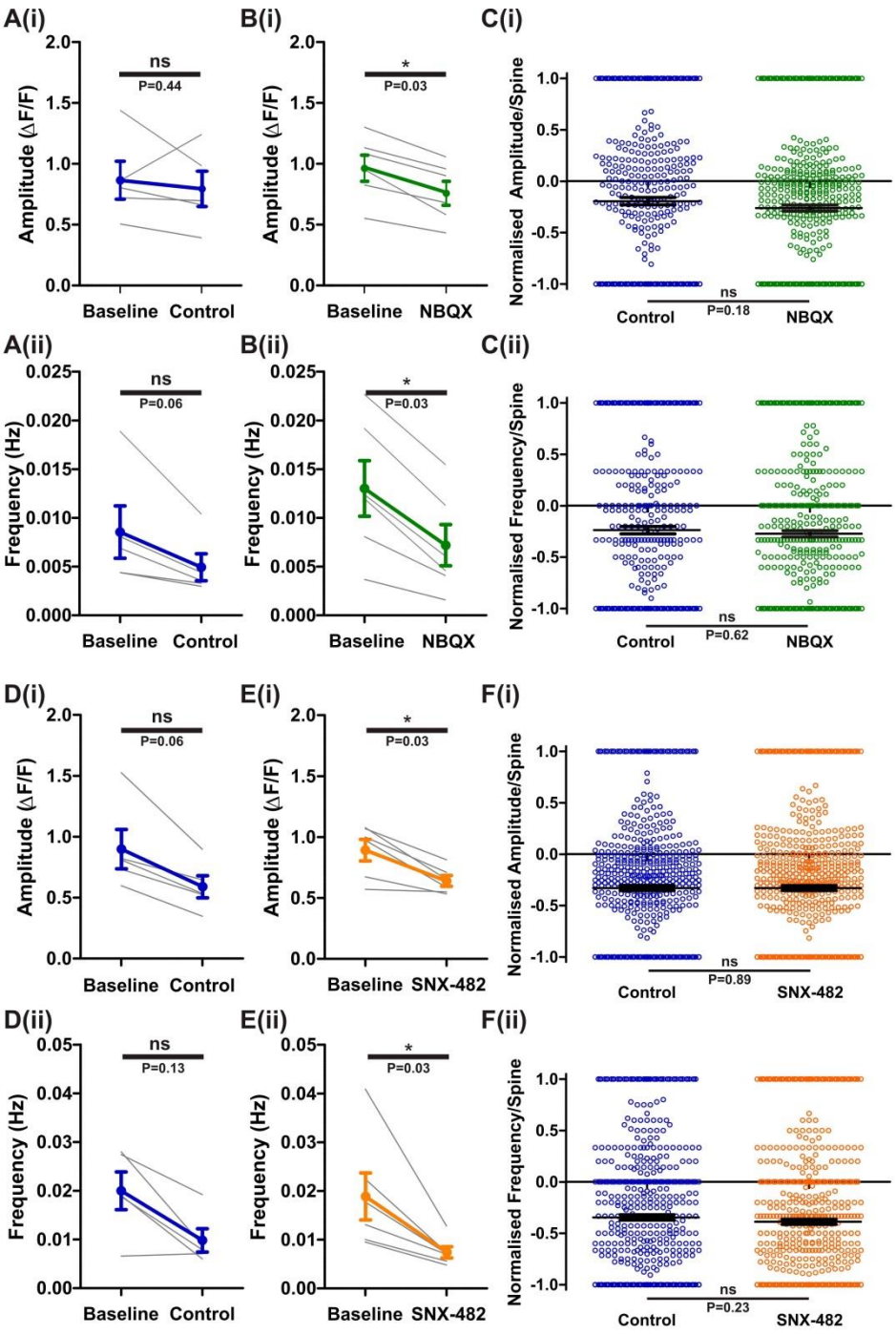

Figure 4.2.3 Contribution of AMPA receptors and R-type voltage-gated calcium channels to QCTs. (A) Faint grey lines indicate the mean amplitude **(i)** and frequency **(ii)** for each cell in baseline and control conditions. Bold blue lines show the mean and S.E.M for all cells (n=5 cells). **(B)** Faint grey lines indicate the mean amplitude **(i)** and frequency **(ii)** for all cells in baseline and NBQX (10 μM) conditions. Bold green lines show the mean and S.E.M for each cell (n=6 cells). **(C)** Summary of the difference in amplitude **(i)** and frequency **(ii)** at individual spines between baseline and control (blue) or NBQX (green) conditions. Control n=451 spines; NBQX=573 spines. **(D)** Faint grey lines indicate the mean amplitude **(i)** and frequency **(ii)** for each cell in baseline and control conditions. Bold blue lines show the mean and S.E.M for all cells (n=5 cells). **(E)** Faint grey lines indicate the mean amplitude **(i)** and frequency **(ii)** for each cell in baseline and SNX-482 (500 nM) conditions. Bold orange lines show the mean and S.E.M for all cells (n=6 cells). **(F)** Summary of the difference in amplitude **(i)** and frequency **(ii)** at individual spines between baseline and control (blue) or SNX-482 (orange) conditions. Control n=637 spines; SNX-482=679 spines. For cell-wide data statistics used were Wilcoxon signed rank tests. For within spine data statistics used were Mann-Whitney tests. Significance and P values are indicated for each graph.

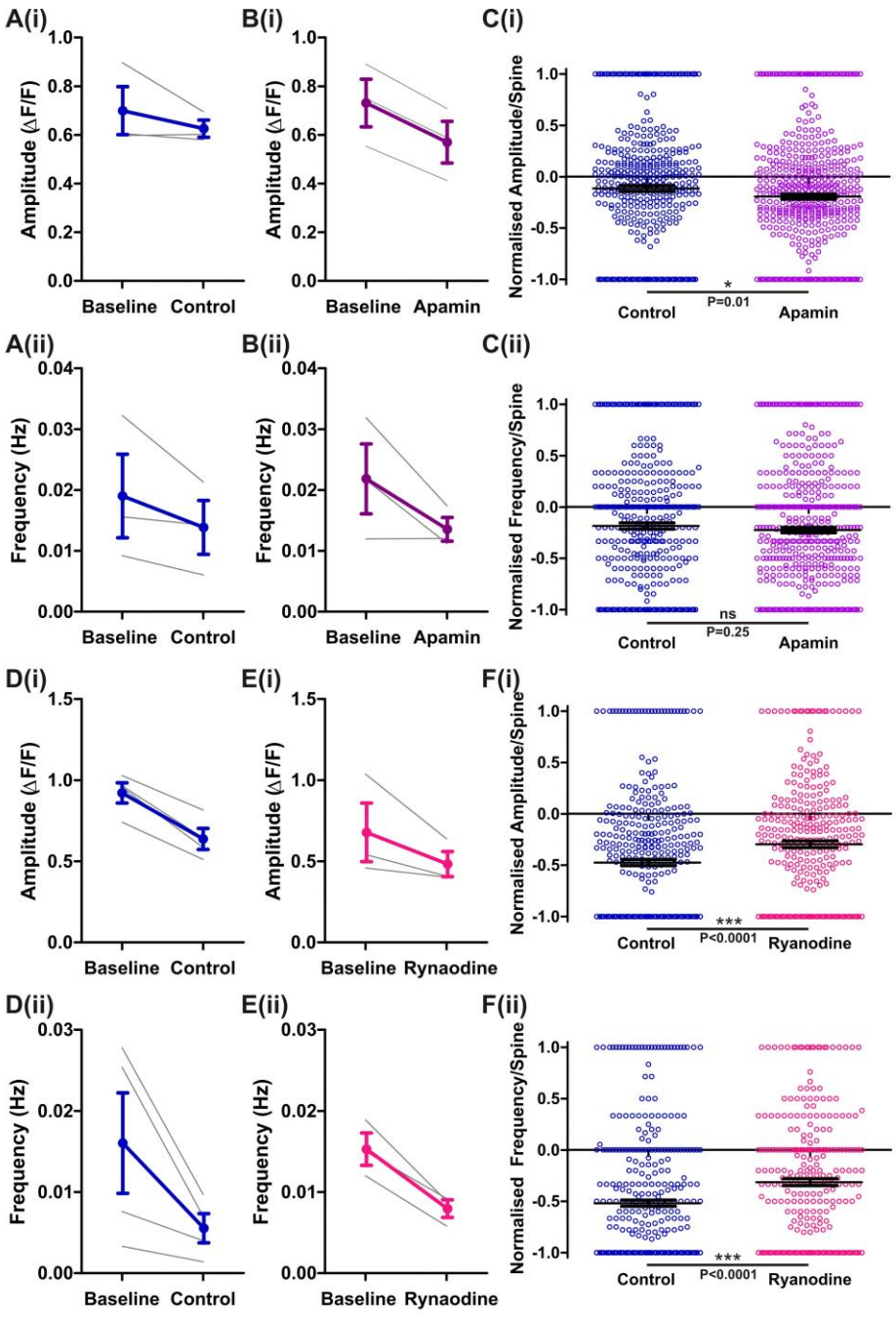

Figure 4.2.4 Contribution of calcium-activated potassium channels and internal stores to QCTs. (A) Faint grey lines indicate the mean amplitude **(i)** and frequency **(ii)** for each cell in baseline and control conditions. Bold blue lines show the mean and S.E.M for all cells (n=3). **(B)** Faint grey lines indicate the mean amplitude **(i)** and frequency **(ii)** for each cell in baseline and apamin (100 nM) conditions. Bold purple lines show the mean and S.E.M for all cells (n=3 cells). **(C)** Summary of the difference in amplitude **(i)** and frequency **(ii)** at each spine between baseline and control (blue) or apamin (purple) conditions. Control n=432 spines; apamin=540 spines. For cell-wide data low n numbers prevented the use of meaningful statistics. For within spine data statistics used were Mann-Whitney tests. Significance and P values are indicated for each graph. **(D)** Faint grey lines indicate the mean amplitude **(i)** and frequency **(ii)** for each cell in baseline and control conditions. Bold blue lines show the mean and S.E.M for all cells (n=4 cells). **(E)** Faint grey lines indicate the mean amplitude **(i)** and frequency **(ii)** for each cell in baseline and ryanodine (30 μM) conditions. Bold pink lines show the mean and S.E.M for all cells (n=3 cells). **(F)** Summary of the difference in amplitude **(i)** and frequency **(ii)** at each spine between baseline and control (blue) or ryanodine (pink) conditions. Control n=393 spines; ryanodine=363 spines. Mann-Whitney test, significance and P values are indicated below each graph.

4.2.2 Variability in QCT amplitude and frequency

Large variability in quantal neurotransmission has been observed in most neuronal types of the CNS (Forti et al., 1997; Andrásfalvy et al., 2003). Many studies have tried to elucidate whether the majority of this cell-wide variability is accounted for by synaptic events at different synapses, or whether there is high variability at single synapses. This problem is outlined in the schematic in Figure 4.2.5 A(i) which shows for simplicity two traces of mEPSCs recorded at the cell body. The first shows variability in amplitude, as indicated by the length of lines, and the second shows variability in frequency. In reality a single trace would show heterogeneity in both amplitude and frequency. When recording at a single site it is difficult to distinguish where this variability arises. The schematic in Figure 4.2.5 A(ii) demonstrates how the same trace (top; cell body) can be reproduced by different patterns of activity in spines (as labelled). Firstly, each spine may exhibit highly homogeneous mEPSC properties in terms of amplitude or frequency, but individual spines may be very different from each other. Or secondly, amplitude and frequency can be highly variable both between spines, but also within the same spine. The spatial information provided by imaging of QCTs at dendritic spines allows the separation of these two scenarios. Here, both the amplitude and instantaneous frequency of all QCTs recorded over entire dendritic trees are highly variable (Figure 4.2.5 B). Cumulative frequencies demonstrate that the amplitudes of QCTs have a broad distribution, an approximately ten-fold difference in magnitude within the same cell (Figure 4.2.5 B(i)). The majority (80%) of QCTs show low instantaneous frequencies (<0.4 Hz), but each cell also exhibits high frequency events up to 2-3 Hz (Figure 4.2.5 B(ii)). The example cell in Figure 4.2.6 shows various example traces where the variability of QCTs at single spines is demonstrated. Strikingly, there is large intraspine variability in QCT amplitude. For spines that show 5 or more QCTs there is on average a co-efficient of variation (CV) in amplitude of 0.58 (n=1208 spines from 36 cells).

Subsequently, we were interested in investigating the underlying origins of this high intraspine quantal variability. First we wanted to confirm that high CV values were not a consequence of a temporal trend of changing QCT amplitude. The control pharmacological experiments conducted in this chapter (Figure 4.2.2) indicate that QCT activity levels decrease significantly during a period of 10 minutes. When QCT amplitude for all cells was plotted over the 3 minute period of image acquisition, decreases in QCT amplitude as well as integral and instantaneous frequency were observed. However, the slope of the correlation is low and therefore time-dependent changes in amplitude cannot account for the large 0.58 CV recorded here (Figure 4.2.7 A). In our experiments, CV was calculated from traces recorded with a frame rate of ~6 Hz. QCT events could be clearly resolved at this frequency; however, it is possible that the peak

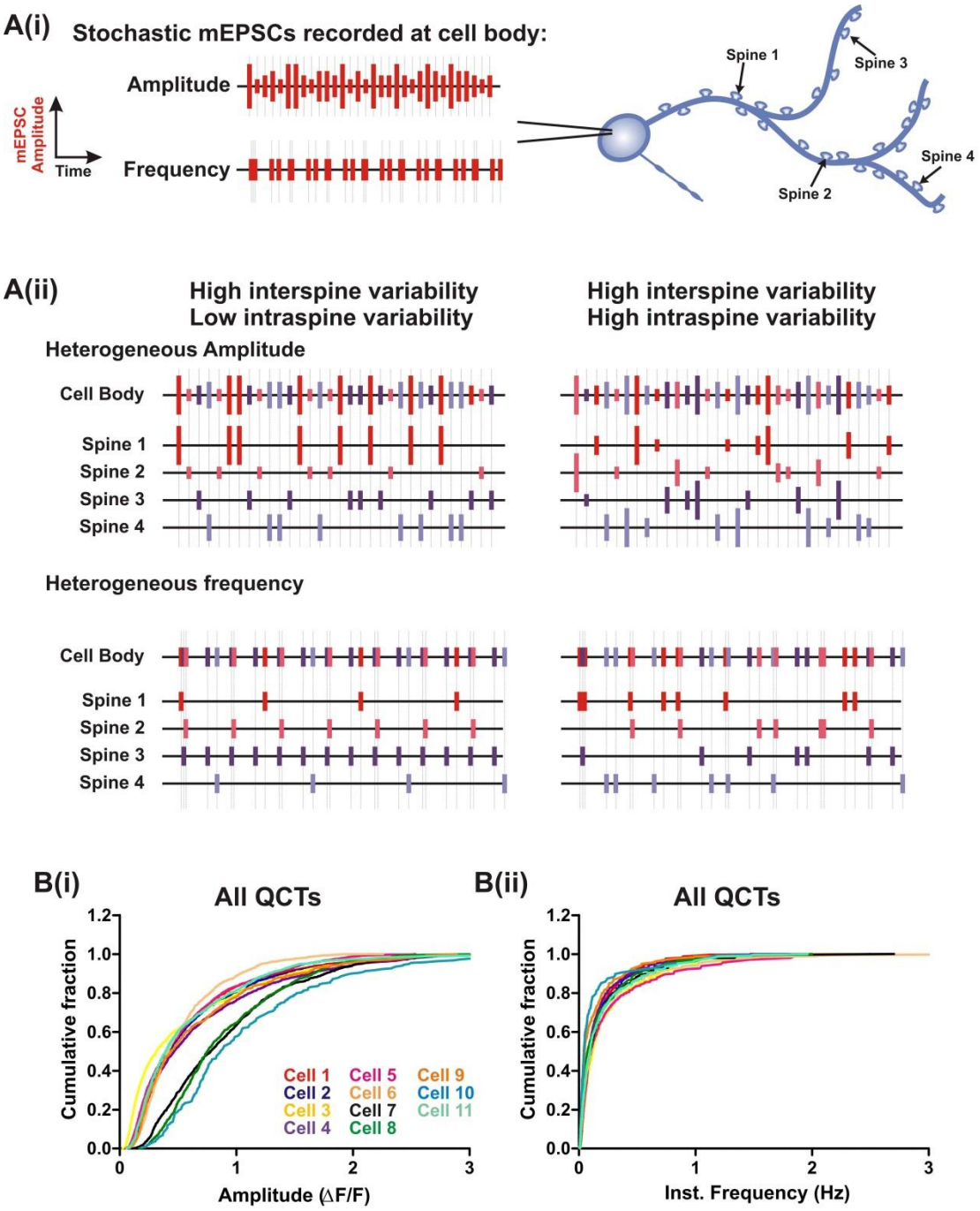

Figure 4.2.5 Cell-wide QCT amplitude and frequency are highly heterogeneous. (A(i)) A schematic demonstrating the high variability of miniature EPSC (mEPSC) amplitude and frequency recorded at the cell body. **(A(ii))** mEPSC variability can originate as either interspine or intraspine variability. For the heterogeneous amplitude schematics the length of each line along a trace represents the magnitude of mEPSCs. The contribution of four spines to a trace recorded at the cell body is shown by colour-coding. Note relative contribution from each spine to the 'recording' at the cell body is different depending on whether intraspine variability is low or high. A similar schematic is shown for frequency. **(B)** Cumulative frequencies describing the distribution of amplitudes **(i)** and instantaneous frequencies **(ii)** of QCTs for each cell. Each cell is colour-coded as labelled in **(i)**.

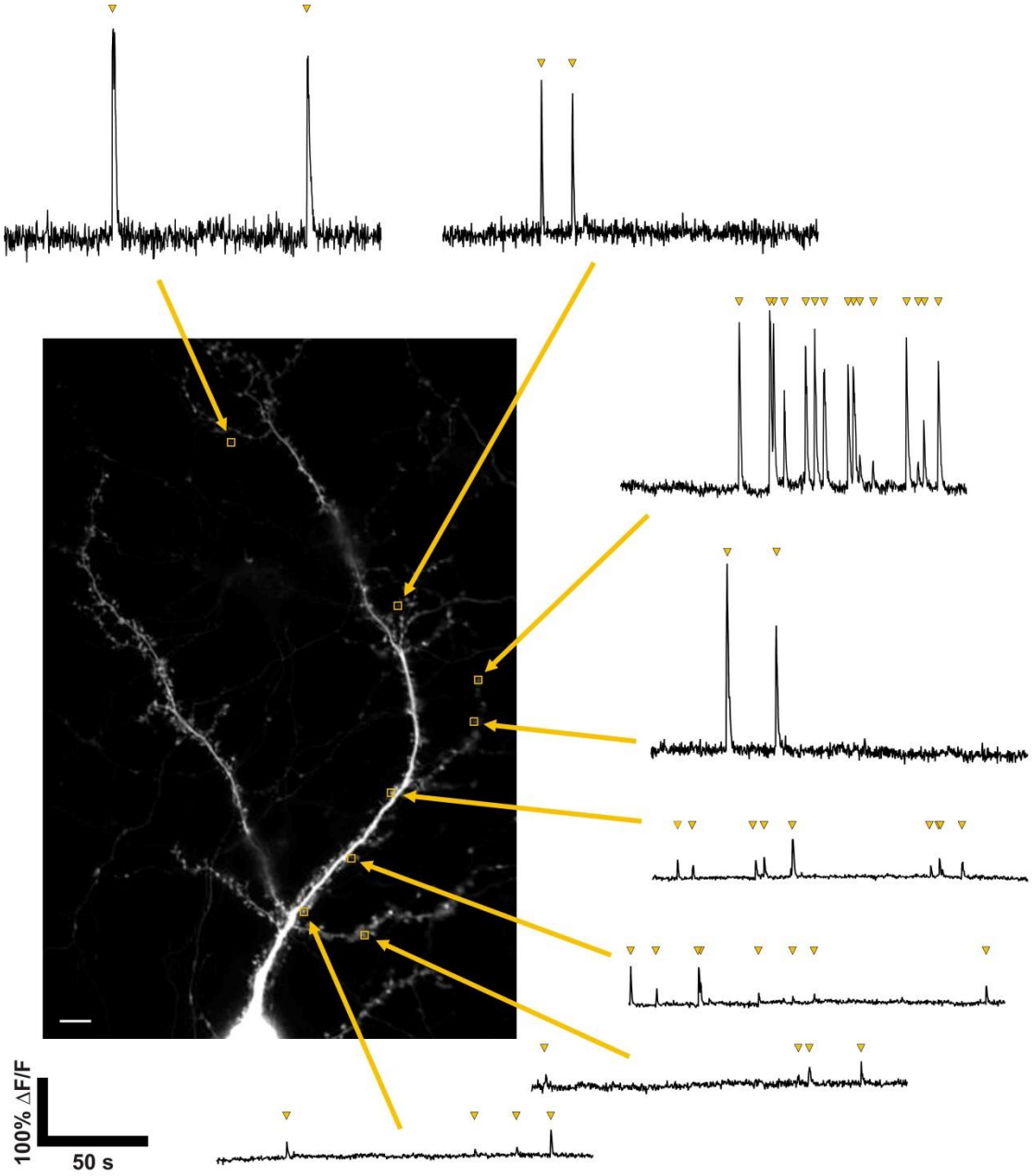

Figure 4.2.6 QCTs have both a large interspine and intraspine variability. A typical hippocampal neuron expressing GCaMP3. Scale bar = 10μm. Yellow squares indicate the ROIs used to generate ΔF/F traces of activity for single spines. Yellow arrow heads indicate QCTs. Note the large range of amplitudes recorded at single spines. Scale for all traces is found bottom left.

amplitude of each QCT is not properly estimated (due to under-sampling) and that this could lead to added heterogeneity. We therefore chose to increase our temporal resolution by performing linescan imaging of dendritic spines at a frame rate of ~120 Hz (Figure 4.2.7 B-C). Traces of spine activity recorded from linescan imaging remained highly variable (Figure 4.2.7 D) and in spines which exhibited 5 or more events a high CV of 0.51 was calculated (n= 47 spines from 4 cells) which was not significantly different from the CV recorded at ~6 Hz. We conclude that our imaging methods have sufficient temporal resolution to accurately measure CV in individual spines.

We next wanted to target possible pre- and postsynaptic sources of this large intraspine variability in QCT amplitude. Potential presynaptic sources include variability in (1) the number of glutamate molecules released by vesicles, (2) the location within the active zone (synaptic/perisynaptic) of vesicle fusion and (3) the number of vesicles that fuse per event (multivesicular release). Postsynaptic sources include variability in (1) the mode of calcium entry, (2) the properties of postsynaptic receptors (short-term alterations, such as desensitisation) and (3) changes in spine geometry affecting calcium concentration and compartmentalisation.

Initially, the responsibility of pre- or postsynaptic compartments for this heterogeneity was determined. To test the contribution of presynaptic sources, glutamate was uncaged repetitively at single spines, using a constant uncaging stimulus, and the CV of postsynaptic calcium transients calculated at that spine. The uncaging stimulus is highly controlled and uncages identical concentrations of glutamate per trial at the same location, therefore bypassing presynaptic variability. Short pulses of UV light (405 nm, 0.025-0.25 ms) induced robust postsynaptic calcium transients which were highly localised to dendritic spines (Figure 4.2.8 B-C). We have previously shown that short uncaging pulses induce postsynaptic calcium transients, which are similar in terms of dendritic spine localisation and amplitude to QCTs (Chapter 1, Figure 3.2.11). Postsynaptic calcium transients remain highly variable when triggered by repetitive uncaging (CV= 0.5 from 13 cells) as seen by the variability in the traces of single uncaging trials (Figure 4.2.8 C, grey traces). This high CV was caused by fluctuations in response amplitudes which were random over time (Figure 4.2.8 D). In summary, the large CV calculated on repetitive glutamate uncaging suggests variability in QCT amplitude is not presynaptic in origin.

The above finding indicates that the source of QCT amplitude variability is likely postsynaptic. Although there are many calcium effectors including calcium permeable channels, calcium pumps and calcium binding proteins that could alter postsynaptic calcium concentrations, a

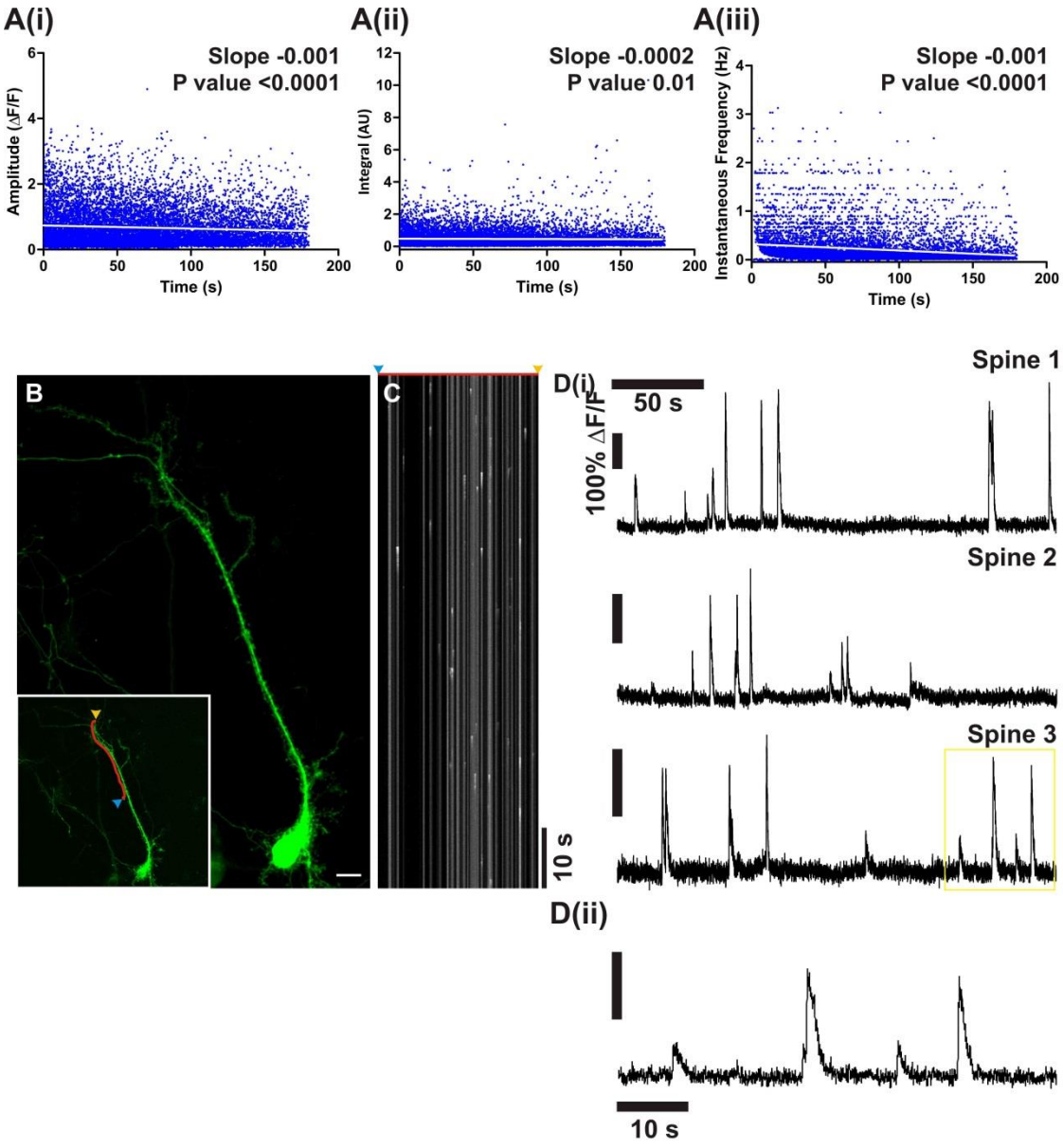

Figure 4.2.7 High variability of intraspine QCT amplitude is not due to time-dependent rundown in QCT amplitude or limitations in temporal resolution. (A) Scatter plots of amplitude **(i)**, integral **(ii)** and instantaneous frequency **(iii)** during the imaging period (n=11 cells, 12534 spines). Spearman correlation; slope and P values are shown top right. **(B)** A typical hippocampal neuron expressing GCaMP3. Scale bar = 10 µm. Inset: red line indicates the region used to record the linescan in **(C)**, drawn to pass through multiple spine heads. The blue arrow indicates the start, and the yellow arrow the end position. **(C)** An example linescan recording. The red line and arrows above indicate the spatial extent of the scan as in **(B). (D(i))** ΔF/F traces from three linescans concatenated for three different spines. Note the high variability in amplitude at each example spine. **(D(ii))** Zoom in of ΔF/F trace area indicated by yellow box from Spine 3.

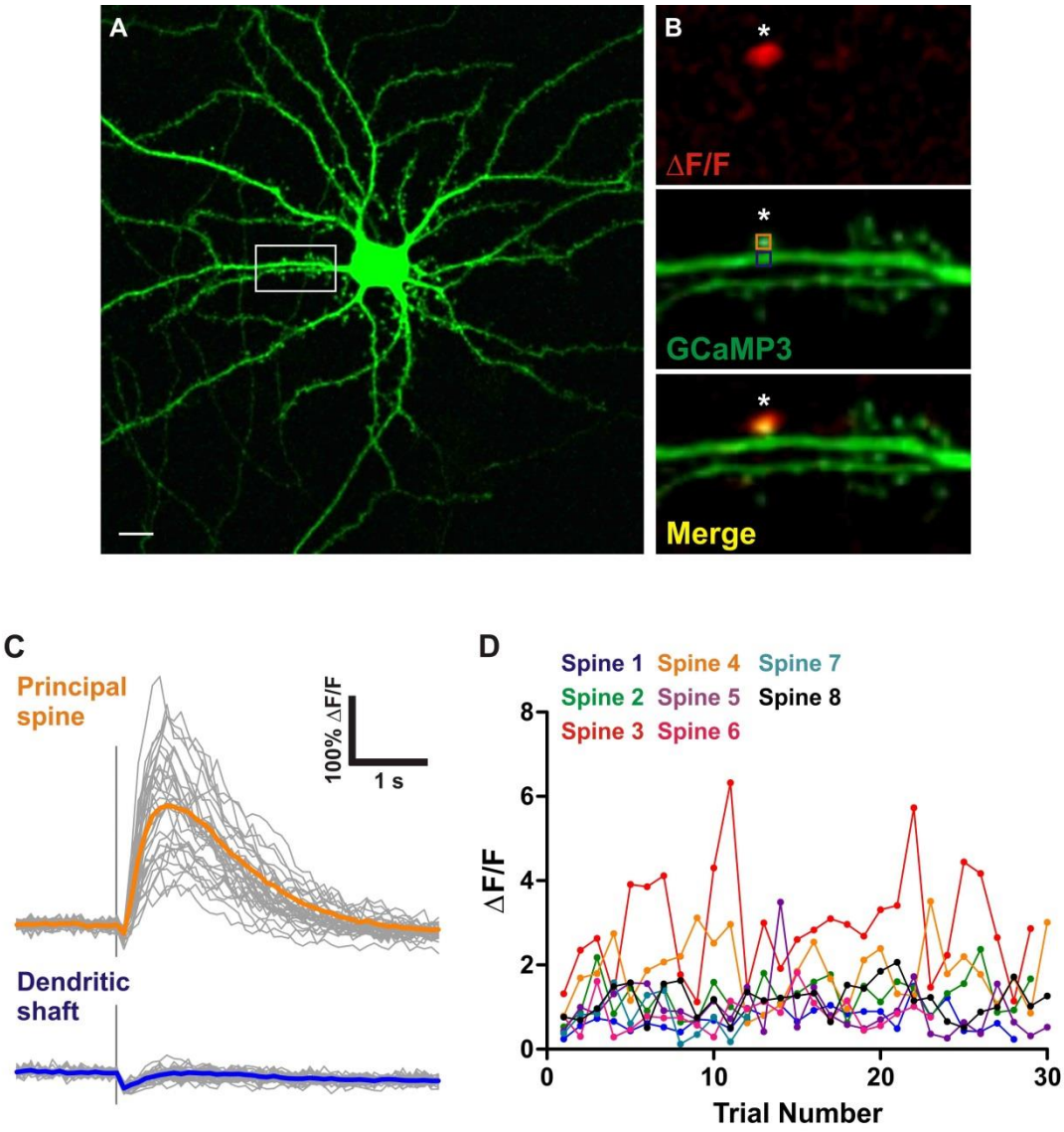

Figure 4.2.8 Repetitive uncaging of glutamate at single spines induces calcium transients with high variability in amplitude (A) Typical hippocampal neuron expressing GCaMP3. White box indicates area enlarged in **(B)**. Scale bar = 10μm. **(B)** Repetitive uncaging of glutamate was performed at a single spine with UV laser (405nm, 0.05 ms pulse) at a single point (indicated by the white asterisk). Top panel shows a ΔF/F summary image of an uncaging induced calcium transient. Middle panel shows GCaMP3 expression within this dendritic segment, with the positions of the ROIs used to calculate the colour-matched ΔF/F traces shown in **(C)** overlaid. Bottom panel is a merge of the above panels. **(C)** Faint grey traces show responses for each uncaging trial delivered every 15 seconds at the principal spine and dendritic shaft as labelled (n=33 trials). Mean responses for the principal spine and dendritic shaft are shown by bold orange and blue traces, respectively. **(D)** The amplitudes of calcium transients are plotted as a function of uncaging trial number for all spines tested as colour-coded (n=8 spines). Note that the amplitudes do not follow any obvious pattern and appear stochastic over time.

few principal players were selected which could amplify or depress NMDA receptors mediated QCTs. Using a pharmacological approach we determined that inhibiting AMPA RECEPTORs, R-type VGCCs, ryanodine receptors (calcium release from internal stores) or SK-calcium activated potassium channels with 10 µM NBQX, 500nM SNX-482, 30 µM Ryanodine and 100nM Apamin respectively, had no effect on the CV of amplitude in spines which exhibited 5 or more QCTs compared to control (Figure 4.2.9). Another possible source of variability is from NMDA receptor desensitisation , which has previously been studied as a possible mechanism underlying AMPA receptor mediated quantal variability (Forti et al., 1997). An inverse relationship between amplitude and inter-QCT interval would indicate a role for NMDA receptor desensitisation and indeed it was found that QCT amplitude is inversely correlated with instantaneous frequency, meaning that small inter-QCT intervals predict smaller amplitude QCTs (Figure 4.2.10).

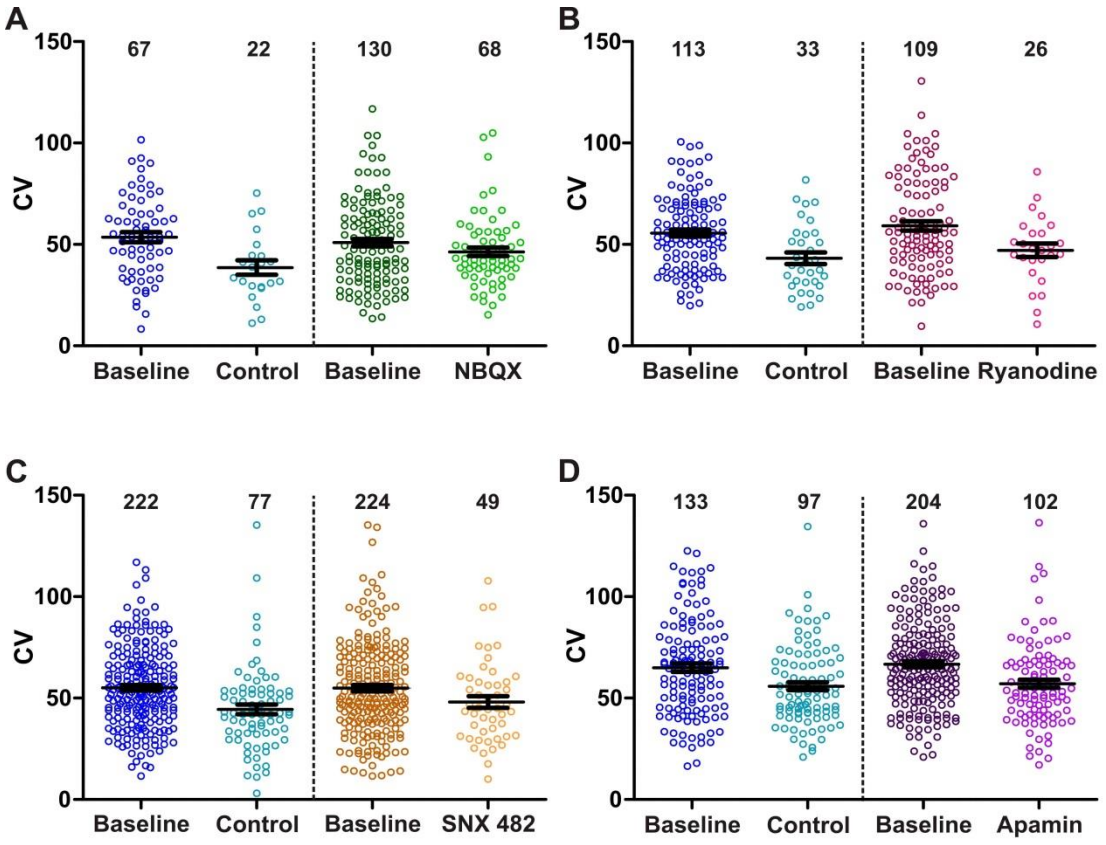

Figure 4.2.9 AMPA receptors, internal stores, R-type VGCCs and SK calcium-activated potassium channels do not contribute to high intraspine amplitude variability. (A-D) Each point represents the co-efficient of variation (CV) of an individual spine which exhibited 5 or more events in baseline and control or drug conditions as indicated. n numbers of spines are indicated above each condition. **(A)** 10 µM NBQX, **(B)** 30 µM Ryanodine, **(C)** 500 nM SNX-482 and **(D)** 100 nM Apamin.

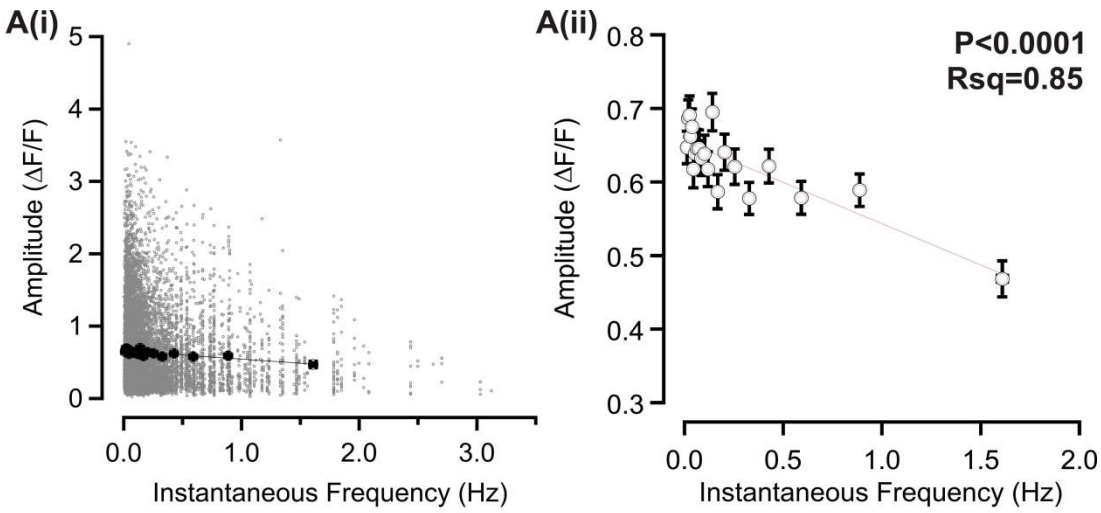

Figure 4.2.10 High instantaneous frequency predicts lower QCT amplitudes. (A(i)) Correlation of QCT amplitude against instantaneous frequency (n=6015 QCTs from 11 cells). Bold black line indicates the mean amplitude within 21 bins spanning instantaneous frequency (each bin = 286 QCTs). **(A(ii))** A summary of mean QCT amplitude for each bin of instantaneous frequency (as shown by black points in **(i)**) plus S.E.M values. Statistic used is Pearson's co-efficient; P value and R squared value are shown top right of the plot.

4.2.3 The spatial distribution of activity across dendritic trees

We have shown here there is a large variability in QTCs amplitude and frequency. We next wanted to understand how these synaptic calcium events were distributed across entire dendritic trees. For this purpose live imaging of neurons was performed where entire dendritic tress were included within the imaging window. The dendritic tree of the neuron was subsequently traced and ROIs picked for each spine along the traced dendrites, then each ROI was assigned to its corresponding dendrite. In this way we were able to establish the position of each spine along the dendrite of a neuron. To define the dendritic location of spines three measures were used: (1) relative distance, defined as the distance of an ROI to the soma normalised by the distance from the soma to the furthest branch tip; (2) the number of nodes (branch points) between each ROI and the soma and (3) the absolute distance of each ROI to the soma (Figure 4.2.11 A-B). The amplitude, integral and instantaneous frequency of each QCT (from 11 cells) showed interesting relationships when plotted against the different distance metrics (Figure 4.2.11 C-E). The amplitude and integral, which are highly related metrics, both show a positive relationship with relative distance, in that large QCTs are found closer to branch tips (Figure 4.2.11 C-D). However, no correlation was observed with either direct distance to the soma or number of nodes. On the other hand, the instantaneous frequency of QCTs appears randomly distributed across the dendritic tree, with no clear relationship found with any distance metric (Figure 4.2.11 E).

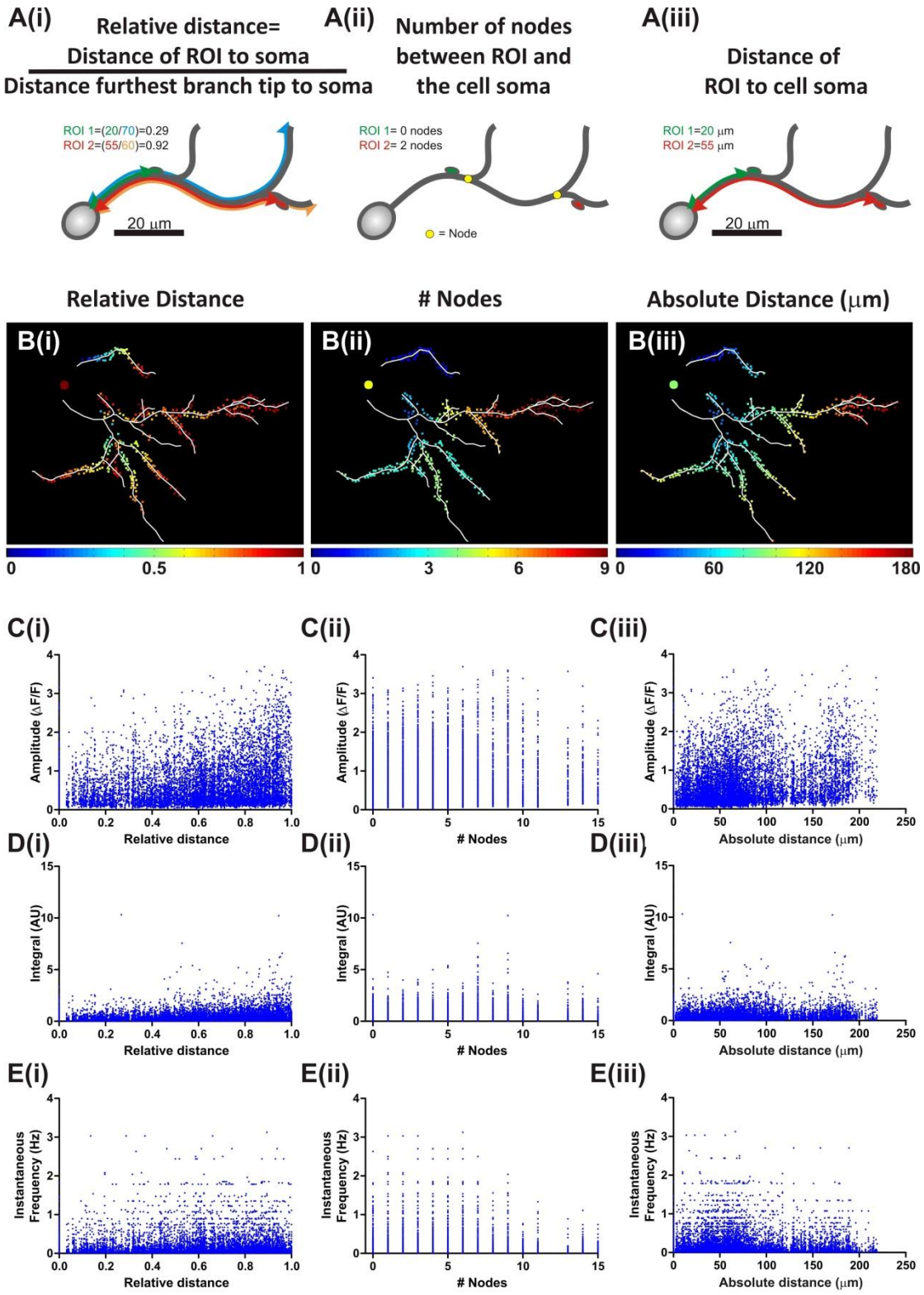

Figure 4.2.11 The distribution of activity across dendritic trees. (A) A schematic detailing three metrics used to define dendritic tree position of ROIs; relative distance as indicated by the calculation **(i)**, number of nodes (branch points) between ROI and soma **(ii)** and absolute distance from the soma **(iii)**. **(B)** Tracings of an example cell with ROIs (squares) colour-coded for dendritic tree position according to relative distance **(i)**, number of nodes **(ii)** and absolute distance **(iii)**. Scales are located below each image. **(C-E)** Activity metrics for each QCT; amplitude **(C)**, integral **(D)** and instantaneous frequency **(E)** as a function of relative distance **(i),** number of nodes **(ii)** and absolute distance **(iii).** For amplitude and integral n=12534 QCTs from 11 cells, instantaneous frequency n=6015 QCTs from 11 cells.

While a positive relationship of QCT amplitude with relative distance can be observed, the large scatter of QCT amplitudes, especially at high relative distance, confounds a meaningful and simple statistical correlation of this data (Figure 4.2.11 C(i)). In addition, there is a bias in the number of ROIs at high relative distances. It is possible that the large number of high amplitude QCTs at high relative distances is a probabilistic consequence of relatively large sample size closer to branch tips. To address this, QCTs were grouped into ten bins dependent on metric distance (Figure 4.2.12 A). Figure 4.2 12 B shows ten histograms of the distribution of QCT amplitude, one for each bin of relative distance. Interestingly, the peak centres of each histogram, determined by fitted curves, are very similar for all relative distance bins ranging from 0.17 to 0.25 peak ΔF/F. This indicates that at all relative distances small amplitude QCTs dominate. However, when cumulative frequencies of QCT amplitude are generated for each relative distance bin, we found that plots for high relative distances are shifted to the right for QCT amplitude in comparison to lower relative distances (Figure 4.2.12 C(i)). This indicates that larger amplitude QCTs do indeed preferentially occur closer to branch tips. A similar trend was observed for the other distance metrics (Figure 4.2.12 C(ii) and (iii)).

When the spatial distribution of integral QCT values are assessed using the same analysis we find similar results to QCT amplitude, i.e. a tendency for high bin number cumulative frequencies to show a right-ward shift in integral compared to low bin number cumulative frequencies for all distance metrics, but with relative distance exhibiting the most robust scaling (Figure 4.2.13 A). There may be a small rightward shift in the cumulative frequencies of instantaneous frequency at low relative distance which suggests that low frequency events occur at spines which are located closer to branch tips (Figure 4.2.13 B).

The cumulative frequencies are summarised in simple scatter plots where the 80th percentile value for each bin is plotted over either relative distance, number of nodes or absolute distance (Figure 4.2.13 C). Here, it is clear that the strongest distance-dependence relationships are found with relative distance. QCT amplitude and integral get significantly larger with increasing relative distance, whereas instantaneous frequency gets significantly smaller. In fact, when mean amplitude per spine is plotted against the mean frequency of that spine we observe a significant inverse relationship, supporting the differential correlations for amplitude and impulse frequency observed against relative distance (Figure 4.2.13 D).

Another important characteristic of QCTs is the high variability in amplitude (see Figure 4.2.5-6). It was therefore important to determine whether the spines that exhibit a high CV for QCT amplitudes are spatially biased to a particular area of the dendritic tree. At first glance, cumulative frequencies of the coefficient of variation (CV) were very similar in distribution for all relative distances (Figure 4.2.13 E). However, when summarising these values a very small

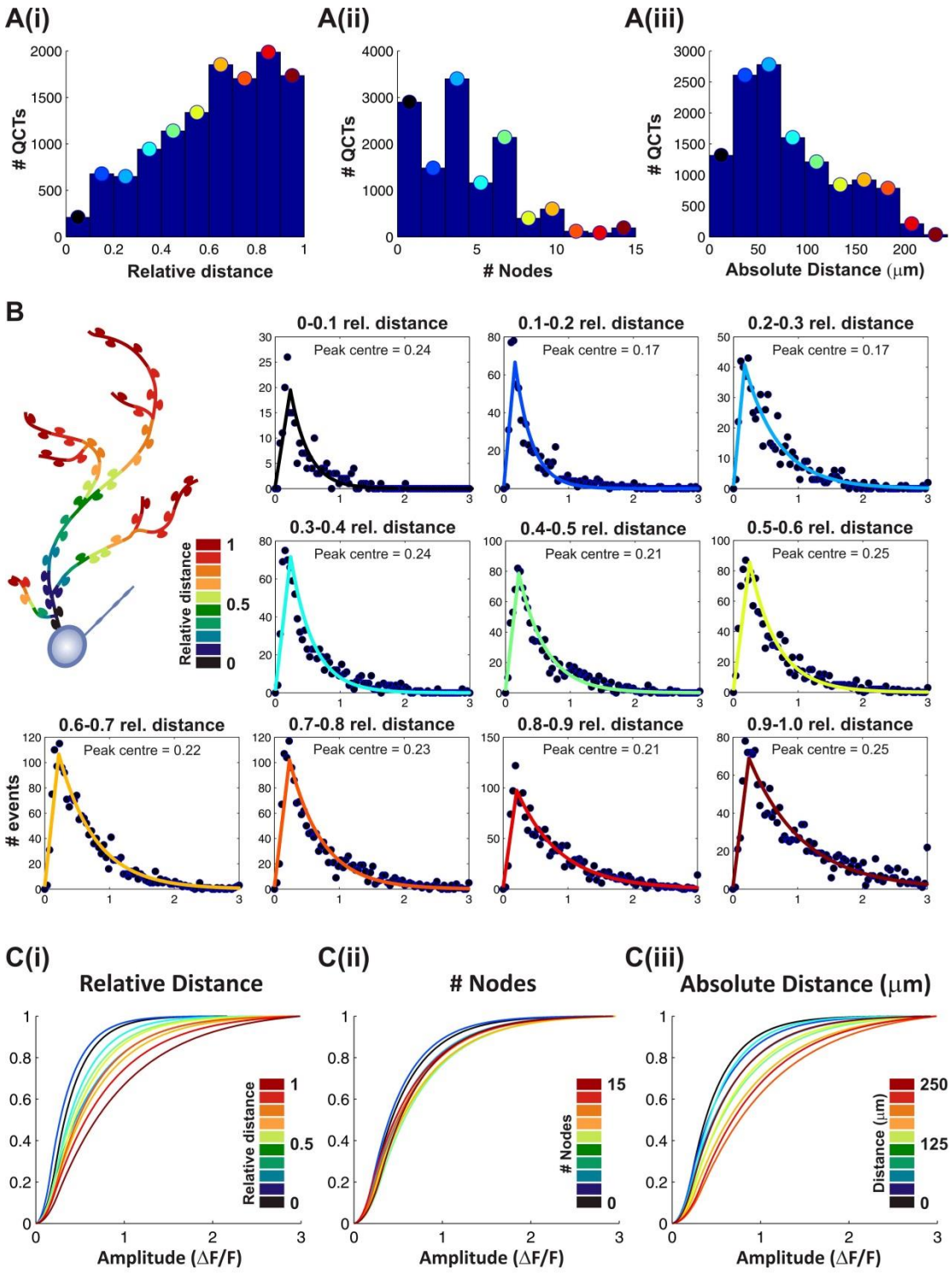

Figure 4.2.12 QCT amplitude scales with relative distance but not number of nodes, nor distance from soma. (A) Histograms of the number of QCTs occurring at different dendritic tree locations measured using relative distance **(i)**, number of nodes **(ii)** and absolute distance from soma **(iii)**. Histogram bins are colour-coded by dendritic tree location. **(B)** Schematic of a neuron with spines colour-coded for relative distance as per histogram in **(A(i))**. Ten histograms, one for each bin of relative distance, each colour coded as the schematic neuron. Each histogram shows the distribution of QCT amplitudes for each relative distance bin. Two-component fitted distributions show the peak centre of amplitude for each relative distance bin, as indicated at the top of each plot. **(C)** Cumulative frequencies of QCT amplitude for each binned distance metric; relative distance **(i)**, number of nodes **(ii)** and absolute distance from soma **(iii)**. Key is to the right for each plot. All data calculated from n=12534 QCTs from 11 cells.

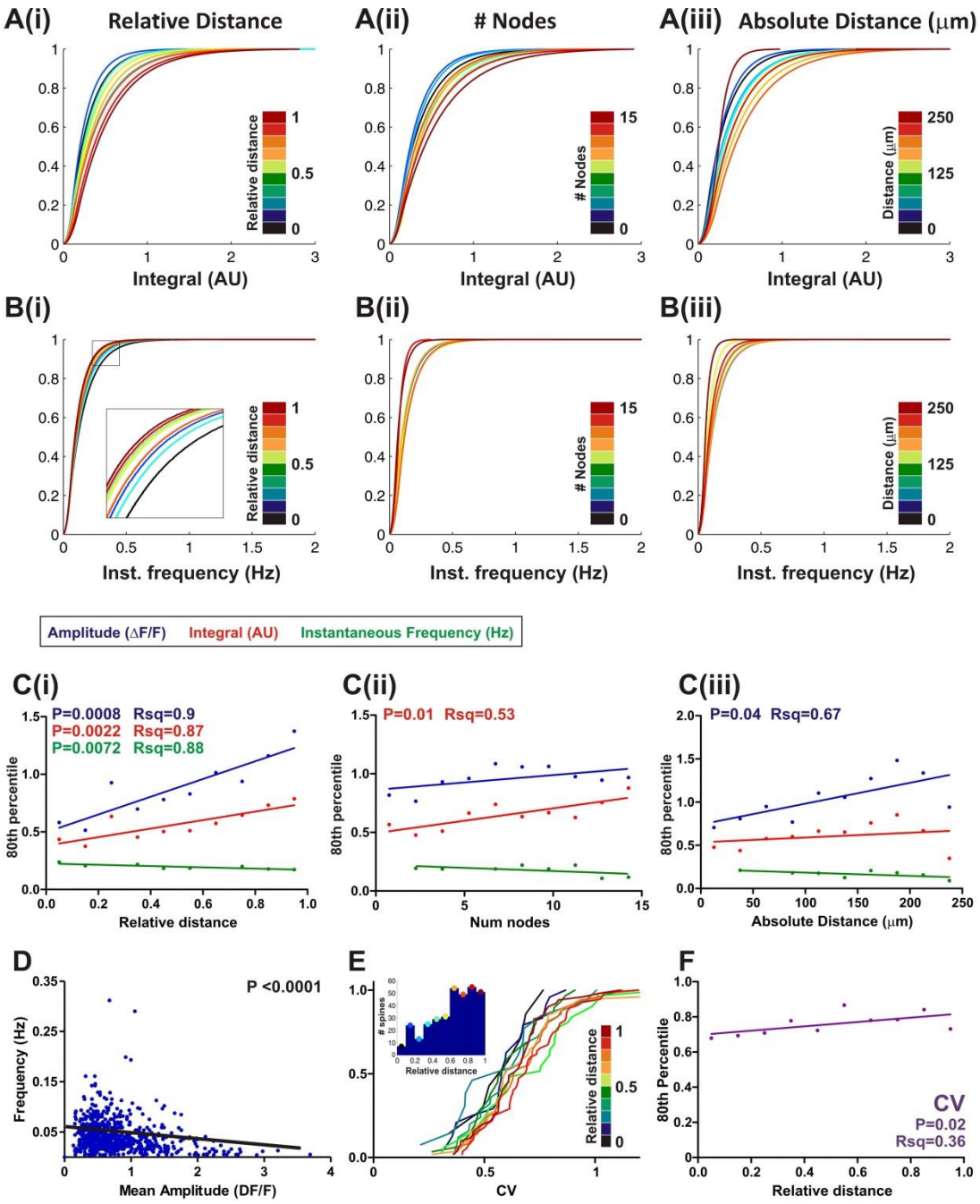

Figure 4.2.13 Distance dependence of the integral, instantaneous frequency and CV of QCTs. (A-B) Cumulative frequencies of integral **(A)** and instantaneous frequency **(B)** for relative distance **(i)**, number of nodes **(ii)** and absolute distance from soma **(iii)**. Each plot is colour-matched a distance metric bin shown in the key to the right. For **(B (i))** the black box indicates the area enlarged in the inset. Integral: n=12534 QCTs from 11 cells; instantaneous frequency n=6015 QCTs from 11 cells. **(C)** Plot of the 80th percentile values for values for amplitude (blue), integral (red) and instantaneous frequency (green) obtained from the cumulative plots, as a function of relative distance relative distance **(i)**, number of nodes **(ii)** or absolute distance from soma **(iii)**. Spearman's co-efficient. Colour-coded P- and R-squared values are shown top left of each plot. (**D)** A scatter plot of mean frequency per spine over mean amplitude per spine (n=746 spines from 4 cells). Spearman's co-efficient; P value shown top right of plot. **(E)** Cumulative frequencies of CV for QCT amplitude for each bin for relative distance. CV was calculated for each spine exhibiting 5 or more QCTs (n=338 spines). The distribution of number of spines with 5 events or more for binned relative distance is shown as an inset. **(F)** Plot of the 80th percentile values for CV obtained from the cumulative plots as a function of relative distance. Spearman's co-efficient; P- and R-squared values are shown bottom right of each plot.

direct correlation was seen between CV with distance (Figure 4.2.13 F), so that more distant spines showed more variable response properties. Although the functional significance of this is not immediately clear, the difference in CV between proximal and distal spines is relatively small and may not have a large impact on the postsynaptic neuron.

All experiments outlined in this Chapter were analysed using ΔF/F as the response metric, where the change in fluorescence of a QCT within an ROI is normalised by the median baseline fluorescence within that ROI. Baseline fluorescence is determined by two factors, firstly the number of GCaMP3 molecules present, and secondly by the basal calcium concentration. If basal calcium concentrations are not evenly distributed across the dendritic tree the ΔF/F read-out of activity would be skewed. For example, if distal spines have lower calcium concentrations and therefore lower fluorescence intensities at rest, the normalised ΔF/F values would be relatively higher than in proximal regions of the dendritic tree. To tackle this problem a cytosolic red fluorophore was co- expressed with GCaMP3 which fills the entire neuron (Figure 4.2.14 A). The intensity of the indicator at different cellular regions is simply a read-out of the number of fluorophore molecules present and is independent of calcium concentration. In GCaMP3 and TagRFP co-expressing neurons the basal intensity of GCaMP3 expressed within different spines was highly correlated with TagRFP intensity suggesting that baseline GCaMP3 intensity can be taken as a good read-out of the number of fluorophore molecules present (Figure 4.2.14 B). This correlation also demonstrated the necessity of using a normalisation factor in the response metric as a large range of basal levels of fluorescence intensity was observed for different spines. To further control for any issues arising from possible problems related to basal GcaMP3 normalisation, neurons co-expressing GCaMP3 and TagRFP were used to measure QCTs. In this case, QCT amplitude was calculated using an alternative response metric which normalises the GCaMP3 response (ΔG) by TagRFP intensity (R) giving the metric ΔG/R. Unsurprisingly given the high correlation of resting GCaMP3 and TagRFP intensities within individual spines, amplitudes calculated using the ΔF/F and ΔG/R metrics are highly correlated (Figure 4.2.14 C). Indeed, a distance-dependent correlation in ΔG/R amplitudes with relative distance is observed, which is less robust than with absolute distance and number of nodes and is similar to the result observed using ΔF/F in a separate group of cells (Figure 4.2.14 D-F).

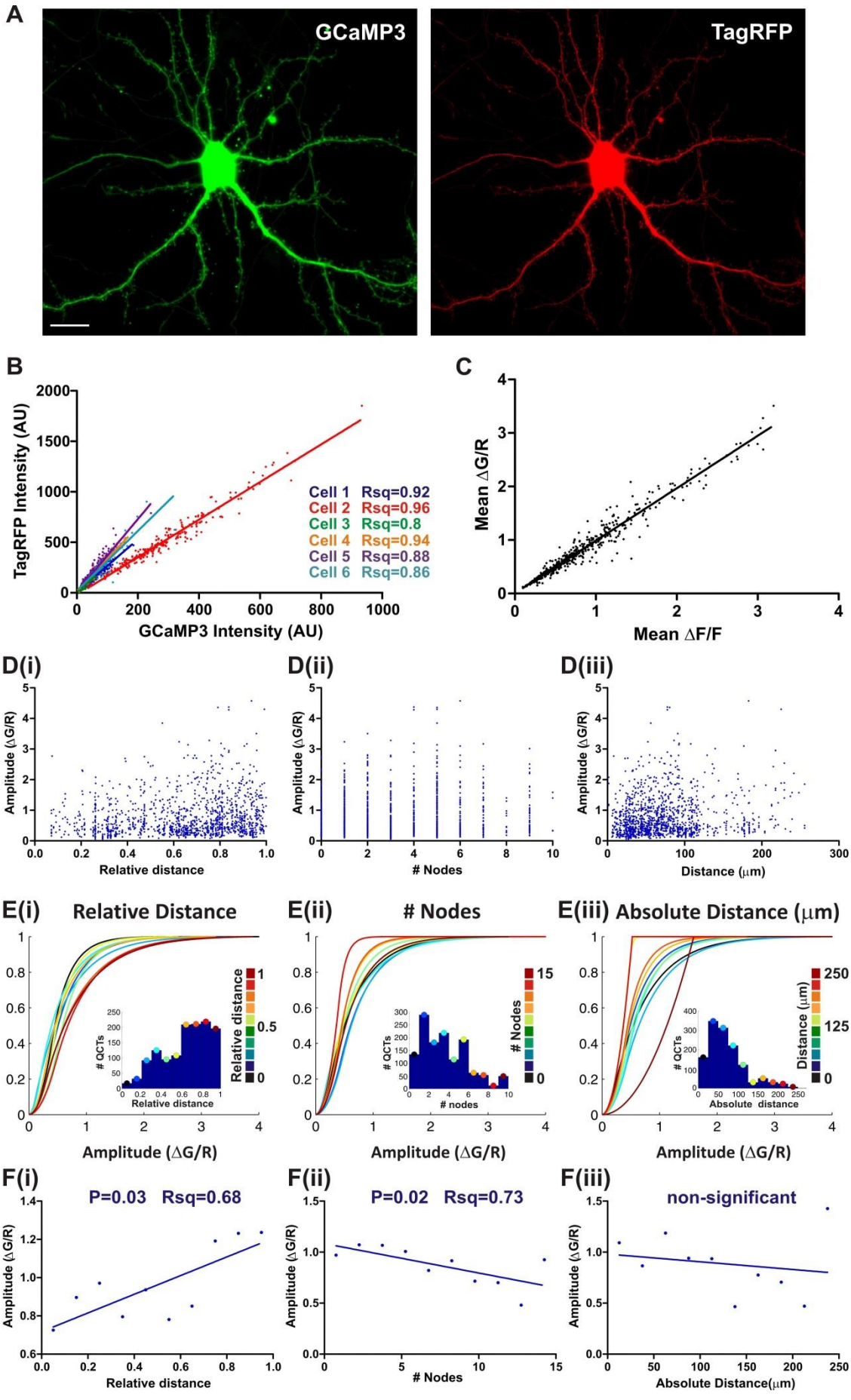
A
GCaMP3
TagRFP
B
TagRFP Intensity (AU)
GCaMP3 Intensity (AU)
Cell 1 Rsq=0.92
Cell 2 Rsq=0.96
Cell 3 Rsq=0.8
Cell 4 Rsq=0.94
Cell 5 Rsq=0.88
Cell 6 Rsq=0.86
C
Mean ΔG/R
Mean ΔF/F
D(i)
Amplitude (ΔG/R)
Relative distance
D(ii)
# Nodes
D(iii)
Distance (μm)
E(i) Relative Distance
E(ii) # Nodes
E(iii) Absolute Distance (μm)
# QCTs
Relative distance
nodes
Absolute distance
Amplitude (ΔG/R)
F(i)
P=0.03 Rsq=0.68
F(ii)
P=0.02 Rsq=0.73
F(iii)
non-significant
Absolute Distance(μm)

Figure 4.2.14 The ΔG/R response metric reports QCTs similar to the ΔF/F metric. (A) A typical hippocampal neuron co-expressing GCaMP3 and TagRFP. Scale bar = 10 µm. **(B)** Correlation of basal GCaMP3 and TagRFP fluorescence intensities for the same dendritic spines, from individual cells as colour-coded. Spearman co-efficient, P<0.0001 for all cells, R squared values are colour matched and reported bottom right. **(C)** Correlation of ΔF/F and ΔG/R values calculated as the mean of all QCTs recorded at individual spines (n-506 spines from 5 cells). Spearman co-efficient, P<0.0001 for all cells, R squared = 0.95. **(D)** QCT amplitude calculated using ΔG/R over distance metrics; relative distance **(i),** number of nodes **(ii)** and absolute distance **(iii)**, n = 1308 QCTs. **(E)** Cumulative frequencies for QCT amplitude calculated using ΔG/R for relative distance **(i)**, number of nodes **(ii)** and absolute distance **(iii)**. Irregular cumulative frequencies occur when low n-numbers prevent adequate fitting. Inset histograms show the number of QCTs within each distance metric bin. Each plot is colour-matched to a distance metric bin shown in the key to the right of each plot. **(F)** Plot of the 80th percentile values for ΔG/R amplitude obtained from the cumulative plots as a function of relative distance **(i)**, number of nodes **(ii)** and absolute distance **(iii)**. Spearman's co-efficient; P- and R-squared values are shown top centre of each plot.

4.2.3.1 How do functional correlations with dendritic distance arise?

The data presented so far has not revealed any underlying mechanism for distance-dependent increases in QCT amplitude. However, there are a number possible mechanisms that could help explain this interesting property, including systematic changes in the distribution of glutamate receptors or in the morphology of dendritic spines. The experiment performed above in TagRFP co-expressing neurons gave insight that spine morphology may indeed have a role to play. Using TagRFP fluorescence intensity as a proxy for spine size/volume showed that spines were smaller (dimmer fluorescence) closer to branch tips (Figure 4.2.15 B yellow arrowheads) compared to spines located closer to the cell body (Figure 4.2.15 B blue arrowheads). More specifically, there was an inverse relationship of TagRFP intensity against relative distance (Figure 4.2.15 C). Accounting for possible bias by the large number of ROIs at high relative distances, the data was binned for relative distance (Figure 4.2.15 D; histograms). Cumulative frequencies were generated for each bin, showing a rightward shift in TagRFP intensity at low relative distance (Figure 4.2.15 D) and a clear correlation when plotting the 80th percentile response for each cumulative frequency plot against relative distance (Figure 4.2.15 E). It has previously been shown that small spines have smaller spine necks and therefore spine heads that are tightly isolated from the dendrite, while the converse is true of larger spines (Noguchi et al., 2005). The functional outcome of this difference in neck resistivity is that calcium transients recorded at the spine head are larger for small spines than for large ones (Nimchinsky et al., 2004; Noguchi et al., 2005, 2011). Although only a correlation, our findings suggest that the amplitude of QCTs may in fact be determined by spine morphology.

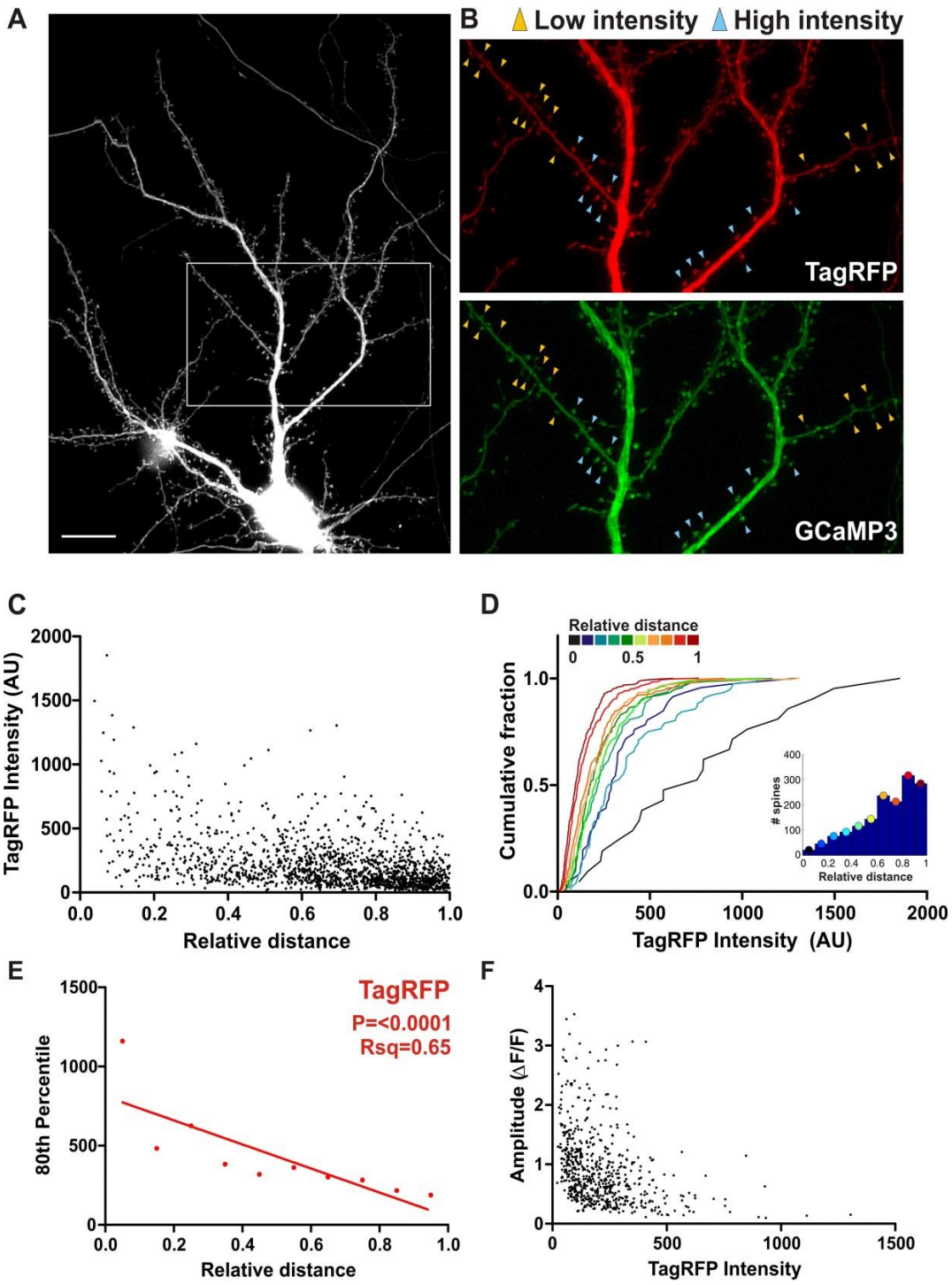

Figure 4.2.15 TagRFP intensity scales with relative distance across dendritic trees. **(A)** A typical hippocampal neuron co-expressing GCaMP3 and TagRFP. White box indicates the area shown in **(B)**. Scale bar = 10 µm. **(B)** Expression patterns of TagRFP and GCaMP3 within a dendritic section. Yellow arrowheads indicate spines which are low intensity and light blue arrowheads indicate high intensity spines. Note that the highlighted less intense spines (yellow arrows) are located closer to branch tips. **(C)** TagRFP intensity for each spine as a function of relative distance (n= 1554 spines from 6 cells). **(D)** Cumulative frequency plots for TagRFP intensity for each spine (shown in **(C)**) taken from the binned data (histogram inset). Each plot is colour-matched to a different bin for relative distance shown in the key top left. **(E)** Plot of the 80th percentile values for Tag RFP intensity obtained from the cumulative plots as a function of relative distance. Spearman's co-efficient; P- and R-squared values are shown on the plot. **(F)** Mean QCT amplitude as a function of TagRFP intensity for each spine (n=616 spines from 6 cells).

Nevertheless, a second mechanism for relative distance-dependent increases in QCT amplitude may be due to a relative distance-dependent scaling in the numbers of NMDA receptors per spine. This possibility was assessed using immunocytochemistry against specific postsynaptic proteins on GCaMP3 transfected neurons. PSD-95 is thought to cluster NMDA receptors and AMPA receptors to the postsynaptic density, and as such the accumulation of PSD-95 at a synapse has been used as a proxy for synapse strength (Nusser et al., 1998; Sheng and Kim, 2011). NMDA receptors are tetrameric channels composed of multiple subunits, of which the GluN1 (or NR1) subunit is compulsory. Here, immunocytochemistry against a PSD-95 or GluN1 led to punctate staining that co-localised with GCaMP3 labelled dendritic spines (Figure 4.2.16 A and D). The intensity of PSD-95 or GluN1 staining was measured in spines located across the dendritic tree and then plotted against relative distance. A trend can be observed where both PSD-95 and GluN1 intensities are higher at low relative distances (Figure 4.2.16.B and F). This is also seen when cumulative frequencies of PSD-95 and GluN1 intensity are generated for different bins of relative distance (see histogram inset) (Figure 4.2.16 C and G) and summarised in Figures 4.2.16 D and H. This inverse correlation for both PSD-95 and GluN1 with relative distance indicates that smaller PSD-95 accumulations and thus weaker synapses are found at higher relative distances, i.e. closer to branch tips, and that larger amplitude QCTs are not a direct consequence of increased NMDA receptor numbers. Importantly, these immunostaining results agree well with the distribution in spine morphology described above (Figure 4.2.15) as the number of glutamate receptors has been shown to correlate strongly with spine size (Mackenzie et al., 1999; Matsuzaki et al., 2001; Sheng and Kim, 2011).

The above result suggests that the relative distance correlation of QCT amplitude is postsynaptic in origin, specifically in relation to spine size and spine neck resistance. To test that presynaptic strength does not determine the relationship of relative distance with QCT amplitude, glutamate uncaging was performed at spines located across the dendritic tree (Figure 4.2.17 A). If QCT amplitude is a consequence of spine size and neck resistance a relative distance-dependent correlation should be maintained.

Characterisation of PSDGCaMP3 using glutamate uncaging (Chapter 3, 3.2.11) determined that short UV uncaging pulses (0.1-0.5 ms in duration) triggered postsynaptic calcium transients of a similar amplitude, kinetics and spine localisation as those triggered by quantal release. Here, an uncaging pulse of 0.25 ms was used at all spines for all cells which generated small calcium transients which were highly localised to individual spine heads. To overcome the issue of variability in postsynaptic calcium transient amplitude to uncaging (see Figure 4.2.8) responses were taken as the mean of 5 uncaging events (Figure 4.2.17 B). The traces in Figure 4.2.16 B show the variability between uncaging responses at the same spines and also variability in the

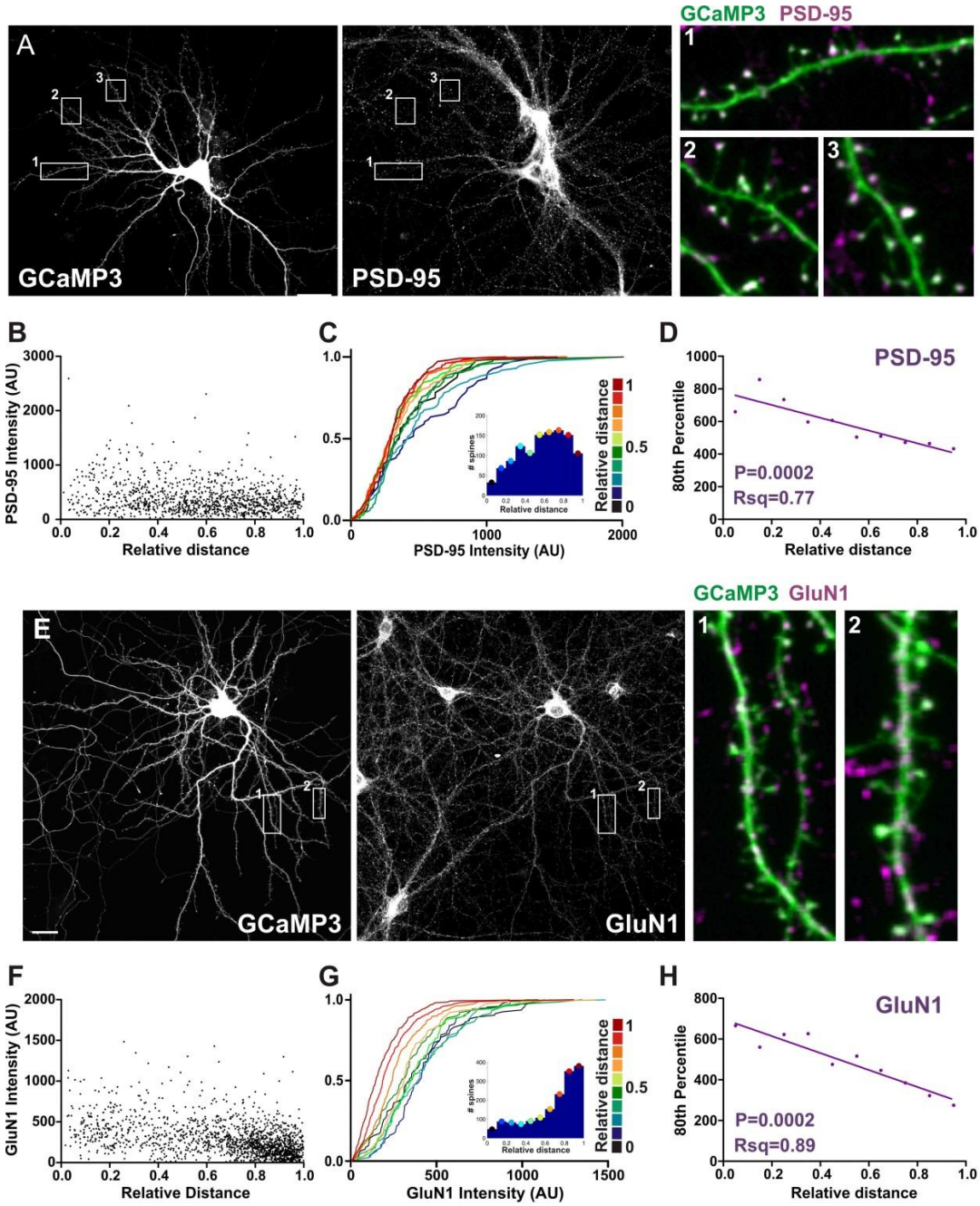

Figure 4.2.16 PSD-95 and GluN1 inversely scale with relative distance. (A) An example of a GCaMP3 expressing hippocampal neuron stained for PSD-95. White boxes correspond to the areas shown in the zoomed regions to the right, numbered appropriately. Scale bar = 10 µm. **(B)** PSD-95 intensity for each spine as a function of relative distance (n= 1143 spines from 2 cells). **(C)** Cumulative frequency distributions for PSD-95 intensity for each spine (shown in **(B)**). Each plot is colour-matched to a different bin for relative distance shown in the key to the right. Inset histograms show the number of spines within each relative distance bin. **(D)** Plot of the 80th percentile values for PSD-95 intensity obtained from the cumulative plots as a function of relative distance. Spearman's co-efficient; P- and R-squared values are shown on the plot. **(E)** An example of a GCaMP3 expressing hippocampal neuron stained for GluN1. White boxes correspond to the areas shown in the zoomed regions to the right, numbered accordingly. Scale bar = 10 µm. **(F)** GluN1 intensity for each spine over the relative distance (n= 1604 spines from 2 cells). **(G)** Cumulative frequencies for GluN1 intensity for each spine (shown in **(F)**). Each plot is colour-matched to a different bin for relative distance shown in the key to the right. Inset histograms show the number of spines within each relative distance bin. **(H)** Plot of the 80th percentile values for GluN1 intensity obtained from the cumulative plots as a function of relative distance Spearman's co-efficient; P- and R-squared values are shown on the plot.

mean amplitude of calcium between spines. Although two of the spines highlighted here (Spine 1 and 3) are both located close to branch tips and so have similar relative distances, the calcium transients recorded at these two spines are very different in amplitude. There is no correlation when the mean amplitude of calcium transients from all spines are plotted against relative distance, neither as a group of three cells, nor within individual cells (Figure 4.2.17 C). Although the immediate conclusion from this experiment is to assume that distance-dependent increases in postsynaptic calcium events are presynaptic in origin, the low number of uncaging events in this experimental set may not be sufficient to properly establish this. Future work is needed to rule out that relative distance-dependent changes in presynaptic properties may lead to scaling in calcium transient amplitude.

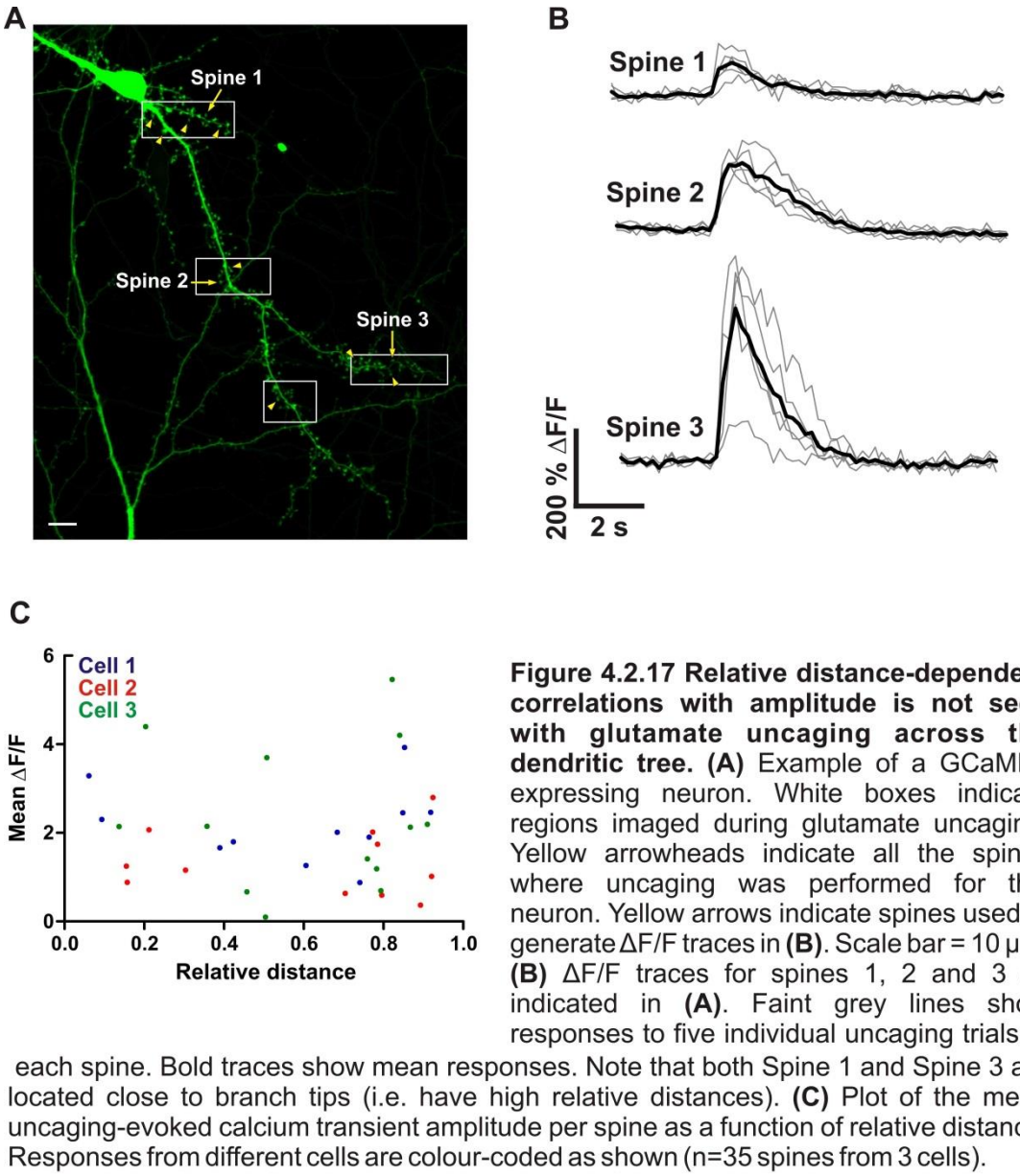

Figure 4.2.17 Relative distance-dependent correlations with amplitude is not seen with glutamate uncaging across the dendritic tree. (A) Example of a GCaMP3 expressing neuron. White boxes indicate regions imaged during glutamate uncaging. Yellow arrowheads indicate all the spines where uncaging was performed for this neuron. Yellow arrows indicate spines used to generate ΔF/F traces in **(B)**. Scale bar = 10 µm. **(B)** ΔF/F traces for spines 1, 2 and 3 as indicated in **(A)**. Faint grey lines show responses to five individual uncaging trials at each spine. Bold traces show mean responses. Note that both Spine 1 and Spine 3 are located close to branch tips (i.e. have high relative distances). **(C)** Plot of the mean uncaging-evoked calcium transient amplitude per spine as a function of relative distance. Responses from different cells are colour-coded as shown (n=35 spines from 3 cells).

4.3 Discussion

4.3.1 Postsynaptic calcium transients in dendritic spines of cultured hippocampal neurons

In this chapter we record calcium transients using GCaMP3 expressed in dendritic spines of mature dissociated hippocampal neurons. We were able to measure spontaneous postsynaptic responses in the presence of TTX, suggesting they were caused by glutamate released from single presynaptic vesicles. These quantal calcium transients (QCTs) were highly localised to dendritic spines and mediated by NMDA receptors with no contribution or modulation from AMPA receptors, internal stores or R-type VGCCs or SK calcium-activated potassium channels, in agreement with previous findings (Murphy et al., 1995; Mainen et al., 1999; Yuste et al., 1999; Kovalchuk et al., 2000).

4.3.2 Single spine variability in quantal calcium transient amplitude

In our experiments we found that both the amplitude and frequency of QCTs were highly variable. To examine this further we focused on the large variability displayed in QCT amplitude at single synapses. Quantal variability has been studied by measuring AMPA and NMDA receptor currents electrophysiologically at the cell soma or large dendrites. One important drawback of this approach is that the origins of synaptic events are not known. While minimal stimulation of presynaptic fibres or local perfusion of hypertonic solution aims to activate single postsynaptic sites, the possibility that multiple synapses are activated cannot be ruled out. It is perhaps more useful to record function at identified synapses using optical techniques, such as calcium imaging. Previous studies recording NMDA receptor variability via calcium imaging however, have been beset by a number of limitations. Many studies have chosen to employ small fields of view or linescans of single spines which, while increasing temporal resolution, will greatly reduce the sample sizes that can be obtained (Murphy et al., 1995; Conti and Lisman, 2003; Bloodgood and Sabatini, 2007). In addition, many studies used synthetic calcium dyes which can leak out of neurons and accumulate within intracellular organelles reducing signal to noise ratio and thus the sensitivity of recordings (Murphy et al., 1995; Conti and Lisman, 2003; Bloodgood and Sabatini, 2007). Here, the GECI GCaMP3 was used generating robust signals which could be recorded simultaneously at many identifiable postsynaptic sites. Within this large sample (n=1208 spines from 36 cells) we found that individual spines show QCTs that vary widely in amplitude (CV=0.58), which is similar to previous reports of NMDA receptor-mediated variability recorded at single synapses (Conti

and Lisman, 2003; Bloodgood and Sabatini, 2007). As the variability for all events from all synapses has a CV of 0.9 (from 8752 QCTs from 36 cells), we find that intraspine variability accounts for the majority (76%) of total variability. A similar CV value (CV = 0.51) was also observed when performing line-scan imaging at selected synapses, which sacrifices sample size for high temporal resolution. This demonstrates that the above results are not due to possible filtering problems as a consequence of slow acquisition rates.

The origin of high CV values could be either presynaptic, postsynaptic or both. Dissecting out which compartment is responsible requires selective stimulation and read-out of each compartment without influence of the other. We achieved this by bypassing the presynaptic bouton and generating postsynaptic calcium transients elicited by uncaging glutamate at individual spines. Repetitive uncaging resulted in highly variable responses (CV = 0.5), similar in magnitude to that observed for spontaneous events. This result rules out a presynaptic origin and instead suggests that the high degree of variability in calcium transients observed here is mainly postsynaptic. This is in contrast with a study which, by releasing fixed concentrations of glutamate via ionophoresis, showed a large decrease in NMDA receptor mediated currents measured at the cell soma with a drop in CV from ~0.65 to ~0.1 (McAllister and Stevens, 2000). In addition, the amplitudes of AMPA and NMDA receptor currents are highly correlated which suggests that AMPA and NMDA receptors share the same source of variability. For AMPA receptors the current evidence, while by no mean coherent, suggests a presynaptic origin, caused by either variability in vesicle diameter or multiquantal release (Bekkers et al., 1990; Frerking et al., 1995; Conti and Lisman, 2003; Wu et al., 2007). However, AMPA receptors will behave differently to NMDA receptors. For instance, NMDA receptors have a far higher affinity (~500 fold) for glutamate than AMPA receptors and are therefore less likely to be influenced by small changes in glutamate concentration at the synaptic cleft (Murnick et al., 2002). This means the underlying origin of variability may be different for NMDA and AMPA receptors, with our above result suggesting a postsynaptic mechanism. Possible postsynaptic sources for variability include (1) receptor saturation, (2) channel noise (3) variable contributions to QCTs from other possible postsynaptic calcium sources and also (4) receptor desensitisation.

While not investigated directly here, it has been shown that quantal glutamate concentrations are unlikely to saturate the NMDA receptor response as mEPSCs larger than those engendered by quantal release are recorded in response to local glutamate perfusions (Mainen et al., 1999; McAllister and Stevens, 2000). Our approach unfortunately does not give us the resolution to address channel noise. By adopting a pharmacological approach we could assess the recruitment of other sources of spine calcium entry such as AMPA receptors, R-type VGCCs, SK calcium-activated potassium channels and internal stores in contributing to quantal variability.

Adopting a pharmacological approach we determined that none of these sources play a role in QCT variability (Figure 4.2.9).

In order to determine if NMDA receptors were desensitised during quantal release we examined the relationship between QCT amplitude with inter-QCT interval. A strong inverse correlation was found suggesting that some form of short term plasticity occurs to depress responses when QCT frequency is high. This may arise from receptor desensitisation, a mechanism which has been suggested to underlie some forms of short-term depression (Fioravante and Regehr, 2011). Thus, the frequency of QCTs may determine a proportion of the observed variability in QCT amplitude. However, it is clear from the raw data (Figure 4.2.10 A(i)) that at low instantaneous frequencies, where receptors are unlikely to be desensitised, there is the potential for a far wider range of amplitudes than at higher frequency. This is supported by uncaging data, where glutamate is uncaged at a low frequency (0.07 Hz) yet a high CV of 0.5 is recorded. Thus, the question remains what is the source of quantal variability at low frequencies.

In summary, uncaging experiments shown in this chapter suggest that QCT variability is postsynaptic. This finding is not in agreement with other studies where focal glutamate ionophoresis was repeated at single spines (McAllister and Stevens, 2000). The reason for this discrepancy is not known but may be linked to differences in recording techniques. For the ionophoresis experiment, variability was calculated from the slow NMDA component of mEPSCs recorded at the cell body, thus their results rely on the reliability of separating the fast AMPA and slow NMDA receptor components. Here, NMDA receptor calcium transients were recorded directly at the synapse. While our glutamate uncaging result suggests a postsynaptic origin for variability with some contribution from NMDA receptor desensitisation, we are yet to elucidate the postsynaptic mechanism responsible. One possible explanation that hasn't yet been tested is that variability is governed by rapid changes in spine morphology which can affect the compartmentalisation of calcium within the spine head (see Future work, section 4.3.7).

4.3.3 Relative distance-dependent correlations along dendritic branches

By recording QCTs from entire dendritic trees we have been able to describe the spatial distribution of excitatory drive onto single hippocampal neurons. Three metrics were used to define the dendritic tree location of individual synapses; relative distance, absolute distance from the soma and number of nodes. Each metric was chosen as they read out different facets

of the dendritic morphology. Relative distance takes into account both distance from the cell body and distance to the branch tip, and as such tells us about synapse position within a branch, and incidentally about branch diameter (see below). The absolute distance is the distance of the synapse to the cell body and is the most widely used metric to describe synapse position along dendritic morphology. This metric is also important to determine how processes occurring at the cell body influence individual synapses. The final metric used was the number of nodes. This metric was chosen to determine if synapses read out the drop in branch diameter as occurs when dendrites bifurcate at branch points.

Interestingly, we found that larger QCTs, both in terms of amplitude and integral, were more likely to be found at higher relative distances i.e. closer to branch tips. While the integral is also positively correlated with distance from the cell soma, this finding is less robust. Interestingly, instantaneous frequency is negatively correlated with relative distance meaning high frequency spines are found closer to the cell body. This is in agreement with the finding that amplitude and instantaneous frequency are negatively correlated (Figure 4.2.10 and 4.2.13 D). Thus, we find that QCTs are not randomly distributed across the dendritic tree but show a form of distance-dependent scaling.

To further understand how synapses are distributed along dendritic trees we also examined the size or volume of spines, measured indirectly from the fluorescence intensity of an activity invariant genetic fluorophore, TagRFP. Using this measure we found that spines appeared to decrease in size as they approached a branch tip. This was in agreement with previous findings showing a gradual decrease in spine volume along oblique branches of CA1 neurons in the hippocampus (Katz et al., 2009). In addition, we also performed staining for two postsynaptic proteins: the scaffolding protein PSD-95 and the GluN1 subunit of NMDA receptors. PSD-95 immuno-intensity is highly related to AMPA receptor number (El-Husseini et al., 2000; Elias et al., 2006) and GluN1 immuno-intensity reports the number of NMDA receptors as this subunit is crucial to NMDA receptor assembly (Bloodgood and Sabatini, 2009). Here too, we find a strong inverse correlation of staining with relative distance, indicating smaller and weaker synapses are found along dendrites towards branch tips. Again, this agrees well with previous reports, where the volume of postsynaptic spines was shown to correlate well with the number of both AMPA receptors and NMDA receptors (Nusser et al., 1998; Mackenzie et al., 1999; Matsuzaki et al., 2001). In addition postsynaptic and presynaptic strength are also well known to correlate (Harris and Stevens, 1989; Schikorski and Stevens, 1997; Kay et al., 2011b; Holderith et al., 2012) . In agreement with our results, it has been found that the immunostaining of determinants of presynaptic strength, including VGlut, Bassoon, VAMP2, Synapsin, vGAT, Syntaxin, Munc18 and Syt, were more intense proximal to the cell soma (de

Jong et al., 2012). In addition, it was shown that larger readily-releasable pool sizes were found in more proximal compared to distal dendrites in dissociated hippocampal neurons (de Jong et al., 2012). These findings suggest that both the pre and postsynaptic elements which relate to synaptic strength are matched and that both pre and postsynaptic strength are inversely correlated with dendritic distance. Together, these fit a model where smaller spines have fewer glutamate receptors and are more likely to be found towards the tip of dendritic branches.

Yet the question remains how does this inverse correlation of spine size/volume and synaptic strength with relative distance fit with our findings that QCT amplitude is positively correlated with relative distance? Again, previous findings are crucial to interpreting our data. There is now much evidence showing that the amplitude of synaptic calcium transients elicited by the activation of NMDA receptors are inversely correlated to spine volume (Nusser et al., 1998; Noguchi et al., 2005, 2011). In other words, larger spines have smaller synaptic calcium events. Although somewhat paradoxical, the reason for this inverse correlation lies in another structural feature of spines; that small spines have narrower and longer spine necks than larger spines (Noguchi et al., 2005). As a result, large spines, although they have more NMDA receptors, allow calcium ions to leak out into the dendritic shaft resulting in a smaller calcium concentration at the spine head compared to smaller spines. The latter have necks with high resistance that can better compartmentalise calcium ions, maintaining high concentrations within a small spine head volume.

The above discussion outlines a scenario where spine size/volume decreases along branches towards branch tips but the compartmentalisation of calcium by the decreasing spine neck diameter of smaller spines increases the amplitude of calcium transients with relative distance (Figure 4.3.1). This describes a postsynaptic origin for observed increased in calcium transients with distance. To test this glutamate uncaging was performed when the same concentration of glutamate was released at different spines across the dendritic tree. If calcium transient amplitude is a postsynaptic effect we should observe a relative distance-dependent correlation. However, this was not the case. The reliability of this result is limited by a low sample size (35 spines) due to the low throughput approach of recording at single spines, therefore simply uncaging at many more spines may yet provide confirmation of our hypothesis.

In summary, relative distance-dependent increases in QCT amplitude seen in this chapter may be a consequence of the biophysical properties of small volume dendritic spines. Yet the questions ‘how does this scaling-arise?’ and ‘what it is for?’ remain.

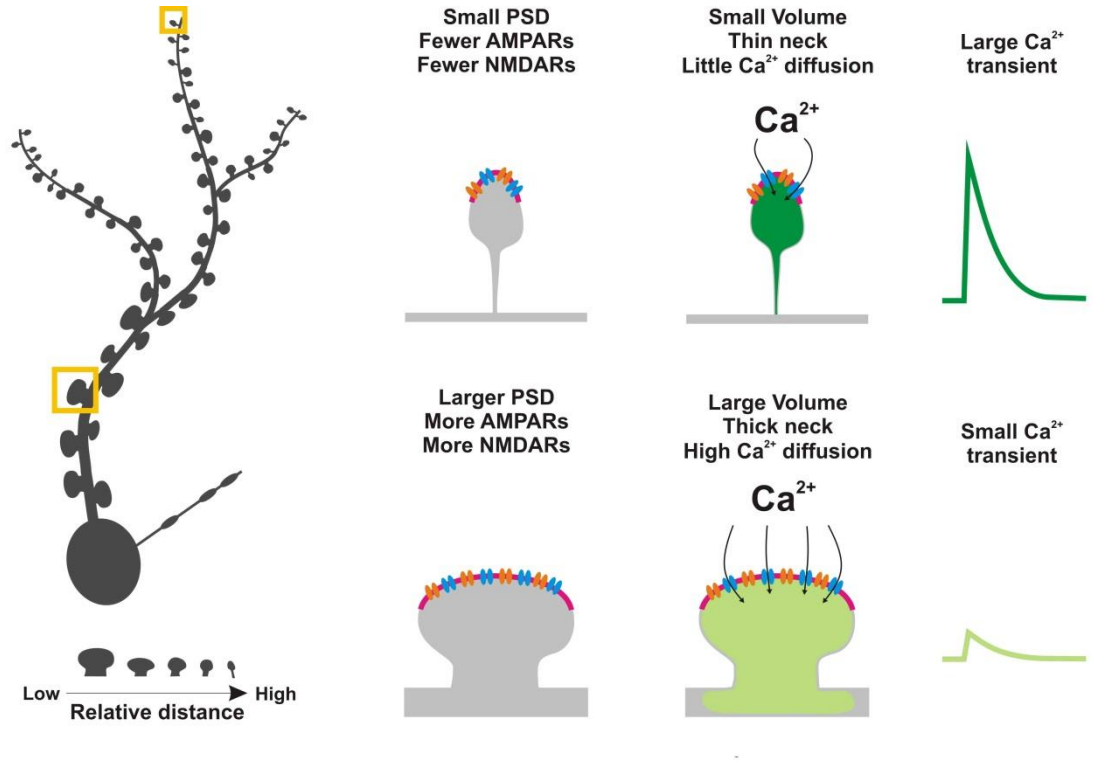

Figure 4.3.1 Putative mechanism for spines at high relative distance having larger calcium transients. Spine size along dendrites decreases towards branch tips. The smaller distal spines have thinner and longer spine necks than the larger proximal spines. Small spines have smaller postsynaptic densities (PSDs) and fewer AMPA and NMDA receptors. However, calcium influx is highly compartmentalised due to the restrictive spine neck leading to larger calcium transients. Conversely, large spines have larger PSDs and more AMPA and NMDA receptors. Calcium influx is not well compartmentalised with calcium leaking out into the dendrites leading to a smaller spine calcium transients.

4.3.4 Putative mechanisms to assemble distance-dependent scaling

We can imagine that distance-dependent scaling may be a product of either cell-wide or local signals which would endow positional information to each spine. An example of a cell-wide signal is the bpAP. This wave of depolarisation that initiates at the axon initial segment propagates antidromically into the dendritic tree, and attenuates with increasing absolute distance from the site of initiation. Therefore the size of the bpAP acts as a marker of dendritic location which could specify individual spines with a positional identity. However, the distance-dependent correlation with QCT amplitude described here is most robust for *relative* distance, not *absolute* distance from the soma, which is a metric not well reported by bpAPs. The relative distance metric describes the location of individual spines within branches implying that our correlation is reliant on local information signalling within branch location. This kind of

information could be obtained from the structure of individual branches, which are characterised by a tapering in their diameter as they approach a tip end. One functional consequence of this tapering is a gradual increase in impedance as the branch, thins which can act locally to alter dendritic environment along a branch. How spines sample this environment, and the local signal that is transduced is difficult know, although a feedback mechanism involving local synaptic responses governed by the local impedance of the dendrite could be possible.

Most neuronal cell types will have dendrites which taper to a sealed end, and they will have this morphology from initial dendritic specification. Therefore, if distance dependent scaling of spine volume and concurrent information is set up by consequence of dendrite morphology we would hypothesise that distance-dependent scaling should be detected independent of cell-type specific dendritic shapes and developmental stage. If distance-dependent scaling is not seen this may suggest a more cell-wide signal. The contribution of activity can be assessed by simply blocking AP firing using TTX during spine development, but specifically isolating bpAPs is more difficult. This could be achieved by overexpressing potassium channels genetically restricted to the somatodendritic compartment through fusion with Myosin Va, for example (Lewis et al., 2009).

What does relative distance-dependent scaling mean for a cell? We can think of the large calcium transients recorded here as simply a read out of small spine volume, therefore scaling may be related to the other effects of being a small spine, such as having fewer AMPA and NMDA receptors. As summarised above, smaller spines are found closer to branch tips where dendritic branches are thinner and have higher input impedances which can amplify voltage signals in the dendrite. It has been suggested that if spines had equal volumes along a branch, and therefore equal numbers of AMPA and NMDA receptors, then the initiation of dendritic spikes would be biased towards the activation of distal synapses where high input impedance will amplify signals, rendering more proximal synapses redundant and reducing the efficiency of information transfer (Katz et al., 2009). Therefore, decreasing spine volume and synapse strength distally may act to normalise the contribution of all spines to the generation of a branch output.

The functional role in this distance dependent correlation may be directly related to a requirement for higher calcium concentrations distally. Certainly calcium is involved in the initiation of many biochemical cascades, and its role in the induction of synaptic plasticity has been particularly well studied. Therefore, there is a possibility that increased calcium influx at distal synapses might exist because distal synapses are simply more plastic. The reason why they would need to be more plastic is not known. In the hippocampus different areas of the

dendritic tree receive different afferent inputs. The dendrites of the SR receive Schaffer collateral (SC) input from CA3 neurons, dendrites of the SLM receive perforant path (PP) innervation from the entorhinal cortex, while the basal dendrites receive SC and PP as well as CA1 collateral input. Therefore, we can speculate that these different innervations may have different plasticity requirements.

4.3.5 Rundown in QCT amplitude may represent a biological process

In this chapter we find that in control conditions, over a ten minute period, both the amplitude and frequency of QCTs decrease (Figure 4.2.2). We do not know why this occurs. We can speculate that GCaMP3 may suffer from photoinstability, as has been demonstrated for other GECIs (Akerboom et al., 2013a; Walker et al., 2013). Photoinstability should be diminished when using laser scanning confocal microscopy where the excitation dwell time for each pixel is dramatically decreased. However, this was not the case, suggesting that rundown in QCT amplitude and frequency over time could reflect a biological process. The NMDA receptor Mg^{2+} block, while largely stochastic at resting membrane potentials (Jahr and Stevens, 1990), will act as a gate to decrease NMDA receptor activation. Here, in zero Mg^{2+} conditions NMDA receptors are directly activated by glutamate release, triggering calcium influx into the spine. It is possible that this calcium influx, known under various stimulation conditions to exert plastic effects, may activate mechanisms local to the spine to decrease QCT amplitude and frequency. This theory can be tested in the future by observing whether spines which exhibit higher amounts of calcium influx also show a greater rundown in response amplitude over time.

4.3.6 ΔF/F is a suitable metric for recording QCTs

During this project we wanted to confirm that the ΔF/F metric is suitable for measurement of QCTs. Normalising signals by baseline is necessary because basal GCaMP3 concentrations were highly variable between different spines. The concern was that our baseline levels of GCaMP3 fluorescence may represent more than just the number of GCaMP3 molecules present, and may instead relate to cell wide differences in resting intracellular calcium concentrations. To explore this, TagRFP, a red protein fluorophore, was co-transfected into cells. This intensity of this fluorophore is not affected by intracellular calcium concentrations but is instead related to the number of molecules present, and thus the size of the compartment. Here we found that baseline GCaMP3 levels, used to normalise ΔF signals, were highly correlated for TagRFP intensities recorded at the same spines. This indicates that the ΔF/F metric is a suitable

measure for recording QCTs. In addition, on analysing QCTs from TagRFP and GCaMP3 co-expressing neurons we used TagRFP intensity to normalise signals and generated the ΔG/R metric. We found that using the ΔG/R metric the correlation between amplitude and relative distance was preserved. This relationship is perhaps less clear than that produced using ΔF/F metric on a separate set of neurons. This is likely due to the fact that the number of QCTs recorded with ΔG/R are only ~10% of the number recorded using ΔF/F (12534 versus 1308 QCTs). While this data confirms that the ΔF/F metric is reasonable, further experiments will be conducted in neurons co-expressing TagRFP as this represents a more reliable metric.

4.3.7 Future work

The experiments outlined in this chapter have demonstrated that QCT variability likely originates from a postsynaptic source, but this source has yet to be elucidated. One avenue not yet tested is variability spine neck diameter. As discussed above, the magnitude of calcium transients in dendritic spines is highly dependent on spine neck diameter (Noguchi et al., 2005). Furthermore it has been shown that spine volume and neck diameter can be altered in a calcium dependent manner during LTP (Noguchi et al., 2005). Rapid reversible changes in the spine neck diameter therefore could produce variability in QCT amplitude. The spine cytoskeleton is actin rich and does not contain microtubules, thus changes in spine neck diameter might be rapidly regulated by actin polymerisation (Honkura et al., 2008). To test whether dynamic regulation of spine morphology the stabilisation of actin filaments *in vitro to* prevent actin polymerisation can be achieved by perfusion with the cell-permeant drug 'Jasplakinolide'. If spine neck variability underlies QCT amplitude variability under these conditions we would expect to see a decrease in the CV.

Our interpretation of the results in this Chapter on the distance-dependence of QCT amplitude proposes a mechanism whereby increasing calcium transient amplitude towards branch tips reflects the decreasing size of spines and spine neck diameters at more distal sites. We have made this conclusion based on the literature (Katz et al., 2009; de Jong et al., 2012) in addition to the finding that TagRFP intensity as well as PSD-95 and GluN1 immuno-intensity decrease with relative distance. While our experimental findings support our hypothesis they do not give a direct measure for spine size or spine neck diameter. This could be achieved by using serial section electron microscopy on cultured neurons to gain exact measures of spine neck size and volumes along dendritic branches.

5 Chapter 5: The structural and functional development of direction- and orientation-selectivity in the larval zebrafish *in vivo*

5.1 Introduction

The components of the visual system and their development is fairly well characterised in the zebrafish. However, the field is lacking a detailed description of the functional development of many cell classes. Recently, focus has been placed on elucidating the circuitry underlying orientation- and direction-selectivity in the larval zebrafish. An understanding of how different functional cell types become wired into the visual circuitry can give essential insight into the connectivity of orientation- and direction-selective cells.

A recent study, study by Lowe et al., (2013), used a transgenic larval zebrafish, where SyGCaMP3 was expressed in the entire population of RGCs. The action potential output of these RGCs was recorded in their axons in the optic tectum. Populations of OS and DS RGCs were recorded at different timepoints during the development of the zebrafish visual system. This study found that anterior, dorsocaudal and ventrocaudal preferring classes of DS RGCs are present from the earliest time point imaged (3 dpf) and were spatial clustered by functional class within the superior SFGS of the tectal neuropil (Figure 5.1). The DS RGC inputs were invariant in terms of both functional properties and lamination zones in the tectal neuropil from 3 to 10 dpf. This pattern is suggestive of circuit hard-wiring during development. Conversely, OS inputs were much more dynamic over development (Figure 5.1). At 3 dpf only the population preferring motion along the vertical axis are recorded which occupy a broad region across the laminar axis of SFGS at the posterior tectal pole. At 7 dpf all four populations of OS RGCs are present; horizontal, vertical and two populations flanking the vertical group (29˚ and 140˚). These populations show lamination preferentially in the central laminae of SFGS but are also diffusely distributed, especially the vertical and 29˚ populations, across the entire laminar axis of the SGSF. The horizontal and 140˚ populations are broadly invariant both in terms of angle centre and lamination zone between 7 and 10 dpf. However, there is a shift angle centre of around 9˚ for both the vertical and 29˚ population. Most striking is the spatial refinement of terminations of the vertical population from broadly spanning the SFGS to a bilaminar distribution. One lamination remains in the central lamina of SGSF, where these inputs are already concentrated at 7 dpf, but the second lamina in the deep border of SFGS is specified later between 7 and 10 dpf (Lowe et al., 2013).

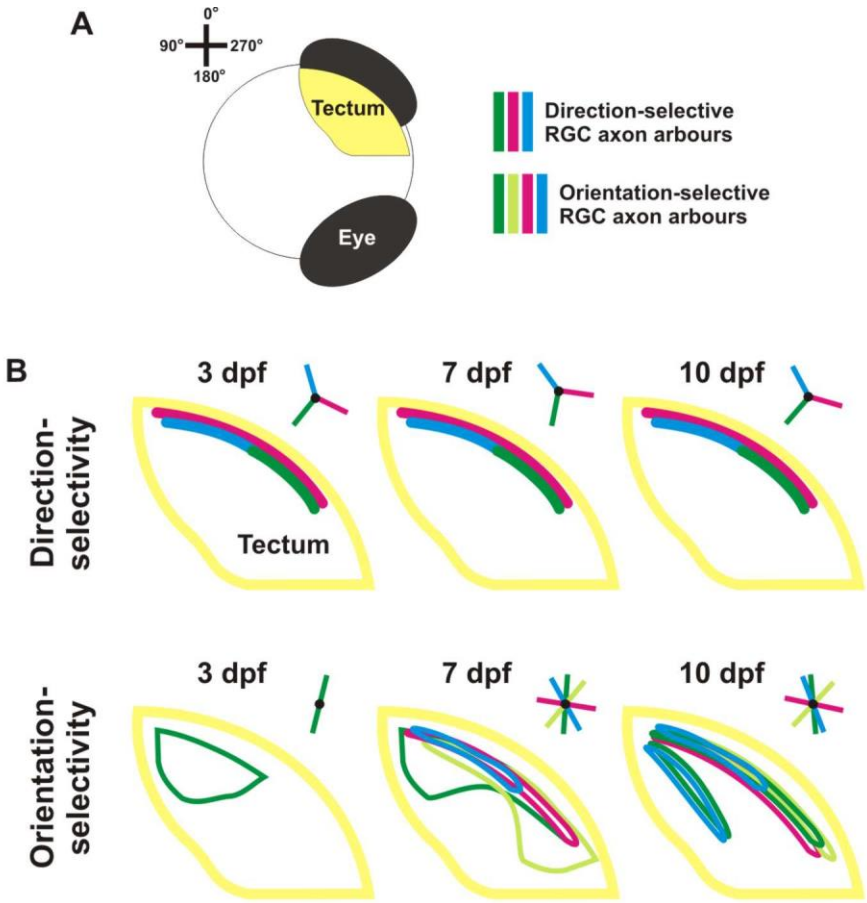

Figure 5.1 The development of direciton- and orientation-selective RGC axon termination zones within the tectal neuropil. (A) A schematic of the larval zebrafish brain. Cross-hairs show the directions of moving bars in relation to the orientation of the zebrafish. Coloured bars represent the different classes of direction- and orientation-selective RGC axon arbours, as used in **(B)**. **(B)** Schematics outlining the laminations zones of direction- and orientation-selective RGC axons in the tectal neuropil at 3, 7, and 10 days post fertilisation (dpf). The preferred angles of each class are summarised in colour-matched pin-wheels top right of each schmatic. Note **(1)** that functional classes tend to cluster in space and **(2)** that all classes direction-selective RGCs are present at 3 dpf and arbour positions are invariant over development while orientation selective classes of RGCs are not all present at 3 dpf and lamination zones are dynamic over development. Data from Lowe *et al*., (2013).

The aim of this chapter was to assess the functional development of single RGCs and tectal cells. Using calcium indicators to read out orientation- and direction-selectivity we could follow individual identified neurons over a period of several days. Imaging the directional tuning of individual RGC axons or tectal cells in the accessible tectum was non-invasive and allowed us to also follow the structural development of cellular processes. This technique was used to address specific questions linked to the developmental RGC population study outlined above (Lowe et al., 2013). Are the structural and functional properties of single direction-selective RGCs invariant over development? While the above study indicates this is the case, population

studies cannot rule out the possibility that DS RGC axons imaged at each time point are from different cells (Lowe et al., 2013). The population study finds that OS RGCs are developmentally dynamic in terms of termination zones. By recording the structural and functional development of single RGCs we ask if changes in termination zones are a consequence of; (a) structurally invariant arbours refining their functional properties, (b) remodelling of axon arbours to alter laminar positioning, or (c) both simultaneously. In addition, the population study showed that non-vertical OS RGC populations emerge later in development. We ask whether this is a consequence of; (a) delayed RGC invasion of the tectum, or (b) a gain of orientation-selectivity for RGCs already present in the tectum. Finally, the functional development of orientation- and direction-selective tectal cells is yet to be determined. One aim of this chapter was to investigate how the orientation-selectivity of individual tectal cells are affected by the integration of potentially noisy RGC inputs during development.

5.2 Results

The aim of the experiments detailed in this chapter was to examine how individual direction- and orientation- selective neurons of the retinotectal system of the larval zebrafish develop. Experiments conducted within the laboratory have previously characterised the classes of direction- and orientation-selective (DS and OS respectively) RGCs present in the larval zebrafish at 7 days post fertilisation (dpf; Nikolaou et al., 2012). This study used a population-based approach where functional responses from the entire population of RGC axon arbours, expressing SyGCaMP3 and terminating in the optic tectum, were measured in response to drifting bar visual stimulation. It was discovered that functionally similar classes of RGC axon arbours clustered within specific laminas of the tectal neuropil. DS RGCs clustered in the superficial layers of SFGS whereas OS inputs laminated in the deeper SFGS (Nikolaou et al., 2012; Lowe et al., 2013).

By performing similar imaging experiments at 3, 7 and 10 dpf a follow up study described how the functional properties and spatial organisation of DS and OS RGC inputs to the tectum develop (Lowe et al., 2013). It was found that DS inputs are invariant in terms of tuning properties and spatial organisation at these time points. At 3 dpf only one of the four classes of OS RGCs found in the 10 dpf larvae are present in the tectum. OS RGC development is therefore characterised by the late emergence of three OS classes, although once present, the tuning curves of all four OS classes remain relatively invariant. In addition, during development refinement is observed in the termination zones of OS RGC axon arbours. Population studies cannot identify and record from the same cells over time. Therefore, the possibility cannot be ruled out that populations of DS and OS RGCs at different stages are made up from different individual RGCs, which are themselves functionally dynamic over these stages. In addition, it is not possible using a population approach to understand the functional characteristics of individual RGCs prior to their emergence as OS cells.

5.2.1 The functional development of single SyGCaMP3-expressing RGCs in response to moving bar stimuli

To address these questions we adopted an approach in which single RGCs were labelled with SyGCaMP3. This allowed longitudinal analysis of RGC axon arbour structure and function. Sparse patches of punctate SyGCaMP3 expression were found within the tectal neuropil indicating the labelling of presynaptic boutons belonging to an RGC (Figure 5.2.1 A(i)). Weak

SyGCaMP3 expression was observed in inter-bouton regions which, when digitally amplified post-hoc, permitted tracing of the structure of RGC axon arbours (Figure 5.2.1 A(ii)). The functional properties of these single RGCs were assessed at single optical planes (Figure 5.2.1 A(iii)) using the same approaches that were used to analyse populations of RGCs(Nikolaou et al., 2012; Lowe et al., 2013). Confocal imaging was used to record changes in SyGCaMP3 fluorescence in response to visual stimulation presented to the contralateral eye. The visual stimulus consisted of dark bars drifting in 12 different directions across the visual field of the larval zebrafish. Drifting bar stimulation has previously been used to characterise direction- and orientation-selectivity in the zebrafish visual system (Gabriel et al., 2012; Grama and Engert, 2012; Nikolaou et al., 2012; Hunter et al., 2013), and here, induced robust responses in single RGC axon arbours (Figure 5.2.1 B). In some cases the magnitude of the SyGCaMP3 response differed according to direction, i.e. some directions were preferred over others (Figure 5.2.1 B-C). All presynaptic boutons belonging to a single arbour shared the same profile of response to the moving bars (Figure 5.2.1 C). We analysed the functional properties of single RGCs using voxel-wise analysis, consistent with the RGC population studies previously published (Nikolaou et al., 2012; Lowe et al., 2013). This approach gave a functional readout without morphological bias, and thus based on the functional properties of voxels we could identify if more than one cell was labelled. Profiles of responses across voxels belonging to the same cell were generally homogeneous (polar plots; Figure 5.2.1 D). However, variability was found in orientation selectivity index (OSI) values calculated from voxels belonging to the same cell, demonstrating how sensitive this measure is to small fluctuations in signal (Figure 5.2.1 D).

To examine the functional development of single RGCs, responses to drifting bar stimuli were recorded from single SyGCaMP3 expressing RGCs at three time points during their maturation; 3, 5 and 7 dpf. At 3 dpf RGC axons are arriving in the tectal territory and beginning to innervate the tectum, and in the retina RGCs have immature dendrites that are beginning to laminate in the IPL (Stuermer, 1988; Mumm et al., 2006). At 7 dpf the zebrafish retinotectal system is relatively mature, and the arbour size and the number of presynaptic sites of RGC axons have plateaued (Meyer and Smith, 2006). In addition, the larvae are able to carry out complex visually-guided behaviours such as prey capture (Bilotta, 2000; Gahtan et al., 2005). 5 dpf represents an intermediate time point in the maturation of the larval visual system.

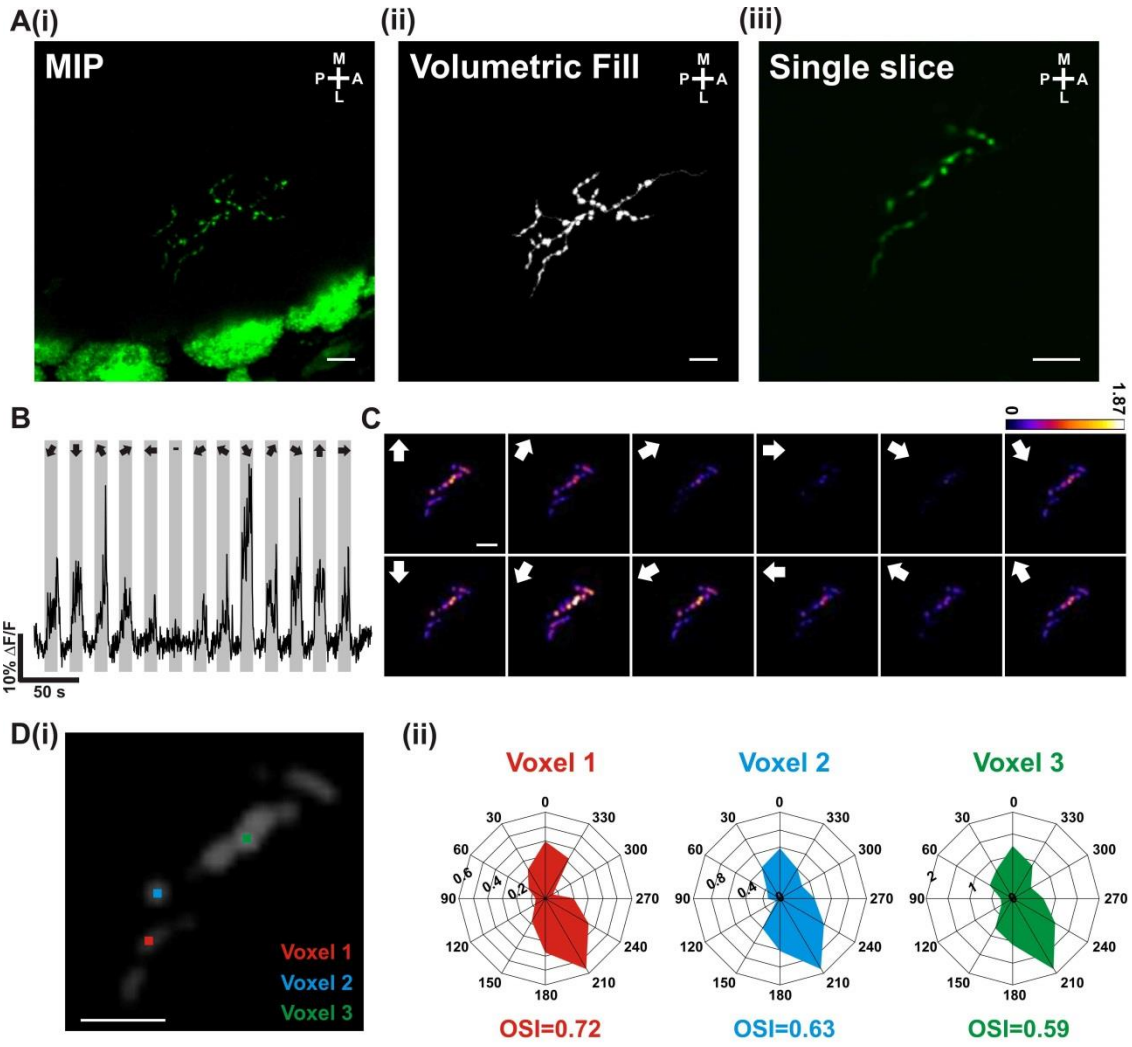

Figure 5.2.1 Analysing the functional and structural properties of single RGC axon arbours in the larval zebrafish. (A) A single RGC axon arbour in the tectal neuropil of a 7dpf larval zebrafish expressing SyGCaMP3. **(i)** A maximum intensity projection (MIP). Note the punctate expression pattern. **(ii)** A volumetric fill shows the structure of the arbour. **(iii)** A typical single slice used in functional imaging. Image orientation is shown top right (L, lateral; M, medial; A, anterior and P, posterior). **(B)** Mean ΔF/F trace from an ROI encompassing all responding voxels during a tuning experiment for the cell shown in **(A)**. Stimulus epochs are shown as grey blocks with the direction of motion indicated by arrows (the dash indicates the 'blank' epoch when only a mean grey screen was shown). **(C)** A montage of summary integral ΔF/F response images to bars drifting in 12 different directions. The direction of motion is indicated by the arrows in the top left of each panel. Voxels are colour-coded according to integral ΔF/F (scale top right). **(D)** Functional properties can be assessed for each voxel within a timeseries. **(i)** Three typical voxels are highlighted. **(ii)** Colour-coded polar plots generated from the integral ΔF/F response to each of 12 directions of moving bar for the single voxels indicated in **(i)**. The orientation selective index (OSI) value is shown for each voxel below the polar plot. All scale bars = 10 µm.

5.2.1.1 Developmental refinement of single orientation-selective RGCs

The developmental study of the population of RGCs targeting the tectum demonstrated that at 3 dpf only vertically-tuned OS RGCs are present in the tectum (Lowe et al., 2013). Vertical OS RGCs span the superficial to deep layers of the SFGS at 3 dpf, targeting only the anterior tectal pole. Over development this lamination pattern alters and at 10 dpf vertical OS cells span the laminar axis of the tectum within two discrete laminae. Between 3 and 7 dpf three other OS RGC populations emerge in the tectal neuropil. These non-vertical OS RGC classes tend to be more restricted to their mature lamination zones during development (Lowe et al., 2013). This dynamic picture of OS RGC development may be underpinned by changes in the behaviour of single RGCs. In particular, changes in termination zones may occur through (1) structurally invariant arbours refining their functional properties, (2) OS axon arbours remodelling to change their relative positioning within the tectum or (3) both may occur simultaneously. In addition, the emergence of OS functional classes later in development may be due to the late arrival of these axons to the tectum, or as above, a refinement in functional properties. Below three example RGCs are described which outline developmental profiles for orientation-selectivity.

Example RGC 1 (Figure 5.2.2). As the larvae grew from 3 to 7 dpf, the RGC axon arbour labelled here also elaborated, from a very simple to a more complex structure, containing many presynaptic boutons (Figure 5.2.2 A). While this arbour grew along the anteroposterior and mediolateral axes, the orthogonal view of the arbour at all stages showed a planar morphology (Figure 5.2.2 B), characteristic of RGC arbours (Xiao and Baier, 2007). At the earliest stage (3 dpf) when RGC axon arbours are first invading the tectal territory, we found that this cell responded with a transient response at light onset but not offset during full field flash stimulation, but did not respond to the drifting bar stimulus (Figure 5.2.2 C(i) and D(i)). Two days later in development it was found that this RGC retained responsivity to the onset of full field flash stimulation but interestingly also showed robust responses to drifting bar stimuli (Figure 5.2.2 C(ii) and D(ii)) which were also observed at 7 dpf (Figure 5.2.2 C(iii)).

A quantitative description of responses to the drifting bar stimuli demonstrated a striking refinement in response properties between 5 and 7 dpf. The OSI was used to define the response properties of each voxel. A stringent threshold of >0.5 OSI was applied to indicate orientation-selectivity. Small noisy fluctuations in the size of responses for each direction resulted in voxels from the same cell showing slightly different functional quantifications (see Figure 5.2.1 D polar plots and OSI values). At 5 dpf this cell was not classed as OS (mean OSI 0.34), but two days later in development at 7 dpf it was classed as OS (mean OSI 0.66).

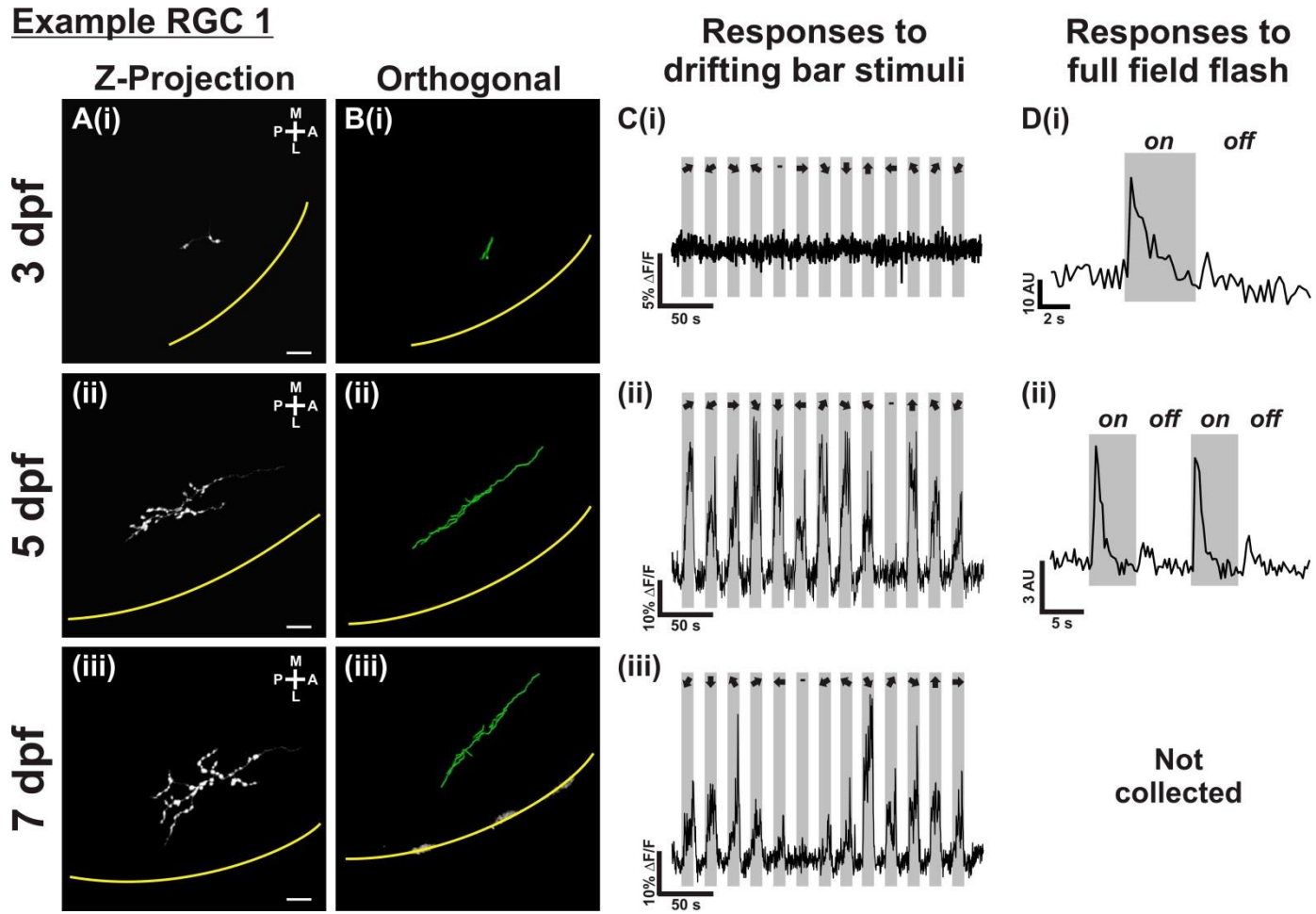

Figure 5.2.2 Example RGC 1: Qualitative analysis of structural and functional development. (A) Volumetric fills from tracings of a single RGC axon arbour at 3 dpf **(i)**, 5 dpf **(ii)** and 7 dpf **(iii)**. Image orientation is shown top right (L, lateral; M, medial; A, anterior and P, posterior). Scale bars =10 µm. **(B)** Rotated tracings show the orthogonal view of the RGC axon arbour shown in **(A)** at 3 dpf **(i)**, 5 dpf **(ii)** and 7 dpf **(iii)**. **(C)** Mean ΔF/F trace from an ROI encompassing all responding voxels during a tuning experiment performed at 3 dpf **(i)**, 5 dpf **(ii)** and 7 dpf **(iii)**. Stimulus epochs are shown as grey blocks with the direction of motion indicated by arrows (the dash indicates the 'blank' epoch). **(D)** Raw fluorescence traces from an ROI encompassing all responding voxels during full field flash stimulation at 3 dpf **(i)** and 5 dpf **(ii)**. Periods of light exposure are indicated by grey blocks.

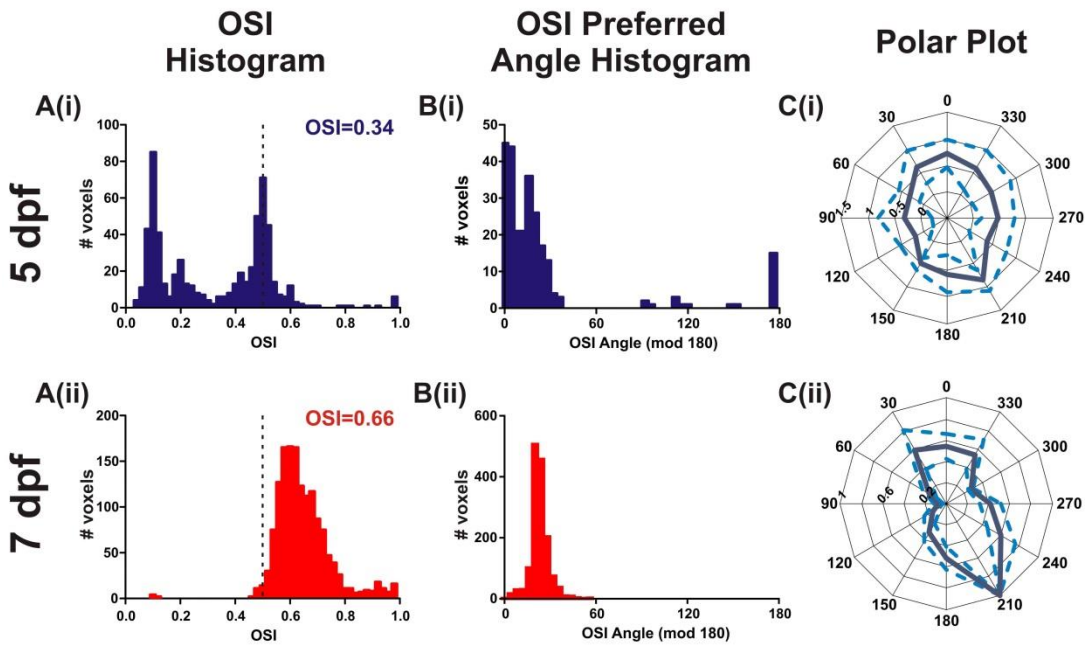

Figure 5.2.3 Example RGC 1: Quantitative analysis of orientation-selectivity at different developmental stages. Quantifications were conducted on data grouped from multiple tuning experiments of a single RGC arbour at both 5 and 7 dpf (n=3 timeseries for each time point). **(A)** Histogram of OSI values of responsive voxels at 5 **(i)** and 7 dpf **(ii)**. Dotted line indicates the 0.5 OSI threshold; values > 0.5 = OS. Mean OSI values are shown top right. **(B)** Histogram of OSI preferred angles of responsive voxels with OSI values greater than 0.5 at 5 **(i)** and 7 dpf **(ii)**. Angles are modulated around 180 degrees. **(C)** Polar plots of response profiles at 5 **(i)** and 7 dpf **(ii)**; navy plots are mean polar plots, light blue dotted plots are mean +/- standard deviation polar.

Unsurprisingly, at 7 dpf this cell showed a classic OS polar plot with large magnitude responses along the 30/210˚ axis, and very small responses orthogonal to the preferred angle (120/300˚). A histogram of the preferred angle of each OS voxel when modulated around 180˚ showed a narrow preference for motion along the vertical axis clustering at ~30˚ (Figure 5.2.3 C(ii)). In contrast, the polar plot at 5 dpf showed a broad response profile. However, responses are not equal to all 12 directions; the majority of voxels >0.5 OSI showed a preference for motion along the vertical axis clustering on the OSI angle histogram from 0-30˚, indicating that this cell may be in the process of refining to orientation-selective. In summary, this example RGC shows a refinement in its functional properties over time. From 3 to 5 dpf we see a 'turning on' in the ability of this cell to respond to drifting bar stimuli. From 5 to 7 dpf we see a refinement in this cell's responses to drifting bars, developing from a broadly tuned cell into a vertically tuned OS RGC.

Refinement in orientation-selectivity of RGCs is supported by two further example RGCs; example RGC 2 (Figure 5.2.4) and example RGC 3 (Figure 5.2.5). As above, for example RGC 2

growth of axon arbours was observed between 3 and 7 dpf in the anteroposterior and mediolateral extent, while remaining planar in the laminar axis throughout development (Figure 5.2.4 A). Functional imaging at 3 dpf produced small, noisy responses to moving bar stimuli which did not fulfil the criteria for required for voxel-wise analysis (Figure 5.2.4 B). A polar plot generated from these responses, however, described this cell as generally non-tuned at 3 dpf (Figure 5.2.4 E(i)). Two days later in development this RGC exhibited robust responses to moving bars, and was classed as highly OS (mean OSI 0.96). Once classified as OS, this cell was invariant, retaining high orientation-selectivity at 7 dpf (mean OSI 0.95). The OSI angle histogram shows a clear preference for motion along the vertical axis, with very similar distributions of preferred angles at both 5 and 7 dpf. The responses of this cell at 5 and 7 dpf were summarised in polar plots, which showed classical orientation-selective tuning, especially at 7 dpf. In summary this cell responds weakly and noisily to moving bars early in development but between 3 and 5 dpf this cell rapidly develops into a highly OS RGC.

We were able to follow the growth of the axon arbour of example RGC 3 from 3 to 7 dpf, and found, common with the two previously described example RGCs, that whilst the arbour extended anteroposteriorly and mediolaterally, it remained planar at all stages (Figure 5.2.5 A). Example RGC 3 was unresponsive to drifting bars at 3 dpf, but did respond to the onset and offset of full field flash stimulation at this stage (Figure 5.2.5 B). Responses to drifting bars were robust at 5 and 7 dpf and showed refinement in orientation-selectivity over time, but the development of this cell was retarded in respect to the other example cells. This cell was broadly tuned at 5 dpf with no single voxel displaying an OSI value greater than 0.5 (mean OSI 0.22; Figure 5.2.4 B(ii)). At 7 dpf, while this cell was not classed as orientation-selective (mean OSI 0.32) we found a shift in OSI values toward orientation selectivity (Figure 5.2.4 B(ii)). The preferred angle at 7 dpf for OS voxels was homogeneous in its tuning to motion along the horizontal axis (~80˚; Figure 5.2.5 D). The responses of this cell at 5 and 7 dpf were summarised in polar plots, which showed a move from highly unselective, broadly tuned functional properties towards orientation-selectivity for motion along the horizontal axis (90/270˚). In summary, this cell 'turns on' in its ability to report drifting bar stimuli from 3 to 5 dpf. While the development of orientation-selectivity in this cell is retarded in respect to the other example cells we do see an increase in the number of OS voxels between 5 and 7 dpf, and these voxels all show a preference for motion along the horizontal axis.

Example RGC 2

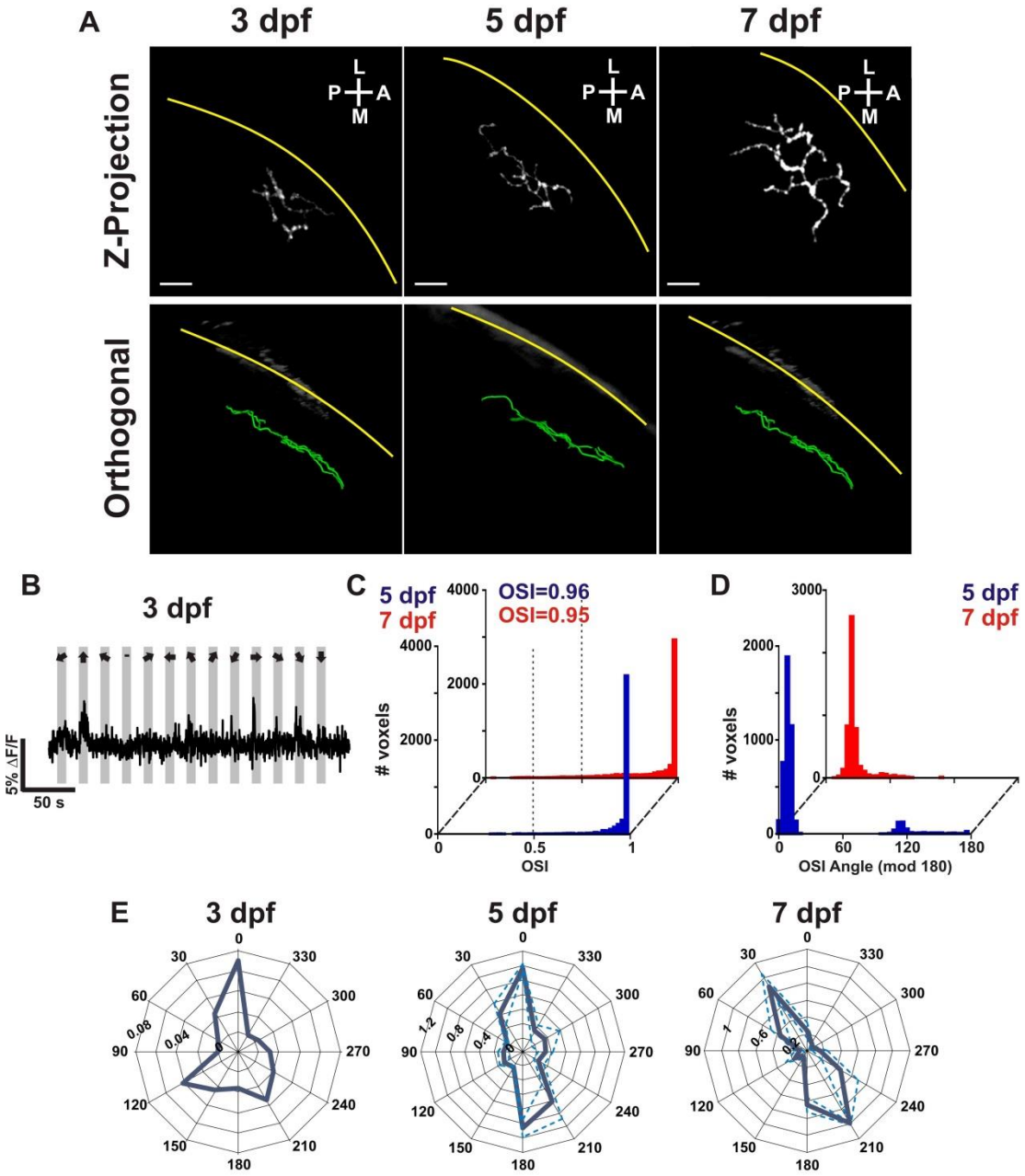

Figure 5.2.4 Example RGC 2: Structural analysis and description of orientation-selectivity at different development at stages. (A) Top panels show volumetric fills from tracings of a single RGC axon arbour at 3, 5 and 7 dpf. Image orientation is shown top right (L, lateral; M, medial; A, anterior and P, posterior). Scale bars =10 µm. Bottom panels show rotated tracings displaying the orthogonal view of the RGC axon arbours in the top panels. **(B)** Mean ΔF/F trace from an ROI encompassing all responding voxels during a tuning experiment performed at 3 dpf. Stimulus epochs are shown as grey blocks with the direction of motion indicated by arrows (the dash indicates the 'blank' epoch). **(C-E)** Quantitative analysis of orientation-selectivity using data grouped from multiple tuning experiments for each time point (5 dpf n=3 timeseries, 7 dpf n=4 timeseries) with the exception of **(E(i))**; 3 dpf n=1 timeseries. **(C)** Histogram of OSI values of all responsive voxels colour-coded for developmental time point (5 dpf blue and 7 dpf red). Dotted line indicates the 0.5 OSI threshold; values > 0.5 = OS. Mean OSI values are shown top centre. **(D)** Histogram of OSI preferred angles of responsive voxels with OSI values greater than 0.5 colour-coded for each time point as in (C). Angles are modulated around 180 degrees. **(E)** Polar plots; navy plots are mean polar plots, light blue dotted plots are mean +/- standard deviation polar plots.

Example RGC 3

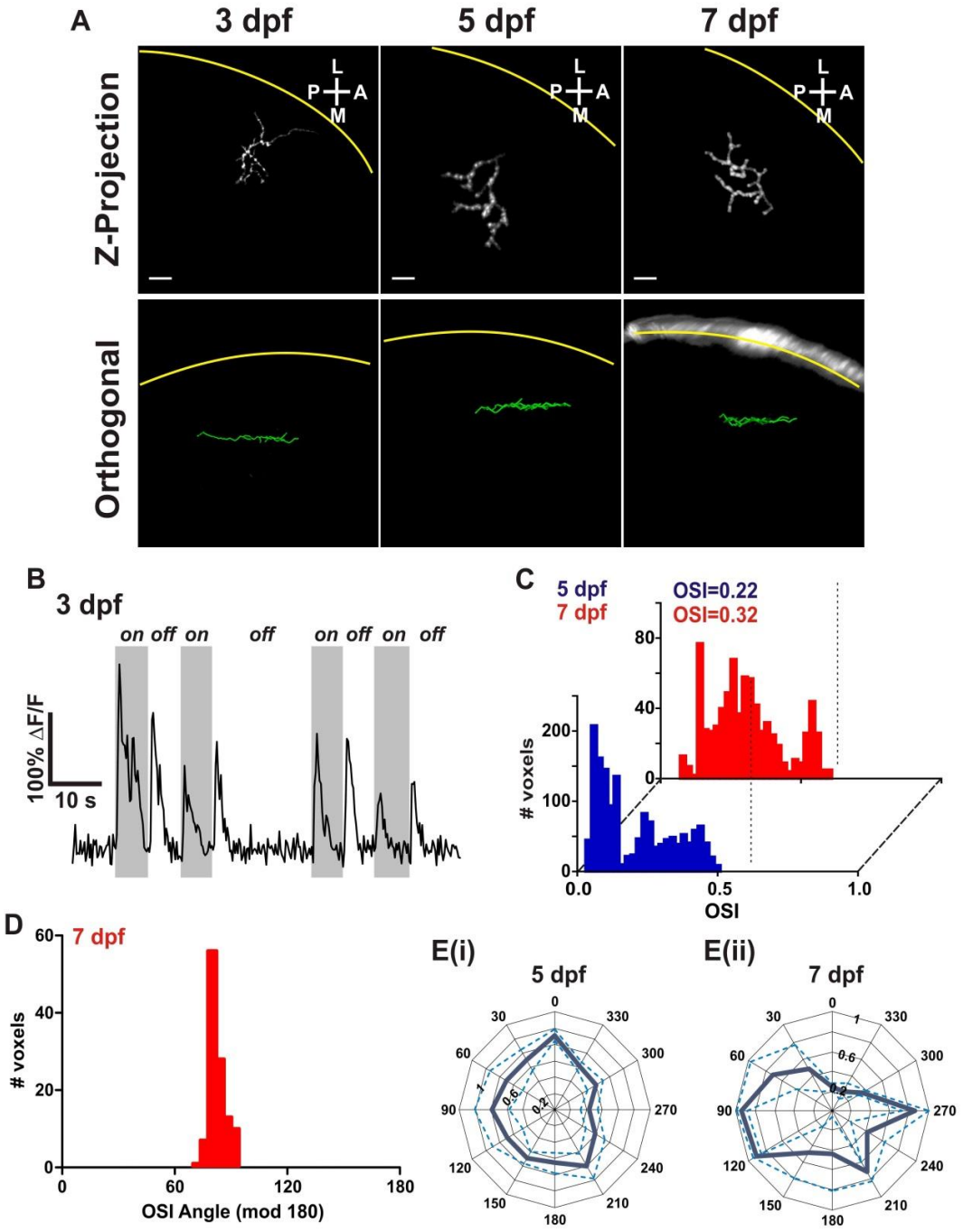

Figure 5.2.5 Example RGC 3: Structural analysis and description of orientation-selectivity at different development at stages. (A) Top panels show volumetric fills from tracings of a single RGC axon arbour at 3, 5 and 7 dpf. Image orientation is shown top right (L, lateral; M, medial; A, anterior and P, posterior). Scale bars =10 µm. Bottom panels show rotated tracings displaying the orthogonal view of the RGC axon arbours in the top panels. **(B)** Mean ΔF/F trace from an ROI encompassing all responding voxels during full-field stimulation performed at 3 dpf. Periods of light exposure are indicated by grey blocks. **(C-E)** Quantitative analysis of orientation-selectivity using data grouped from multiple tuning experiments for each time point (both 5 and 7 dpf n=3 timeseries). **(C)** Histogram of OSI values of all responsive voxels colour-coded for developmental time point (5 dpf blue and 7 dpf red). Dotted line indicates the 0.5 OSI threshold; values > 0.5 = OS. Mean OSI values are shown top centre. **(D)** Histogram of OSI preferred angles of responsive voxels with OSI values greater than 0.5 at 7 dpf. Angles are modulated around 180 degrees. **(E)** Polar plots of response profile at 5 **(i)** and 7 dpf **(ii)**; navy plots are mean polar plots, light blue dotted plots are mean +/- standard deviation polar plots.

5.2.1.2 Developmental invariance of a single direction-selective RGC

It has previously been shown that the axon arbours of DS RGCs are present in the optic tectum from early retinotectal development (3 dpf) and are largely invariant in tuning properties and topography throughout development and following dark-rearing (Lowe et al., 2013). However, as it is not possible to image the same RGCs at multiple time points, population studies cannot rule out the possibility that DS RGC axons imaged at each time point are from different cells. Here, the structural and functional properties of a singly-labelled DS RGC were recorded at 3 and 5 dpf. Unfortunately the arbour could not be located at 7 dpf, likely due to the transient expression of SyGCaMP3. In common with the OS RGC examples above, we found that the axon arbour of this DS RGC elaborated over development, yet maintained at both time points a planar morphology, as seen from the orthogonal view (Figure 5.2.6 A). This RGC responded robustly to moving bars from the earliest time point tested (3 dpf). The direction-selective index (DSI) was used to define the response properties of each voxel. A stringent threshold of >0.5 DSI was applied to indicate direction-selectivity. The vast majority of responsive voxels of this cell had DSI values >0.5 at both 3 and 5 dpf (Figure 5.2.6 B) suggesting this cell was highly direction-selective at both stages. The DSI angle histogram indicates that this cell at both 3 and 5 dpf had a preference for anterior (270˚) motion (Figure 5.2.6 C). The polar plots were highly similar at both 3 and 5 dpf, coherent in a preference for anterior (~270˚) motion (Figure 5.2.6 D). In summary, this cell shows direction-selectivity for anterior motion from 3 dpf, and this selectivity is sustained throughout development.

5.2.2 The functional development of single RGECO expressing tectal neurons in response to moving bar stimuli

RGCs pass visual information to their postsynaptic partners, the tectal neurons. It has previously been shown in our laboratory (Hunter et al., 2013) and by others (Niell and Smith, 2005; Ramdya and Engert, 2008; Gabriel et al., 2012; Grama and Engert, 2012) that tectal neurons of the larval zebrafish show direction- and orientation-selectivity. Population studies of RGC and tectal cell orientation-selectivity find that cells can be grouped into four classes each tuned for motion along a similar axis; vertical, horizontal axis, as well as 2 populations flanking the vertical axis (29˚ and 140˚). However, the development of orientation-selectivity is not known. If tectal cells receive feed-forward OS RGC input as has been suggested (Hunter et al., 2013), knowing that OS RGCs refine during development how do tectal cells integrate this potentially noisy information as they develop?

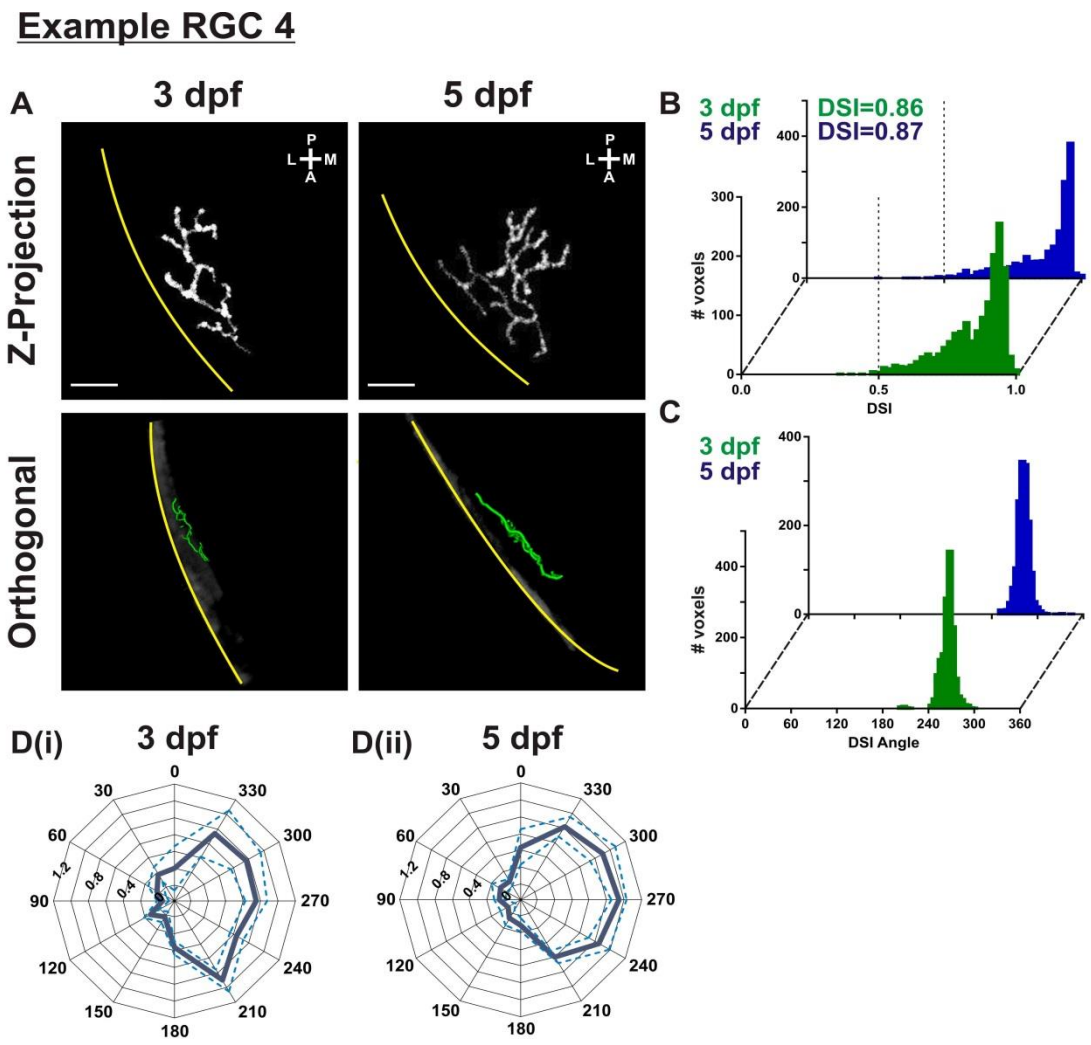

Figure 5.2.6 Example RGC 4: Structural analysis and description of direction-selectivity at different development at stages. (A) Top panels show volumetric fills from tracings of a single RGC axon arbour at 3 and 5 dpf. Image orientation is shown top right (L, lateral; M, medial; A, anterior and P, posterior). Scale bars =10 µm. Bottom panels show rotated tracings displaying the orthogonal view of the RGC axon arbours. **(B-D)** Quantitative analysis of direction-selectivity using data grouped from multiple tuning experiments for each time point (both 5 and 7 dpf n=4 timeseries). **(B)** Histogram of direction-selective index (DSI) values of all responsive voxels colour-coded for developmental time point (3 dpf green and 5 dpf blue). Dotted line indicates the 0.5 DSI threshold; values > 0.5 = DS. Mean DSI values are shown top centre. **(C)** Histogram of DSI preferred angles of responsive voxels with DSI values greater than 0.5. Different developmental time points are colour-coded as in **(B)**. **(D)** Polar plots of response profile at 3 **(i)** and 5 dpf **(ii)**; navy plots are mean polar plots, light blue dotted plots are mean +/- standard deviation polar plots.

5.2.2.1 Development of single orientation-selective tectal neurons

To address this question we used a similar strategy to above, where single tectal neurons were labelled with the GECI 'RGECO', a cytosolic GECI which permits visualisation of tectal cell morphology. RGECO is a red shifted indicator and was chosen, with a future aim of conducting two colour functional imaging in the larval zebrafish, to permit simultaneous characterisation of this GECI *in vivo.* We were able to follow the dendritic elaboration of example tectal cell 1

between 4 and 7 dpf (Figure 5.2.7 A). As shown previously, tectal neurons responded well to the drifting bar stimuli (Niell and Smith, 2005; Gabriel et al., 2012; Hunter et al., 2013) and we observed robust responses in the cell body at all stages imaged (Figure 5.2.7 B). At 4 dpf almost all voxels had OSI values greater than 0.5, indicating orientation-selectivity (Figure 5.2.7 D). The OSI angle histogram indicates a preference for motion along the vertical axis (Figure 5.2.7 E). During subsequent development, this orientation-selectivity for vertical motion was retained. A small refinement of this highly selective cell may be shown by an increase in mean OSI value with development (4 dpf 0.82, 5 dpf, 0.87; 7 dpf, 0.94; Figure 5.2.7 D). This orientation-selectivity is summarised in the polar plots (Figure 5.2.7 C). In summary, this tectal cell is highly tuned for motion along the vertical axis at 4 dpf, a selectivity which is invariant up to 7 dpf, although some small refinement in mean OSI value is observed.

Mosaic labelling of cells often led to GECI expression in multiple tectal cells. For xxample tectal cell 2 (Figure 5.2.8) the position of cell bodies in relation to each other allowed for the identification of the same cell over time (Figure 5.2.8 A). However, intertwining of the dendrites rendered it impossible to distinguish the dendritic architecture of the cell of interest. The following example tectal cell demonstrated responses to moving bars at 3 dpf, an early time point in the development of retinotectal connectivity. The polar plot at 3 dpf showed a quite broad profile of responses to all directions, but with a clear bias for motion around the vertical poles (Figure 5.2.8 B). On quantitative analysis this cell was indeed classified as OS (mean OSI 0.65) at 3 dpf (Figure 5.2.8 C). The preferred OSI angle of OS voxels showed a preference for vertical motion (0/180˚; Figure 5.2.8 D). However, immaturity in tuning is shown by broad distributions of OSI values and preferred angles (Figure 5.2.8 C-D). Following 2 days further development the polar plot increased in coherence for a preference for motion along the vertical axis (0/150˚) compared to 3 dpf (Figure 5.2.8 B). This refinement in orientation-selectivity is reflected by a large increase in the mean OSI value from 0.65 at 3 dpf to 0.92 at 5 dpf, and a narrowing in preferred angle distribution (Figure 5.2.8 C-D). In summary, this cell, as above, exhibits orientation-selectivity early in development (3 dpf) however, shows refinement in this orientation-selectivity between 3 and 5 dpf.

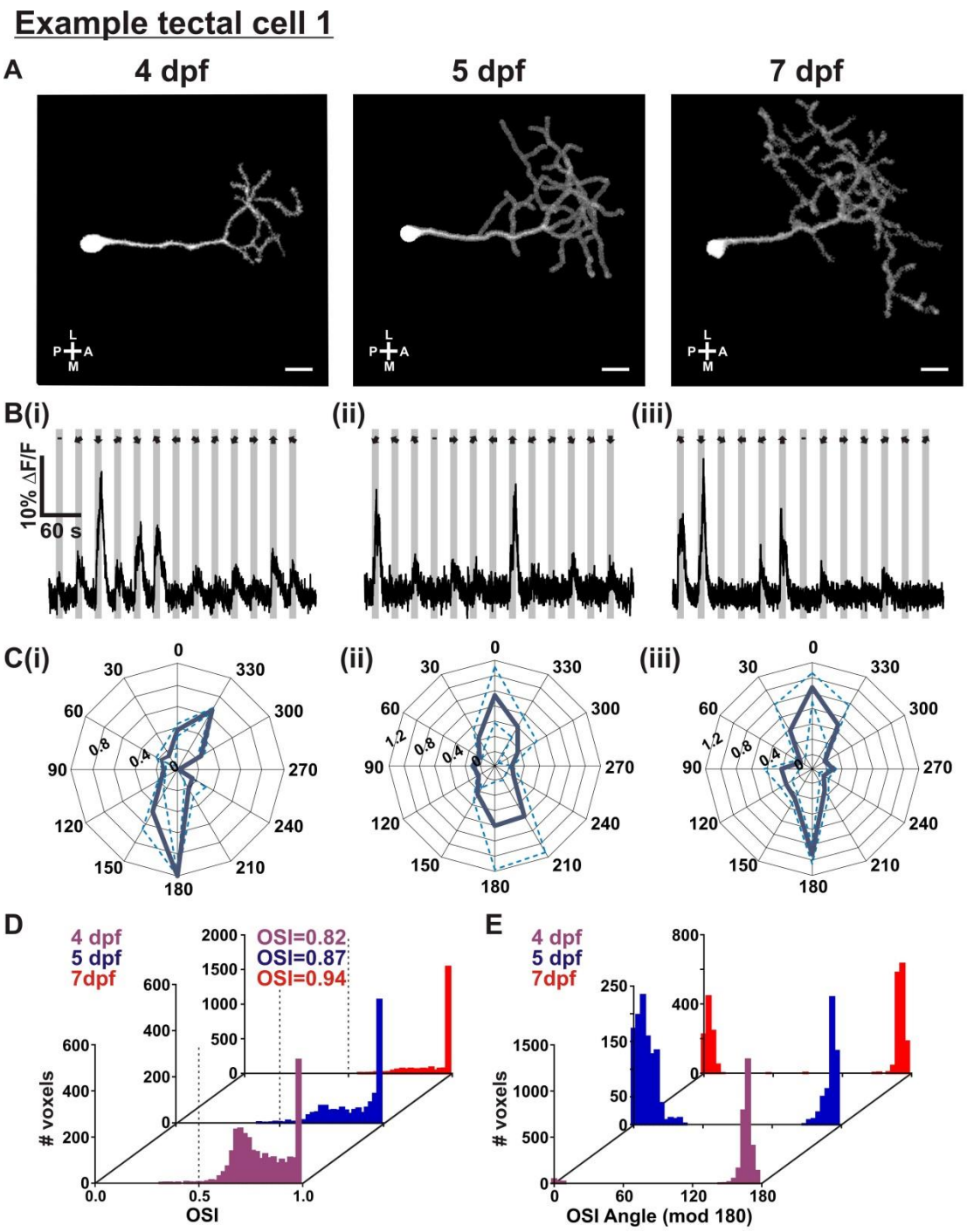

Figure 5.2.7 Example tectal cell 1: Qualitative and quantitative analysis of structural and functional development. (A) Volumetric fills of tracings from a single tectal neuron expressing RGECO at 4, 5 and 7 dpf. Image orientation is shown bottom left (L, lateral; M, medial; A, anterior and P, posterior). Scale bars =10 µm. **(B)** Mean ΔF/F trace from an ROI encompassing all responding voxels during a tuning experiment performed at 4 dpf **(i)**, 5 dpf **(ii)** and 7 dpf **(iii)**. Stimulus epochs are shown as grey blocks with the direction of motion indicated by arrows (the dash indicates the 'blank' epoch). **(C-E)** Quantitative analysis of orientation-selectivity using data collected from multiple tuning experiments at each time point (4 dpf n=3 timeseries, 5 dpf n= 2 timeseries, 7 dpf n=3 timeseries). **(C)** Polar plots; navy plots are mean polar plots, light blue dotted plots are mean +/- standard deviation polar plots for 4 dpf **(i)**, 5 dpf **(ii)** and 7 dpf **(iii)**. **(D)** Histogram of OSI values of all responsive voxels colour-coded for developmental time point (4 dpf pink, 5 dpf blue and 7 dpf red). Dotted line indicates the 0.5 OSI threshold; values > 0.5 = OS. Mean OSI values are shown top centre. **(E)** Histogram of OSI preferred angles of responsive voxels with OSI values greater than 0.5. Angles are modulated around 180 degrees. Different developmental time points are colour-coded as above.

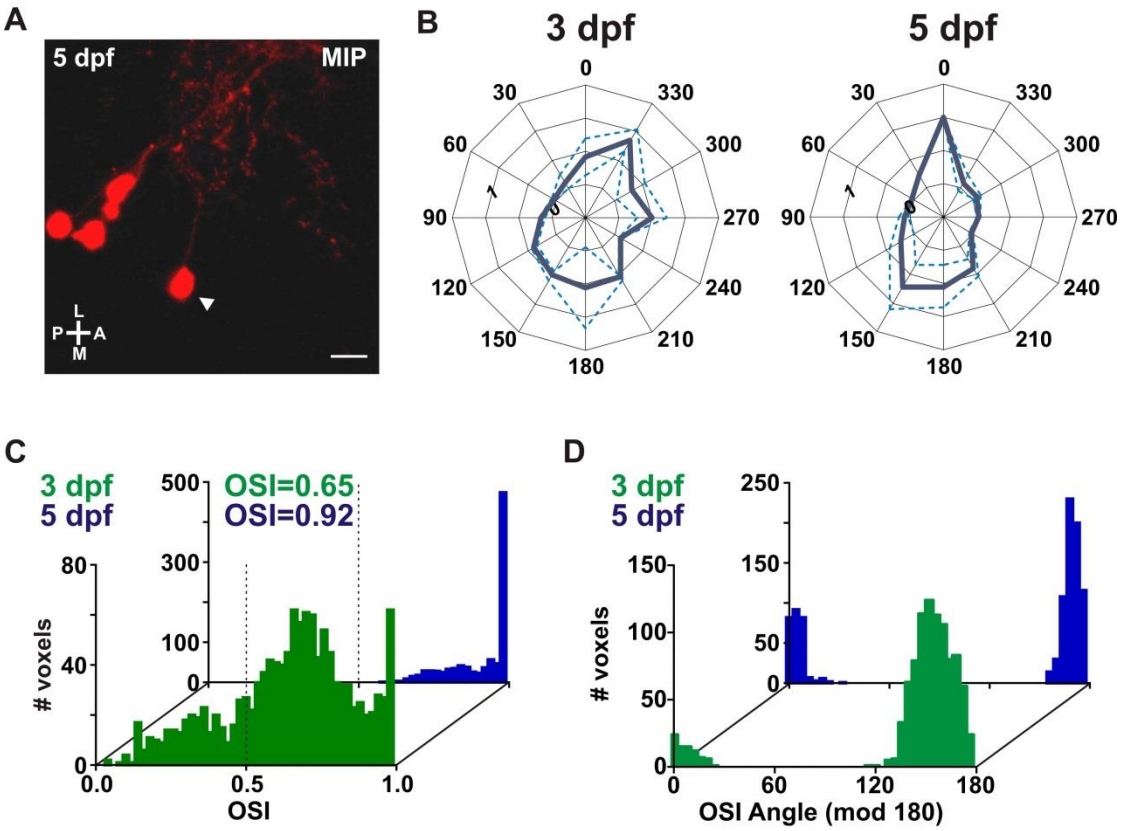

Figure 5.2.8 Example tectal cell 2: Quantitative analysis of functional development. **(A)** MIP of a group of tectal cells expressing RGECO. The cell of interest is set apart from the others (indicated with a white arrowhead). Note that dendritic structure cannot be elucidated. Image orientation is shown bottom left (L, lateral; M, medial; A, anterior and P, posterior). **(B-D)** Quantitative analysis of orientation-selectivity using data grouped from multiple tuning experiments for each time point (both 3 and 5 dpf n=2 timeseries). **(B)** Polar plots of response profile at 3 **(i)** and 5 dpf **(ii)**; navy plots are mean polar plots, light blue dotted plots are mean +/- standard deviation polar plots. **(C)** Histogram of OSI values of all responsive voxels colour-coded for developmental time point (3 dpf green and 5 dpf blue). Dotted line indicates the 0.5 OSI threshold; values > 0.5 = OS. Mean OSI values are shown top centre. **(D)** Histogram of OSI preferred angles of responsive voxels with OSI values greater than 0.5 at 3 **(i)** and 5 dpf **(ii)**. Angles are modulated around 180 degrees.

5.2.2.2 Morphological examination of vertically tuned OS tectal cells

Our strategy for expressing RGECO often labelled vertically tuned OS tectal cells. We found three highly tuned vertical OS tectal cells which had good expression of GECI in their dendrites allowing structural assessment (Figure 5.2.9). We were interested in investigating whether these functional homologs also shared morphological features (Figure 5.2.8 A). The dendritic tree of each cell arbourised in the *stratum fibrosum et griseum superficiale* (SFGS) where the majority of RGC visual inputs laminate, however, the tectal cell dendrites were not laminar in configuration. Interestingly, all the cells showed an asymmetric elaboration of their dendritic trees in the posterolateral quadrant. The age matched examples (Cell 1 and 3) show large dendritic trees (total branch length: Cell1, 854 µm; Cell 3, 884 µm) which extend across a large

portion of the anterior-posterior axis of the tectum (Cell 1, 95.23 µm; Cell 3, 91.81µm). In addition, for all three cells we found a small proximal branch, emanating from the primary dendrite (yellow arrows).

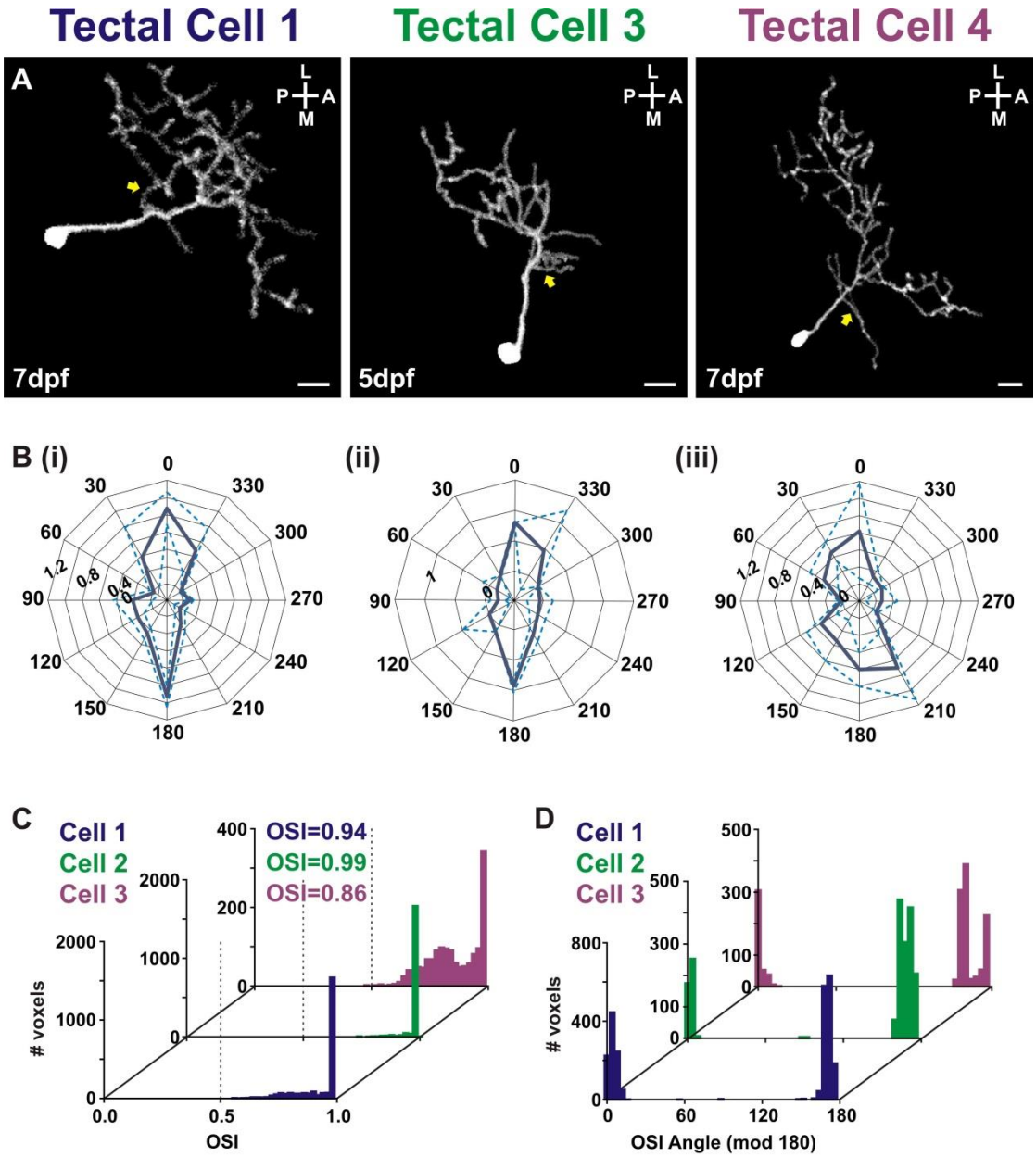

Figure 5.2.9 Morphological similarities of vertically tuned orientation-selective neurons. (A) Volumetric fills of tracings of a single tectal neurons at 5 dpf and 7 dpf as labelled. Image orientation is shown top right (L, lateral; M, medial; A, anterior and P, posterior). Yellow arrows indicate short proximal branches emanating from primary dendrites. Scale bars = 10 µm. **(B-D)** Quantitative analysis of orientation-selectivity using data from multiple timeseries for each time point (Cell1, n=3 timeseries; Cell 2, n=2 timeseries; Cell 3, n=2 timeseries). **(B)** Polar plots for Cell 1 **(i)**, Cell 3 **(ii)** and Cell 4 **(iii)**. Navy plots are mean polar plots, light blue dotted plots are mean +/- standard deviation polar plots. **(C)** Histograms of OSI values of all responsive voxels colour-coded for each cell (Cell 1, blue, Cell 3 green, Cell 4 magenta). Dotted line indicates the 0.5 OSI threshold; values > 0.5 = OS. Mean OSI values are shown top centre. **(D)** Histogram of OSI preferred angles of responsive voxels with OSI values greater than 0.5 from each cell, colour-coded as in **(C)**. Angles are modulated around 180 degrees.

5.3 Discussion

The aim of this chapter was to chart the development of orientation- and direction-selectivity in RGCs and tectal cells. To do this, single cells were labelled with GECIs and their functional responses to moving bars recorded at different developmental stages. By recording from identified cells over time detailed information can be gathered about the functional and structural development of RGCs and tectal cells. However, this technique is extremely low throughput evinced by the small number of examples outlined in this Chapter. This is due to several factors; (1) while mosaic injection of plasmids labels small numbers of cells, if even two cells are labelled overlapping of arbours can make identification at serial time points and structural assessment difficult. (2) Many cells do not respond to moving bar stimuli. Of cells which do respond to moving bars the majority are neither DS nor OS (Lowe et al., 2013). (3) Our method of labelling cells is transient meaning GECI expression fades over the timecourse of the experiment, therefore it is not always possible to collect data from multiple time points from the same cell. This being the case, it is difficult to draw direct conclusions from this data alone, but when considered together with the population studies recently conducted in the lab, can give powerful insight into the development of orientation- and direction-selectivity in the larval zebrafish (Nikolaou et al., 2012; Hunter et al., 2013; Lowe et al., 2013).

5.3.1 The functional and structural development of an example direction-selective RGC

In a developmental population study characterising the orientation- and direction-selectivity of all RGC axons terminating in the zebrafish optic tectum, it was found that three classes of DS RGCs were already present in the tectum at 3 dpf, an early stage in retinal and retinotectal development (Lowe et al., 2013). This study determined at the population level that these classes of DS RGCs remained invariant in terms of tuning properties and spatial organisation within the tectum up to 10 dpf (Lowe et al., 2013). In this chapter a single RGC axon arbour was identified which was found to be selective for anterior motion at 3 dpf, a direction known to be preferred for a class of RGCs (Nikolaou et al., 2012). This identified RGC was functionally invariant over development as it retained direction-selectivity for anterior motion at 5 dpf. In addition, while this RGC axon arbour elaborated between 3 and 5 dpf it remained laminar and in close proximity to the skin. This agrees with population data which shows that the neuropil lamination zones of DS RGC axon arbours in the tectum are in the superficial SFGS and that this lamination is invariant over development (Nikolaou et al., 2012; Lowe et al., 2013). It is not

possible using a population approach to rule out the possibility that DS RGC axons imaged at each time point are from different cells. While more examples tracked over longer timescales would be ideal, the single DS example RGC recorded here suggests that individual DS RGCs are functionally invariant over development. Together, the single DS RGC data and the population imaging study suggest that DS circuits are developmentally hard-wired (Lowe et al., 2013).

5.3.2 The functional and structural development of example orientation-selective RGCs

In the developmental population study by Lowe *et al*., (2013) at 3 dpf three of the four OS RGC populations recorded at 7 and 10 dpf are not yet present. There are three scenarios of the behaviour of OS RGC arbours in the tectum at 3 dpf to explain this; (1) these populations of OS RGCs have not invaded the tectal neuropil, (2) they have invaded the neuropil but do not respond to the moving bar stimuli, or (3) they have invaded the neuropil but exhibit non-selective responses to moving bars (i.e. they respond to all directions) and so do not reach the threshold for orientation-selectivity. Furthermore, at 3 dpf only the population of vertically-tuned OS RGC responses were found in the tectal neuropil and the functional organisation of these inputs are developmentally dynamic in terms of their laminar organisation (Lowe et al., 2013). This can come about either from functional refinement, where there is a loss or gain of selectivity for motion along the vertical axis, or from structural refinement of arbours in which physical changes in arbour shape could alter the laminar profile of vertically-tuned OS RGCs. Analysis of single OS RGCs was used to address this questions since it allows the both the structural and functional development of identified OS-RGCs to be tracked over time. In this chapter, at 3 dpf the functional properties of three individual RGC axon arbours, which were later identified as OS (or en route to OS), were recorded. Example RGCs 1 and 3 showed no responses to moving bar stimuli at 3 dpf. Small and immature responses to moving bar stimuli were recorded from example RGC 2 at 3 dpf. These examples indicate that while OS RGCs have invaded the optic tectum at 3 dpf they are not functionally mature (in contrast to DS RGCs). Therefore the lack of OS responses at 3 dpf in the developmental population study is due, at least in part, to the slow emergence of motion detection in some RGCs rather than a developmental delay in the innervation of the tectum by OS RGCs. Interestingly, while example cells 1 and 3 do not respond to moving bar stimuli they do show robust responses to full field light stimulation indicating that these cells are wired into the circuitry underlying ON- and OFF-responses in the IPL, and that the development of ON/OFF responses precede that of orientation-selectivity.

In the developmental population study, between the 3 and 7 dpf time points the three populations of OS RGCs not present at 3 dpf emerge and vertical OS RGCs are found more diffusely throughout the deeper layers of SFGS in lamination zones not observed at 3 dpf. If the emergence of these OS cells reflects the gain of responsiveness to moving bar stimuli, these cells can either be OS on first responding to moving bar stimuli, or may refine over time. In order to differentiate between these scenarios RGCs were recorded at 5 dpf as well as 7 dpf. In this chapter it was shown that at 5 dpf all example cells respond robustly to moving bar stimuli but with each cell developing OS properties at different rates. Example RGC 1 is classed as OS for motion along the vertical axis at 7 dpf but at 5 dpf the cell was not orientation tuned, showing a broad response profile to all directions. This example RGC indicates that OS RGCs can acquire orientation-selectivity after passing through a period of non-selectivity. The two other example RGCs show similar trends of refinement. Unsurprisingly, the most responsive cell at 3 dpf (example RGC 2) is the most developed at 5 dpf showing high orientation-selectivity for motion along the vertical axis. This selectivity is maintained at 7 dpf indicating that once the circuitry conferring orientation-selectivity has been set-up it is maintained but that OS cells become OS at different developmental stages. Consistent with this idea, example RGC 3 is less selective (more broadly tuned) at 7 dpf. At this time point it shows a higher mean OSI value than at it did at 5 dpf with the polar plot at 7 dpf indicating a preference for motion along the horizontal axis. The staggering of the development of orientation-selectivity may likely relate to when these RGCs are born and when they invade the tectal neuropil, and in addition may reflect the axis-selectivity of different cells. This data suggests that between 5 and 7 dpf RGCs destined to be OS respond to moving bar stimuli, but responses earlier in development have a tendency to be more broadly tuned, refining over time.

The single cell approach also allows the documentation of the structure of RGC axon arbours and their gross positioning within the tectal neuropil. As mentioned above, in the developmental population study by Lowe et al (2013) termination zones for vertical OS populations refine over the laminar axis of the tectum over time. A possible explanation for this would be that single RGC arbours extend into multiple laminae, and that these arbours refine to a single planar morphology over time. However, we find here that all RGC axons form single laminar arbours at every developmental stage. Therefore, differences in lamination zones during development are solely a consequence of the changing functional, as opposed to structural, properties of RGC axons arbours.

5.3.3 Putative mechanisms for differential developmental programming of direction- and orientation-selective RGCs

It would be interesting to understand the underlying mechanisms that lead to DS RGCs being hard-wired while OS RGCs are more functionally dynamic. It is interesting to note that DS and OS RGCs are differentially affected by dark rearing; DS RGCs are unaffected in both functional properties and neuropil lamination zones, while OS RGCs show some alterations in preferred angle centres and fragmented termination zones (Lowe et al., 2013). This suggests that visual drive is required to some extent for the proper functional development of OS, but not DS, RGCs. Interestingly, in the mouse, the development of direction-selectivity occurs prior to eye-opening and in animals lacking acetylcholine mediated spontaneous retinal waves. Therefore, visual experience appears not to be a requirement for the development of direction-selectivity in both the zebrafish and the mouse (Elstrott et al., 2008; Elstrott and Feller, 2010).

The circuitry underlying direction-selectivity is set-up within the IPL of the retina through the connections between RGCs, starburst amacrine cells and bipolar cells (Weng et al., 2005; Wei et al., 2011; Yonehara et al., 2011). While less is known about orientation-selectivity, in the rabbit retina orientation-selectivity is set up by amacrine cell GABAergic and glycinergic inhibition of bipolar cells in the IPL which connect with OS RGCs (Venkataramani and Taylor, 2010). It is possible that different programmes of dendritic specification within the IPL could underlie DS and OS differential developmental regimes. It has been shown that most singly-labelled RGCs show laminar stratifications in the IPL early in development, but proceed to undergo an extended period of addition or elimination of stratifications (Mumm et al., 2006). This study had a relatively small sample size and could not identify between different RGC subtypes. Therefore, it is possible that not all RGC subtypes were sampled and so it is not known whether both OS and DS RGCs would undergo dendritic remodelling within the IPL. It is possible that hardwiring of DS RGCs may be achieved by preferential synaptic matching with amacrine and bipolar cells which express a matching molecular code. It has been shown in mice that ON-OFF DS RGC subtypes selectively expressed the cell-surface molecules Cadherin 6, Collagen XXVα1, and Matrix metalloprotease 17. While confirming that different classes of DS RGCs have their own molecular identity, these cell surface molecules may be important for intercellular matching within the IPL (Kay et al., 2011a). Additionally, a number of molecules from the Ig superfamily are expressed within the IPL including contactins, sidekicks and Dscams, which may set up laminar targeting of RGC dendrites within the IPL through homophilic interaction of pre and postsynaptic partners (Yamagata and Sanes, 2012).

5.3.4 The functional and structural development of vertically-tuned orientation-selective tectal cells

It has been shown in two population studies within the zebrafish tectum that both RGCs and tectal cells show orientation-selectivity along the same axes; 29˚, 81˚, 140˚ and 176˚ suggesting that tectal cells sample orientation-selective information from RGCs (Hunter et al., 2013; Lowe et al., 2013). Previously in this chapter we have ascertained that for RGCs orientation-selectivity emerges through a period of functional refinement. It is interesting to examine how tectal cells develop in the midst of changing RGC inputs.

To address this, in this chapter two example tectal cells were labelled with the GECI RGECO and their responses to moving bars and structure recorded over development. Robust responses to moving bars were recorded at the earliest time points tested (3/4 dpf), with both cells exhibiting orientation-selectivity for motion along the vertical axis. For example, tectal cell 1 functional properties are relatively invariant from 4 to 7 dpf, whereas example tectal cell 2 shows refinement in orientation-selectivity between 3 and 5 dpf. At these early time points within the tectal neuropil there are RGC axons which are OS for vertical motion (Lowe et al., 2013) and also RGC axons which are in the process of refining their orientation-selectivity. Tectal cells can either (1) make preferential synaptic connections with OS tuned RGCs, or (2) make synaptic contacts with both OS RGCs and non-tuned OS RGCs.

The orientation-selectivity of both example tectal cells at 3 dpf perhaps suggests that preferential contacts are made between OS tectal cells and RGCs which are already orientation-selective at 3/4 dpf. The invariance in functional properties of example tectal cell 1 between 4 and 7 dpf supports this scenario. This could come about if the presynaptic boutons of RGCs that display immature non-tuned functional properties are not competent in making functional synapses with tectal neurons. However, while example tectal cell 2 is classed as OS at 3 dpf, it displays orientation-selectivity to a much higher degree at 5 dpf. This refinement does not fit a model where only tuned OS RGCs make contacts with OS tectal cells. This can be explained by OS tectal cells making synaptic connections with tuned OS RGCs and non-tuned but refining OS RGCs. This could come about as a consequence of synaptic matching through a molecular code or by a tectal cell patterning programme dictating dendrite stratification within the laminae of emerging OS RGC inputs. Therefore, the refinement of tectal cell orientation-selectivity can simply be a consequence of the refinement of orientation-selectivity of the OS RGCs synapsing onto it. In addition, high tectal cell orientation-selectivity early in development can be determined through a relative bias in synapse strength promoting OS-tuned input. A spike threshold will filter noisy information from non-tuned inputs so that tectal cell output is

biased towards for the stronger suprathreshold OS-tuned input. This scenario can account for the differences between example tectal cells 1 and 2 if it is considered that example tectal cell 2 modulates its spike threshold over development either intrinsically or via intratectal connectivity.

Functional examination of example tectal cell 1 revealed robust OS responses at 4 -7 dpf. Between these time points the dendritic tree of this cell enlarges substantially. During this period it is known that tectal cell dendrites are making many new synaptic connections, with the number of postsynaptic sites being formed plateauing between 6 and 8 dpf (Niell et al., 2004). However, there is no major difference in the tuning properties of this cell between 4 and 7 dpf prompting the question why is this elaboration of the dendritic arbour necessary? The elaboration of the dendritic tree may expand the receptive field of the cell through wider contact with retinotopically arranged RGC inputs. In addition, increasing the number of inputs reporting a stimulus feature will improve the reliability of the tectal cell readout to this feature. In this study only the orientation-selectivity of this cell is considered. This growth may be indicative of the development of connectivity underlying the detection of other stimuli that are not probed using the drifting bar stimulus.

In this chapter the labelling of single tectal cells permitted the determination of the dendritic structure of three functionally identified vertically-tuned OS cells. Structural analysis showed that these cells also share morphological characteristics. The dendritic trees of these example cells are large and asymmetric and thus likely integrate information from a large number of inputs over a large area of visual space. These example tectal cells have dendrites which are not strictly laminar, but as vertically-tuned OS RGCs have the most diffuse termination of all the OS populations even at 7 dpf, it is likely that these vertically-tuned OS tectal cells receive OS RGC input from several laminae. Horizontally-tuned OS RGCs terminate in a single identified neuropil lamina by 7 dpf, so the horizontal tectal cell class may be expected to have more laminar dendritic trees (Lowe et al., 2013).

5.3.5 Future Work

As outlined above this work suffers from a low sample size. This can be addressed by using functional tools that specifically label direction- or orientation-selective subsets of RGCs or tectal cells. In the mouse several transgenic mice which selectively label direction-selective RGC subtypes exist (Kim et al., 2008; Wei et al., 2011; Yonehara et al., 2011). As of yet no direction- or orientation-selective RGC subtype specific lines exist in the zebrafish. Recently,

specific-promoters have been found that drive expression in two subset of tectal neurons which show bias for either rostral to caudal or caudal to rostral motion (Gabriel et al., 2012). In our laboratory BAC clones are currently being developed in order to find direction-and orientation-selective retinotectal cell types.

In the study by Mumm *et al*., (2006) the laminar specification of dendrites in the IPL was examined over development. It would be exciting to combine functional imaging of single RGCs within the retina over development while following dendritic laminations in the IPL over time. We might predict that the functionally hard-wired DS RGCs would not undergo dendritic stratification remodelling following initial lamination, while the relatively dynamic OS RGCs would as they search for the correct presynaptic partners.

As mentioned above, the specificity of tuned versus non-tuned input onto a tectal cell may determine the behaviour of that cell. A possible approach to identify the tuning of excitatory input onto a single tectal cell would be the record glutamate release from RGCs using the genetically-encoded glutamate sensor iGluSNFR. In this experiment, labelling of a single tectal cell with RGCO will elucidate the functional output of the cell, whilst expression of iGluSNFR and imaging at postsynaptic sites can be used to examine the tuned or non-tuned nature of synaptic inputs simultaneously.

6 Summary

In this thesis 3 main projects were tackled; (1) a characterisation of the properties of newly-engineered GECIs, (2) a dissection of postsynaptic calcium transients following spontaneous neurotransmitter release measured using GCaMP3 in dissociated hippocampal neurons and (3) a developmental description of the direction- and orientation-selectivity of single cells of the larval zebrafish retinotectal system. Below I will outline the main findings from these projects.

Genetically-encoded calcium indicators have been identified as highly useful tools for imaging neural activity. Their advantages over synthetic indicators stem from their ability to be introduced into genetically defined populations of neurons or single cells, which avoids more invasive methods of loading. This genetic-encoding also permits long-term chronic imaging. These advantages of GECIs have motivated the development of iteratively improved generations. As new tools are engineered it is important to the relationship of their response properties to patterns of neural activity; their ability to detect single action potentials, the range of activity over which responses are linear and their kinetics. In Chapter 3 we undertook the characterisation of RGECO, a red-shifted GECI, and compared it to the performance of GCaMP3, a well-established and widely used GECI (Seelig et al., 2010; Gabriel et al., 2012; Huber et al., 2012a; Wachowiak et al., 2013). RGECO was found to compare well with GCaMP3, showing similar changes in fluorescence, sensitivity, dynamic range and kinetics. However, we discovered a new property of RGECO, which can be described as a rundown in its reliability to report neural activity under intense fluorescence excitation. The experiments performed here allowed a description of this rundown as solely dependent on excitation light, which in turn allowed a restoration of reliability by using confocal, as opposed to widefield microscopy. In addition, two presynaptically-targeted GECIs, SyGCaMP3 and SyRGECO, which were generated in the lab, were characterised. Overall, these GECIs performed similarly in response to electrical stimulation. However, the synaptic targeting of these indicators increased their light-dependent sensitivity, showing rundown even under lower light paradigms, such as those obtained using confocal microscopy. The red-shifted nature of R-GECO makes this GECI an especially exciting tool for use in combination with other GFP-based optical tools. One particularly exciting use that extends from the findings in Chapter 5 would be to determine the timing, position and tuning of excitatory inputs onto tectal cell dendrites using the green-shifted glutamate sensor, iGluSNFR, during a direction-tuning experiment in the larval zebrafish. Simultaneous functional imaging of tectal cell output using RGECO will allow the relationship between the excitatory drive and neuronal output to be directly determined *in vivo* (see Chapter 5 section 5.3.5).

Experiments conducted in Chapter 4 of this thesis took advantage of the excellent signals of cytoplasmic GCaMP3 and used it to image spontaneous neurotransmitter release in individual dendritic spines of dissociated hippocampal neurons. These postsynaptic calcium transients were subsequently found to be dependent solely on NMDA receptor activation and to be a reliable reporter of presynaptic glutamate release. Using this approach we could observe the spatiotemporal distribution of excitatory input onto a single hippocampal neuron. In doing so, we observed that at single spines, QCT amplitude was highly variable. While quantal variability has been well documented, the source of this variability remains contentious (Liu et al., 1999; Karunanithi et al., 2002; Conti and Lisman, 2003; Franks et al., 2003; Raghavachari and Lisman, 2004). A major aim of this chapter was therefore to investigate the origins of quantal variability. Using repetitive glutamate uncaging we established that QCT variability was solely a postsynaptic feature, without any presynaptic involvement. We also carried out pharmacological investigation of likely postsynaptic sources of variability and were able to exclude most non-NMDA receptor sources of dendritic spine calcium. While NMDA receptors did show desensitisation at high frequency, at low frequencies variability was still large. The ultimate origin of quantal variability is therefore left undiscovered, but continuing pharmacological and molecular work should illuminate this interesting question. One current hypothesis extends the idea of spine shape in controlling the concentration of calcium at the spine and looks to establish if spine neck diameter or length (and therefore diffusion across the neck) is continuously being modulated. Since actin is critical in setting spine and neck shape, initial experiments will interfere with actin dynamics to assess its role in the heterogeneity of spine calcium responses.

The second part of this chapter included a dissection on how QCTs are distributed across the dendritic tree. We found that in spines closer to branch tips calcium transients were larger in amplitude than those recorded at spines more proximal to the cell body. This effect is reminiscent of dendritic-scaling whereby larger amplitude currents are found at more distal synapse than more proximal synapses. Dendritic scaling acts to normalise currents recorded at the cell body, as distal signals are more attenuated during propagation to the soma compared to more proximal signals. One aim of this chapter was to understand the underlying cause of large calcium transients within distal spines. Interestingly we found that distal spines were smaller and had smaller PSDs and, therefore, less glutamate receptors than more proximal spines. We believe that the important variable for determining the amplitude of calcium transients is spine size/volume or, more specifically, spine neck diameter which scales with spine volume. Spine necks act as physical barriers to intracellular calcium diffusion away from the spine head, thus small spines with thinner necks will compartmentalise calcium better, generating larger amplitude calcium events. This hypothesis will need to be corroborated with

exact measurements of spine volumes and spine sizes along single dendritic branches which can be performed using electron microscopy. Yet the questions remain; why do distal spines have larger calcium transients, and what job may they be performing at the distal sites?

The aim of Chapter 5 was to characterise the maturation of direction-and orientation selectivity in individual RGCs and tectal cells in the larval zebrafish within their first week of development. The larval zebrafish is a particularly interesting model in which to study visual system development as the larvae can see prior to the full structural maturation of visual circuits. Therefore, it was of particular interest in this Chapter to explore how the neuronal output of individual cells may change during this period of intense remodelling. Interestingly, we found that the functional tuning of both DS RGCs, and to a certain extent OS tectal cells, is minimally affected by visual system development and dendritic growth. However, this was not the case for OS RGCs which appear to mature in step with the visual system and go through a period of functional refinement. These findings have interesting implications as to what mechanisms different cells employ to allow for different patterns of maturation. For instance, for cells which are invariant in their functional tuning, are inputs onto these cells hard-wired so that only correct contacts are made, or does some form of dendritic computation take place between the dendrites and the soma that confers the functional properties of a cell?

These projects, while covering a range of neuroscience, showcase the *in vitro* and *in vivo* amenability of GECIs, which allow non-invasive chronic functional imaging as was required for Chapter 5, and a dissection of the spatial extent of activity as was required for Chapter 4.

Bibliography

Akerboom J et al. (2012) Optimization of a GCaMP calcium indicator for neural activity imaging. J Neurosci Off J Soc Neurosci 32:13819–13840.

Akerboom J et al. (2013a) Genetically encoded calcium indicators for multi-color neural activity imaging and combination with optogenetics. Front Mol Neurosci 6:2.

Akerboom J et al. (2013b) Genetically encoded calcium indicators for multi-color neural activity imaging and combination with optogenetics. Front Mol Neurosci 6:2.

Amthor FR, Keyser KT, Dmitrieva NA (2002) Effects of the destruction of starburst-cholinergic amacrine cells by the toxin AF64A on rabbit retinal directional selectivity. Vis Neurosci 19:495–509.

Amthor FR, Oyster CW, Takahashi ES (1984) Morphology of on-off direction-selective ganglion cells in the rabbit retina. Brain Res 298:187–190.

Andrasfalvy BK, Magee JC (2001) Distance-dependent increase in AMPA receptor number in the dendrites of adult hippocampal CA1 pyramidal neurons. J Neurosci Off J Soc Neurosci 21:9151–9159.

Andrásfalvy BK, Smith MA, Borchardt T, Sprengel R, Magee JC (2003) Impaired regulation of synaptic strength in hippocampal neurons from GluR1-deficient mice. J Physiol 552:35–45.

Araya R, Jiang J, Eisenthal KB, Yuste R (2006) The spine neck filters membrane potentials. Proc Natl Acad Sci U S A 103:17961–17966.

Beaulieu C, Colonnier M (1985) A laminar analysis of the number of round-asymmetrical and flat-symmetrical synapses on spines, dendritic trunks, and cell bodies in area 17 of the cat. J Comp Neurol 231:180–189.

Bekkers JM, Richerson GB, Stevens CF (1990) Origin of variability in quantal size in cultured hippocampal neurons and hippocampal slices. Proc Natl Acad Sci U S A 87:5359–5362.

Berridge MJ (1998) Neuronal calcium signaling. Neuron 21:13–26.

Betz WJ, Bewick GS (1992) Optical analysis of synaptic vesicle recycling at the frog neuromuscular junction. Science 255:200–203.

Biehlmaier O, Neuhauss SCF, Kohler K (2003) Synaptic plasticity and functionality at the cone terminal of the developing zebrafish retina. J Neurobiol 56:222–236.

Bilotta J (2000) Effects of abnormal lighting on the development of zebrafish visual behavior. Behav Brain Res 116:81–87.

Bilotta J, Saszik S, Sutherland SE (2001) Rod contributions to the electroretinogram of the dark-adapted developing zebrafish. Dev Dyn Off Publ Am Assoc Anat 222:564–570.

Bliss TVP, Collingridge GL (2013) Expression of NMDA receptor-dependent LTP in the hippocampus: bridging the divide. Mol Brain 6:5.

Bloodgood BL, Sabatini BL (2007) Nonlinear regulation of unitary synaptic signals by CaV(2.3) voltage-sensitive calcium channels located in dendritic spines. Neuron 53:249–260.

Bloodgood BL, Sabatini BL (2009) NMDA Receptor-Mediated Calcium Transients in Dendritic Spines. In: Biology of the NMDA Receptor (Van Dongen AM, ed) Frontiers in Neuroscience. Boca Raton (FL): CRC Press. Available at: http://www.ncbi.nlm.nih.gov/books/NBK5276/ [Accessed September 22, 2013].

Bloomfield SA (1994) Orientation-sensitive amacrine and ganglion cells in the rabbit retina. J Neurophysiol 71:1672–1691.

Burgess HA, Schoch H, Granato M (2010) Distinct retinal pathways drive spatial orientation behaviors in zebrafish navigation. Curr Biol CB 20:381–386.

Burrill JD, Easter SS Jr (1994) Development of the retinofugal projections in the embryonic and larval zebrafish (Brachydanio rerio). J Comp Neurol 346:583–600.

Catterall WA (2011) Voltage-gated calcium channels. Cold Spring Harb Perspect Biol 3:a003947.

Catterall WA, Few AP (2008) Calcium channel regulation and presynaptic plasticity. Neuron 59:882–901.

Chen T-W, Wardill TJ, Sun Y, Pulver SR, Renninger SL, Baohan A, Schreiter ER, Kerr RA, Orger MB, Jayaraman V, Looger LL, Svoboda K, Kim DS (2013) Ultrasensitive fluorescent proteins for imaging neuronal activity. Nature 499:295–300.

Chen X, Nelson CD, Li X, Winters CA, Azzam R, Sousa AA, Leapman RD, Gainer H, Sheng M, Reese TS (2011) PSD-95 is required to sustain the molecular organization of the postsynaptic density. J Neurosci Off J Soc Neurosci 31:6329–6338.

Conti R, Lisman J (2003) The high variance of AMPA receptor- and NMDA receptor-mediated responses at single hippocampal synapses: Evidence for multiquantal release. Proc Natl Acad Sci 100:4885–4890.

De Jong APH, Schmitz SK, Toonen RFG, Verhage M (2012) Dendritic position is a major determinant of presynaptic strength. J Cell Biol 197:327–337.

Del Bene F, Wyart C, Robles E, Tran A, Looger L, Scott EK, Isacoff EY, Baier H (2010) Filtering of visual information in the tectum by an identified neural circuit. Science 330:669–673.

DEL CASTILLO J, KATZ B (1954) Quantal components of the end-plate potential. J Physiol 124:560–573.

Dodge FA Jr, Rahamimoff R (1967) Co-operative action a calcium ions in transmitter release at the neuromuscular junction. J Physiol 193:419–432.

Dreosti E, Odermatt B, Dorostkar MM, Lagnado L (2009) A genetically encoded reporter of synaptic activity in vivo. Nat Methods 6:883–889.

Easter SS Jr, Nicola GN (1996) The development of vision in the zebrafish (Danio rerio). Dev Biol 180:646–663.

Easter SS, Nicola GN (1997) The development of eye movements in the zebrafish (Danio rerio). Dev Psychobiol 31:267–276.

Eilers J, Augustine GJ, Konnerth A (1995) Subthreshold synaptic Ca2+ signalling in fine dendrites and spines of cerebellar Purkinje neurons. Nature 373:155–158.

El-Husseini AE, Schnell E, Chetkovich DM, Nicoll RA, Bredt DS (2000) PSD-95 involvement in maturation of excitatory synapses. Science 290:1364–1368.

Elias GM, Funke L, Stein V, Grant SG, Bredt DS, Nicoll RA (2006) Synapse-specific and developmentally regulated targeting of AMPA receptors by a family of MAGUK scaffolding proteins. Neuron 52:307–320.

Elstrott J, Anishchenko A, Greschner M, Sher A, Litke AM, Chichilnisky EJ, Feller MB (2008) Direction selectivity in the retina is established independent of visual experience and cholinergic retinal waves. Neuron 58:499–506.

Elstrott J, Feller MB (2010) Direction-selective ganglion cells show symmetric participation in retinal waves during development. J Neurosci Off J Soc Neurosci 30:11197–11201.

Emptage N, Bliss TV, Fine A (1999) Single synaptic events evoke NMDA receptor-mediated release of calcium from internal stores in hippocampal dendritic spines. Neuron 22:115–124.

Emptage NJ, Reid CA, Fine A (2001) Calcium stores in hippocampal synaptic boutons mediate short-term plasticity, store-operated Ca2+ entry, and spontaneous transmitter release. Neuron 29:197–208.

FATT P, KATZ B (1952) Spontaneous subthreshold activity at motor nerve endings. J Physiol 117:109–128.

Fenno L, Yizhar O, Deisseroth K (2011) The development and application of optogenetics. Annu Rev Neurosci 34:389–412.

Fioravante D, Regehr WG (2011) Short-term forms of presynaptic plasticity. Curr Opin Neurobiol 21:269–274.

Forti L, Bossi M, Bergamaschi A, Villa A, Malgaroli A (1997) Loose-patch recordings of single quanta at individual hippocampal synapses. Nature 388:874–878.

Franks KM, Stevens CF, Sejnowski TJ (2003) Independent sources of quantal variability at single glutamatergic synapses. J Neurosci Off J Soc Neurosci 23:3186–3195.

Frerking M, Borges S, Wilson M (1995) Variation in GABA mini amplitude is the consequence of variation in transmitter concentration. Neuron 15:885–895.

Gabriel JP, Trivedi CA, Maurer CM, Ryu S, Bollmann JH (2012) Layer-Specific Targeting of Direction-Selective Neurons in the Zebrafish Optic Tectum. Neuron 76:1147–1160.

Gahtan E, Tanger P, Baier H (2005) Visual prey capture in larval zebrafish is controlled by identified reticulospinal neurons downstream of the tectum. J Neurosci Off J Soc Neurosci 25:9294–9303.

Grama A, Engert F (2012) Direction selectivity in the larval zebrafish tectum is mediated by asymmetric inhibition. Front Neural Circuits 6:59.

Gulledge AT, Carnevale NT, Stuart GJ (2012) Electrical advantages of dendritic spines. PloS One 7:e36007.

Harnett MT, Makara JK, Spruston N, Kath WL, Magee JC (2012) Synaptic amplification by dendritic spines enhances input cooperativity. Nature 491:599–602.

Harris KM, Stevens JK (1989) Dendritic spines of CA 1 pyramidal cells in the rat hippocampus: serial electron microscopy with reference to their biophysical characteristics. J Neurosci Off J Soc Neurosci 9:2982–2997.

Helmchen F, Imoto K, Sakmann B (1996) Ca2+ buffering and action potential-evoked Ca2+ signaling in dendrites of pyramidal neurons. Biophys J 70:1069–1081.

Hendel T, Mank M, Schnell B, Griesbeck O, Borst A, Reiff DF (2008) Fluorescence changes of genetic calcium indicators and OGB-1 correlated with neural activity and calcium in vivo and in vitro. J Neurosci Off J Soc Neurosci 28:7399–7411.

Hering H, Sheng M (2001) Dendritic spines: structure, dynamics and regulation. Nat Rev Neurosci 2:880–888.

Higley MJ, Sabatini BL (2012) Calcium signaling in dendritic spines. Cold Spring Harb Perspect Biol 4:a005686.

Holderith N, Lorincz A, Katona G, Rózsa B, Kulik A, Watanabe M, Nusser Z (2012) Release probability of hippocampal glutamatergic terminals scales with the size of the active zone. Nat Neurosci 15:988–997.

Honkura N, Matsuzaki M, Noguchi J, Ellis-Davies GCR, Kasai H (2008) The subspine organization of actin fibers regulates the structure and plasticity of dendritic spines. Neuron 57:719–729.

Hu M, Easter SS (1999) Retinal neurogenesis: the formation of the initial central patch of postmitotic cells. Dev Biol 207:309–321.

Hubel DH, Wiesel TN (1962) Receptive fields, binocular interaction and functional architecture in the cat's visual cortex. J Physiol 160:106–154.2.

Hubel DH, Wiesel TN (1974) Sequence regularity and geometry of orientation columns in the monkey striate cortex. J Comp Neurol 158:267–293.

Huber D, Gutnisky DA, Peron S, O'Connor DH, Wiegert JS, Tian L, Oertner TG, Looger LL, Svoboda K (2012a) Multiple dynamic representations in the motor cortex during sensorimotor learning. Nature 484:473–478.

Huber D, Gutnisky DA, Peron S, O'Connor DH, Wiegert JS, Tian L, Oertner TG, Looger LL, Svoboda K (2012b) Multiple dynamic representations in the motor cortex during sensorimotor learning. Nature 484:473–478.

Hunter PR, Lowe AS, Thompson ID, Meyer MP (2013) Emergent Properties of the Optic Tectum Revealed by Population Analysis of Direction and Orientation Selectivity. J Neurosci 33:13940–13945.

Jahr CE, Stevens CF (1990) Voltage dependence of NMDA-activated macroscopic conductances predicted by single-channel kinetics. J Neurosci Off J Soc Neurosci 10:3178–3182.

Karunanithi S, Marin L, Wong K, Atwood HL (2002) Quantal size and variation determined by vesicle size in normal and mutant Drosophila glutamatergic synapses. J Neurosci Off J Soc Neurosci 22:10267–10276.

Kasai H, Matsuzaki M, Noguchi J, Yasumatsu N, Nakahara H (2003) Structure-stability-function relationships of dendritic spines. Trends Neurosci 26:360–368.

Katz B, Miledi R (1970) Further study of the role of calcium in synaptic transmission. J Physiol 207:789–801.

Katz Y, Menon V, Nicholson DA, Geinisman Y, Kath WL, Spruston N (2009) Synapse distribution suggests a two-stage model of dendritic integration in CA1 pyramidal neurons. Neuron 63:171–177.

Kay JN, Finger-Baier KC, Roeser T, Staub W, Baier H (2001) Retinal ganglion cell genesis requires lakritz, a Zebrafish atonal Homolog. Neuron 30:725–736.

Kay JN, Huerta ID la, Kim I-J, Zhang Y, Yamagata M, Chu MW, Meister M, Sanes JR (2011a) Retinal Ganglion Cells with Distinct Directional Preferences Differ in Molecular Identity, Structure, and Central Projections. J Neurosci 31:7753–7762.

Kay L, Humphreys L, Eickholt BJ, Burrone J (2011b) Neuronal activity drives matching of pre- and postsynaptic function during synapse maturation. Nat Neurosci 14:688–690.

Kim I-J, Zhang Y, Yamagata M, Meister M, Sanes JR (2008) Molecular identification of a retinal cell type that responds to upward motion. Nature 452:478–482.

Kinoshita M, Ito E, Urano A, Ito H, Yamamoto N (2006) Periventricular efferent neurons in the optic tectum of rainbow trout. J Comp Neurol 499:546–564.

Kolb H, Nelson R, Mariani A (1981) Amacrine cells, bipolar cells and ganglion cells of the cat retina: A Golgi study. Vision Res 21:1081–1114.

Kovalchuk Y, Eilers J, Lisman J, Konnerth A (2000) NMDA receptor-mediated subthreshold Ca(2+) signals in spines of hippocampal neurons. J Neurosci Off J Soc Neurosci 20:1791–1799.

Levick WR (1967) Receptive fields and trigger features of ganglion cells in the visual streak of the rabbit's retina. J Physiol 188:285–307.

Lewis TL, Mao T, Svoboda K, Arnold DB (2009) Myosin-dependent targeting of transmembrane proteins to neuronal dendrites. Nat Neurosci 12:568–576.

Lister JA, Robertson CP, Lepage T, Johnson SL, Raible DW (1999) nacre encodes a zebrafish microphthalmia-related protein that regulates neural-crest-derived pigment cell fate. Dev Camb Engl 126:3757–3767.

Liu G, Choi S, Tsien RW (1999) Variability of neurotransmitter concentration and nonsaturation of postsynaptic AMPA receptors at synapses in hippocampal cultures and slices. Neuron 22:395–409.

London M, Häusser M (2005) Dendritic computation. Annu Rev Neurosci 28:503–532.

Lowe AS, Nikolaou N, Hunter PR, Thompson ID, Meyer MP (2013) A Systems-Based Dissection of Retinal Inputs to the Zebrafish Tectum Reveals Different Rules for Different Functional Classes during Development. J Neurosci 33:13946–13956.

Lutcke H, Murayama M, Hahn T, Margolis DJ, Astori S, zum Alten Borgloh SM, Gobel W, Yang Y, Tang W, Kugler S, Sprengel R, Nagai T, Miyawaki A, Larkum ME, Helmchen F, Hasan MT (2010) Optical Recording of Neuronal Activity with a Genetically-Encoded Calcium Indicator in Anesthetized and Freely Moving Mice. Front Neural Circuits 4 Available at: http://www.ncbi.nlm.nih.gov/pmc/articles/PMC2866455/ [Accessed August 13, 2013].

MacGillavry HD, Kerr JM, Blanpied TA (2011) Lateral organization of the postsynaptic density. Mol Cell Neurosci 48:321–331.

Mackenzie PJ, Kenner GS, Prange O, Shayan H, Umemiya M, Murphy TH (1999) Ultrastructural correlates of quantal synaptic function at single CNS synapses. J Neurosci Off J Soc Neurosci 19:RC13.

Magee JC, Cook EP (2000) Somatic EPSP amplitude is independent of synapse location in hippocampal pyramidal neurons. Nat Neurosci 3:895–903.

Magee JC, Johnston D (1995) Synaptic activation of voltage-gated channels in the dendrites of hippocampal pyramidal neurons. Science 268:301–304.

Mainen ZF, Malinow R, Svoboda K (1999) Synaptic calcium transients in single spines indicate that NMDA receptors are not saturated. Nature 399:151–155.

Mangrum WI, Dowling JE, Cohen ED (2002) A morphological classification of ganglion cells in the zebrafish retina. Vis Neurosci 19:767–779.

Mank M, Santos AF, Direnberger S, Mrsic-Flogel TD, Hofer SB, Stein V, Hendel T, Reiff DF, Levelt C, Borst A, Bonhoeffer T, Hübener M, Griesbeck O (2008) A genetically encoded calcium indicator for chronic in vivo two-photon imaging. Nat Methods 5:805–811.

Mao T, O'Connor DH, Scheuss V, Nakai J, Svoboda K (2008) Characterization and subcellular targeting of GCaMP-type genetically-encoded calcium indicators. PloS One 3:e1796.

Marshel JH, Kaye AP, Nauhaus I, Callaway EM (2012) Anterior-posterior direction opponency in the superficial mouse lateral geniculate nucleus. Neuron 76:713–720.

Marvin JS, Borghuis BG, Tian L, Cichon J, Harnett MT, Akerboom J, Gordus A, Renninger SL, Chen T-W, Bargmann CI, Orger MB, Schreiter ER, Demb JB, Gan W-B, Hires SA, Looger LL (2013) An optimized fluorescent probe for visualizing glutamate neurotransmission. Nat Methods 10:162–170.

Matsuzaki M, Ellis-Davies GC, Nemoto T, Miyashita Y, Iino M, Kasai H (2001) Dendritic spine geometry is critical for AMPA receptor expression in hippocampal CA1 pyramidal neurons. Nat Neurosci 4:1086–1092.

McAllister AK, Stevens CF (2000) Nonsaturation of AMPA and NMDA receptors at hippocampal synapses. Proc Natl Acad Sci U S A 97:6173–6178.

Meek J (1981) A Golgi-electron microscopic study of goldfish optic tectum. I. Description of afferents, cell types, and synapses. J Comp Neurol 199:149–173.

Meek J, Schellart NA (1978) A Golgi study of goldfish optic tectum. J Comp Neurol 182:89–122.

Megías M, Emri Z, Freund TF, Gulyás AI (2001) Total number and distribution of inhibitory and excitatory synapses on hippocampal CA1 pyramidal cells. Neuroscience 102:527–540.

Meyer MP, Smith SJ (2006) Evidence from in vivo imaging that synaptogenesis guides the growth and branching of axonal arbors by two distinct mechanisms. J Neurosci Off J Soc Neurosci 26:3604–3614.

Miesenböck G, De Angelis DA, Rothman JE (1998) Visualizing secretion and synaptic transmission with pH-sensitive green fluorescent proteins. Nature 394:192–195.

Molnár E (2011) Long-term potentiation in cultured hippocampal neurons. Semin Cell Dev Biol 22:506–513.

Mumm JS, Williams PR, Godinho L, Koerber A, Pittman AJ, Roeser T, Chien C-B, Baier H, Wong ROL (2006) In vivo imaging reveals dendritic targeting of laminated afferents by zebrafish retinal ganglion cells. Neuron 52:609–621.

Murnick JG, Dubé G, Krupa B, Liu G (2002) High-resolution iontophoresis for single-synapse stimulation. J Neurosci Methods 116:65–75.

Murphy TH, Baraban JM, Wier WG (1995) Mapping miniature synaptic currents to single synapses using calcium imaging reveals heterogeneity in postsynaptic output. Neuron 15:159–168.

Murthy VN, Sejnowski TJ, Stevens CF (1997) Heterogeneous release properties of visualized individual hippocampal synapses. Neuron 18:599–612.

Nagai T, Yamada S, Tominaga T, Ichikawa M, Miyawaki A (2004) Expanded dynamic range of fluorescent indicators for Ca2+ by circularly permuted yellow fluorescent proteins. Proc Natl Acad Sci U S A 101:10554–10559.

Nelson R, Famiglietti EV Jr, Kolb H (1978) Intracellular staining reveals different levels of stratification for on- and off-center ganglion cells in cat retina. J Neurophysiol 41:472–483.

Nevin LM, Robles E, Baier H, Scott EK (2010) Focusing on optic tectum circuitry through the lens of genetics. BMC Biol 8:126.

Nicholson DA, Trana R, Katz Y, Kath WL, Spruston N, Geinisman Y (2006) Distance-dependent differences in synapse number and AMPA receptor expression in hippocampal CA1 pyramidal neurons. Neuron 50:431–442.

Niell CM, Meyer MP, Smith SJ (2004) In vivo imaging of synapse formation on a growing dendritic arbor. Nat Neurosci 7:254–260.

Niell CM, Smith SJ (2005) Functional imaging reveals rapid development of visual response properties in the zebrafish tectum. Neuron 45:941–951.

Niell CM, Stryker MP (2008) Highly selective receptive fields in mouse visual cortex. J Neurosci Off J Soc Neurosci 28:7520–7536.

Nikolaev A, Leung K-M, Odermatt B, Lagnado L (2013) Synaptic mechanisms of adaptation and sensitization in the retina. Nat Neurosci 16:934–941.

Nikolaou N, Lowe AS, Walker AS, Abbas F, Hunter PR, Thompson ID, Meyer MP (2012) Parametric functional maps of visual inputs to the tectum. Neuron 76:317–324.

Nimchinsky EA, Yasuda R, Oertner TG, Svoboda K (2004) The number of glutamate receptors opened by synaptic stimulation in single hippocampal spines. J Neurosci Off J Soc Neurosci 24:2054–2064.

Noguchi J, Matsuzaki M, Ellis-Davies GCR, Kasai H (2005) Spine-neck geometry determines NMDA receptor-dependent Ca2+ signaling in dendrites. Neuron 46:609–622.

Noguchi J, Nagaoka A, Watanabe S, Ellis-Davies GCR, Kitamura K, Kano M, Matsuzaki M, Kasai H (2011) In vivo two-photon uncaging of glutamate revealing the structure-function relationships of dendritic spines in the neocortex of adult mice. J Physiol 589:2447–2457.

Nusser Z, Lujan R, Laube G, Roberts JD, Molnar E, Somogyi P (1998) Cell type and pathway dependence of synaptic AMPA receptor number and variability in the hippocampus. Neuron 21:545–559.

O'Rourke NA, Cline HT, Fraser SE (1994) Rapid remodeling of retinal arbors in the tectum with and without blockade of synaptic transmission. Neuron 12:921–934.

Odermatt B, Nikolaev A, Lagnado L (2012) Encoding of luminance and contrast by linear and nonlinear synapses in the retina. Neuron 73:758–773.

Ohki K, Chung S, Kara P, Hübener M, Bonhoeffer T, Reid RC (2006) Highly ordered arrangement of single neurons in orientation pinwheels. Nature 442:925–928.

Ohkura M, Sasaki T, Sadakari J, Gengyo-Ando K, Kagawa-Nagamura Y, Kobayashi C, Ikegaya Y, Nakai J (2012) Genetically encoded green fluorescent Ca2+ indicators with improved detectability for neuronal Ca2+ signals. PloS One 7:e51286.

Osakada F, Mori T, Cetin AH, Marshel JH, Virgen B, Callaway EM (2011) New rabies virus variants for monitoring and manipulating activity and gene expression in defined neural circuits. Neuron 71:617–631.

Palmer AE, Giacomello M, Kortemme T, Hires SA, Lev-Ram V, Baker D, Tsien RY (2006) Ca2+ indicators based on computationally redesigned calmodulin-peptide pairs. Chem Biol 13:521–530.

Pang ZP, Shin O-H, Meyer AC, Rosenmund C, Südhof TC (2006) A gain-of-function mutation in synaptotagmin-1 reveals a critical role of Ca2+-dependent soluble N-ethylmaleimide-sensitive factor attachment protein receptor complex binding in synaptic exocytosis. J Neurosci Off J Soc Neurosci 26:12556–12565.

Priebe NJ, Ferster D (2005) Direction selectivity of excitation and inhibition in simple cells of the cat primary visual cortex. Neuron 45:133–145.

Prieto ML, Wollmuth LP (2010) Gating modes in AMPA receptors. J Neurosci Off J Soc Neurosci 30:4449–4459.

Raghavachari S, Lisman JE (2004) Properties of quantal transmission at CA1 synapses. J Neurophysiol 92:2456–2467.

Ramdya P, Engert F (2008) Emergence of binocular functional properties in a monocular neural circuit. Nat Neurosci 11:1083–1090.

Reid CA, Fabian-Fine R, Fine A (2001) Postsynaptic calcium transients evoked by activation of individual hippocampal mossy fiber synapses. J Neurosci Off J Soc Neurosci 21:2206–2214.

Ribrault C, Sekimoto K, Triller A (2011) From the stochasticity of molecular processes to the variability of synaptic transmission. Nat Rev Neurosci 12:375–387.

Robles E, Filosa A, Baier H (2013) Precise lamination of retinal axons generates multiple parallel input pathways in the tectum. J Neurosci Off J Soc Neurosci 33:5027–5039.

Robles E, Smith SJ, Baier H (2011) Characterization of genetically targeted neuron types in the zebrafish optic tectum. Front Neural Circuits 5:1.

Sabatini BL, Svoboda K (2000) Analysis of calcium channels in single spines using optical fluctuation analysis. Nature 408:589–593.

Sampedro MN, Bussineau CM, Cotman CW (1981) Postsynaptic density antigens: preparation and characterization of an antiserum against postsynaptic densities. J Cell Biol 90:675–686.

Schikorski T, Stevens CF (1997) Quantitative ultrastructural analysis of hippocampal excitatory synapses. J Neurosci Off J Soc Neurosci 17:5858–5867.

Schiller J, Schiller Y, Clapham DE (1998) NMDA receptors amplify calcium influx into dendritic spines during associative pre- and postsynaptic activation. Nat Neurosci 1:114–118.

Schmitt EA, Dowling JE (1999) Early retinal development in the zebrafish, Danio rerio: light and electron microscopic analyses. J Comp Neurol 404:515–536.

Schneggenburger R, Zhou Z, Konnerth A, Neher E (1993) Fractional contribution of calcium to the cation current through glutamate receptor channels. Neuron 11:133–143.

Scott EK, Baier H (2009) The cellular architecture of the larval zebrafish tectum, as revealed by gal4 enhancer trap lines. Front Neural Circuits 3:13.

Seelig JD, Chiappe ME, Lott GK, Dutta A, Osborne JE, Reiser MB, Jayaraman V (2010) Two-photon calcium imaging from head-fixed Drosophila during optomotor walking behavior. Nat Methods 7:535–540.

Segev I (2006) What do dendrites and their synapses tell the neuron? J Neurophysiol 95:1295–1297.

Shaner NC, Lin MZ, McKeown MR, Steinbach PA, Hazelwood KL, Davidson MW, Tsien RY (2008) Improving the photostability of bright monomeric orange and red fluorescent proteins. Nat Methods 5:545–551.

Sheng M, Kim E (2011) The postsynaptic organization of synapses. Cold Spring Harb Perspect Biol 3.

Smetters D, Majewska A, Yuste R (1999) Detecting action potentials in neuronal populations with calcium imaging. Methods San Diego Calif 18:215–221.

Smith MA, Ellis-Davies GCR, Magee JC (2003) Mechanism of the distance-dependent scaling of Schaffer collateral synapses in rat CA1 pyramidal neurons. J Physiol 548:245–258.

Spacek J, Hartmann M (1983) Three-dimensional analysis of dendritic spines. I. Quantitative observations related to dendritic spine and synaptic morphology in cerebral and cerebellar cortices. Anat Embryol (Berl) 167:289–310.

Sterratt DC, Groen MR, Meredith RM, van Ooyen A (2012) Spine calcium transients induced by synaptically-evoked action potentials can predict synapse location and establish synaptic democracy. PLoS Comput Biol 8:e1002545.

Stuermer CA (1988) Retinotopic organization of the developing retinotectal projection in the zebrafish embryo. J Neurosci Off J Soc Neurosci 8:4513–4530.

Südhof TC (2008) Neurotransmitter release. Handb Exp Pharmacol:1–21.

Sumbre G, Poo M-M (2013) Monitoring tectal neuronal activities and motor behavior in zebrafish larvae. Cold Spring Harb Protoc 2013.

Sutton MA, Ito HT, Cressy P, Kempf C, Woo JC, Schuman EM (2006) Miniature neurotransmission stabilizes synaptic function via tonic suppression of local dendritic protein synthesis. Cell 125:785–799.

Svoboda K, Helmchen F, Denk W, Tank DW (1999) Spread of dendritic excitation in layer 2/3 pyramidal neurons in rat barrel cortex in vivo. Nat Neurosci 2:65–73.

Takamori S et al. (2006) Molecular anatomy of a trafficking organelle. Cell 127:831–846.

Thiagarajan TC, Lindskog M, Tsien RW (2005) Adaptation to synaptic inactivity in hippocampal neurons. Neuron 47:725–737.

Tian L, Hires SA, Mao T, Huber D, Chiappe ME, Chalasani SH, Petreanu L, Akerboom J, McKinney SA, Schreiter ER, Bargmann CI, Jayaraman V, Svoboda K, Looger LL (2009) Imaging neural activity in worms, flies and mice with improved GCaMP calcium indicators. Nat Methods 6:875–881.

Venkataramani S, Taylor WR (2010) Orientation selectivity in rabbit retinal ganglion cells is mediated by presynaptic inhibition. J Neurosci Off J Soc Neurosci 30:15664–15676.

Wachowiak M, Economo MN, Díaz-Quesada M, Brunert D, Wesson DW, White JA, Rothermel M (2013) Optical Dissection of Odor Information Processing In Vivo Using GCaMPs Expressed in Specified Cell Types of the Olfactory Bulb. J Neurosci 33:5285–5300.

Walker AS, Burrone J, Meyer MP (2013) Functional imaging in the zebrafish retinotectal system using RGECO. Front Neural Circuits 7:34.

Wall MJ, Usowicz MM (1998) Development of the quantal properties of evoked and spontaneous synaptic currents at a brain synapse. Nat Neurosci 1:675–682.

Wallace DJ, Meyer zum Alten Borgloh S, Astori S, Yang Y, Bausen M, Kügler S, Palmer AE, Tsien RY, Sprengel R, Kerr JND, Denk W, Hasan MT (2008) Single-spike detection in vitro and in vivo with a genetic Ca2+ sensor. Nat Methods 5:797–804.

Wei W, Hamby AM, Zhou K, Feller MB (2011) Development of asymmetric inhibition underlying direction selectivity in the retina. Nature 469:402–406.

Weitz AC, Behrend MR, Lee NS, Klein RL, Chiodo VA, Hauswirth WW, Humayun MS, Weiland JD, Chow RH (2013) Imaging the response of the retina to electrical stimulation with genetically encoded calcium indicators. J Neurophysiol 109:1979–1988.

Weng S, Sun W, He S (2005) Identification of ON-OFF direction-selective ganglion cells in the mouse retina. J Physiol 562:915–923.

Wenthold RJ, Petralia RS, Blahos J II, Niedzielski AS (1996) Evidence for multiple AMPA receptor complexes in hippocampal CA1/CA2 neurons. J Neurosci Off J Soc Neurosci 16:1982–1989.

Williams SR, Stuart GJ (2002) Dependence of EPSP efficacy on synapse location in neocortical pyramidal neurons. Science 295:1907–1910.

Wu X-S, Xue L, Mohan R, Paradiso K, Gillis KD, Wu L-G (2007) The origin of quantal size variation: vesicular glutamate concentration plays a significant role. J Neurosci Off J Soc Neurosci 27:3046–3056.

Xiao T, Baier H (2007) Lamina-specific axonal projections in the zebrafish tectum require the type IV collagen Dragnet. Nat Neurosci 10:1529–1537.

Xu J, Pang ZP, Shin O-H, Sudhof TC (2009) Synaptotagmin-1 functions as the Ca2+-sensor for spontaneous release. Nat Neurosci 12:759–766.

Yamada Y, Mikoshiba K (2012) Quantitative comparison of novel GCaMP-type genetically encoded Ca(2+) indicators in mammalian neurons. Front Cell Neurosci 6:41.

Yamagata M, Sanes JR (2012) Expanding the Ig superfamily code for laminar specificity in retina: expression and role of contactins. J Neurosci Off J Soc Neurosci 32:14402–14414.

Yamashita T, Ishikawa T, Takahashi T (2003) Developmental increase in vesicular glutamate content does not cause saturation of AMPA receptors at the calyx of held synapse. J Neurosci Off J Soc Neurosci 23:3633–3638.

Yasuda R, Sabatini BL, Svoboda K (2003) Plasticity of calcium channels in dendritic spines. Nat Neurosci 6:948–955.

Yonehara K, Balint K, Noda M, Nagel G, Bamberg E, Roska B (2011) Spatially asymmetric reorganization of inhibition establishes a motion-sensitive circuit. Nature 469:407–410.

Yoshida K, Watanabe D, Ishikane H, Tachibana M, Pastan I, Nakanishi S (2001) A key role of starburst amacrine cells in originating retinal directional selectivity and optokinetic eye movement. Neuron 30:771–780.

Yuste R, Majewska A, Cash SS, Denk W (1999) Mechanisms of calcium influx into hippocampal spines: heterogeneity among spines, coincidence detection by NMDA receptors, and optical quantal analysis. J Neurosci Off J Soc Neurosci 19:1976–1987.

Zhao C, Dreosti E, Lagnado L (2011a) Homeostatic Synaptic Plasticity through Changes in Presynaptic Calcium Influx. J Neurosci 31:7492–7496.

Zhao X, Chen H, Liu X, Cang J (2013) Orientation-selective Responses in the Mouse Lateral Geniculate Nucleus. J Neurosci Off J Soc Neurosci 33:12751–12763.

Zhao Y, Araki S, Wu J, Teramoto T, Chang Y-F, Nakano M, Abdelfattah AS, Fujiwara M, Ishihara T, Nagai T, Campbell RE (2011b) An expanded palette of genetically encoded Ca^{2+} indicators. Science 333:1888–1891.

Zito K, Scheuss V (2009) NMDA Receptor Function and Physiological Modulation: Encyclopedia of Neuroscience. Ed. Squire, L.R. Elsevier Academic Press.